CERN - LHCC-2013-006
ATLAS - TDR-20-2013
June, 2013

ATLAS

New Small Wheel

Technical Design Report

Technical Design Report
New Small Wheel

Issue:	1
Reference:	CERN-LHCC-2013-006
	ATLAS-TDR-020
Created:	June 2013
Last modified:	July 2013
Prepared by:	ATLAS Collaboration

In order to benefit from the expected high luminosity performance that will be provided by the Phase-I upgraded LHC, the first station of the ATLAS muon end-cap system (Small Wheel, SW) will need to be replaced. The New Small Wheel (NSW) will have to operate in a high background radiation region (up to 15 kHz/cm^2) while reconstructing muon tracks with high precision as well as furnishing information for the Level-1 trigger. These performance criteria are demanding. In particular, the precision reconstruction of tracks for offline analysis requires a spatial resolution of about 100 µm, and the Level-1 trigger track segments have to be reconstructed online with an angular resolution of approximately 1 mrad. The NSW will have two chamber technologies, one primarily devoted to the Level-1 trigger function (small-strip Thin Gap Chambers, sTGC) and one dedicated to precision tracking (Micromegas detectors, MM). The sTGC are primarily deployed for triggering given their single bunch crossing identification capability. The MM detectors have exceptional precision tracking capabilities due to their small gap (5 mm) and strip pitch (approximately 0.5 mm). Such a precision is crucial to maintain the current ATLAS muon momentum resolution in the high background environment of the upgraded LHC. The MM chambers can, at the same time, confirm the existence of track segments found by the muon end-cap middle station (Big Wheels) online. The sTGC also has the ability to measure offline muon tracks with good precision, so the sTGC-MM chamber technology combination forms a fully redundant detector system for triggering and tracking both for online and offline functions. This detector combination has been designed to be able to also provide excellent performance for the eventual High Luminosity LHC upgrade.

The ATLAS Collaboration

Argentina
Universidad de Buenos Aires, Buenos Aires

Universidad Nacional de La Plata, La Plata

Armenia
Yerevan Physics Institute, Yerevan

Australia
University of Adelaide, Adelaide

Research Centre for High Energy Physics, Melbourne University, Melbourne

University of Sydney, School of Physics, Sydney

Austria
Institut für Astro- und Teilchenphysik, University of Innsbruck, Innsbruck

Fachhochschule Wiener Neustadt (FHWN), Wiener Neustadt

Azerbaijan Republic
Institute of Physics, Azerbaijan Academy of Sciences, Baku

Republic of Belarus
Institute of Physics, National Academy of Sciences of Belarus, Minsk

National Centre for Particle & High Energy Physics, Minsk

Brazil
Universidade Federal de Juiz de Fora, Universidade Federal do Rio De Janeiro, COPPE/EE/IF, Rio de Janeiro, Universidade Federal de Sao Joao del Rei and Universidade de Sao Paulo

Canada
University of Alberta, Edmonton

University of Carleton, Carleton

University of Montreal, Group of Particle Physics, Montreal, Quebec

Department of Physics, McGill University, Montreal

Simon Fraser University, Burnaby, BC

Department of Physics, University of Toronto, Toronto

TRIUMF, Vancouver and York University, Toronto

Department of Physics, University of British Columbia, Vancouver

University of Victoria, Victoria

CERN
European Laboratory for Particle Physics (CERN), Geneva

Chile
Joint team from Pontificia Universidad Católica de Chile, Santiago and Universidad Técnica Federico Santa María, Valparaíso

China
Chinese cluster formed by IHEP Beijing, Nanjing, Shandong and Heifei

Colombia
Universidad Antonio Narino (UAN), Bogotá

Czech Republic
Palacký University, Olomouc

Academy of Sciences of the Czech Republic, Institute of Physics and Institute of Computer Science, Prague

Charles University in Prague, Faculty of Mathematics and Physics, Prague

Czech Technical University in Prague, Faculty of Nuclear Sciences and Physical Engineering, Faculty of Mechanical Engineering, Prague

Denmark
Niels Bohr Institute, University of Copenhagen, Copenhagen

France
Laboratoire d'Annecy-le-Vieux de Physique de Particules (LAPP), CNRS-IN2P3, Annecy-le-Vieux

Laboratoire de Physique Corpusculaire, Université Blaise Pascal, CNRS-IN2P3, Clermont-Ferrand

Laboratoire de Physique Subatomique et de Cosmologie de Grenoble (LPSC), CNRS-IN2P3, Université Joseph Fourier, Grenoble

Centre de Physique de Particules de Marseille (CPPM), CNRS-IN2P3, Marseille

Laboratoire de l'Accélérateur Linéaire (LAL), CNRS-IN2P3, Orsay

Laboratoire de Physique Nucléaire et de Hautes Energies (LPNHE), Universités de Paris VI et VII, CNRS-IN2P3, Paris

Commisariat à l'Energie Atomique et aux Energies Alternatives (CEA), DSM/IRFU, Centre d'Etudes de Saclay, Gif-sur-Yvette

Georgia
Institute of Physics of the Georgian Academy of Sciences and Tbilisi State University, Tbilisi

Germany

Physikalisches Institut, University of Bonn, Bonn

Deutsches Elektronen-Synchrotron (DESY), Hamburg and Zeuthen

TU Dortmund, Experimentelle Physik IV, Dortmund

Technical University Dresden, Dresden

Fakultät für Mathematik und Physik, Albert-Ludwigs-Universität, Freiburg

Justus-Liebig-Universität, Giessen

Fakultät für Physik, II. Physikalisches Institut, Georg-August-Universität, Göttingen

Ruprecht-Karls-Universität Heidelberg, Kirchhoff-Institut für Physik and Zentrales Institut für Technische Informatik (ZITI), Heidelberg

Institut für Physik, Humboldt Universität, Berlin

Institut für Physik, Universität Mainz, Mainz

Sektion Physik, Ludwig-Maximilians-Universität München, München

Max-Planck-Institut für Physik, München

Fachbereich Physik, Universität Siegen, Siegen

Fachbereich Physik, Bergische Universität, Wuppertal

Julius-Maximilians-University, Würzburg

Greece
National Technical University of Athens, Athens

University of Athens, Athens

University of Thessaloniki, High Energy Physics Department and Department of Mechanical Engineering, Thessaloniki

Israel
Department of Physics, Technion, Haifa

School of Physics, Tel Aviv University, Tel Aviv

Department of Particle Physics, The Weizmann Institute of Science, Rehovot

Italy
Dipartimento di Fisica dell' Università di Bologna e I.N.F.N., Bologna

Dipartimento di Fisica dell' Università della Calabria e I.N.F.N., Cosenza

Laboratori Nazionali di Frascati dell' I.N.F.N., Frascati

Dipartimento di Fisica dell' Università di Genovae I.N.F.N., Genova

Dipartimento di Fisica dell' Università di Lecce e I.N.F.N., Lecce

Dipartimento di Fisica dell' Università di Milano e I.N.F.N., Milano

Dipartimento di Scienze Fisiche, Università di Napoli 'Federico II' e I.N.F.N., Napoli

Dipartimento di Fisica Nucleare e Teorica dellÕ Università di Pavia e I.N.F.N., Pavia

Dipartimento di Fisica dell' Università di Pisa e I.N.F.N., Pisa

Dipartimento di Fisica dell' Università di Roma I 'La Sapienza e I.N.F.N., Roma

Dipartimento di Fisica dell' Università di Roma II 'Tor Vergata' e I.N.F.N., Roma

Dipartimento di Fisica dell' Università di R oma III 'Roma Tre' e I.N.F.N., Roma

Dipartimento di Fisica dell' Università di Udine e I.N.F.N., Udine, I.C.T.P. e I.N.F.N., Trieste

Japan
Hiroshima Institute of Technology, Hiroshima

KEK, High Energy Accelerator Research Organization, Tsukuba

Kobe University, Kobe

Department of Physics, Kyoto University, Kyoto

Kyoto University of Education, Kyoto

Kyushu University, Kyushu

Nagasaki Institute of Applied Science, Nagasaki

Nagoya University, Nagoya

Faculty of Science, Okayama University, Okayama

Osaka University, Osaka

Faculty of Science, Shinshu University, Matsumoto

International Center for Elementary Particle Physics and Department of Physics, The University of Tokyo

Tokyo Institute of Technology, Tokyo

Physics Department, Tokyo Metropolitan University, Tokyo

Institute of Physics, University of Tsukuba, Tsukuba

Waseda University, Tokyo

Morocco
Faculté des Sciences Ain Chock, Université Hassan II, Casablanca, Université Mohamed Premier et LPTM, Oujda, Université Cadi Ayyat et LPHEA, Marrakech, CNESTEN et Université Mohamed V, Rabat

Netherlands
FOM - Institute SAF NIKHEF and University of Amsterdam/NIKHEF, Amsterdam

Radboud University Nijmegen and NIKHEF, Nijmegen

Norway
University of Bergen, Bergen

University of Oslo, Oslo

Poland
Institute of Nuclear Physics (IFJ PAN), Polish Academy of Sciences, Cracow

Faculty of Physics and Applied Computer Science, AGH University of Science and Technology and Marian Smoluchowski Institute of Physics, Jagiellonian University, Cracow

Portugal
Laboratorio de Instrumentacao e Física Experimental de Partículas (LIP), in collaboration with: University of Lisboa, University of Coimbra, University Católica-Figueira da Foz, University Nova de Lisboa, Lisbon and University of Granada

Romania
National Institute of Physics and Nuclear Engineering, Institute of Atomic Physics, Bucharest, ITIM, Cluj Napoca, West University, Timisoara and University Politehnica Bucharest

Russia
Institute for Theoretical and Experimental Physics (ITEP), Moscow

P.N. Lebedev Institute of Physics, Moscow

Moscow Engineering & Physics Institute (MEPhI), Moscow

Moscow State University, Moscow

Budker Institute of Nuclear Physics (BINP), Novosibirsk

State Research Center of the Russian Federation - Institute for High Energy Physics (IHEP), Protvino

Petersburg Nuclear Physics Institute (PNPI), St. Petersburg

JINR
Joint Institute for Nuclear Research, Dubna

Serbia
Institute of Physics, University of Belgrade and Vinca Institute of Nuclear Sciences, Belgrade

Slovak Republic
Bratislava University, Bratislava, and Institute of Experimental Physics of the Slovak Academy of Sciences, Kosice

Slovenia
Jožef Stefan Institute and Department of Physics, University of Ljubljana, Ljubljana

South Africa
University of Cape Town, University of Johannesburg (UJ) and University of the Witwatersrand (WITS), Johannesburg

Spain
Institut de Física d'Altes Energies (IFAE), Universitat Autónoma de Barcelona, Bellaterra (Barcelona)

Physics Department, Universidad Autónoma de Madrid, Madrid

Instituto de Física Corpuscular (IFIC), Centro Mixto UVEG-CSIC, Valencia and Instituto de Microelectrónica de Barcelona, Bellaterra (Barcelona)

Sweden
Fysiska institutionen, Lunds universitet, Lund

Royal Institute of Technology (KTH), Stockholm

Stockholm University, Stockholm

University of Uppsala, Department of Physics and Astronomy, Uppsala

Switzerland
University of Bern, Albert Einstein Center for Fundamental Physics, Laboratory for High Energy Physics, Bern

Section de Physique, Université de Genève, Geneva

Taipei
Academia Sinica, Taipei

Turkey
Department of Physics, Ankara University, Gazi University and TOBB ETU, Ankara

Department of Physics, Bogazici University, Dogus University and Gaziantep University, Istanbul

United Kingdom
School of Physics and Astronomy, The University of Birmingham, Birmingham

University of Sussex, Brighton

Cavendish Laboratory, University of Cambridge, Cambridge

University of Warwick, Coventry

School of Physics & Astronomy, University of Edinburgh, Edinburgh

Department of Physics and Astronomy, University of Glasgow, Glasgow

Physics Department, Lancaster University, Lancaster

University of Liverpool, Liverpool

Department of Physics, Queen Mary and Westfield College, University of London, London

Department of Physics, Royal Holloway, University of London, Egham

Department of Physics and Astronomy, University College London, London

Department of Physics and Astronomy, University of Manchester, Manchester

Department of Physics, Oxford University, Oxford

Rutherford Appleton Laboratory, Science and Technology Facilities Council, Didcot

Department of Physics, University of Sheffield, Sheffield

United States of America
State University of New York at Albany, New York

Argonne National Laboratory, Argonne, Illinois

University of Arizona, Tucson, Arizona

Department of Physics, The University of Texas at Arlington, Arlington, Texas

Lawrence Berkeley National Laboratory and University of California, Berkeley, California

Physics Department of the University of Boston , Boston, Massachusetts

Brandeis University, Department of Physics, Waltham, Massachusetts

Brookhaven National Laboratory (BNL), Upton, New York

University of Chicago, Enrico Fermi Institute, Chicago, Illinois

Nevis Laboratory, Columbia University, Irvington, New York

University of Texas at Dallas, Dallas, Texas

Department of Physics, Duke University, Durham, North Carolina

Department of Physics, Hampton University, Virginia

Department of Physics, Harvard University, Cambridge, Massachusetts

Indiana University, Bloomington, Indiana

Iowa State University, Ames, Iowa

University of Iowa, Iowa City, Iowa

University of California, Irvine, California

Louisiana Tech University, Louisiana

University of Massachusetts, Amherst, Massachusetts

Massachusetts Institute of Technology, Department of Physics, Cambridge, Massachusetts

Michigan State University, Department of Physics and Astronomy, East Lansing, Michigan

University of Michigan, Department of Physics, Ann Arbor, Michigan

Department of Physics, New Mexico University, Albuquerque, New Mexico

Department of Physics, New York University, New York

Northern Illinois University, DeKalb, Illinois

Ohio State University, Columbus, Ohio

Department of Physics and Astronomy, University of Oklahoma

Oklahoma State University, Oklahoma

University of Oregon, Eugene, Oregon

Department of Physics, University of Pennsylvania, Philadelphia, Pennsylvania

University of Pittsburgh, Pittsburgh, Pennsylvania

Institute for Particle Physics, University of California, Santa Cruz, California

SLAC National Accelerator Laboratory, Stanford, California

Physics Department, Southern Methodist University, Dallas, Texas

State University of New York at Stony Brook, New York

Tufts University, Medford, Massachusetts

High Energy Physics, University of Illinois, Urbana, Illinois

Department of Physics, Department of Mechanical Engineering, University of Washington, Seattle, Washington

Department of Physics, University of Wisconsin, Madison, Wisconsin

Yale University, New Haven, Connecticut

Contents

1 Overview

1.1 Introduction

The Large Hadron Collider (LHC) complex will be upgraded in several phases which will allow the reach of the physics program to be significantly extended. Following the first long shutdown (LS1) during 2013-2014, the accelerator energy will be increased to close to the design 7 TeV per beam and the luminosity will reach or exceed the design value of $1 \times 10^{34}\,\mathrm{cm}^{-2}\,\mathrm{s}^{-1}$. After the second long shutdown (LS2) in 2018, the accelerator luminosity will be increased to $2\text{–}3 \times 10^{34}\,\mathrm{cm}^{-2}\,\mathrm{s}^{-1}$, allowing ATLAS to collect approximately 100 fb^{-1}/year. A subsequent upgrade step is planned which will make significant changes to the interaction point (IP) region in addition to improvements to other parts of the accelerator complex. These improvements will result in the luminosity increasing to $5 \times 10^{34}\,\mathrm{cm}^{-2}\,\mathrm{s}^{-1}$ (with luminosity leveling) [1]. The integrated luminosity with this ultimate upgrade will be $3000\,\mathrm{fb}^{-1}$ after about 10 years of operation.

The ATLAS experiment [2] was designed for a broad physics programme, including the capability of discovering the Higgs boson over a wide mass range and performing searches for the production of heavy particles that would indicate physics beyond the standard model, such as SUSY particles, as well as searches for other massive objects. In order to take advantage of the improved LHC operation the ATLAS detector must be upgraded to have better performance at higher luminosity, following the same schedule as the LHC upgrade. Figure 1.1 shows an approximate timeline for the planned LHC and ATLAS upgrades.

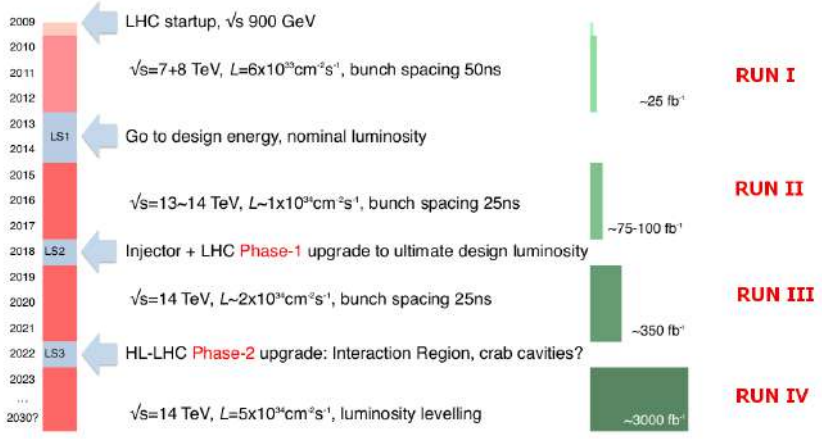

Figure 1.1: An approximate timeline of the scheduled LHC and ATLAS upgrades.

The main focus of the Phase-I ATLAS upgrade (2018) [3] is on the Level-1 trigger. The objective is to sharpen the trigger threshold turn-on as well as discriminate against background while maintaining the low transverse momentum (p_{T}) threshold for single leptons (e and μ) and keeping the Level-1 rate at a manageable level. Upgrades are planned for both the muon and the calorimeter trigger systems, without which the single lepton Level-1 triggers would have to be either pre-scaled or p_{T} threshold raised, resulting in a significant loss of acceptance for many interesting physics processes. The Phase-II upgrade [4] of ATLAS includes a full replacement of the central tracking system as well as major upgrades of the trigger and readout systems.

The recent discovery of the Higgs boson at a mass of about 125 GeV has engendered detailed studies of the nature of the new boson. Continuing these studies with higher statistics and higher energy will be a major topic for the forthcoming upgraded LHC physics programme. The ATLAS detector will be used to probe new physics beyond the standard model - such as by precise measurements of the Higgs coupling to gauge bosons and fermions and studies of Higgs rare decays ($H \to \mu\mu$, Higgs self-coupling etc.), together with a comparison with the standard model expectations. While high luminosity will provide more data, it is essential that the ATLAS detector is still able to operate in the higher background environment and while maintaining its performance as good as that at lower luminosities. The importance of these upgrades to various physics cases are discussed in section 1.3 and also in [5].

1.2 Upgrade of the muon spectrometer: New Small Wheels

The Phase-I upgrade of the ATLAS muon spectrometer [6] focuses on the end-cap region. Figure 1.2 shows a cross section of the ATLAS detector in z-y plane. The barrel system covers the η region of $|\eta| < 1.0$ whereas the end-cap system covers the $1.0 < |\eta| < 2.7$ for muon tracking and $1.0 < |\eta| < 2.4$ for Level-1 trigger. The barrel and end-cap systems consist of three stations each, measuring the muon momentum based on the curvature in the ATLAS toroid magnets.

At high luminosity the following two points are of particular importance:

- The performance of the muon tracking chambers (in particular in the end-cap region) degrades with the expected increase of cavern background rate. An extrapolation from the observed rates at the lower luminosity conditions of the 2012 run to high luminosity and high energy conditions indicates a substantial degradation of tracking performance, both in terms of efficiency and resolution in the inner end-cap station (at z=7 m), the 'Small Wheels'. Given that the high resolution muon momentum measurement crucially depends on the presence of measured points at the Small Wheel level (i.e. in front of the end-cap toroid magnet), this degradation is detrimental for the performance of the ATLAS detector.
- The Level-1 muon trigger in the end-cap region is based on track segments in the TGC chambers of the middle muon station (End-cap Muon detector, EM) located after the end-cap toroid magnet[1]. The transverse momentum, p_{T}, of the muon is determined by the angle of the segment with respect to the direction pointing to the interaction point. A significant part of the muon trigger rate in the end-caps is background. Low energy particles, mainly protons, generated in the material located between the Small Wheel and the EM station, produce fake triggers by hitting the end-cap trigger chambers at an angle similar to that of real high p_{T} muons. An analysis of 2012 data demonstrates that approximately 90% of the muon triggers in the end-caps are fake. As a consequence the rate of the Level-1 muon trigger in the end-cap is eight to nine times higher than that in the barrel region.

[1] The TGC of the Small Wheel is currently only used for the measurement of azimuthal coordinate, complementary to the radial coordinate by the MDTs.

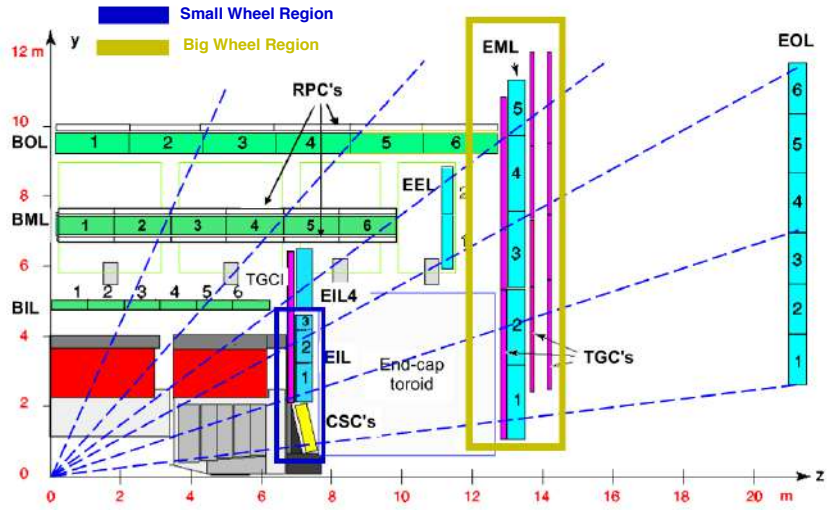

Figure 1.2: A z-y view of 1/4 of the ATLAS detector. The blue boxes indicate the end-cap Monitored Drift Tube chambers (MDT) and the yellow box in the Small Wheel area the Cathode Strip Chambers (CSC). The green boxes are barrel MDT chambers. The trigger chambers, Resistive Plate chambers (RPC) and Thin Gap Chambers (TGC), are indicated by the outlined white and the magenta boxes. This is a cut-out on the muon spectrometer at the large sectors, hence the names 'End-cap Inner Large' (EIL), 'End-cap Middle Large' (EML) and 'End-cap Outer Large' (EOL). The detector regions of the Small Wheel and Big Wheel are also outlined.

Both of these two issues represent a serious limitation on the ATLAS performance beyond design luminosity: reduced acceptance of good muon tracking, and an unacceptable rate of fake high p_{T} Level-1 muon triggers coming from the forward direction.

In order to solve the two problems together, ATLAS proposes to replace the present muon Small Wheels with the 'New Small Wheels' (NSW). The NSW is a set of precision tracking and trigger detectors able to work at high rates with excellent real-time spatial and time resolution. These detectors can provide the muon Level-1 trigger system with online track segments of good angular resolution to confirm that muon tracks originate from the IP. In this way the end-cap fake triggers will be considerably reduced. With the proposed NSW the ATLAS muon system will maintain the full acceptance of its excellent muon tracking at the highest LHC luminosities expected. At the same time the Level-1 low p_{T} (typically $p_{\mathrm{T}} > 20\,\mathrm{GeV}$) single muon trigger rate will be kept at an acceptable level.

The η coverage of the proposed NSW (and the existing Small Wheel) is $1.3 < |\eta| < 2.7$. The remaining region of the inner station $1.0 < |\eta| < 1.3$ is covered by the existing EIL4 detectors of the current muon end-cap system. The TGC chamber in EIL4 will be used to provide a rough confirmation that a particle has traversed the end-cap toroid zone, reducing the fake end-cap triggers in this region. The EIL4 chambers however only cover about 50% of the full azimuthal angle, while the rest of the space taken by the barrel toroid coils. A plan for a small scale upgrade is being studied to fill the uncovered region.

Prior to the installation of the NSW in 2018, the existing TGC chambers of the Small Wheel and EIL4 will be integrated in the end-cap trigger system during LS1 to reduce fake triggers within a limited acceptance $1.0 < |\eta| < 1.9$. Due to the small number of layers (2 layers/chamber) and coarse spatial segmentation of the existing detector, only a rough hit position can be used

for confirmation of the end-cap trigger. The expected rate reduction is about 30%. This will be deployed during Run II after LS1 to improve the end-cap Level-1 trigger and to test the basic concept of the trigger upgrade using the NSW.

The design of the NSW meets the requirement for a very good segment angle resolution of 1 mrad at the Level-1 trigger. Background in the NSW high track density environment can be heavily suppressed using this angular resolution. It is also an important step towards a further improvement of the muon Level-1 trigger system foreseen in the Phase-II upgrade for even higher luminosity (chapter 15). For the Phase-II upgrade the Level-1 latency will be increased so that more selective triggers from the calorimeter and the new Level-1 track trigger as well as the muon system can be applied. The Phase-II upgrade will substantially improve the p_{T} resolution of the Level-1 muon trigger, sharpening the threshold turn-on and reducing the contribution from muons of lower p_{T} below the nominal threshold. This will be achieved by using the information of the precision tracking detectors (Monitored Drift Tubes, MDT) as part of the muon end-cap trigger system and by combining it with the segment angle provided by the NSW.

1.3 Impact on physics performance

In this section it is shown that a single-muon trigger with a threshold of 20–25 GeV is of great importance for the future ATLAS physics program, particularly in light of the recent discovery of a Higgs boson with a mass of 125 GeV. For several decay and production modes of the Higgs boson a single-lepton trigger in this p_{T} range is important. With the current Small Wheel detector the trigger rate for such a trigger is prohibitively large at the high luminosities expected after LS2.

The rate of the single muon Level-1 trigger will increase proportionally to the instantaneous luminosity as the rates of muons in the system and background tracks increase. Other effects such as event pileup will not be an issue for the muon system. The plateau efficiency for the single μ Level-1 trigger is currently about 70% in the barrel (due mainly to acceptance holes) and about 90% in the end-cap. This trigger efficiency is expected to be maintained also at higher luminosity conditions.

Table 1.1 shows a comparison of expected muon Level-1 rate for the present system and the upgrade with the NSW at $L = 3 \times 10^{34}\,\mathrm{cm}^{-2}\,\mathrm{s}^{-1}$, $\sqrt{s} = 14\,\mathrm{GeV}$and 25 ns bunch spacing. Also compared is a scenario of dropping the end-cap from the single muon Level-1 trigger. The allowed

Table 1.1: Expected Level-1 rate (based on 2011 data at 7 TeV) for luminosity $3 \times 10^{34}\,\mathrm{cm}^{-2}\,\mathrm{s}^{-1}$, $\sqrt{s} =$ 14 GeV and 25 ns bunch spacing for different p_{T} threshold with and without the NSW upgrade. The extrapolation uncertainty to 14 TeV is also shown.

L1MU threshold (GeV)	Level-1 rate (kHz)
$p_{\mathrm{T}} > 20$	60 ± 11
$p_{\mathrm{T}} > 40$	29 ± 5
$p_{\mathrm{T}} > 20$ barrel only	7 ± 1
$p_{\mathrm{T}} > 20$ with NSW	22 ± 3
$p_{\mathrm{T}} > 20$ with NSW and EIL4	17 ± 2

total Level-1 rate is 100 kHz, which is determined by the readout bandwidth of the ATLAS subsystems, and this limit will stay until the time of the Phase-II upgrade when significant changes

in the trigger and readout systems will take place. The possible allocation of single lepton Level-1 rates will be about 20 kHz for muons. For the p_{T} threshold at 20 GeV, the muon rate is 60 kHz and thus three times higher than the target rate. Setting the threshold to 40 GeV reduces the rate only by a factor of two such that it still exceeds the target rate by 50%. The reason for the rate reduction not being more significant is the limited momentum resolution of the muon trigger system in this high p_{T} range. An alternative scenario would be to drop the end-cap part from the single muon trigger while maintaining a low p_{T} threshold in the barrel part only. Impacts of higher threshold and restricted acceptance are discussed in section 1.3.1.

For some of the final states involving two or more leptons, di- or multi-lepton triggers may be used where the p_{T} threshold can be kept at lower value, 10-20 GeV. However it is at the cost of reduced efficiency, loss of redundancy and complication in understanding the efficiency as a function of η, p_{T} and other parameters. In the absence of strong correlations, which will be the case for the decays of massive objects, the efficiency for the di-lepton trigger is a product of individual efficiencies. For events with two muons the efficiency of a di-muon trigger is 40–20% lower than for single-muon triggers depending on whether the muons are in the barrel or in the end-caps. The result is a significant loss of Level-1 efficiency. With the Phase-1 upgrade using the NSW, a low p_{T} single muon Level-1 trigger will be possible up to a luminosity of $3 \times 10^{34}\,\mathrm{cm}^{-2}\,\mathrm{s}^{-1}$. Combined triggers, such as di-lepton or lepton + τ triggers, are however useful for specific combination of final state objects where a low p_{T} threshold is important. With the NSW, even at a low p_{T} threshold (e.g. 10 GeV) contamination of muon candidates with fake segments will still be suppressed, improving the quality and rate of combined triggers.

Without the upgrade, the precision tracking capability will be compromised in the Small Wheel region at high luminosity. This impacts the physics performance of the muon spectrometer as discussed in section 1.3.2.

1.3.1 Losing low p_{T} single lepton Level-1 trigger

Higgs production in pp collisions is mainly due to the gg fusion process in which the p_{T} of the produced Higgs bosons tends to be low. In the process $H \to WW^* \to \ell\nu\ell\nu$, leptons from the W decays are also of low p_{T}, particularly the subleading lepton which usually comes from the W^*. Figure 1.3 [7] shows the distribution of lepton p_{T} in the analysis of the $H \to WW^* \to \ell\nu\ell\nu$ process at $\sqrt{s} = 8$ TeV. Clearly seen is that the leptons from the Higgs signals have relatively low p_{T}. A

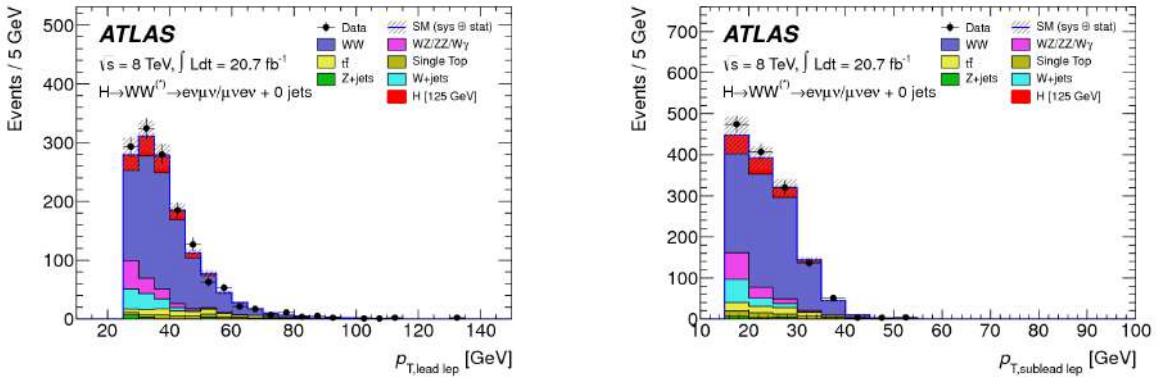

Figure 1.3: p_{T} of the leading (left) and the next to leading (right) leptons, in the candidate events for the $H \to WW^* \to \ell\nu\ell\nu$ channel. The Higgs signal is indicated by the red histogram.

large fraction of the Higgs signals would be lost if the Level-1 p_{T} thresholds had to be raised (e.g. to 40 GeV) at high luminosity in order to keep the Level-1 rate manageable. Another possibility would be not to use the end-cap trigger and to restrict the low p_{T} single muon trigger to only the barrel region ($|\eta| < 1.0$). In this case, the acceptance for the $H \to WW^*$ process would be reduced to about 60%.

With an increased integrated luminosity, Higgs production by the vector boson fusion (VBF) process will become useful overcoming its lower cross-section and taking advantage of its distinct signature. An example is the process $H \to \tau\tau$, where low p_{T} lepton triggers are crucial. Figure 1.4 shows a simulated distribution of leptons in τ pair final states from Higgs decays produced by the VBF process ($m_H = 125\,\mathrm{GeV}$). Within the acceptance $|\eta| < 2.5$, the fraction of events with the

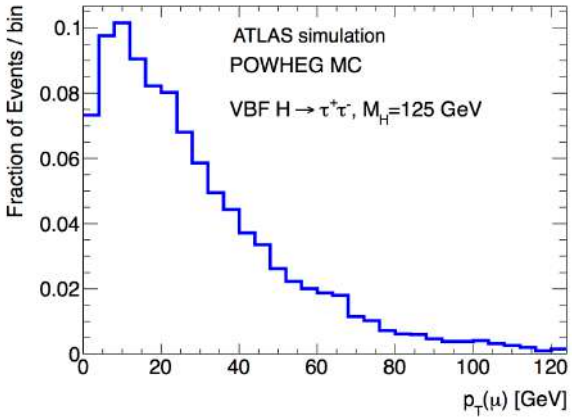

Figure 1.4: The p_{T} distribution of leptons in τ pair final states from simulated Higgs decays, produced by the VBF process ($m_H = 125\,\mathrm{GeV}$, $\sqrt{s} = 14\,\mathrm{TeV}$).

leading muons having p_{T} above 25 GeV is 60% whereas this fraction goes down to 28% for a p_{T} threshold at 40 GeV.

With a large integrated luminosity (a few 100 fb^{-1}) ATLAS may proceed to a precise determination of the Higgs couplings to gauge bosons and fermions using production processes independent of the decay mode, such as Higgs-strahlung from W ($pp \to WH$), where leptons from W decays are used to trigger these events. This process can be used to study systematically the decays into WW, $b\bar{b}$ and $\tau^+\tau^-$ final states. Figure 1.5 shows a simulated distribution of lepton p_{T} from W decays in the WH production process. The lepton spectrum in this process is harder compared to the inclusive $H \to WW^*$ production discussed above. Nevertheless low p_{T} thresholds are still required in order not to lose a significant fraction of WH signal at the level-1 trigger.

Table 1.2 shows a comparison of efficiency from a simulation study for the present detector and the upgrade with NSW for WH with $H \to bb$ and for $H \to WW$. The efficiencies when restricting the single lepton trigger within the barrel region only are also presented. An efficiency loss of 28% is expected for the $H \to WW^*$ case as shown in table 1.2.

Low p_{T} lepton triggers are also important for many SUSY searches where leptons are produced through cascade decays. The kinematic distribution of the final state objects depends on the mass relation between particles in the cascade as well as the couplings. Any increases in the lepton trigger threshold (and other objects like jets and $E_{\mathrm{T}}^{\mathrm{miss}}$) lead to a reduction in experimental sensitivity over the available parameter space of SUSY models. For example, figure 1.6 shows a comparison of sensitivity for two different lepton p_{T} thresholds, 35 GeV with respect to 25 GeV,

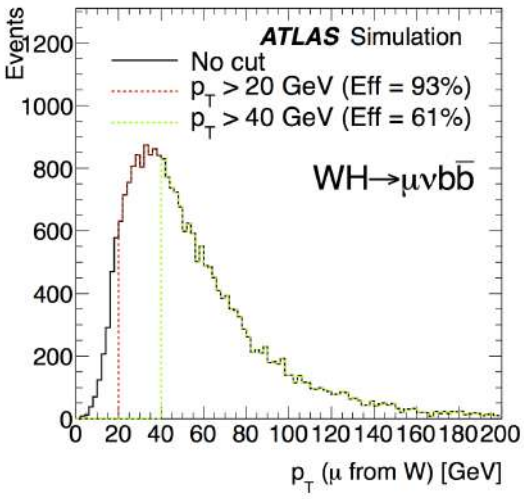

Figure 1.5: Lepton p_{T} from W decays in the WH production channel ($m_H = 125\,\mathrm{GeV}$, $\sqrt{s} = 8\,\mathrm{TeV}$, $\int L = 500\,\mathrm{fb}^{-1}$, lepton $|\eta| < 2.4$).

Table 1.2: The efficiency for WH associated production $pp \to WH$ with $W \to \mu\nu$ and two decay modes of a 125 GeV SM Higgs boson to $H \to b\bar{b}$ and $H \to W^+W^- \to \mu\nu qq'$.

L1MU threshold (GeV)	$H \to b\bar{b}$ (%)	$H \to W^+W^-$ (%)
$p_{\mathrm{T}} > 20$	93	94
$p_{\mathrm{T}} > 40$	61	75
$p_{\mathrm{T}} > 20$ barrel only	43	72
$p_{\mathrm{T}} > 20$ with NSW	90	92

for the process of gluino pair production with each of the gluinos decaying into $q\bar{q}W\tilde{\chi}^0$ [3]. The efficiency is generally lower with higher p_{T} threshold, and this is particularly true for the parameter space giving small mass differences. Similar situations are found in other SUSY processes such as the searches for sleptons and electroweak gauginos.

1.3.2 Losing high quality tracking in end-cap

The potential degradation in tracking efficiency and resolution is expected to have the worst impact for high momentum muons ($p_{\mathrm{T}} > 100\,\mathrm{GeV}$) where the momentum resolution is primarily determined by the muon spectrometer.

A precise measurement of the muon p_{T} requires the presence of track segments in all three muon stations. Losing Small Wheel segments leads to a loss of high quality muon tracking. MDTs lose hits at high occupancy conditions due to the long dead time (of about 800 ns). The CSCs, located at the region with the highest background conditions and having only four detection layers, are also affected by high occupancy arising from overlaps of multiple hits on the readout strips.

Physics cases requiring good p_{T} resolution for high momentum muons include searches for high mass Z', W' and the pseudo-scalar Higgs boson (A) in supersymmetry models, decaying into

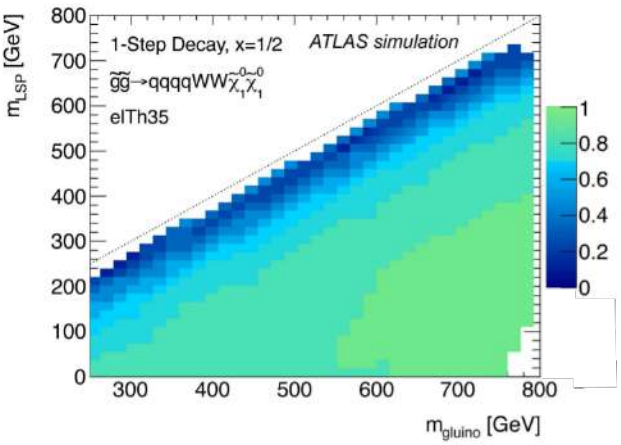

Figure 1.6: Efficiency ratio for two different lepton p_{T} thresholds, 35 GeV relative to 25 GeV.

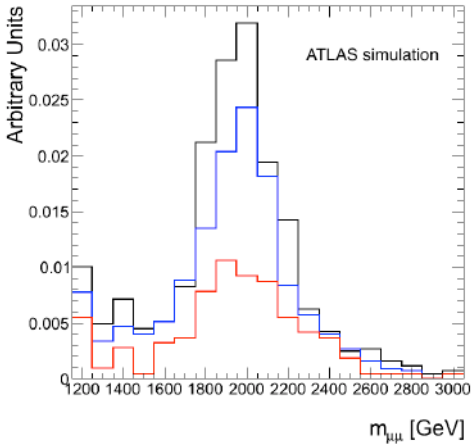

Figure 1.7: Reconstructed $\mu\mu$ mass in the simulated $Z' \to \mu\mu$ events with three different levels of background realized by the data overlay technique. The black, blue and red histograms correspond to luminosity of 0.3, 3 and $5 \times 10^{34}\,\mathrm{cm}^{-2}\,\mathrm{s}^{-1}$ respectively.

muons. High occupancy in the present Small Wheels is studied by overlaying multiple zero-biased data events collected during the 8 TeV LHC runs on simulated events (for details see section 2.2). The loss of efficiency for reconstructing $Z' \to \mu\mu$ can be seen in figure 1.7. Events were selected by the full Z' analysis chain, requiring segments in all three muon stations (for good p_{T} resolution), both muons in the region $1.3 < |\eta| < 2.0$ where the MDT provide the precision measurement. The signal is reduced by 30% for overlaying 10 and 70% for overlaying 20 zero-bias events, corresponding to luminosities of $3 \times 10^{34}\,\mathrm{cm}^{-2}\,\mathrm{s}^{-1}$ and $5 \times 10^{34}\,\mathrm{cm}^{-2}\,\mathrm{s}^{-1}$, respectively.

The fraction of events with at least one muon in the end cap is 58% and scaling the inefficiency to the full Z' angular distribution an overall efficiency of about 25% is obtained at a luminosity of $5 \times 10^{34}\,\mathrm{cm}^{-2}\,\mathrm{s}^{-1}$

2 Muon Small Wheel detector requirements for Run III and beyond

The upgrade proposed in this document concerns the Small Wheel muon end-caps, which will be installed as part of the Phase-I upgrade of the ATLAS detector before the start of Run III in 2018. During Run III the peak instantaneous luminosity is expected to reach 2-3$\times 10^{34}\,\mathrm{cm}^{-2}\,\mathrm{s}^{-1}$ corresponding to 55-80 mean interactions per bunch crossing. In 2022 a further upgrade of the LHC and ATLAS is planned (the Phase-II upgrade), achieving an instantaneous luminosity of $5\times 10^{34}\,\mathrm{cm}^{-2}\,\mathrm{s}^{-1}$, corresponding to 140 pileup events. ATLAS is expected to operate another 5-10 years after that upgrade to accumulate a total integrated luminosity of 3000 fb^{-1}. The New Small Wheel thus has to be designed such that it can operate efficiently for both run III and beyond for more than 10 years and should be able to tolerate the high particle fluencies expected during these running periods. To take into account some safety margin, the detector design is required to be adequate for a maximum inst. luminosity of $7\times 10^{34}\,\mathrm{cm}^{-2}\,\mathrm{s}^{-1}$, 200 pileup events, and an integrated luminosity of 3000 fb^{-1}.

In this chapter first the operating conditions for Run III are described, particularly the expected hit rates due to backgrounds. In the following sections the requirements for precision tracking and for triggering are described.

2.1 Operating conditions for Run III

Background hits in the muon spectrometer arise primarily from low energy photons and neutrons. They are generated by synchronous proton collisions with the bunch crossing that triggers the ATLAS data-taking mechanism (in-time background), or by collisions that happen one to several bunch crossings earlier (out-of-time background). The resulting particles are generically referred to as 'cavern background'.

In order to predict the expected cavern background rates after the various accelerator upgrades, two elements are required: an accurate measurement of the observed background at the current operational conditions and a reliable Monte-Carlo extrapolation to higher energy and luminosity. Figure 2.1 shows the ratio of the measured hit rates to the corresponding simulation values using FLUGG [8] for the existing muon (MDT) chambers. This ratio is in general between 0.5 and 1.7. As a consequence this current background simulation can be used to predict, within a factor of two, counting rates in the muon system for different detector geometries and beam energies. It is therefore very useful to define the exact geometry of the detector and of the shielding around it, as relative comparisons between configurations can be made.

The background rate is a steep function of the radial distance from the beam line, being highest for the detectors closer to the beam pipe. Direct hit rate measurements using the muon detector have been performed at the current luminosities to study this dependency [9]. Figure 2.2 (a) shows the measurements in the Small Wheel region for the MDT and CSC detectors (Cathode Strip Chambers, used in the inner part of the present end-cap Small Wheel). The discontinuity at r=210 cm is caused by the different sensitivities of the MDT and CSC to the cavern background. A FLUGG simulation is also shown in the same figure. By using either the CSC or the MDT

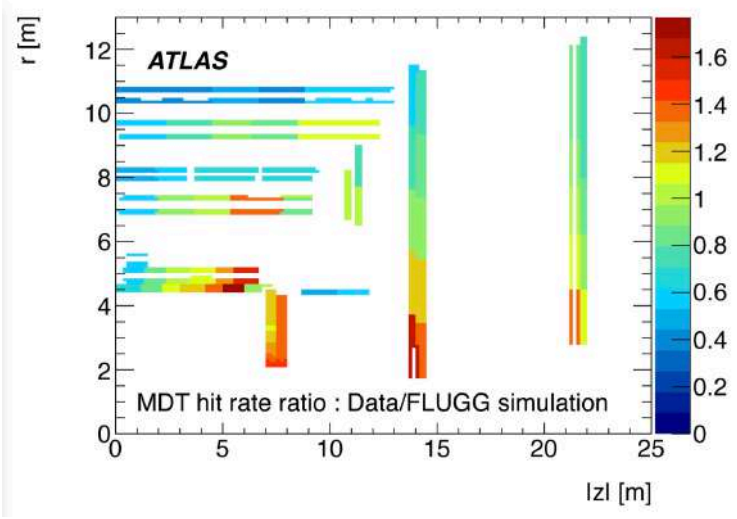

Figure 2.1: Ratio of measured to simulated MDT hit rate during a 7 TeV run at an average luminosity of $1.9 \times 10^{33}\,\mathrm{cm}^{-2}\,\mathrm{s}^{-1}$ (50 ns bunch spacing).

r-dependence of the cavern background from Fig. 2.2 (a) and scaling to higher luminosities and extrapolating to the full range the blue and red curves are correspondingly obtained. The yellow band in (b) indicates the area corresponding to a hit rate of 200–300 kHz per tube of the MDT detectors in the Small Wheel.

Figure 2.2 (b) shows the observed hit rates in the MDT (r >210 cm) and the CSC (r <200 cm), scaled to the value corresponding to the nominal Run III luminosity of $3 \times 10^{34}\,\mathrm{cm}^{-2}\,\mathrm{s}^{-1}$.

Figure 2.2 can be used to estimate the maximum hit rate expected. Given the linear dependence of the hit rate to the luminosity, at the maximum Phase-II luminosity of $7 \times 10^{34}\,\mathrm{cm}^{-2}\,\mathrm{s}^{-1}$ the hit rate will be approximately $15\,\mathrm{kHz/cm}^2$ (assuming conservatively the MDT sensitivity for the future detector). This linearity has been established experimentally by studying hit rates and currents in several muon detectors at LHC runs of various luminosities [9]. This linearity can for example be seen in Fig.2.3 where the current measured in the ATLAS muon Resistive Plate Chambers (RPC) is plotted as a function of the instantaneous LHC luminosity.

All the above is based on the measurements at $\sqrt{s}$=7 TeV. The ratio of background rate at $\sqrt{s}$=14 TeV and 7 TeV is about 1.3 in the Small Wheel region according to the Monte Carlo simulation using FLUGG. This increase will however be compensated by the consolidation work expected during the Long Shutdown period 1 (LS1); e.g. new additional shielding will be installed in the narrow gap between the end-cap calorimeter cryostat and the JD shielding, and the current steel beam pipe will be replaced by an aluminum one in the region of the end-cap calorimeter and the end-cap toroiod coils. Assuming for the various gas detectors proposed for the NSW a similar sensitivity to the current MDT, the prediction of $15\,\mathrm{kHz/cm}^2$ is taken as the maximum expected value for these detectors at $\sqrt{s}$=14 TeV.

To tolerate the large particle fluencies expected, it has to be verified that the new detectors (including trigger and readout electronics) do not age significantly with up to about 1 Coulomb/cm^2 for a planar detector or the equivalent for a wire chamber.

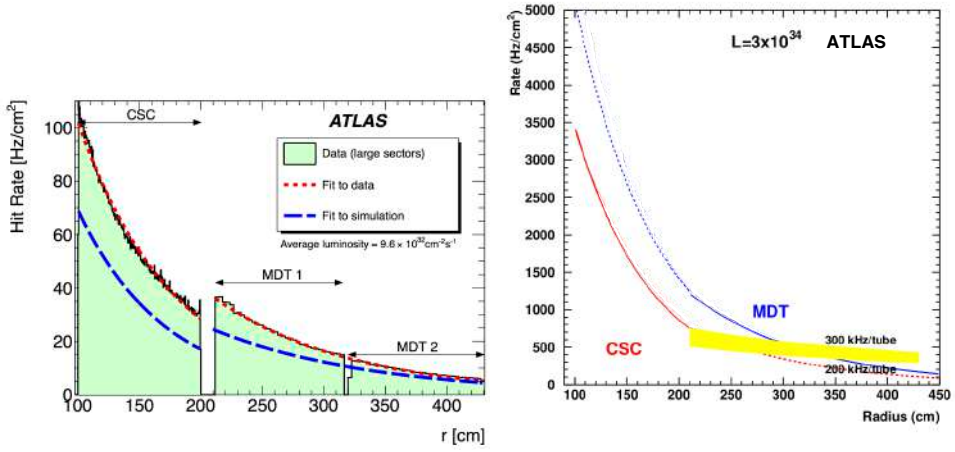

(a) (b)

Figure 2.2: a) Measured hit rate in the region of the Small Wheel for $\mathcal{L} = 9.6 \times 10^{32}\,\mathrm{cm}^{-2}\,\mathrm{s}^{-1}$ at $\sqrt{s} = 7\,\mathrm{TeV}$ in the CSC and MDT chambers as function of the radial distance from the beam line. b) Extrapolated hit rate in the CSC and MDT regions for a luminosity of $3 \times 10^{34}\,\mathrm{cm}^{-2}\,\mathrm{s}^{-1}$] at $\sqrt{s} = 7\,\mathrm{TeV}$ as a function of the radial distance from the beam line. Also indicated is the range of tube rates of 200-300 kHz.

2.2 Precision tracking performance

Track segments in the muon spectrometer are built from hits in a given station of the detector. Segments from different stations are then linked together to form tracks. The single tube hit efficiency and the segment finding efficiency of the MDT is shown in Fig. 2.4 as measured in test beam as function of the hit rate [10–12]. The efficiency decreases linearly with increasing hit rate. At a hit rate of 300 kHz (the maximum rate expected for a luminosity of $1 \times 10^{34}\,\mathrm{cm}^{-2}\,\mathrm{s}^{-1}$) it already reaches hit inefficiencies of about 35%. The segment finding efficiency are higher since only a subset of all available hits is required but for rates beyond 300 kHz it also decreases dramatically. With tube rates above 300 kHz, the segment inefficiency becomes sizable and results in a degradation of spectrometer performance. High background rate also causes degradation of the position resolution due to space charge effects. It is evident from Fig. 2.2 (b) that at a luminosity of $3 \times 10^{34}\,\mathrm{cm}^{-2}\,\mathrm{s}^{-1}$ a big fraction of the Small Wheel MDT system will have to operate with tube rate much above 300 kHz. Hence the current MDT system will have substantial inefficiencies at the luminosities and backgrounds expected after Phase I upgrade.

A study has been performed overlaying real events to determine the impact on the current End-cap Inner (EI) chambers—the MDT used in the current Small Wheel for precision track measurements. The overlay method for simulating event pileup at high luminosity is described in detail in [13]. Here 10 Zero Bias events are overlaid to produce one event at a corresponding higher luminosity. The Zero Bias events have been collected in 2012 with a dedicated trigger, with an instantaneous luminosity of $2.6 \times 10^{33}\,\mathrm{cm}^{-2}\,\mathrm{s}^{-1}$. The obtained overlaid events correspond to the background expected at a luminosity of $2.6 \times 10^{34}\,\mathrm{cm}^{-2}\,\mathrm{s}^{-1}$. The results for this study are shown in Fig. 2.5. Only the EI MDT chambers closest to the beam-line are shown for simplicity. In

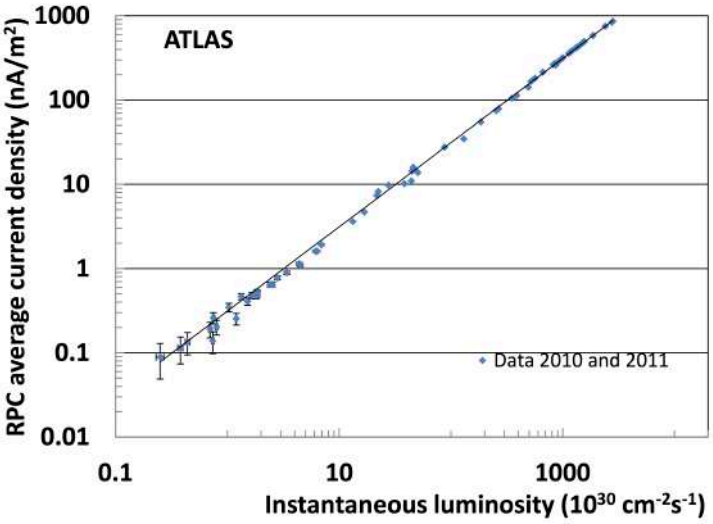

Figure 2.3: Current density in the ATLAS muon RPC detector as a function of the LHC instantaneous luminosity, over four orders of magnitude. The line fitted gives a linear dependence of the current density to the instantaneous luminosity with a slope of $0.312 \pm 0.001\,\mathrm{nA\,m^{-2}\,cm^{-2}\,s^{-1}}$.

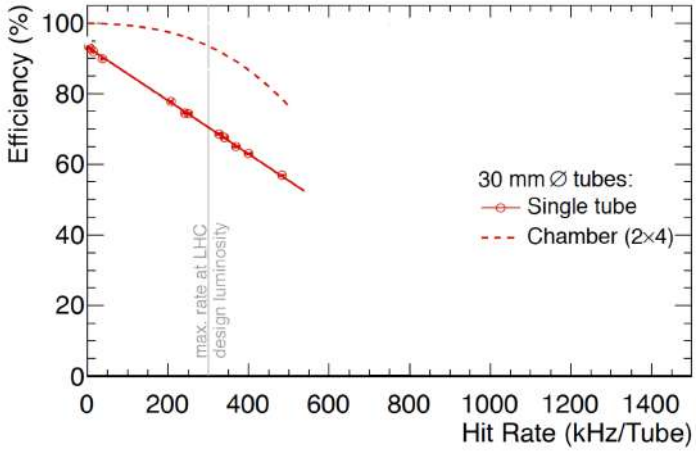

Figure 2.4: MDT tube hit (solid line) and track segment efficiency (dashed line, referring to a MDT chamber with 2x4 tube layers) as a function of tube rate estimated with test-beam data. Instantaneous luminosity of $1 \times 10^{34}\,\mathrm{cm^{-2}\,s^{-1}}$ is referred in this plot as 'design luminosity'. Points on the plots are result of test beam measurements.

Fig. 2.5 (Left) the red points correspond to the Zero bias occupancy in these chambers (averaged over the sectors and the two end-caps) scaled up by a factor of 10. The black ones correspond to the result of the overlay with 10 Zero bias events. The total number of hits does not scale linearly with the background level due to saturation taking place. This saturation effect leads to MDT hit efficiency losses of about 35% at high luminosities, and compares well with expectations from Fig. 2.4 based on test beam data. These limitations will severely impact the track reconstruction and therefore a new detector is required for ATLAS to exploit the luminosity delivered after

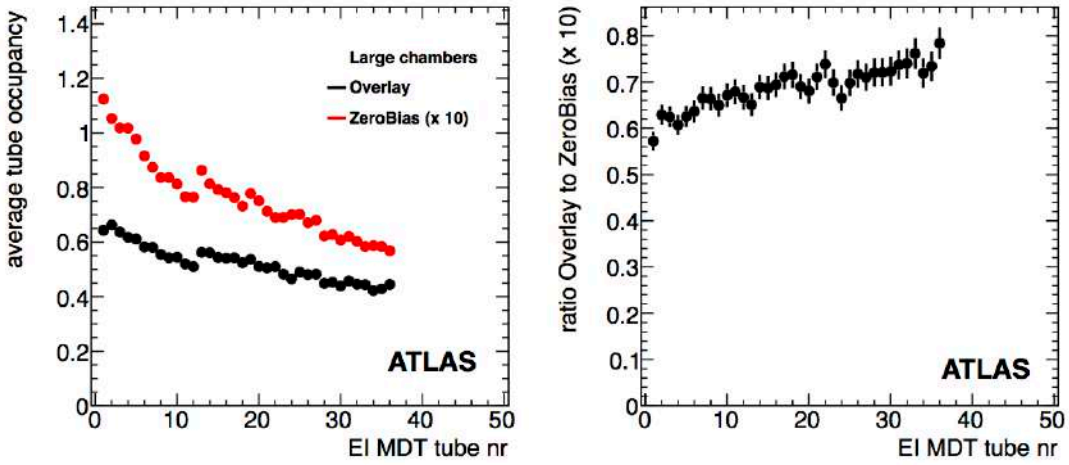

Figure 2.5: Left: The occupancy vs the MDT tube number for the End-cap Inner (EI) chamber (currently the precision detector of the Small Wheel) for Overlay data (black) and Zero Bias data scale up by a factor 10. Right: The ratio of the Overlay to Zero Bias ($\times$ 10) occupancy vs MDT tube number. The overlaid events correspond to the background expected at a luminosity of $2.6 \times 10^{34}\,\mathrm{cm}^{-2}\,\mathrm{s}^{-1}$. The x-axis of both plots is MDT tube number, counting radially from the MDT tube closest to the beam line. (MDT have 3 cm diameter tubes.)

Phase-I. In chapter 6 it is shown that the new detector shows a good and robust performance up to the highest luminsoity.

The performance of a detector that replaces the current one should be at least as good at high luminosity as that of the current detector at low luminosity. It should, therefore, be able to measure the transverse momentum (p_{T}) of passing muons with a precision of 10% for 1 TeV muons in the full pseudorapidity [1] coverage of the Small Wheel (up to $|\eta| = 2.7$). In particular such a detector should have the following characteristics:

- Reconstruct track segments with a position resolution in the bending plane better than 50 µm, to match the performance of the current MDT system. This will ensure that the muon spectrometer has a momentum resolution better than 10% at $p_{\mathrm{T}} \sim 1$ TeV. This performance should not degrade even if a considerable fraction of the detected hits are caused by background particles or if some detector planes are not operational. The required segment position resolution results in a better than 100 µm resolution per plane for the planned 4-layer multi-plane detector that may replace the Small Wheel.
- Segment finding efficiency better than 97% for muons with p_{T} greater than 10 GeV (the segment finding efficiency for the current MDT system).
- Efficiencies and resolutions should not degrade at very high momenta (due to δ rays, showers etc).

[1] ATLAS uses a right-handed coordinate system with its origin at the nominal interaction point (IP) in the centre of the detector, and the z-axis along the beam line. The x-axis points from the IP to the centre of the LHC ring, and the y-axis points upwards. Cylindrical coordinates (r, ϕ) are used in the transverse plane, ϕ being the azimuthal angle around the beam line. Observables labelled 'transverse' are projected into the x–y plane. The pseudorapidity η is defined in terms of the polar angle θ as $\eta = -\ln[\tan(\theta/2)]$.

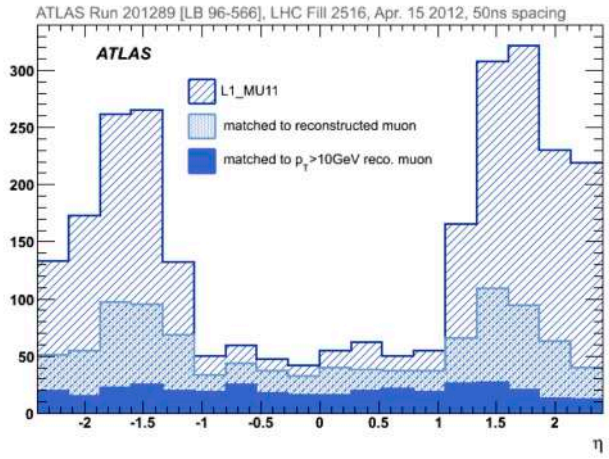

Figure 2.6: η distribution of Level-1 muon signal ($p_{\mathrm{T}} > 10\,\mathrm{GeV}$) (L1_MU11) with the distribution of the subset with matched muon candidate (within $\Delta R < 0.2$) to an offline well reconstructed muon (combined inner detector and muon spectrometer track with $p_{\mathrm{T}} > 3\,\mathrm{GeV}$), and offline reconstructed muons with $p_{\mathrm{T}} > 10\,\mathrm{GeV}$.

- Measure the second coordinate with a resolution of 1–2 mm to facilitate good linking between the MS and the ID track for the combined muon reconstruction..

The background environment in which the NSW will be operating will cause the rejection of many hits as spurious, as they might have been caused by δ-rays, neutron or other background particles. Furthermore in the life-time of the detector, detection planes may fail to operate properly, with very limited opportunities for repairing them. Hence a multi-plane detector is required.

Any new detector that might be installed in the place of the current Small Wheel should be operational for the full life time of ATLAS (and be able to integrate $3000\,\mathrm{fb}^{-1}$). Assuming al least 10 years of operation and the above expected hit rate per second, approximately $10^{12}\,\mathrm{hits/cm}^2$ are expected in total in the hottest region of the detector.

2.3 Trigger selection

Performance studies using collision data have shown the presence of unexpectedly high rates of fake triggers in the end-cap region. Figure 2.6 shows the η distribution of candidates selected by the ATLAS Level-1 trigger as muons with at least 10 GeV. The distribution of those candidates that indeed have an offline reconstructed muon track is also shown, together with the muons reconstructed with $p_{\mathrm{T}} > 10\,\mathrm{GeV}$. More than 80% of the muon trigger rate is from the end-caps ($|\eta| > 1.0$), and most of the triggered objects are not reconstructible offline.

Trigger simulations show that selecting muons with $p_{\mathrm{T}} > 20\,\mathrm{GeV}$ at Level-1 (L1_MU20) one would get a trigger rate at $\sqrt{s}$=14 TeV and at an instantaneous luminosity of $3 \times 10^{34}\mathrm{cm}^{-2}\mathrm{s}^{-1}$ of approximately 60 kHz, to be compared to the total available Level-1 rate of 100 kHz.

In order to estimate the effect of a trigger using the NSW a study has been performed applying offline cuts to the current SW to reduce the trigger rate. Table 2.1 shows the relative rate of L1_MU20 triggers in the $|\eta| > 1.3$ region after successive offline cuts to select high quality muon tracks. The various successive cuts applied are: i) the presence of Small Wheel track segments

Table 2.1: Estimation of the L1_MU20 relative rate in the $|\eta| > 1.3$ region using collision data after applying successively the requirements on the Small Wheel segments. Also shown the efficiency of these cuts for high quality muons ($p_{\mathrm{T}} > 20\,\mathrm{GeV}$) (relative to the number of such offline muons accepted by L1_MU20).

	Relative rate	Efficiency
All L1_MU20		1.00
SW segments > 0	0.64	0.98
dθ cut	0.32	0.95
dL cut	0.14	0.93
Offline $p_{\mathrm{T}} > 20\,\mathrm{GeV}$	0.02	

(SW segments > 0), ii) the Small Wheel segment pointing to the Interaction Point (IP) in θ ($|\mathrm{d}\theta|$ typically less than 10 mrad) (dθ cut) and iii) the Small Wheel segment matches in (η–ϕ) to the triggering segment in the muon Big Wheel ($|\mathrm{d}\eta|$, $|\mathrm{d}\phi|$ typically less than 0.1 rad) (dL cut). The efficiency of these cuts for high quality muons is also shown. Part of the efficiency reduction due to the dθ cut, is caused by the poor angular resolution (long tail) of the CSC ($|\eta|$ =2.0–2.7). A higher signal efficiency is expected if the segment angle resolution of the new detector is as good as that of the MDT over the whole acceptance of the Small Wheel. Therefore a detector that provides angular measurements that allow similar cuts to be made as shown in Table 2.1, would provide an additional rate reduction of more than seven in the $|\eta| > 1.3$ region. It will therefore reduce the L1_MU20 rate in the end-cap to the same level as that in the barrel, and the total L1_MU20 rate to about 22 kHz at a luminosity of $3 \times 10^{34}\mathrm{cm}^{-2}\mathrm{s}^{-1}$.

Figure 2.7 shows the p_{T} distribution of tracks found in the events with L1_MU20 trigger set. It is clearly seen that the angular cuts remove mostly muons with p_{T} much below the trigger threshold. The remaining low p_{T} muons can only be further rejected by improving the p_{T} resolution of the trigger system, foreseen for the Phase-II upgrade of the ATLAS detector.

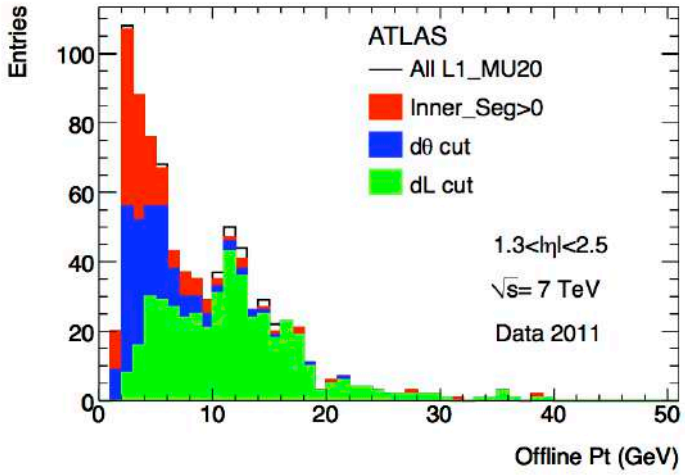

Figure 2.7: p_{T} distribution of muons reconstructed offline in both the muon spectrometer and the inner tracker, requiring $p_{\mathrm{T}} > 20\,\mathrm{GeV}$ at the Level 1 trigger (L1_MU20).

In the present layout, the p_{T} resolution is affected by: i) angular resolution of the current Big Wheel trigger station (approximately 3 mrad), ii) multiple scattering in the end-cap toroid (approximately 0.5 mrad for muons with p_{T} of a few hundred GeV), iii) multiple scattering in the calorimeters (between less than 1 mrad and up to 3 mrad, depending on the muon energy) and iv) finite size of luminous region of pp collision (corresponds to 1–2 mrad depending on η). A precision angle measurement by the Small Wheel can be used to eliminate the contributions iii) and iv) by correcting for these effects track by track, thus removing a part of the smearing effects to improve the p_{T} resolution. The ATLAS Phase-II upgrade will improve the Big Wheel trigger resolution to 1 mrad. Hence a similar resolution of 1 mrad is required at the level of the Small Wheel for a detector that will have to perform adequately for the whole lifetime of the ATLAS experiment.

In summary to reduce the muon Level-1 trigger rate to the level of 20 kHz for muons with $p_{\mathrm{T}} > 20$ GeV, a new Small Wheel triggering detector should provide trigger track segments with the following requirements on their quality:

- Track segment information should arrive at the Sector Logic (the muon trigger electronics that combine information form the various detectors to provide one or more Regions of Interest per bunch crossing) not later than 1.088 microsecond after a collision (the current delay of the Big Wheel TGC).
- Track segment reconstruction for triggering should have an angular resolution of 1 mrad (RMS) or better.
- Track segments should have a granularity better than 0.04×0.04 in the η–ϕ plane to match the one of the current muon trigger system.
- Track segments should be reconstructed online with high efficiency in the full η coverage of the detector ($1.3 < |\eta| < 2.5$).
- The online track segment reconstruction efficiency should be more than 95%.

3 New Small Wheel layout

The proposed NSW detector system is designed to meet all the requirements presented in the previous chapter. The NSW presented here consists of 16 detector planes in two multilayers. Each multilayer comprises four small-strip TGC (sTGC) and four Micromegas (MM) detector planes. The sTGC are primarily deployed for triggering given their single bunch crossing identification capability. The detectors are arranged in such a way (sTGC – MM – MM – sTGC) as to maximize the distance between the sTGCs of the two multilayers. As online track hits are reconstructed with limited accuracy, increased distance between detector multilayers leads to an improved online track segment angle reconstruction resolution. Hence this detector configuration is optimal for the online track resolution. The MM detectors have exceptional precision tracking capabilities due to their small gap (5 mm) and strip pitch (0.5 mm), that exceed the requirements of the previous chapter. For a detailed description of the performance of the two detectors of the proposed NSW, the reader is referred to Chapters 4 and 5.

The choice of eight planes per detector was dictated by the need to provide a robust, fully functional detector system over its whole lifetime. The main issues that have been addressed are operation in a high background environment and detector deterioration with time and their influence on the track segment reconstruction efficiency and resolution. Background neutrons and photons as well as δ rays spoil a number of hits from real tracks. With eight planes per detector, tracks will be reconstructed reliably and with high precision under these conditions. In addition the NSW is expected to operate for the whole life of the ATLAS experiment. The large number of planes will ensure an appropriate detector performance even if some planes fail to work properly. Access and repair opportunities will be rare and, particularly after LS3, activation issues will severely limit the scope of any possible interventions. Furthermore, it may be required for long-term stability reasons to operate the detector planes with their high voltage settings lower than is optimal for full efficiency. Eight planes per detector will once more ensure an overall efficiency close to 100% both for online and offline track reconstruction.

The two NSW detector technologies also complement each other for their corresponding primary functions. sTGC may contribute to offline precision tracking, as they are able to measure track hits with a resolution better than 150 µm (depending on the incident track angle).

For triggering, experience has shown that redundancy is highly important in the forward direction at high luminosities. The MM detectors will be employed as a trigger in addition to the sTGC to provide improved redundancy, robustness and coverage of the forward trigger. In Chapter 6 the simulation for the sTGC trigger performance is described. Preliminary studies of the MM trigger are very encouraging, and additional work is in progress.

3.1 Layout of the Present Small Wheels

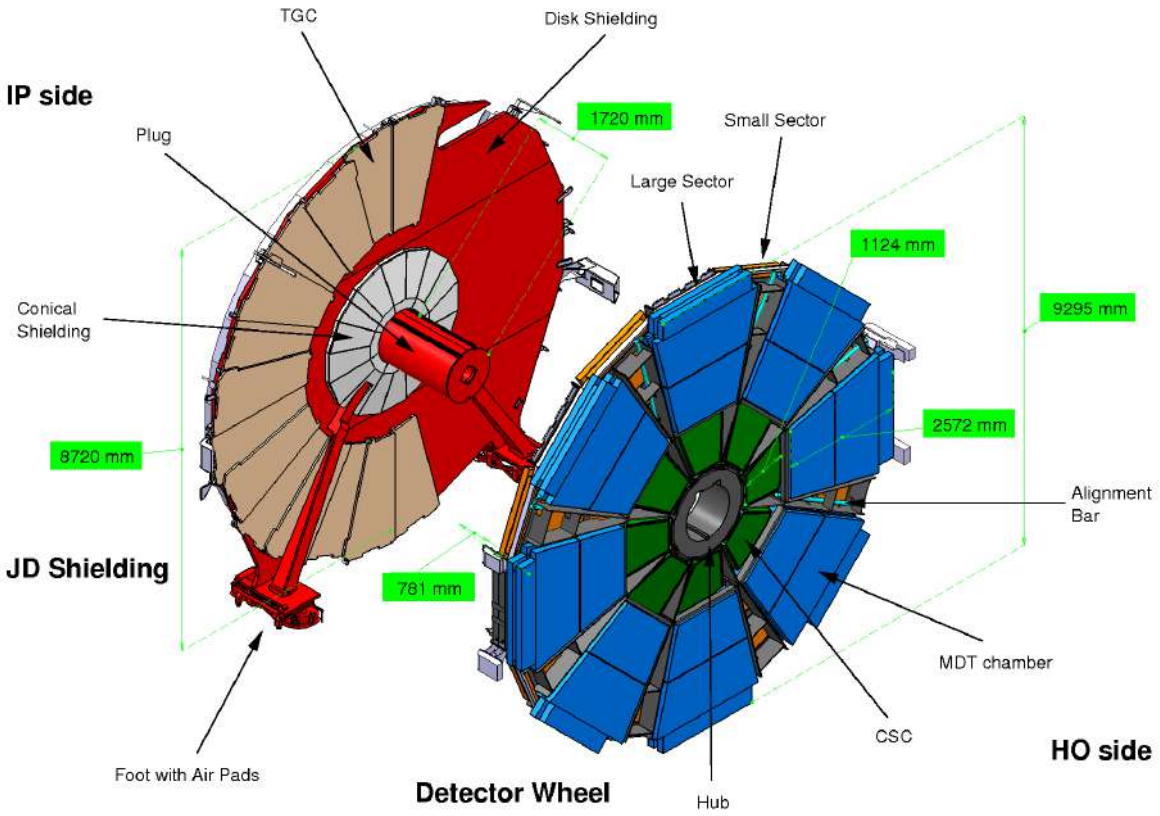

Figure 3.1: Components and layout of a present Small Wheel.

Each of the present Small Wheels [6] consists of two distinct parts:

1. A detector wheel with a mechanical structure to which the precision tracking detectors (MDT chambers and CSCs) and the alignment system are mounted. The mechanical structure consists of an inner massive hub to which radially extending, interconnected, spokes are attached.
2. The JD shielding, a disk shaped shielding covering the full extend of the detector wheel with a cylindrical extension (plug) around the beam pipe at the inner radius. The JD shielding has two feet to support it inside the ATLAS detector. Trigger chambers are mounted on the JD disk.

The detector wheel has no mechanical supports of its own, it is slid unto the plug of the JD shielding. The weight of the mechanical structure and the detectors is transferred by hub of the detector wheel to the JD plug and the JD feet. The assembly of the detector wheel and JD shielding can be moved on air pads on the barrel rail system of the ATLAS experiment. Figure 3.1 shows a drawing of a Small Wheel. The side of a SW or any part thereof facing the interaction point will be referred to as IP side, the side facing away from the interaction point as HO side. The detector wheel with the precision chambers shows the segmentation into 8 small (on the IP side) and 8 large sectors (on the HO side)[1].

[1] see Chapter 3.6.3 for an explanation of the ATLAS muon spectrometer sector scheme

3.2 General mechanical structure of the NSW detectors

The detectors used in the NSW, sTGC and MM, are planar gaseous detectors. While the internal electrode structure of the two detector types is different, the position measurement relies on precision strips on PCB cathode planes in both cases. To stiffen a single detector plane, honeycomb panels are glued to the PCBs. The detector units delivered by the production sites are planes of one detector type assembled to multiplet sandwiches, alternating gas gaps with electrodes, PCBs, and stiffening panels. They usually have a trapezoidal shape.

3.3 Layout requirements

The general NSW layout is dictated by the following requirements:

- compatibility with the existing tracking detectors;
- compatibility with the end-cap alignment system;
- high-precision trigger and tracking capability and
- redundancy of tracking and triggering.

The compatibility with the existing tracking detectors requires the precision coordinate of all chambers to be parallel to the drift tube chambers of the EM and EO wheels within 2 mrad, in order to avoid deteriorating the resolution of the track reconstruction by mixing the precision measurement with the less precise measurement of the second coordinate. This compatibility also determines the minimum size of the NSW chambers as they have to cover the EM and EO MDT chambers in projective geometry for $|\eta| > 1.3$.

The compatibility with the end-cap alignment system requires that some optical sensors are mounted in specific locations on the outer side, facing away from the interaction point, of the NSW to transfer the alignment from the NSW to the EM wheel. Therefore, there should be no obstructions to these sensor positions or to the alignment paths. A system similar to the present alignment bars and chamber sensors seems the natural choice for the NSW alignment system, as there are only few links between the SW and the EM wheel and all chambers in the NSW have to be coupled to these locations. In addition, the present end-cap alignment system is well understood and has delivered excellent performance in the initial LHC runs.

The first two requirements thus imply that the NSW layout be composed of 16 sectors of precision chambers, eight small and eight large ones, as in the rest of the end-cap system (and the present SW) [6].

The third and fourth requirements have implications for the structural design of the single detector stations. Triggers are formed by concurrent hits in multiple detector planes. To obtain the required angular resolution of approximately 1 mrad within the Level-1 latency of 1 μs, the chambers must, at all times, be positioned with respect to each other within a 200 μm tolerance. For offline track reconstruction, alignment system data are needed. However only a few NSW planes can be instrumented with optical sensors. Therefore, for both MM and sTGC detector systems, a robust mechanical coupling of sets of detector planes to achieve a stiff structure in which the relative detector positions do not change is required.

3.4 Integration and system requirements

The NSW detector proposed here is constrained by following global system integration requirements:

- The physical dimensions of the whole detector system, including the mechanical support structure and radiation shields, should not exceed the dimensions of the current Small Wheel. In particular this detector envelope must fit in the space between the end-cap calorimeter and end-cap toroid, $|z| = 6780\,\text{mm}$–$7890\,\text{mm}$ (nominal position).
- The detector should operate at the environmental conditions (temperature, humidity) expected in ATLAS.
- Redundancy and robustness should be designed in the readout electronics, distribution of LV/HV and connection of other services.
- Access must be ensured to services, electronics and other relevant points of the detector for in-situ maintenance.
- The detector must be fully commissioned before installation, to minimize in-situ maintenance.
- The activation of material should be incorporated into the protocols for assembly, installation and access to the detector for maintenance.

3.5 Baseline layout

A baseline layout of the NSW, taking into account the requirements listed in chapter 3.3, is defined:

- The sTGC as primary trigger system and the MM as the primary precision tracking detectors.
- A trigger acceptance of $1.3 < |\eta| < 2.5$.
- A precision tracking acceptance of $1.3 < |\eta| < 2.7$.
- Eight small and eight large sectors span the corresponding EM and EO MDT chamber sectors in projective geometry for the precision tracking.
- Planar detector wheel, i.e. no inclined chambers like the present CSC.
- Eight detection layers of sTGC, eight detection layers of MM in each sector. To maximize the lever arm between the sTGC as primary trigger chambers, the layer order in the z direction is four layers sTGC, four layers MM, an optional spacer and support structure, four layers MM, four layers sTGC.
- Knowledge of the internal positions of the strips in the precision coordinate: $40\,\mu\text{m}$.
- The re-use of the present JD shielding. Modifications of the cone shielding can be considered if necessary to open the required space of the detectors at the innermost radius of the NSW.

The position determination of the detector elements which provide the precision track information (strips in both, the sTGC and MM), has been relaxed from $20\,\mu\text{m}$ of the current MDT chambers to $40\,\mu\text{m}$. The minor impact on the muon momentum resolution is considered acceptable compared to the effort needed to achieve a better geometry on large flat detector structures.

3.6 Coordinate systems and naming conventions

3.6.1 The global ATLAS detector coordinate system

Figure 3.2 shows the global right-handed Cartesian coordinate system of the ATLAS detector [6]. The z-axis is defined along the LHC beam 2 direction (from point 1 towards point 8), the x-axis points towards the center of the LHC ring. The z-x-plane is inclined by $0.704°$ with respect to the horizontal, the y-axis is pointing upwards, normal to the x-z-plane. The angle θ is defined with respect to the z-axis, the pseudo-rapidity as $\eta = -\log\tan(\theta/2)$. In cylindrical coordinates, r is the radial distance from the beam line (z-axis) in the x-y-plane and ϕ is the axis angle to

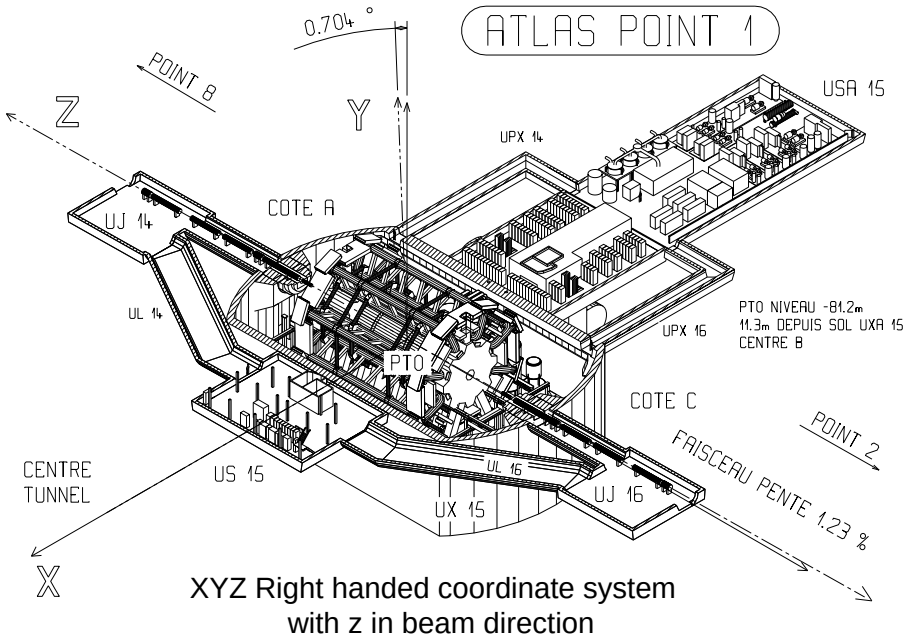

Figure 3.2: The global ATLAS coordinate system [6].

the x-axis. The detector part in the positive z-direction is called side A, the part in the negative z-direction side C.

3.6.2 Local detector coordinate systems

A local, fixed coordinate system is defined for each detector unit, independent of the detector orientation in the ATLAS experiment. A right-handed Cartesian coordinate system is used, see Fig. 3.3. The orientation and the point of origin follow the conventions defined in [6]. The x-z-plane is parallel to the strip planes in the detector unit, with the z-axis along the primary precision coordinate and the x-axis parallel to the second coordinate. The point of origin is located in the mid plane of each unit on the edge which will be closest to the interaction point.

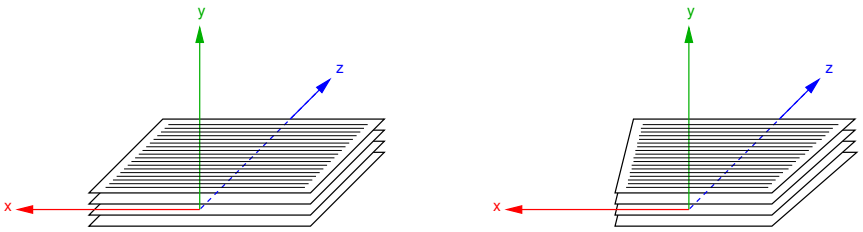

Figure 3.3: The local coordinate system defining the orientation within a detector unit [6]. The precision coordinate is along the z-axis, the strip orientation for its measurement are indicated. Examples are given for rectangular and trapezoidal detector quadruplets.

3.6.3 ATLAS muon spectrometer sector scheme and numbering

The eight cryostats of the barrel toroid magnet impose a division into 16 sectors for the muon instrumentation in the barrel region. Eight so-called large sectors are located in the angular regions between the coils, spanning about 29° in ϕ and eight so-called small sectors are located in the angular regions which include a barrel toroid coil each, spanning about 20° in ϕ. Between each large and each small sector there is an overlap of about 2° in ϕ. For consistency and to keep the concept of the projective arrangement of the muon detectors with respect to the interaction point in the transition region between the barrel and the end-cap, the structure of 16 sectors is replicated in the end-cap region for the precision tracking detectors.

The sectors are numbered consecutively, starting with sector 1 which contains the positive x-axis ($\phi = 0$). The sector numbers increase with increasing ϕ, see Figure 3.4. This numbering scheme implies that the large sectors have odd numbers, and the small sectors even numbers.

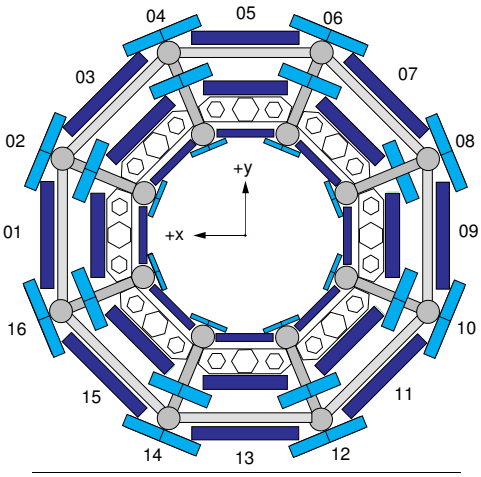

Figure 3.4: Definition of the 16 sectors of the ATLAS muon spectrometer [6].

3.6.4 Assemblies and sub-assemblies

In this section, the detector assemblies used in the description of the layout are illustrated. The smallest and fundamental assembly defined is a sensitive detector element of a specific technology. All other higher order detector units are assembled from these basic components. The full naming scheme used in the NSW and a figure detailing the assemblies are given in appendix A.

Plane: A single detector gas gap with the readout structures.

Multiplet: Assembly of n planes of a single technology (sTGC or MM) in z direction (n = 1 to 4).

Module: Assembly of m multiplets (m $\geq$ 1) in the r direction (in cylindrical coordinates) which constitute a single independent object.

Chamber: Assembly of two modules of a single technology (sTGC or MM) in the z direction and one or more modules in the r direction which constitute a single independent object. A chamber might include an internal or external spacer frame between the modules in the z direction.

Wedge: Assembly of modules of a single technology type (sTGC or MM) in the z direction, covering a full sector in the $r - \phi$ plane.

Sector: 1/16th of the NSW on side A or C (corresponding to a large or small geometric sector), comprised of two sTGC wedges and two MM wedges.

No assumptions on the size of the assemblies are made, except for the wedge and sector types.

3.7 Mechanical environment in the ATLAS experiment

Figure 3.5 shows a drawing of the NSW mechanical environment in the ATLAS experiment. The NSW will be located between the end-cap calorimeter and the end-cap toroid. The nominal

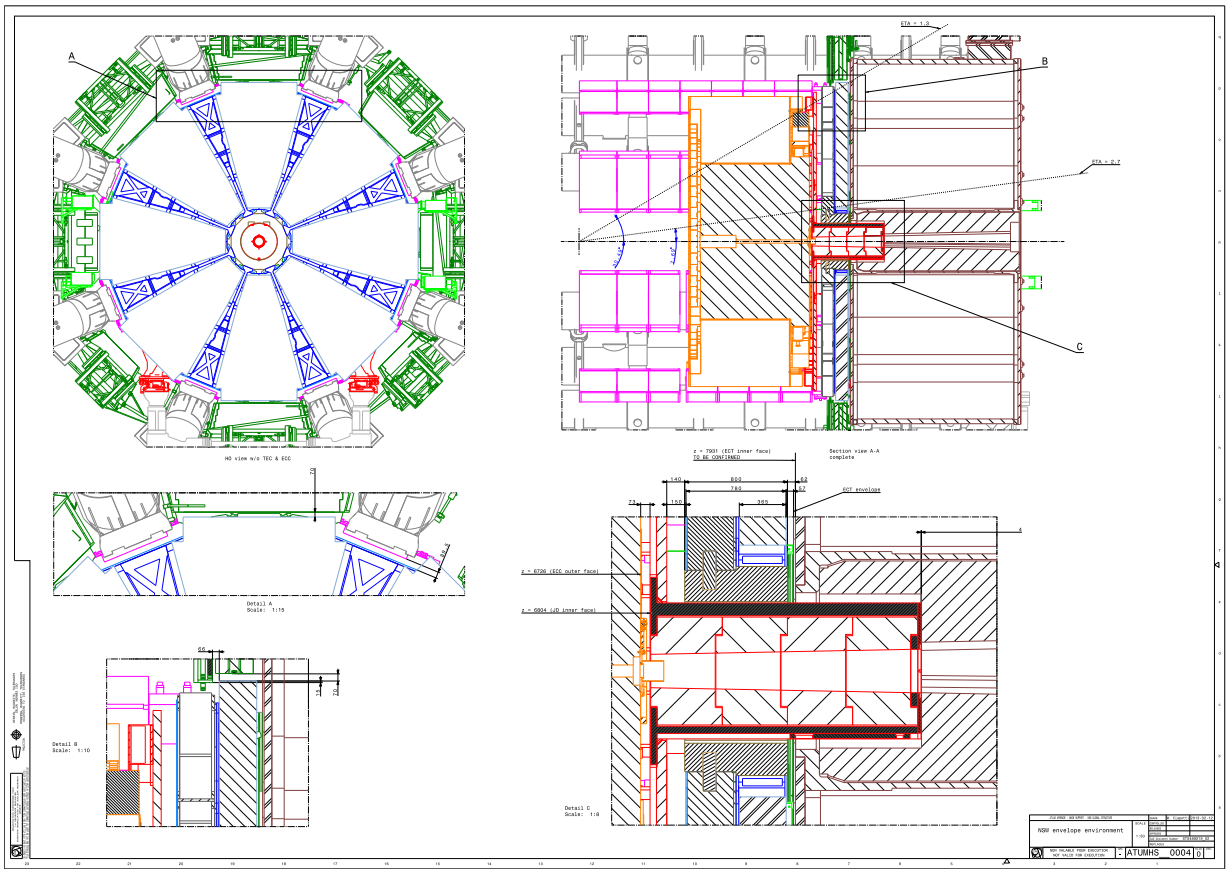

Figure 3.5: The NSW environment in the ATLAS experiment. Upper left: view of the x-y plane. Upper right: view of the x-z plane. The region of minimal acceptance of $1.3 < |\eta| < 2.7$ is indicated. Middle and lower left: Details in the vicinity of the EIL4 MDT chambers. Views of the x-y plane and of the y-z plane. Lower right: Detail of the region near the beam pipe. View of the x-z plane.

position of the IP side of the JD shielding is $|z| = 6804\,\text{mm}$. In the z direction, 1117 mm of space are available between the envelopes of the calorimeter and the end-cap magnet cryostat. The available space in the x-y plane is constrained by the surrounding detector components and the requirement to be able to move the NSW along the z-direction on the barrel rails during the opening of the ATLAS detector for maintenance. The radial dimensions of the small sectors are limited by barrel toroid coils while the large sectors are bounded by the EIL4 MDT chambers and the force transfer brackets of the end-cap toroids on the barrel toroid coils.

3.8 JD shielding

The main part of the forward muon shielding, referred to as the *JD shielding* [14], is located between the end-cap calorimeter and the end-cap muon chambers of the Small Wheel. It will be re-used for the NSW, but slightly modified to accommodate the new planar geometry of the detector wheel.

The present JD shielding consists of three parts, the central cylindrical plug made of brass with an outer stainless steel jacket surrounding the beam pipe, the disk shielding of carbon steel which

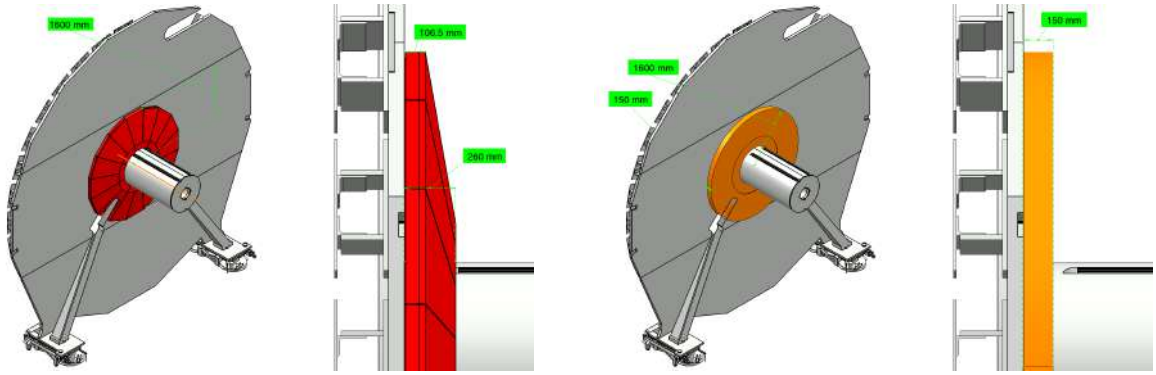

(a) Present shielding.

(b) Example of a modified shielding geometry.

Figure 3.6: The JD shielding designs. The detailed views at the right side show the shape of the shielding of the inner region. The conical shielding (a) will be modified to a disk-like geometry (b) to provide space for the full detector coverage up to $\eta = 2.7$ with a planar detector geometry.

covers the SW muon detectors, and the conical shielding, made of brass and clad by borated[2] polyethylene and a lead layer, at the inner radius of the disk shielding[3]. The conical shielding fills the gap between the disk shielding and the inclined CSC detectors.

The modification of the JD shielding only affects the conical part, which will be replaced by a flat cylinder, again made of high-Z metal material and clad by borated polyethylene covered by a lead layer. The optimal material and the dimensions—both, in r and in z—of the new shielding are currently under study. For the optimization, the expected background hit rates with the different shielding configurations are simulated in the complete muon spectrometer, as changes in the forward shielding will affect not only the inner end-cap region of the NSW, but also the high-η barrel region and the high-η region of the middle end-cap layer of the muon spectrometer. A reduction of the conical shielding to a flat disk will lead to slightly higher background hit rates. This increase might be reduced by adding a second new disk-shape shielding on the IP side of the JD-Disk where about 25 mm of free space to the end-cap calorimeter are available.

The NSW detector wheel will be mounted on two rails on the top the plug and therefore always moves together with the shielding in the experiment, e.g. during the opening of the experiment for maintenance.

Two feet struts, mounted to the plug and extending along the disk in the sectors 11 and 15 permit the movement of the shielding on four airpads along the z direction on the barrel rails during the opening of the ATLAS experiment. These feet constrain the layout of the mechanical support structure of the NSW in the two sectors.

Figure 3.6 shows the layout of the present and of the new JD shieldings. Table 3.1 lists the geometrical parameters of both configurations.

The mass of the present JD shielding is around 83 t, including the airpads. The mass of the new modified shielding will be approximately the same.

[2] 5% of B_2O_3 by weight

[3] The high-Z material metal shielding stops charged particles due to energy loss by electromagnetic or strong interactions. The polyethylene shielding moderates the neutrons which are then captured by the added boron. Secondary photons from the neutron capture are absorbed in the lead layer.

Table 3.1: Geometry of the forward muon (JD) shielding. All dimensions are in mm. For the NSW the conical shielding (second last column) will be replaced by the cylindrical shielding (last column). Note that the inner bore of the plug shielding depends on z and follows the line $|\eta| = 4.6$.

Parameter	Disk	Plug	Conical shielding	Cylindrical shielding
$r_{\min}$	540	129	530	530
$r_{\max}$	4360	529 (540 at Disk)	1660	1660 (prelim.)
$z_{\min}$	6829	6829	6909	6909
$z_{\max}$	6909	8889	7169	7059 (prelim.)

3.9 Mechanical support structure

All detectors of the NSW will be mounted on a single mechanical support structure which in turn sits on the plug of the JD shielding. This support structure, shown in Fig. 3.7, consists of an inner cylindrical hub and radial spokes on which the detectors will be attached. The hub, made of brass to provide additional shielding around the beam pipe, transfers the weight of the structure and the detectors on the JD plug. On the IP side of the hub, eight V-shaped spoke structures surround and support the small sectors. All spokes are identical, except those in sectors 11 and 15 which are shaped to accommodate the feet struts of the JD shielding. On the HO side of the hub, eight identical Y-shaped spoke structures surround and support the large sectors. The spokes are designed to maximize the available space between them and thus the available space for the detectors. They are reinforced with plates and crossbars and are interconnected with azimuthal bars to achieve the necessary rigidity. Apart from the azimuthal bars, an x-y plane with a thickness of 45 mm in the z direction has been kept free in the middle of the structure for the use by the optical alignment system. As for the present SW the outer surface of the hub will be clad by a layer of borated polyethylene covered between the spokes to improve its neutron shielding capabilities.

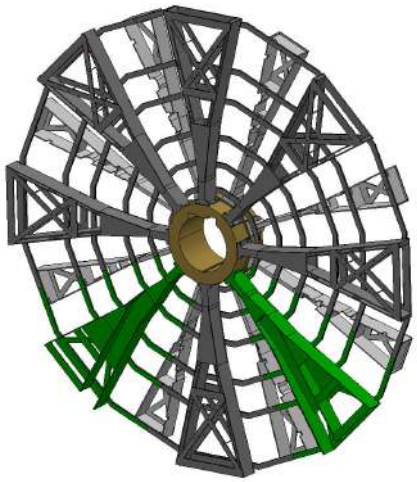

Figure 3.7: Drawing of the NSW mechanical structure, viewed from the IP side. The brown cylinder in the middle is the hub of the NSW, the central structural element which transfers the weight of the detectors and the mechanical structure to the JD shielding. The spokes in green color are modified to accommodate the JD feet struts. Preliminary cut-outs for the optical alignment system are visible on the HO side spokes.

The mechanical structure of the NSW also contains 16 alignment bars upon which are mounted an array of optical sensors. The sensors monitor the detector positions and the positions of the bars with respect to each other forming a reference grid. The eight alignment bars on the HO side carry the polar sensors to link the NSW alignment to the rest of the optical end-cap alignment system of the EM and EO MDT chambers.

The mass of the mechanical support structure of the NSW is estimated to be about 14 t, an increase by 2 t compared to the present mechanical structure.

3.10 Detector layout

The general detector layout follows the existing layout of the end-cap MDT system of the EM and EO layers with eight small and eight large sectors.

3.10.1 Envelopes

Sets of envelopes have been defined for the NSW detectors. The envelopes are inclusive, i.e. they contain the detectors as well as all their services.

The envelopes (Fig. 3.8) have been maximized and simplified in shape, ensuring at the same time that tracks which pass through the active area of a small or large sector in the EM and EO layers can also pass through the active area of the same sector in the NSW. An azimuthal overlap between the detectors of the small and the large sectors of the NSW will allow the verification of the relative alignment with tracks. A distance of about 80 mm between the envelopes and the spokes of the mechanical structure is left free for the detector mounts and for access for maintenance. The defined detector envelopes take into account, and do not interfere with, the alignment plane between the small and large sectors.

3.10.2 Layout

Contrary to the current SW layout which uses individually mounted CSC and MDT chambers in the r direction in each sector, the NSW is based on the idea of using sector sized units composed of sTGC and MM multiplets to be mounted on the NSW support structure. In the z direction the order of the detectors is sTGC–MM–MM–sTGC.

The sTGC detectors of each sector will be pre-assembled into wedges, consisting of three modules in the r direction with four planes each. The modules in the two sTGC wedges of each sector are arranged so that no dead region exists in projective geometry with respect to the IP. Due to the detector frames at the module borders there are however small regions of reduced efficiency where the number of hit planes will be less than 8. Figure 3.9 shows the layout and the dimensions of the sTGC detectors. The shape of the detectors in the large sectors does not follow the envelope, but has been changed to simplify the production of the detector modules. It has no impact on the required acceptance of the active detector area.

The MM detectors of each sector will be combined into a MM chamber, with four detector planes on either side of a spacer frame. Two options exist for the size of the modules (for details on the final design choice see chapter 8):

1. Single sector sized modules (i.e. single module wedges.)
2. Two to four modules in the r direction assembled to a wedge.

If option 2 is chosen, the MM modules would be arranged such that no dead areas, only areas of reduced efficiency, exist. sTGC and MM module sizes would further be chosen to maximize the overall number of detection layers at each position in r.

Figure 3.10 shows the layout of the MM detectors for the wedge option (sector sized modules), Fig. 3.11 for the option of 3 modules in r per sector. In this case, the modules in the two MM wedges of each sector will be arranged such that no dead region exists in projective geometry with respect to the IP. Due to either the spacing of the strip PCBs inside the sector sized wedge or the detector frames at the borders of the modules there are small regions of reduced efficiency where the number of hit planes will be less than 8. As for the sTGC wedges, the shape of the detectors in the large sectors has been modified to simplify the production of the detector modules with no impact on the required acceptance of the active detector area.

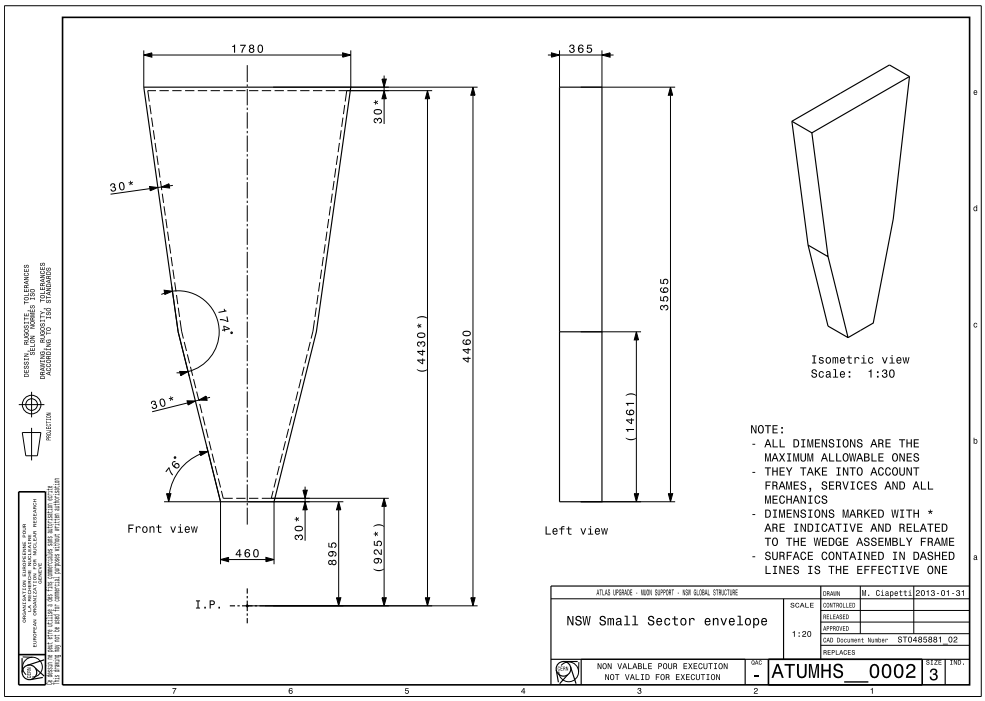

(a) Small sector.

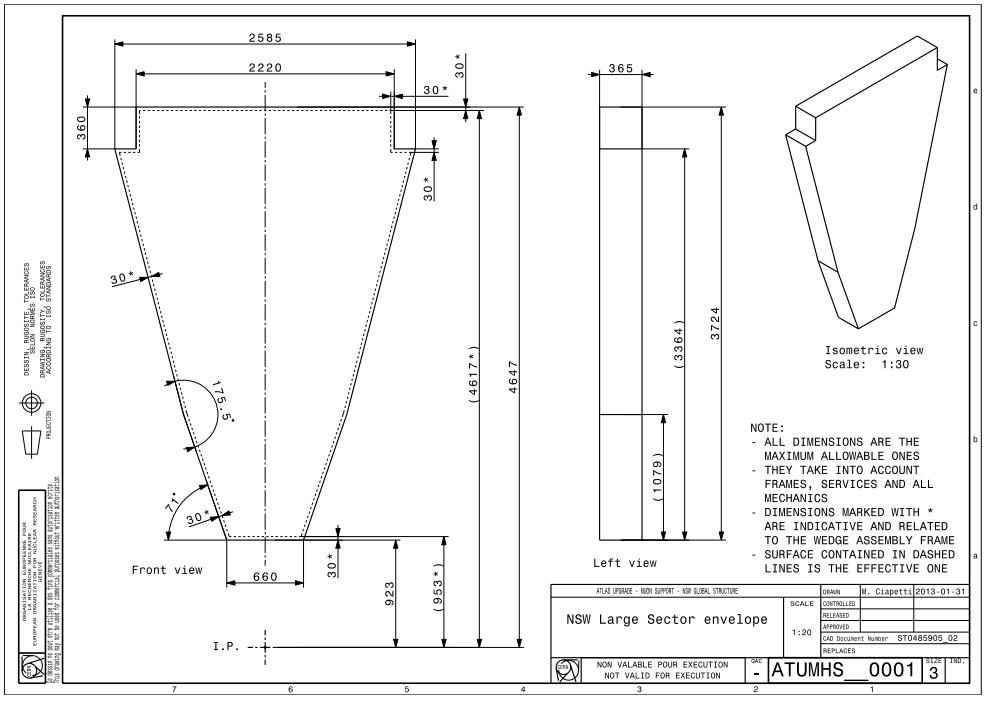

(b) Large sector.

Figure 3.8: The NSW detector envelopes.

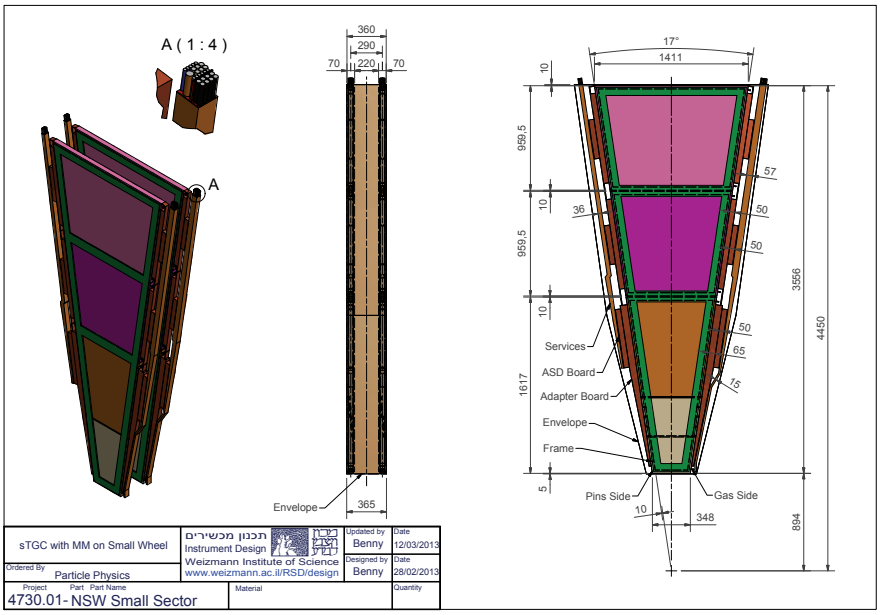

(a) Small sector.

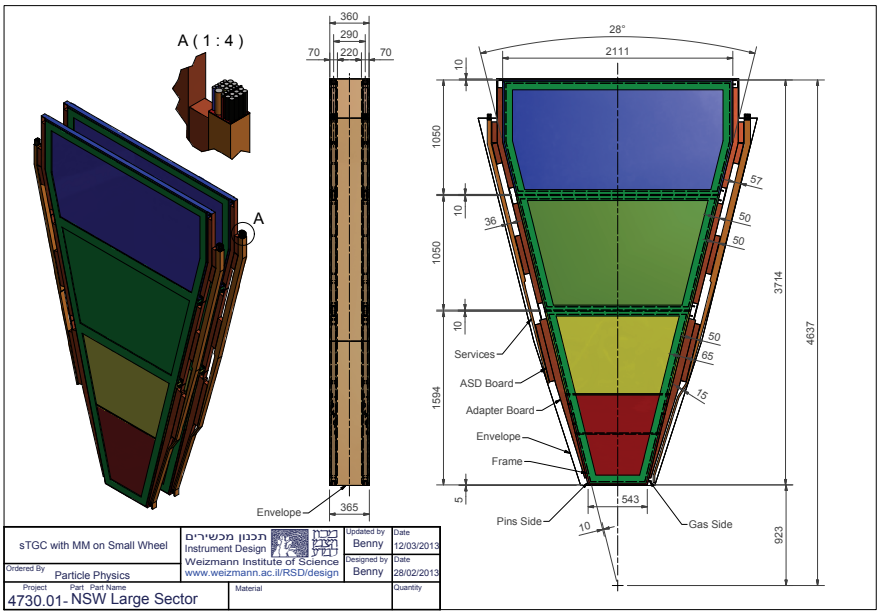

(b) Large sector.

Figure 3.9: Layout of the sTGC detectors including space allocated for services. The active detector area (dashed lines) and the allowed envelopes (full lines) are indicated. Left and middle: Example arrangement of the two sTGC wedges in a sector. The final dimensions in the z-direction between the two wedges will depend on the available space, here the minimum size is given.

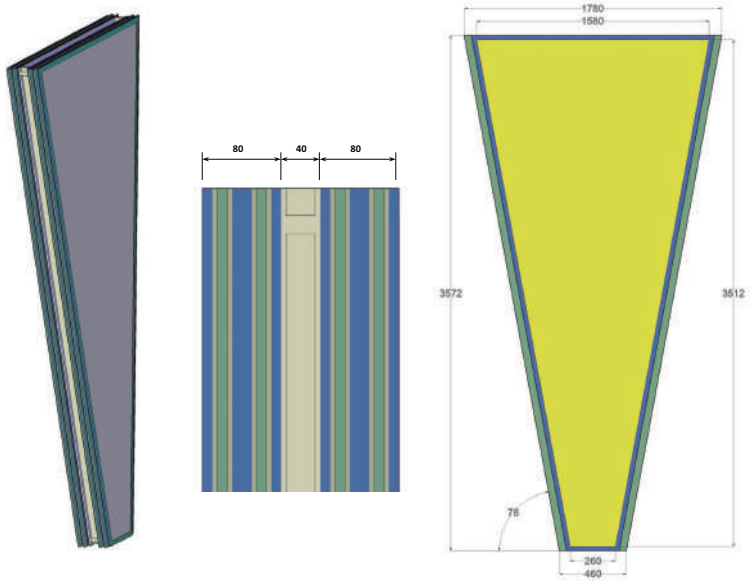

(a) Small sector.

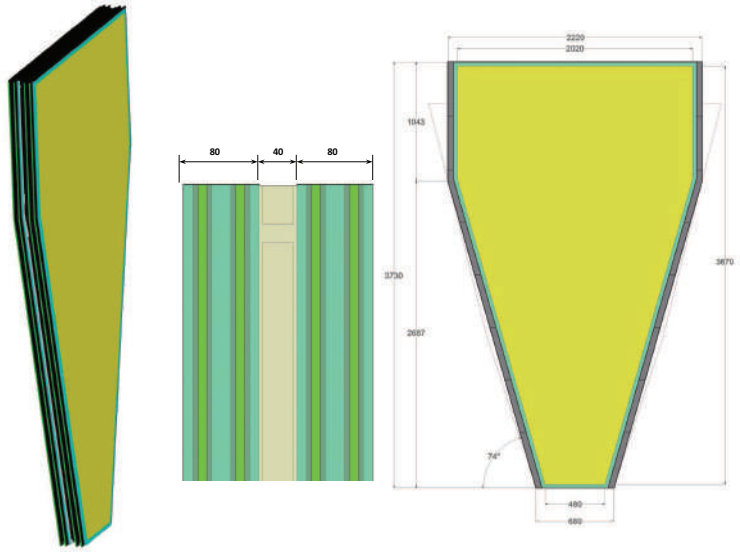

(b) Large sector.

Figure 3.10: Layout of the MM detectors with sector sized modules, including space allocated for services. The active detector area (yellow color), the frame (blue color) and the allowed envelopes (full lines) are indicated. For the small sector, the allowed envelope is completely filled. Left and middle: Example assembly of the two MM wedges in a sector to a MM chamber. The final dimensions in the z-direction between the two wedges will depend on the available space, here the minimum size is given.

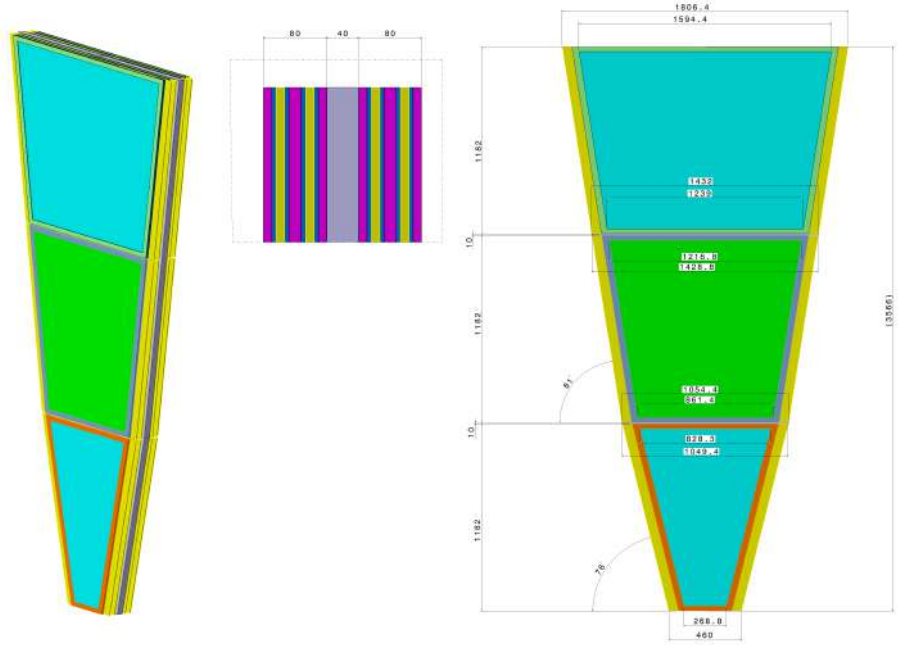

(a) Small sector.

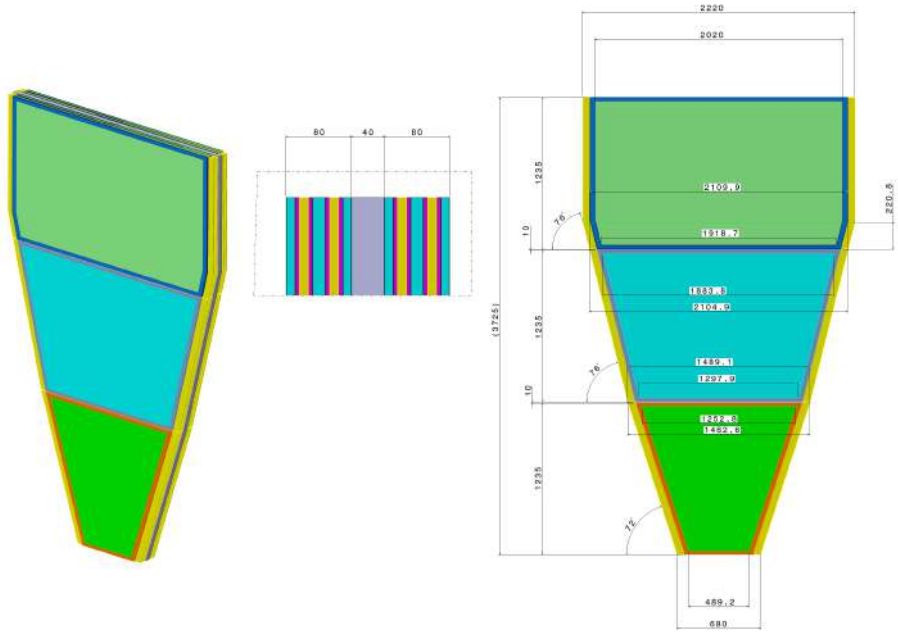

(b) Large sector.

Figure 3.11: Layout of the MM detectors with three modules, including space allocated for services. The active detector area is indicated. Left and middle: Example assembly of the two MM wedges in a sector to a MM chamber.

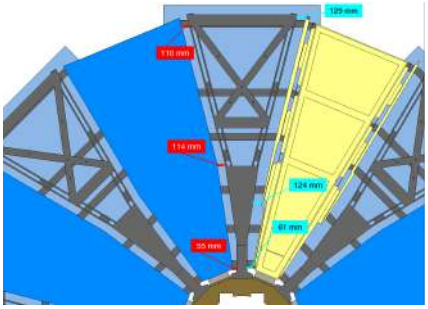

(a) sTGC (small sector).

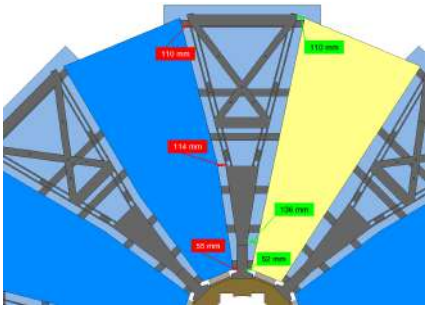

(b) MM (small sector).

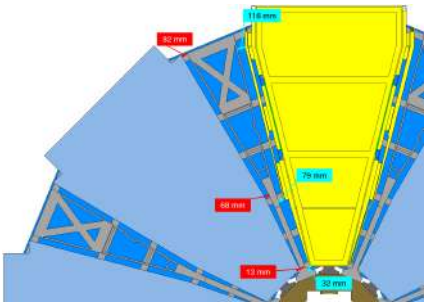

(c) sTGC (large sector).

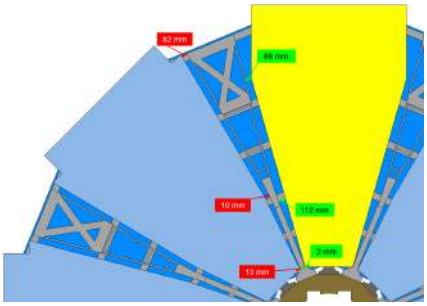

(d) MM (large sector).

Figure 3.12: Layout of the sTGC and MM detectors with services in the The detectors with services (yellow) and the allowed envelopes (blue) are shown. The distances at various points to the NSW structure are indicated for both.

The sTGC wedges will be kinematically mounted on the MM frame at three points and the whole assembly is mounted on the NSW structure using the same three mount points. Figures 3.12 shows the sTGC and MM detectors inside the mechanical support structure of the NSW. In the z-direction the package of sTGC and MM detectors has a minimum dimension of 360 mm including a space of 10 mm between an sTGC wedge and the neighboring MM wedge, as indicated in Fig. 3.9.

The detectors in the small and large sectors are designed to overlap at the sectors' ϕ boundaries. Figure 3.13 shows the overlapping regions of the small and large sectors for the sTGC detectors (a) and the MM detectors (b). The overlap was maximized for both detector types, but it is limited by the services on the chamber sides and the allowed envelopes.

3.11 Weight of the New Small Wheels

The estimated weights of all detector units for the different layout options are given in Table 3.2. The estimate of the weight of the services includes the routing on the NSW rim to each sector. The overall weight of the detectors is about a factor 1.8–2 higher than in the present SW.

Table 3.3 lists the estimated weights of all components of a NSW. For comparison, the total weight of a present SW is about 107000 kg. The higher weight of the NSW is mainly due to the heavier detectors as the numbers of layers and the acceptance have been increased.

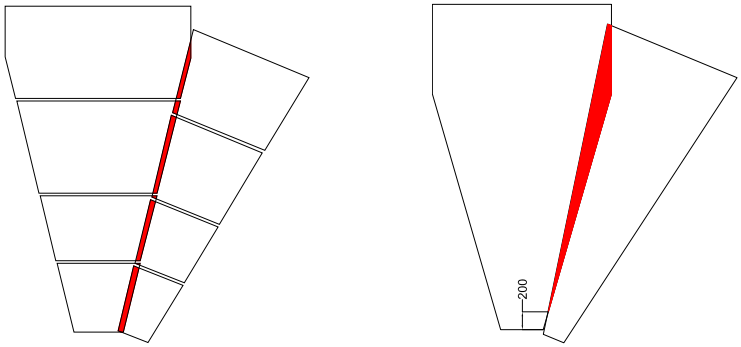

(a) sTGC detectors. (b) MM detectors.

Figure 3.13: Examples of the overlap (red) of the active detector areas of adjacent small and large sectors. The exact overlap area depends on the detector plane.

Table 3.2: Estimated weights of the sTGC and MM detector assemblies for the different options. The total sector weight includes two times the module weights (two quadruplets), two frames in the case of the sTGC, one frame in case of the MM and the services. All weights are given in kg. Final numbers are rounded.

Detector unit	Weight	Weight MM	
	sTGC	Sector-sized module	Multi-module
Module 1 small/large sector	43 / 53	95 / 155	34 / 44
Module 2 small/large sector	34 / 59	—	47 / 65
Module 3 small/large sector	35 / 75	—	58 / 75
Frame small/large sector	30 / 40	45 / 55	90 / 100
Services small/large sector	80 / 80	80 / 80	80 / 80
Total weight small/large sector	365 / 535	315 / 445	450 / 550

Table 3.3: Weights of the NSW components per wheel. The total detector weight depends on the layout option chosen for the MM detectors (sector-sized module/multi-module). All weights are given in kg. The final numbers are rounded.

Component	Weight	Number of components	Total weight
Detectors and services small sector	680 / 815	8	5440 / 6520
Detectors and services large sector	980 / 1085	8	7840 / 8680
Detector mounts	5	48	240
Alignment, sector	40	16	640
Mechanical structure	14000	1	14000
JD shielding	80000	1	80000
Airpads	500	4	2000
Total	—	—	110000 / 112000

4 sTGC detector technology and performance

In Chapter 2 the requirements for the triggering system in the NSW have been defined. The triggering detectors should provide bunch crossing identification, requiring good time resolution, and good angular resolution, better than 1 mrad, for online reconstructed segments, which in turn entails fairly good online spatial resolution. The sTGC detector provides both capabilities as will be demonstrated in this chapter and for this reason is regarded as the main triggering detector in the NSW. It provides also a fair spatial resolution for the offline tracking that will help the precision tracking, specially during the HL-LHC phase.

4.1 sTGC

The basic Small strip Thin Gap Chamber sTGC structure is shown in Fig. 4.1(a). It consists of a grid of 50 µm gold-plated tungsten wires with a 1.8 mm pitch, sandwiched between two cathode planes at a distance of 1.4 mm from the wire plane. The cathode planes are made of a graphite-epoxy mixture with a typical surface resistivity of 100 kΩ/□ sprayed on a 100 µm thick G-10 plane, behind which there are on one side strips (that run perpendicular to the wires) and on the other pads (covering large rectangular surfaces), on a 1.6 mm thick PCB with the shielding ground on the opposite side (see Fig. 4.1(b)). The strips have a 3.2 mm pitch, much smaller than the strip pitch of the ATLAS TGC, hence the name 'Small TGC' for this technology.

A similar type of structure was used in the past for the OPAL Pole-Tip calorimeter, where 400 detectors were constructed and run for 12 years.

The TGC system, used in the present ATLAS muon end-cap trigger system, has passed a long phase of R&D and testing. The basic detector design for the NSW has two quadruplets 35 cm apart in z. Each quadruplet contains four TGC's, each TGC with pad, wire and strip readout.

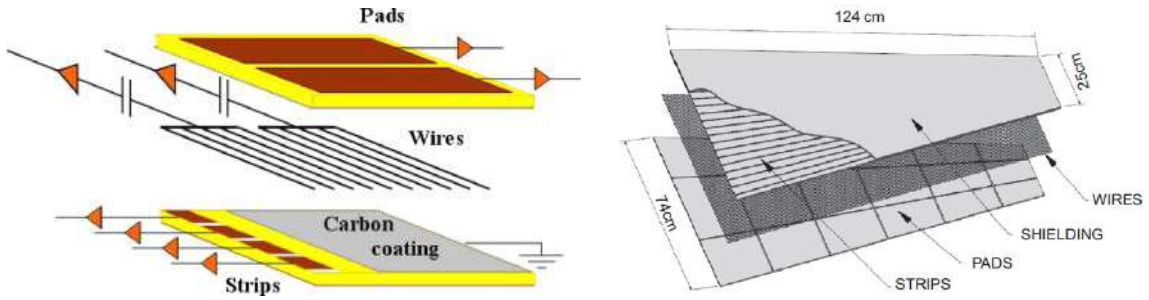

(a) a (b) b

Figure 4.1: The sTGC internal structure.

The pads are used to produce a 3-out-of-4 coincidence to identify muon tracks roughly pointing to the interaction point. They are also used to define which strips are to be readout to obtain a precise measurement in the bending coordinate, for the online muon candidate selection. The azimuthal coordinate, where only about 10 mm precision is needed, is obtained from grouping wires together. The charge of all strips, pads and wires are readout for offline track reconstruction.

4.2 Detector technology and characteristics

The high background of the HL-LHC environment necessitated modifying the TGC technology in order to achieve a very good (approximately 100 μm) position resolution at high count rates. The main emphasis during the development stage was on achieving this performance with the smallest possible number of electronic channels. It is known that space-charge effects are not a limiting rate element for TGC. However the rate capability is limited by the use of the resistive coating in the cathodes, which reduces, under high irradiation, the effective operating voltage of the detector in areas far from the ground contacts. As a consequence a low surface resistivity coating (approximately 100 kΩ/□) has been used, and the capacitance between the strips/pads and the cathode has been increased to keep the same transparency for fast signals.

This optimization, combined with a reduction of the HV and ground decoupling resistors is sufficient for maintaining high efficiency for minimum ionizing particles in large surface detectors subject to detected rates of up to 20 kHz/cm^2 over the full surface. The position resolution required for the trigger function was optimized by building small detectors and studying the position resolution as a function of the strip pitch, maintaining a minimal number of read-out channels.

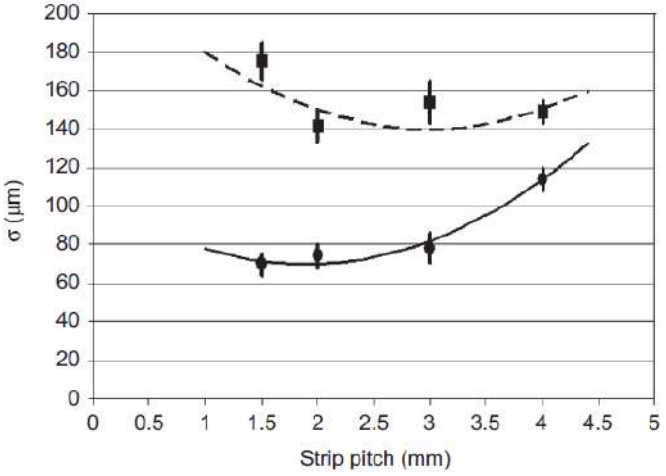

Figure 4.2: Average position resolution for two different incident angles (0-10°, circles) and (20-30°, squares) using charge division between strips. The values shown have been averaged over different HV settings.

The published results [15] are shown in Fig. 4.2 for two different incident angles. A 3.2 mm pitch has therefore been used for sTGC. Following this parameter optimization, the main emphasis was put in constructing and testing large (120 × 70 cm^2) detectors where these concepts could be tested in a realistic environment. The tooling needed for achieving the required alignment between

planes has been developed at the same time. This activity has also provided experience in the operation of large area detectors in a high rate environment. The main conclusions of this series of tests (described below) is:

1. Large area sTGC's can operate without problems under uniform γ irradiation of 20 kHz/cm^2 with high efficiency for minimum ionizing particles.
2. Using a 3.2 mm pitch and centroid finding for strips, obtained by measuring the strip charge, using either a charge integrating or a peak sensitive ADC, a position resolution ranging from 60 μm, at perpendicular incident angle, to 150 μm at 30° incident angle has been achieved in a reproducible way for all five large quadruplets constructed.
3. Detecting cosmic muons under uniform γ irradiation of 17 kHz/cm^2 of detected photons shows no deterioration of the single plane efficiency for minimum ionizing particles.

In order to use the sTGC as a Level-1 trigger device, a fast method to measure the strip charge must be provided; a conventional ADC is too slow. Two alternative methods were evaluated: one using a peak-sensitive Flash-ADC and an other based on Time-over-Threshold. With both methods sTGC can achieve online 150 μm position resolution per layer. The above have been extensively tested in a long test-beam campaign initiated in 2008 (see Section 4.4).

4.3 Detector simulation

The timing performance of the sTGC is critical for triggering. The small gas gap and the strong electric field in a large fraction of the gas volume ensure good timing properties for the sTGC, since the total drift time for most electron is shorter than 25 ns and the high amplification ensures high efficiency even for single clusters. The time spectrum for normally incident muons on an sTGC operated at 2.85 kV was simulated using the Garfield program [16] with a parameterized model which includes the effects of gas gain fluctuations and the electronics threshold. This result, along with experimental measurements using a 0.78 ns least count readout chip, is shown in Fig. 4.3. The experimental and simulated data agree well and demonstrate that 95% of the total events are contained within a 25 ns time window after proper adjustment of window offset.

Since the detector will be exposed to stray magnetic fields from the barrel and end-cap toroids with intensities up to 0.4 T in the ϕ direction, it is necessary to understand the gas properties under magnetic fields. The electron drift velocity and the Lorentz angle as a function of the electric field for the working gas mixture, CO_2:n-pentane (55:45), were simulated under different magnetic fields using the Magboltz package [17] and the results are shown in Fig. 4.4(a) and 4.4(b) respectively. The simulated electron drift velocity is in good agreement with the measured data up to 10 kV/cm without magnetic field [18] and it is also predicted that the drift velocity is unaffected by the presence of magnetic fields up to 1 T orthogonal to the electric field. The small Lorentz angle, less than 3° in a 0.4 T magnetic field, indicates that the increase of the electron drift path due to the presence of magnetic field is negligible. The simulated arrival time spectra of clusters closest to the wires with a 1 T magnetic field either parallel or orthogonal to the wires are very similar to those obtained with no magnetic field as shown in Fig. 4.5. Such timing distributions depend on the incidence angle of the particle in the plane normal to the wires and are narrower for larger incidence angles due to the higher probability of producing clusters near the wire.

The sTGC will also provide precision coordinate measurements in the η direction for Level-1 triggering as well as complementing the tracking information from MM. The charge produced inside the chamber induces signals on 3.2-mm-pitch readout strips which are capacitively coupled

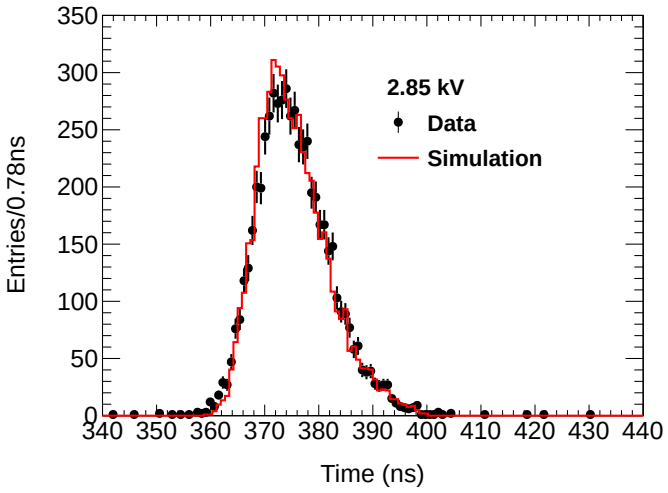

Figure 4.3: Comparison of a simulated time spectrum with experimental data taken using wire voltage of 2.85 kV. The horizontal axis has an arbitrary offset.

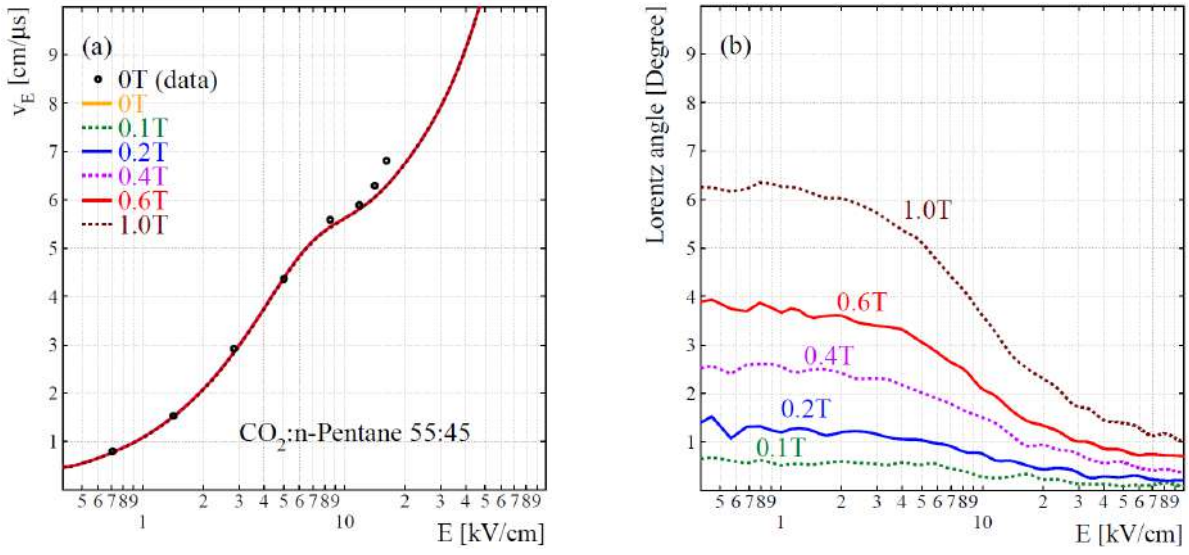

(a) Simulated electron drift velocity as a function of electric field. Lines for different magnetic fields are overlapped.

(b) Lorentz angle as a function of the electric field for different magnetic fields.

Figure 4.4: CO_2:n-pentane (55:45) gas mixture properties. The magnetic field is orthogonal to the electric field.

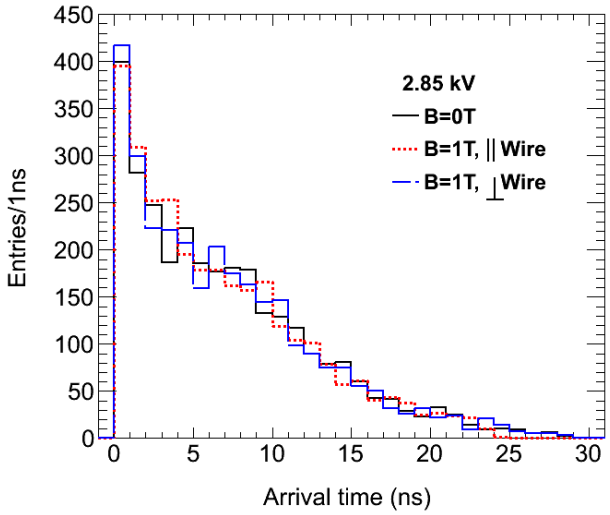

Figure 4.5: Comparison of simulated earliest cluster arrival time distributions for normal incident muon tracks with and without magnetic fields.

to the resistive cathode plane. A simple analytical model, based on the studies of charge dispersion in resistive layer, has been built to derive the charge density distribution function on each strip numerically. The charge ratios between different strips are simulated and compared with the experimental data from muon beam test using ADCs. Good agreements are shown in Fig. 4.6.

4.4 sTGC performance under high background conditions

A major R&D activity was started in 2008 to adapt the TGC technology to the harsh environment expected with the High Luminosity LHC (HL-LHC) upgrade. Outcomes of this activity are described below.

The detectors show no deterioration up to a total irradiation dose of 6 Coulomb/cm^2. This was a very important point for detectors that will have to run for over 15 years in a high radiation environment, with a total dose of up to 1 Coulomb/cm^2 expected at the hottest regions of the detector. The results are reported in [19]. Such irradiation tests are presently being continued at the Pontifical Catholic University of Chile for various gas flow rates and will be further continued at CERN, once the GIF++ facility becomes available, for large area detectors.

The local pulses produced by the passage of a muon through each of the 3600 TGC detectors operating in ATLAS have been monitored throughout the years of ATLAS operation. Fig. 4.7 shows the pulse spectra averaged over all the detectors on one side of the ATLAS experiment for various periods of time. It can be seen that such spectra are constant over the time, even at luminosities of $7.7 \times 10^{33}\,\mathrm{cm}^{-2}\,\mathrm{s}^{-1}$.

The large area detectors performed well (i.e. with high single plane efficiencies) up to background radiation levels of approximately 17 kHz/cm^2 of detected photons (see Fig. 4.9) and 75 Hz/cm^2 of detected neutrons (measurements with 5.5 MeV neutron fluxes two and three times the expected HL-LHC fluxes proved that sTGC single plane efficiency for cosmic rays reduces to 0.99 and 0.96 respectively).

Using a strip readout, one can obtain a position resolution of approximately 60–70 µm per

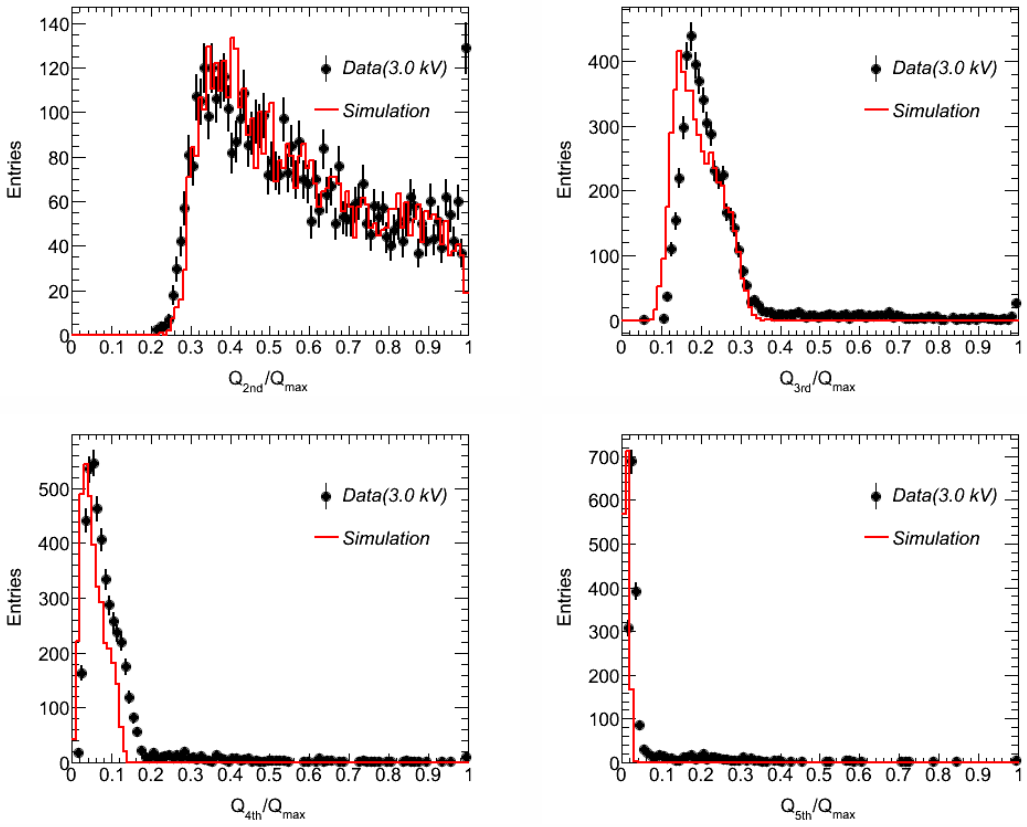

Figure 4.6: The distributions of the ratios of charges induced on various strips to the maximum charge, e.g. Q_{2nd}/Q_{max}, ratio of second largest charge to largest, etc.

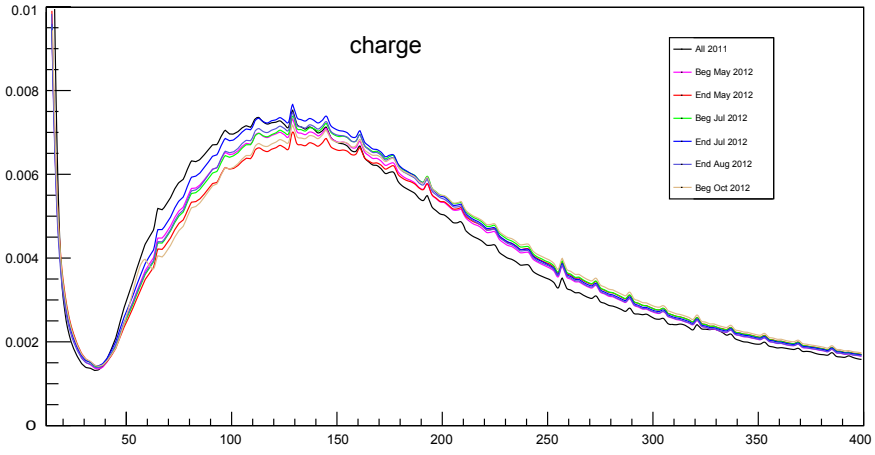

Figure 4.7: Average (for 1278 TGC planes) distribution of charge spectra (in arbitrary ADC units) for minimum ionizing particles for various periods of ATLAS running.

detector-plane in large area detectors at perpendicular incident angle, using the charge measurements, for each single layer. The obtained resolution deteriorates to 150 μm at large angles. This resulted from a parameter optimization described in [15] and the obtained resolution for a large area ($120 \times 70\,\mathrm{cm}^2$) quadruplet (see Fig. 4.8) are described in [19].

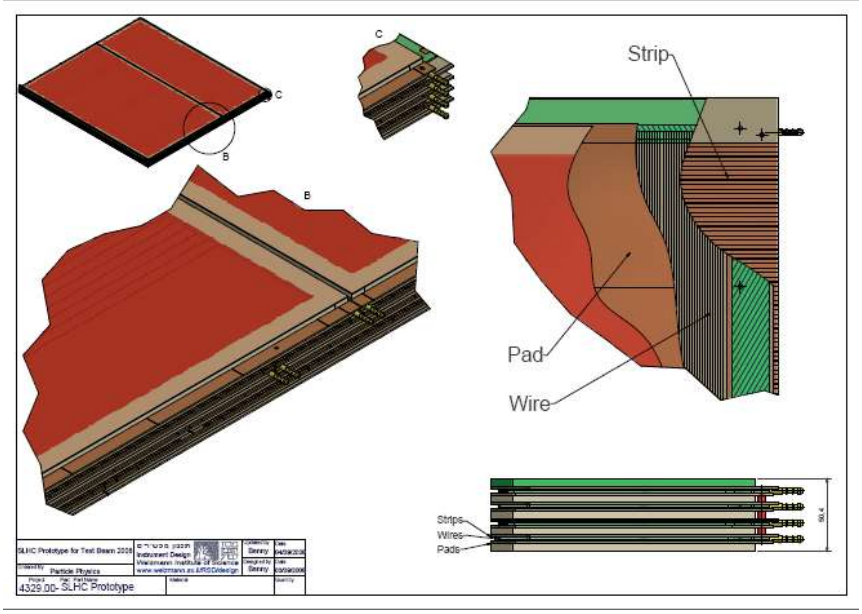

Figure 4.8: Schematic drawing of one of the five large 4-layer detectors that have been constructed and used to perform the tests described above.

Using pure digital output from strips, with signal length proportional to time-over-threshold, a position resolution of 70-100 μm in a large area detector has been achieved for each single layer, which provides the possible alternative of using only pure digital signals for the trigger [20].

In May 2012 a series of tests were performed with two quadruplets of $60 \times 40\,\mathrm{cm}^2$. They were mounted on a precise frame (see Fig. 4.10), used for a precise alignment and a common rotation of the two quadruplets.

The resulting position resolution for the various configurations and readouts are given in Table 4.1. The 'TDC' column refers to a resolution achieved by estimating the strip charge by the time-over-threshold of the signal induced, whereas for 'ADC', a flash ADC provides a precise charge measurement. It can be seen that the achieved results match the trigger requirements (<150 μm at all relevant angles).

Since a new front-end ASIC has been developed, which is common to the sTGC and MM detectors (see Chapter 12), it was important to test the position resolution that can be achieved with this electronics, in particular since the measurements are based on a peak sensing ADC. Furthermore, the new front-end electronics can provide also the peak charge of the nearest neighbors to the strips with signals above threshold. Using this feature, a charge distribution from the strip clusters that contain at least three strips is always obtained, therefore obtaining a high quality centroid, with good position resolution. Fig. 4.11(a) shows the achieved efficiency to obtain a good position measurement point using this nearest neighbor method as compared to a standard charge integrating ADC with a set threshold. The efficiency achieved exceeds 92% for all relevant angles, while the lost 8% are mainly due to a minimum ionizing muon accompanied either by a δ-ray or

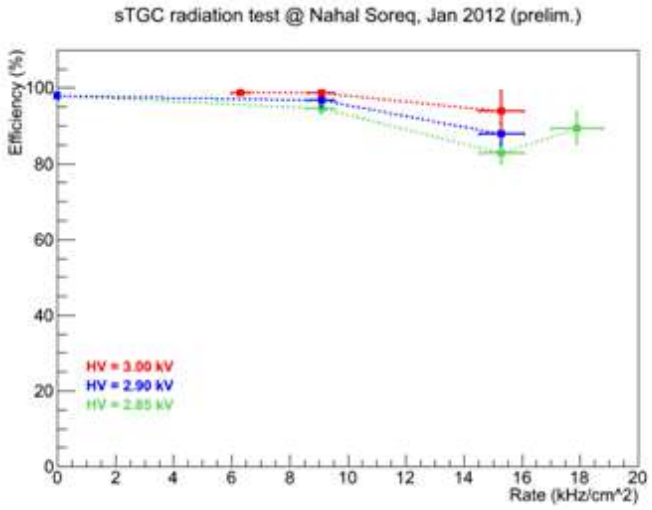

Figure 4.9: Single layer efficiency for detecting minimum ionizing particles as function of the detected photon rate of a $120 \times 70\,\mathrm{cm}^2$ chamber irradiated at the Soreq Nuclear Center.

Figure 4.10: Precise mechanical set-up to align the two quadruplets and measure their characteristics for various positions and angles, with a wide beam

Table 4.1: Position resolution for individual planes as a function of angle for three different horizontal positions using TDC and ADC

Angle	TDC res. (µm)	ADC res. (µm)
0°	105	55
5°	120	70
10°	104	104
15°	135	120
20°	127	156
25°	150	157

a second particle. The position resolution achieved with the new electronics was measured by comparing the position in two neighboring detectors exposed to a high energy muon beam. The results are shown in Fig. 4.11(b) and compared to those obtained with a charge integrating ADC. It can be seen that the same position resolutions are achieved, but with a much higher efficiency. Furthermore, the use of the proposed electronics provides a fast charge output using a flash-ADC or a Peak-to-Time signal, either of which can be used for triggering purposes.

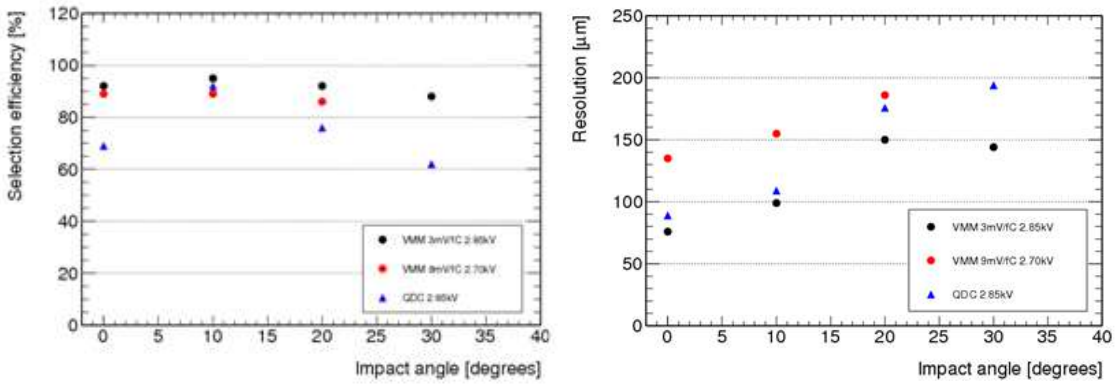

(a) Detection efficiency (hits with at least three strips).

(b) Position Resolution.

Figure 4.11: Performance of the new (VMM) front-end electronics as compared to a charge integrating ADC.

5 Micromegas detector technology and performance

In Chapter 2 the requirements for the precision tracking system in the NSW has been defined. The tracking detectors should provide very good position resolution independent of the particle incident angle, high efficiency even at the highest background rates, and good two track separation to reject delta rays accompayining muons. In this chapter the excellent tracking capabilities of MM detector (better than 100 μm for all particle impact angles in the New Small Wheel) will be demonstrated.

The very fine segmentation of the MM read out strips, together with a reasonably good time resolution, can also be exploited to complement the trigger scheme based on sTGC, adding in the robustness and redundancy of the system.

5.1 Detector technology and characteristics

The micromegas (an abbreviation for 'micro mesh gaseous structure' (MM)) technology was developed in the middle of the 1990's [21]. It permits the construction of thin wireless gaseous particle detectors. MM detectors consist of a planar (drift) electrode, a gas gap of a few millimetres thickness acting as conversion and drift region, and a thin metallic mesh at typically 100–150 µm distance from the readout electrode, creating the amplification region. A sketch of the MM operating principle is shown in Fig. 5.1. In the original design the drift electrode and the amplification mesh were at negative high voltage (HV) potentials, the readout electrode is at ground potential (the HV scheme has been modified for the MM application in ATLAS, see following sections). The HV potentials are chosen such that the electric field in the drift region is a few hundred V/cm, and 40–50 kV/cm in the amplification region. Charged particles traversing the drift space ionize the gas; the electrons liberated by the ionization process drift towards the mesh. With an electric field in the amplification region 50–100 times stronger than the drift field, the mesh is transparent to more than 95% of the electrons. The electron avalanche takes place in the thin amplification region, immediately above the readout electrode. The drift of the electrons in

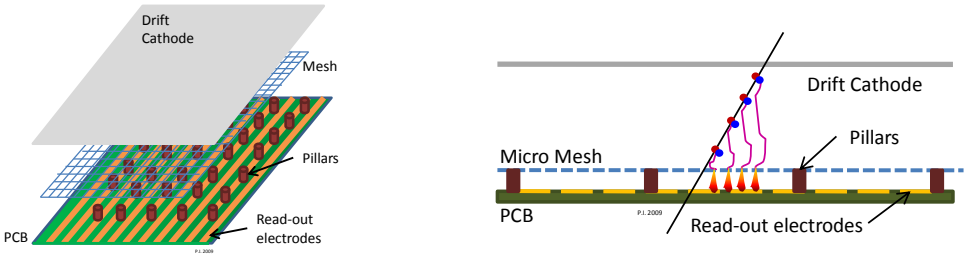

Figure 5.1: Sketch of the layout and operating principle of a MM detector.

the conversion gap is a relatively slow process; depending on the drift gas, the drift distance, and the drift field it typically takes several tens of nanoseconds. On the other hand the amplification process happens in a fraction of a nanosecond, resulting in a fast pulse of electrons on the readout strip. The ions that are produced in the avalanche process move, in the opposite direction of the electrons, back to the amplification mesh. Most of the ions are produced in the last avalanche step and therefore close to the readout strip. Given the relatively low drift velocity of the ions, it takes them about 100 ns to reach the mesh, still very fast compared to other detectors. It is the fast evacuation of the positive ions which makes the MM particularly suited to operate at very high particle fluxes.

MM detectors have been successfully used in high energy particle physics experiments in the past years in application where good spatial resolution at high rates was required [22, 23]. MM were also successfully used as readout chambers of Time Projection Chambers [24, 25].

5.1.1 Spark-protected micromegas

The weak point of the MM original design was their vulnerability to sparking. Sparks occur when the total number of electrons in the avalanche reaches a few 10^7 (Raether limit [26]). High detection efficiency for minimum ionizing muons calls for gas amplification factors of the order of 10^4. Therefore, ionization processes producing more than 1000 electrons over distances comparable to the typical lateral extent of an avalanche (a few hundred microns) carry the risk of sparking, see for example Ref. [27]. Such ionization levels are easily reached by low-energy alpha-particles or slowly-moving charged debris from neutron (or other) interactions in the detector gas or detector materials. Sparks may damage the detector and readout electronics and/or lead to large dead times as a result of HV breakdown.

For the MM detectors to be installed on the New Small Wheel a spark protection system has been developed. By adding a layer of resistive strips on top of a thin insulator directly above the readout electrode the MM become spark-insensitive. The readout electrode is no longer directly exposed to the charge created in the amplification region, instead the signals are capacitively coupled to it. By adding this protection some fraction of the signal height is lost but the chamber can be operated at higher gas gain and thus have spark intensities reduced by about three orders of magnitude. The principle of the resistive spark protection is schematically shown in Fig. 5.2.

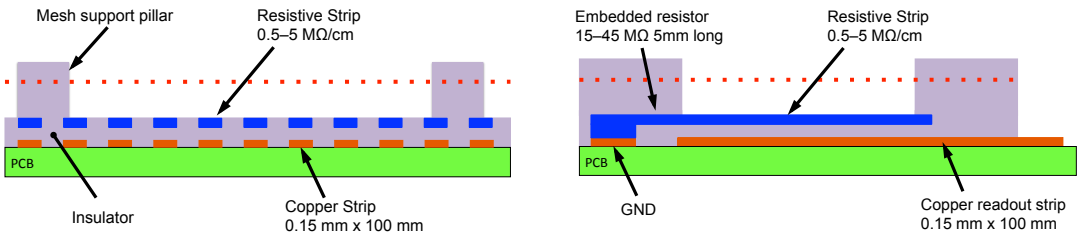

Figure 5.2: Spark protection principle.

The detector concept with resistive strip spark protection has been extensively tested in hadron and neutron test beams up to rates far exceeding the ones expected in ATLAS. Furthermore, a large number of detectors has been exposed to 8 keV X-rays up to rates of several 10 MHz/cm^2. Last but not least, since the beginning of 2011 four small MM detectors have operated faultlessly on

the Small Wheel in the ATLAS cavern as well as two small prototypes in the high rate environment in front of the electromagnetic end-cap calorimeter (EMEC) (see Section 5.5.1).

The largest detectors that have been constructed and operated successfully so far using the resistive-strip protection layer have an active area of $0.92 \times 2.12\,\mathrm{m}^2$.

5.1.2 The micromegas for the NSW

The MM detectors for the NSW differ in at least two points from the original MM scheme. i) the resistive-strip protection scheme is used, as described above. ii) instead of applying negative HV on the amplification mesh and keeping the resistive strips at ground potential, positive HV is applied to the resistive strips and the amplification mesh is connected to ground. This scheme resulted in a more stable operation of the detectors. Thus sparks cease to cause concern. The spark-induced current can be evacuated very quickly to ground through the mesh and the mesh potential does not change[1]. Further advantages of the modified HV scheme are the better focusing of the field lines between the amplification mesh and the resistive strips, leading to a better charge collection on the resistive strips, and a considerable simplification in the detector construction.

Contrary to most of the MM detectors now in operation, in the present implementation the amplification mesh is not integrated in the readout structure. The advantages for large-area detectors are the following: i) the mesh size is only limited to he mesh fabrication size and stretching machines and not to the size of the individual PCBs; ii) it facilitates detector opening and cleaning; iii) it separates PCB production from mechanical construction. Figure 5.3 shows schematically the internal structure of a readout PCB. The readout strips are drawn on 0.5 mm

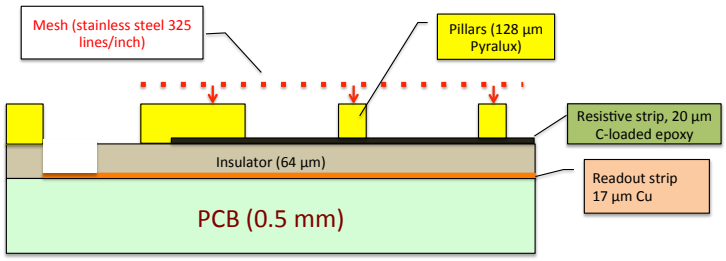

Figure 5.3: Internal structure of the MM readout boards, note that the mesh is not part of the readout PCB.

thick PCBs and then covered by a 64 µm thick layer of insulator, followed by the resistive strips. On top of the resistive strips the mesh support pillars are deposited. The mesh sits on these support pillars, however it is not a part of the readout PCB but a part of the drift panel.

The main detector and operating parameters of the MM detectors for ATLAS are summarized in Table 5.1.

[1] When the mesh is polarized the mesh potential changes in the event of a spark, even if the potential drop is small, and a signal is induced in all strips.

Table 5.1: Main MM detector and operating parameters.

Item/Parameter	Characteristics	Value
Mesh	Stainless steel separate from readout board	325 lines/inch
Amplification gap		128 µm
Drift/conversion gap		5 mm
Resistive strips	Interconnected	R = 10–20 MΩhm/cm
Readout strip pitch		0.425–0.445 mm
Stereo angle	4/8 layers	±1.5°
Total number of strips		2.1 M
Gas	Ar:CO_2	93:7
HV on resistive strips	positive polarity	550 V
Amplification field		40 kV/cm
Drift field		600 V/cm

5.2 Micromegas layout

5.2.1 Wedge layout

The integration of the MM detectors and their overall layout has been described in Chapter 3. They are arranged in large and small sectors. The dimensions of the sectors are chosen such that approximately the same azimuthal overlap of the active areas as in the current Small Wheel is achieved. Each sector comprises of eight MM detection layers, grouped into two multiplets of four layers each (hence quadruplets), separated by a 40 mm thick spacer. Figure 5.4 left shows schematically the arrangement of the detectors in a sector.

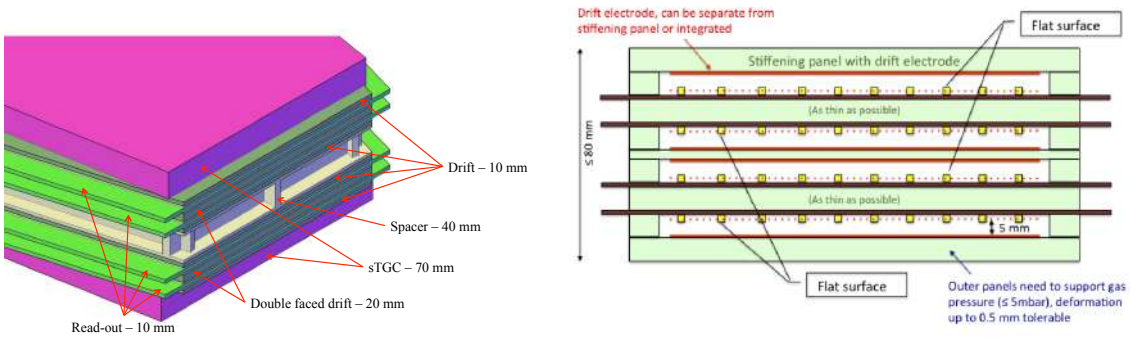

Figure 5.4: Left: arrangement of the detectors in a sector. Right: arrangement of the detectors in a multiplet.

Each multiplet contains four active layers, grouped into two pairs, as illustrated in Fig. 5.4 right. In each pair the detectors are mounted back-to-back. With such an arrangement i) background (tracks not synchronous with trigger signal, i.e. out-of-time with respect to the bunch crossing) will not be collinear in the two neighboring planes and thus can be rejected, ii) systematic shifts of

the recontructed particle positions, due to the deviation of the electrons drift path in a magnetic field (Lorentz angle) cancel out.

The segmentation of the MM sectors in the radial direction is still under discussion. Two approaches are being studied, one based on detector planes covering the full sector, the other splitting the sectors radially into two to four smaller modules. Mechanical prototypes of the two concepts are under construction and will serve to decide which way to go. The timescale for the decision is July 2013.

Independent of the radial segmentation of the detectors the active area of one detection plane will be composed of eight PCBs per sector. In order to stay within the dimensions that most PCB manufacturers can handle [2], the PCBs span the full widths of the sectors, and have a radial extent of 400–500 mm. In the scheme with complete detector planes, all eight PCBs will be glued to a single stiffening panel. In the scheme with four single modules, two PCBs will be glued to each stiffening panel.

The segmentation of the small and large sectors into PCBs is shown in Fig. 5.5 (for the full sector plane implementation). For the case of the four modules, the size of the PCBs in the radial direction would slightly change. In both cases the number of readout strips will be the same leading to small differences in the readout strip pitches for the two options. In the following, to avoid repetition, only the implementation of the full-sector approach is discussed, unless there are major differences.

In order to measure the second coordinate, an arrangement of the readout strips in a stereo configuration was chosen. The readout strips in each second detector layer are inclined by 1.5° with respect to the η-strips. This requires small adjustments to the arrangement of the PCB boards and the routing of the readout strips. Keeping the same strip pitch requires two additional readout chips per layer in the full-sector case, in order to read out the additional strips in the upper left side corners. The few additional strips required in the lower right corners of the sector will not be read out.

Each PCB carries 1024 readout strips with a typical strip pitch of 0.4–0.45 mm. Each PCB board is read out by two readout boards, carrying eight front-end chips (VMM) of 64 channels each. The upper half of the readout strips is read out on one side, the lower half on the other side.

The readout electronics boards are located along the detector sides. The space foreseen for the front-end electronics is 50 mm wide. Another 50 mm are foreseen for the detector frame and the dead space inside the frame, leading to a 100 mm inactive area along the detector side. The corresponding dead area in the radial direction is 30 mm. The active detector area is indicated by the inner lines in the figures. An active overlap is foreseen between the large and small sectors, as described in section 3.

Within a multiplet of four MM layers, two layers (back-to-back) will be equipped with η strips, the other two layers, again back-to-back, with stereo strips. In such a way the full single plane spatial resolution in the bending plane is maintained. The second coordinate precision is about 1.5 mm.

5.2.2 Detector support and alignment

The baseline solution for the MM chambers support is a central spacer on which the two MM wedges are mounted (glued or screwed). This solution can be adopted for both the single- or multi-module wedge, in the latter case the support frame will also act as the connection frame

[2] Usually the machines can handle printed boards dimensions of 600 mm in one dimension, while the other dimension can be up to 2500 mm.

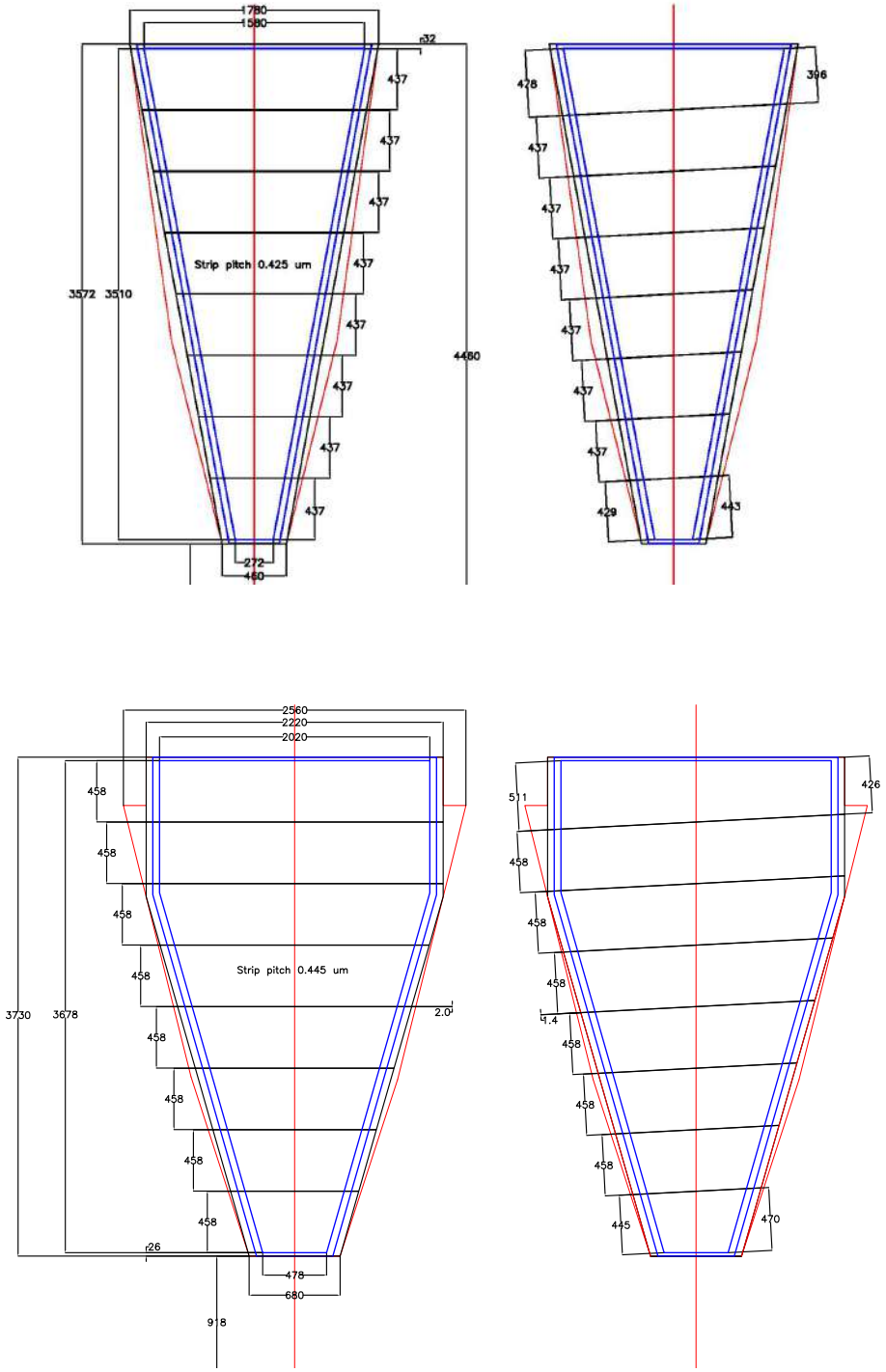

Figure 5.5: Segmentation of the small (top) and large (bottom) sectors into eight PCBs for the η (left) and stereo layers (right).

between the modules. A sketch of the central spacer is shown in Fig. 5.6. The central spacer will be made of aluminum or G-10, the selection of the best material is under evaluation.

Three kinematic mounts on the external frame of the spacer will be used for mounting the assembled sector on the NSW mechanical structure (Fig. 5.6 right). The optical alignment of

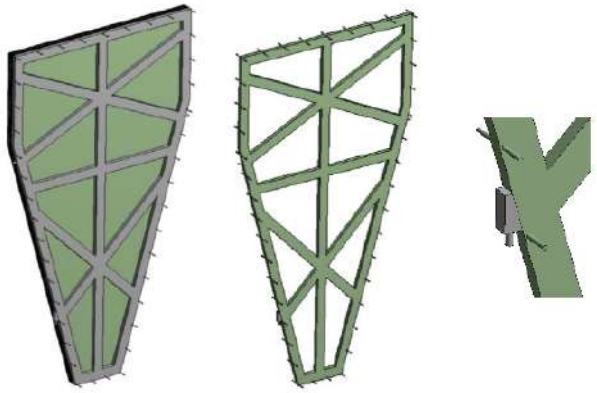

Figure 5.6: The MM central spacer for the full wedge solution. On the right a detailed view of one of the three supports is shown.

the chambers follows the same scheme as used at present for the MDT in ATLAS. An in-plane alignment system, if required, will be integrated into the chamber support frames. For the positioning of the chambers with respect to the alignment bars the alignment equipment can be mounted on the multilayer surfaces on precision pieces that are linked to the PCBs via precision inserts. The NSW alignment system is described in section 10.

The chambers being installed (almost) vertically, deformations of the PCBs due to gravity is not an issue. Calculations show that possible bending in the z direction due to temperature gradients will be less than 100 µm, for temperature gradients of 2 °C between the two sides (in z) of the detector. Such deformations are monitored by the in-plane alignment system. These values clearly depend on the selected material for the central spacer. Simulation studies of these deformation due to gravity and a temperature gradient of 2 ° have been carried out for different materials used for the central spacer and the results are summarized in Table 5.2. The maximum bending, for two MM wedges made of three detector modules each screwed on a G-10 spacer, turns out to be approximately 18 µm.

5.2.3 Detector services

The MM are operated at a moderately high voltage of typically +550 V on the resistive strips and −300 V on the drift cathode. Currents per PCB range from O(μA/m^2) for 10^4 Hz/cm^2 at small radii to a few tens of nA in the chambers at large radii. While the drift electrodes of each multiplet can be supplied by the same HV channel, the resistive strips of each PCB should have their individual HV such that the individual currents can be monitored and, if required, controlled. In addition, the resistive strips will be split in the middle and separate HV will be supplied to either side. This results in 16 HV sections per layer, served by four HV lines. The number of sections fed by each one of the four HV lines is optimized considering the expected hit rate and the surface of the sections: from the inner to the outher radius one HV line serves 2/4/6/4 HV sections, respectively.

Table 5.2: Deformation of MM wedge due to gravity and a temperature gradient of 2 °C between the two sides (in z) of the detector. The study is based on a finite element analysis for the 1- and 3-module wedge solutions and spacer frame of aluminum or G-10. In all cases the modules are screwed to the central spacers.

	Full size wedge aluminum	Full size wedge G-10	3-module wedge aluminum	3-module wedge G-10
Maximum deformation in z direction (µm)	∼30	>100	∼35	∼18
Maximum stress on the spacer (MPa)	∼19	∼7	∼29	∼8

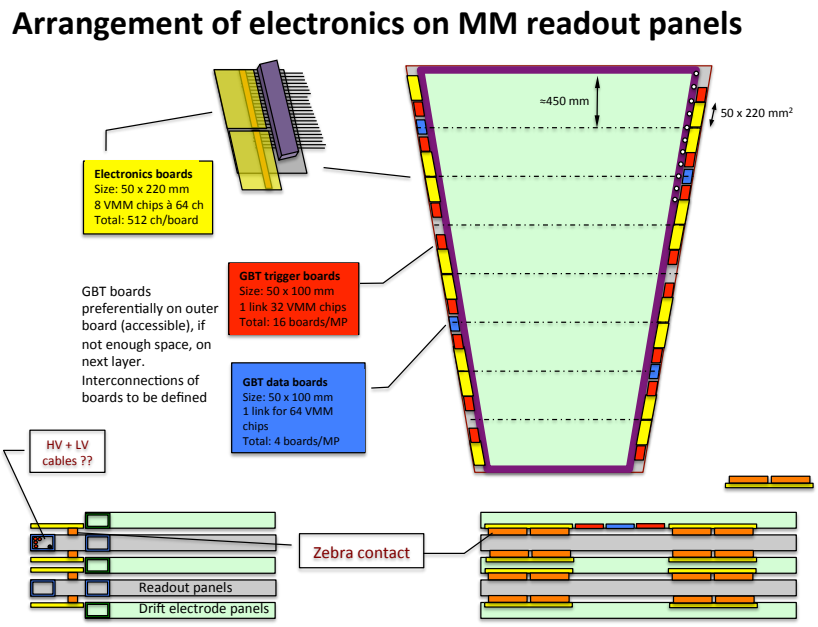

Figure 5.7: Arrangement on a sector plane of the front-end cards and the cards that carry the optical links for the trigger and data streams, schematically.

The on-chamber HV cables will be routed to HV patch panels located on the outer rim of the sectors in an accessible place. For the readout boards, four HV cables per layer or 16 cables per multiplet will be routed to UX15. Two additional cables per multiplet will be used to supply the drift electrode voltage. Including two spare cables, in total 20 HV cables will be routed from each sector multiplet to UX15. A CERN standard cable that carries 23 channels, rated to 3000 V DC (AWG26) has an outer diameter of 11.1 mm. In total 32 of these cables would be required per wheel.

The readout electronics is located on the side of the chambers, as illustrated in Fig. 5.7. It requires low voltage (1.2 V and 1.5 V) and optical fibre connections using the GBT link. The conversion to 1.2 V or 1.5 V will be done on the corresponding front-end or GBT boards. The

Table 5.3: Power consumption per sector.

Equipment	No. of channels	Power consumption per channel	Power consumption total
VMM chips	65536	8 mW	525 W
GBTx (optical links)	40	4 W	160 W

total power for the readout chips and the data transmission is about 22 kW for the two MM wheels, see Table 5.3.

The front-end cards are connected to the readout boards via a solder-less connectors, widely used in industrial solutions (e.g. LCD TVs, cars). They are commercially called Zebra elastomeric connectors[3] and guarantee a highly reliable and redundant connectivity. These are gold-plated wires embedded in a silicon rubber carrier that is placed between the contacts to be interconnected. Silicon rubber is qualified to be radiation hard up to about 10^7 rad or 10^5 Gy [28].

In addition to the front-end boards, two other types of electronics boards are in charge of transmitting the data via optical links to USA15. For the trigger, one trigger card handles the data of four front-end cards or 32 VMM chips. For the read out, data are transmitted by a single data GBT link per plane or 16 front-end cards. The connection between the front-end boards and the trigger and data GBT boards is made by mini coaxial cables with a diameter of less than 1.5 mm.

All detector services will be located at the sides of the chambers in order to maximize the accessibility. Cables and pipes will be integrated into the stiffening panels of the detector as much as possible. This is sketched in Fig. 5.8. HV, LV and signal cables as well as the optical fibres will be located in the stiffening panels. Figure 5.8 also indicates how the cooling of the front-end electronics is going to be implemented. An aluminum bar with channels for the cooling water is integrated into the readout panel below the front-end card. Cooling plates are mechanically attached to this bar to remove the heat through a contact pad, as used presently in the CSC cooling system in ATLAS. Except for the water connections at the top and the bottom of the modules, there are no other connections where potentially leaks may occur.

A parallel gas flow through all layers of a multiplet is foreseen in order to maintain an identical gas pressure in the four gas gaps of a multiplet, possibly in series for all modules in a wedge. This would lead to two gas lines (one in, one out) per multilplet and sector, or four gas lines per sector in total. The gas flow can be as low as a few liters per hour.

Table 5.4 gives an estimate of the cables/sector between the NSW and US15.

5.3 Detector Simulation

Detailed simulations of the MM detectors, with the use of the ANSYS [29], Magboltz [30] and Garfield [16] packages, have been developed to compare with test results and for layout studies. A parametric description of the gas properties was developed in ROOT and an RC circuit model has been used to model the front-end electronics response on a readout strip:

$$f(x) = q_i \left(\frac{x - t_i}{RC} \right)^a e^{-(x-t_i)/RC}$$

[3]Fuji Polymer Industries Co., Ltd.

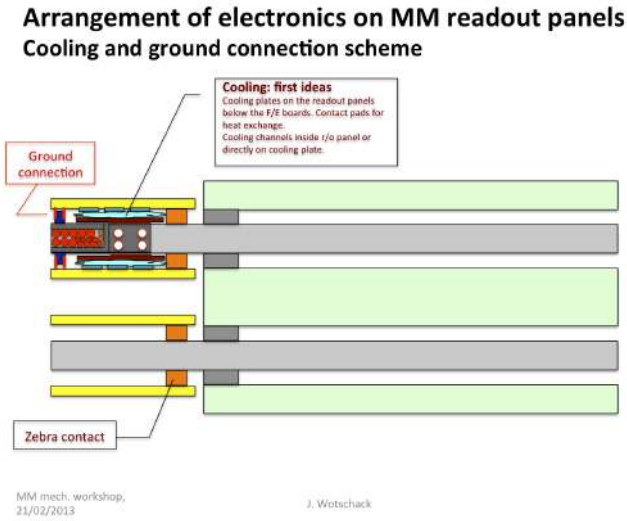

Figure 5.8: Integration of services in a MM sector, schematically.

Table 5.4: Cables per sector between the outer rim of the wheel and the service cavern. The routing of the HV and LV cables is still to be finalized, here only an example is given.

Cable	Number of cables (granularity)	Outer cable diam. (mm)	Cross section of leads (mm^2)
HV	2	11.1	$23 \times 0.14\,mm^2$
LV	2	19	$5 \times 6\,mm^2$
Optical fibre bundles (trigger)	4	15	12 fibres/bundle
Optical fibre bundles (data)	2	10	8 fibres/bundle

where q =charge in number of electrons and t =time of electron arrival.
With the above equation different integration times can be applied at different charge threshold. The output of such a simulation was compared to data acquired during test beam periods with the MM detectors as shown in Fig. 5.9 left. The MM detectors will also provide a trigger signal for the New Small Wheel. The trigger algorithm is based on the strip which gets the first hit from an avalanche. This VMM feature was simulated and compared to real data. Such a comparison is shown in Fig. 5.9 right.

5.4 Single point space resolution

The performance of MM detectors have been extensively studied during several test beam campaigns with high energy particle beams at CERN. Results presented in Section 5.4.1 are mostly based on tests performed at the H6 beam line at the Super Proton Synchrotron (SPS) at CERN in July 2012. The H6 line provides a 120 GeV pion beam with an intensity ranging between 5 and 30 kHz over an area of approximately $2\,cm^2$. The test in magnetic field, described in Section 5.4.2 was carried out, in June 2012, in the H2 SPS beam line which has similar beam characteristics.

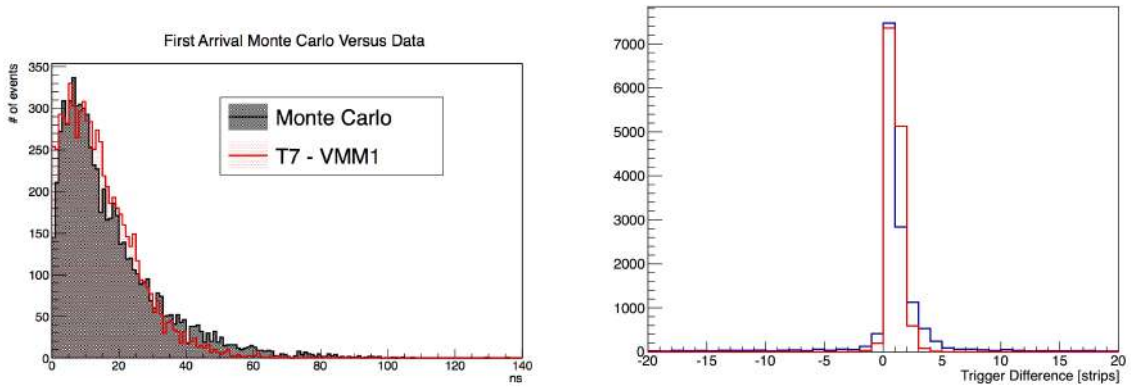

Figure 5.9: Left: comparison of data to Monte Carlo of the earliest arrival signal time of a hit with the first generation of the VMM readout chip. Right: Difference between the first arrival strip as obtained from offline from the read out of the VMM1 chip and the strip selected from the VMM1 for the trigger. Red histogram refers to teast beam data, blue histogram to Monte Carlo expectation.

Front-end readout electronics was based on the 128 channels APV25 ASIC in which detector signals are zero-suppressed, shaped with a CR-RC circuit and sampled at 25 ns frequency. The total acquisition time window was of 675 ns, corresponding to 27 samples.

5.4.1 Spatial resolution for straight and inclined tracks. The μTPC method

The spatial resolution of MM detectors was studied for eight resistive chambers (T1–T8), aligned along the beam line and oriented, in pairs, in a back-to-back configuration. The total lever arm of the system was 600 mm. The detectors were operated with an Ar:CO_2 gas mixture (93:7). The reference operating settings were 600 V/cm electric drift field and an amplification voltage HV_{mesh}=500 V.

Data with beam perpendicular to the MM and at various angles have been recorded and analyzed. The trigger was provided by the coincidence of three scintillators plus a veto. The APV25 chips were operated at a frequency of 40 MHz, completely unsynchronized to the particle beam. A jitter of ±12.5 ns, corresponding to the width of one clock cycle, is introduced by the synchronization of the trigger signal.

The spatial resolution of MM with sub-mm strip pitch and analog readout can easily go below 100 μm for perpendicular tracks by using the cluster charge centroid method [31]. A spatial resolution of about 73 μm has been obtained for all chambers under test, with an average cluster size of approximately 2.4 strips.

With the same perpendicular tracks, global detector inefficiencies have been measured to be in the range of 1–2%, consistent with the partially dead area expected from the presence of the 300 μm diameter pillars separated by 2.5 mm.

For impact angles greater than 10° the μTPC method [31] is used for a local track segment reconstruction in the few-millimeter wide drift gap. It exploits the measurement of the hits time and the highly segmented readout electrodes: the position of each strip gives an x coordinate, while the z coordinate (perpendicular to the strip plane) can be reconstructed from the time measurement of the hit after calibrating the z–t relation ($z = t \times v_{\mathrm{drift}}$), see Fig. 5.10, left.

The hit time is measured for each strip by applying a fit to samples obtained from the shaped

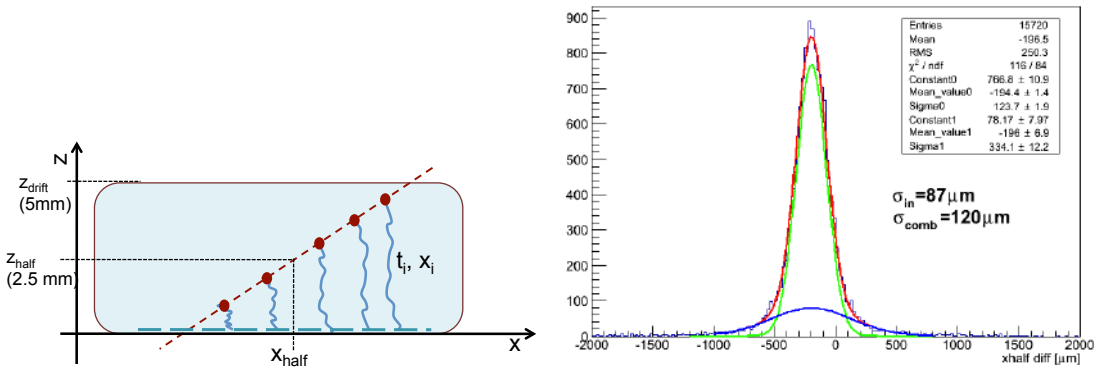

Figure 5.10: Left: principle of the MM μTPC operating mode. Right: distributions of $\Delta_{x_{half}}$ for particle impact angle of 30°. The distribution is fitted with a double Gaussian (red line) accounting for a core distribution (green line) plus tails (blue line). The widths of the two Gaussians are reported in the plot.

output of the charge integrating pre-amplifier. The time resolution obtained with this analysis depends on the impact angle and is approximately 12 ns at 30°. For each event, (x_i, z_i) coordinates are assigned to each hit and fitted with a straight line, from which the best position measurement,'x_{half}' is obtained (as indicated in Fig. 5.10 left).

Tracklet angles are reconstructed with about 70 mrad resolution. The μTPC spatial resolution has been measured by the difference of x_{half} in two chambers with the same orientation ($\Delta_{x_{half}}$). The time jitter is equal in the two chambers and cancels out in the difference. In Fig. 5.10 right the distributions of Δx_{half} for a beam impact angle of 30°, are reported. The single plane resolution is about 90 μm, assuming that it is obtained by the width of the fitted distribution by $\sqrt{2}$.

The results for the MM spatial resolution study are summarized in Fig. 5.11. As expected, the cluster centroid behaves better at small angles (small cluster size) while the μTPC method reaches best performance for larger angles. Moreover,it has been verified that the position determination with the two methods is systematically anti-correlated; for that, a weighted average can improve the resolution further. The result of a simple combination method using a weighted average of the cluster centroid and the μTPC position measurement is also reported in the figure, demonstrating that spatial resolutions below 100 μm is achievable for all impact angles up to 40° (the impact angle range for muons in the NSW is approximately between 8° and 30°).

A cross-check of the previous results was done with a full track reconstruction method; the results obtained are in excellent agreement with the simpler method described above.

5.4.2 Performance of the micromegas detectors in magnetic field.

The MM chambers of the NSW will operate in a magnetic field of a magnitude up to about 0.3 T with different orientations with respect to the chamber planes but a sizable component orthogonal to the MM electric field.

The effect of the magnetic field on the detector operation has been studied with test beam data and simulations. Figure 5.12 shows the drift velocity and the Lorentz angle as a function of the drift field for several values of the magnetic field (perpendicular to electric field) and for an Ar:CO_2 93:7 gas mixture. Figure 5.13 illustrates the effect of the magnetic field on a MM chamber. The drift direction of the ionization electrons is tilted with respect to the electric field direction by

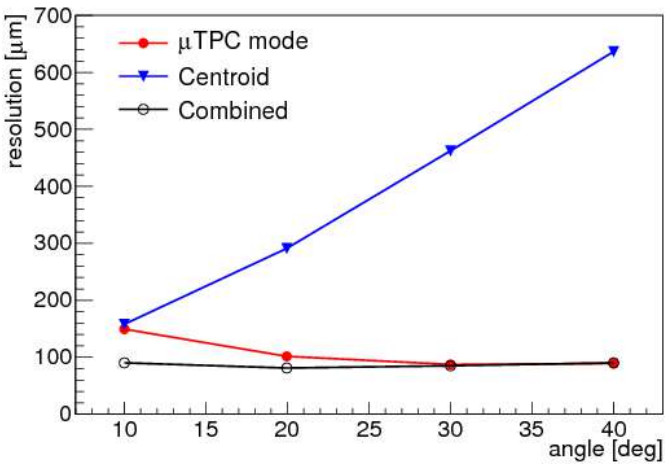

Figure 5.11: MM spatial resolution with charge centroid method (blue triangles), μTPC method (full red circles) and the combination of the two (black open circles) as a function of the particle impact angle.

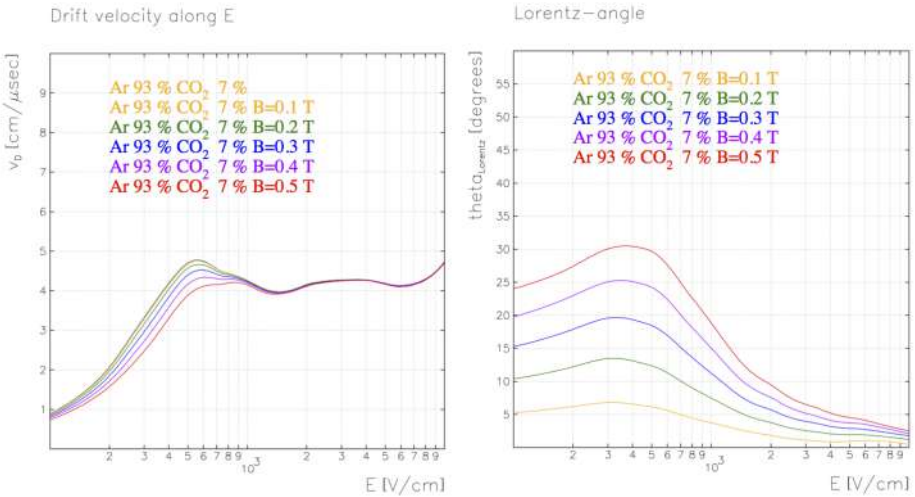

Figure 5.12: Drift velocity along the electric field (left) and Lorentz angle (right) as a function of the drift field for different values of the magnetic field.

the Lorentz angle θ_L; $\tan\theta_L$ is proportional to the magnetic field intensity B. Expected values of θ_L are shown in Fig. 5.12 right. The tilt of the drift direction gives a sizable shift (δx) of the reconstructed hit position of the order of

$$\delta x = (d/2)\tan\theta_L = 2\text{mm} \times B(\text{T})$$

where $d = 5\,\text{mm}$ is the drift gap. This shift affects both centroid and μTPC reconstruction and reaches values up to $400\,\mu\text{m}$. Singular configurations are expected when $\theta = \theta_L$, θ being the inclination angle of the track. In these configurations the ionization cluster is confined to a very small number of strips. On the other hand, when θ and θ_L have different sign, the ionization

cluster is spread over a larger number of strips in such a way that for a fixed charge threshold the number of strips of the cluster is reduced.

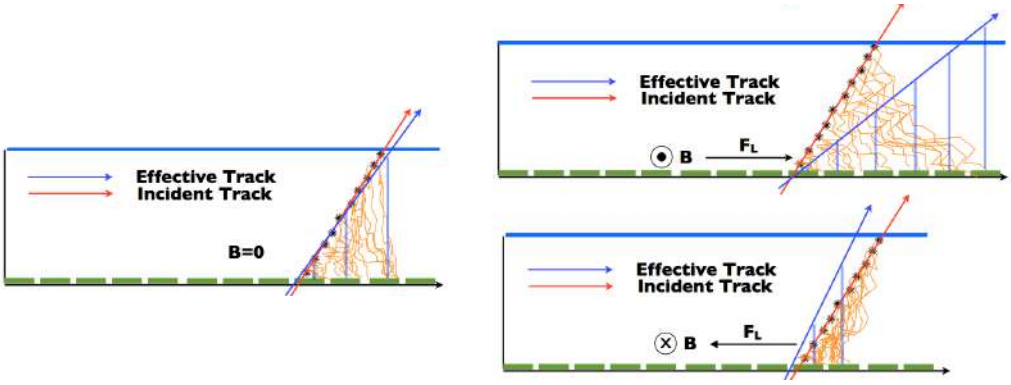

Figure 5.13: Pictorial view of the effect of the magnetic field on the drift in a MM chamber. The real track is shown in red and the reconstructed track in blue; B=0 (left) and B≠0 (right) upward or downward are shown.

Four MM prototypes, of $10\times10\,\mathrm{cm}^2$ active area, have been exposed to the H2 beam at CERN in June 2012. The detectors were installed in a solenoid which can provide a magnetic field up to 1 T orthogonal to the beam line and to the MM electric field. The chambers were operated with the standard gas mixture (Ar:CO_2, 93:7), a drift field of 0.6 kV/cm and an amplification voltage of HV_{mesh}=460–480 V, lower with respect to the usual operating voltage of 500 V. Four chambers assembled in two back-to-back doublets 20 cm apart are studied, T1–T2 and T3–T4, respectively. T1 and T2 had a drift gap of 5 mm, T3 and T4 had a drift gap of 10 mm[4].

The values of θ_L are extracted from the data by measuring the shift of the cluster centroid distributions at the different magnetic field intensities. In Fig. 5.14 the measured values of θ_L are compared to Garfield values. Space resolutions are obtained for the charge centroid x_{cent} and the

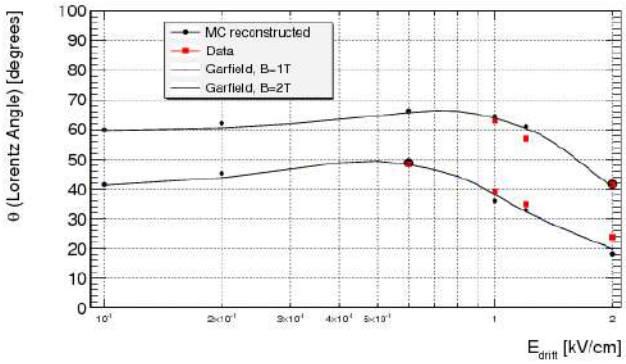

Figure 5.14: Comparison of data (red points) from test beam with Monte Carlo (black points) and Garfield (lines) simulations of the Lorentz angle as a function of the drift field in the MM detector for two different values of the magnetic field.

μTPC estimate x_{half} according to the definitions given in Section 5.4.1. The widths of the core

[4]This configuration was chosen in order to amplify the effect of the Lorentz angle.

Gaussians of the $\Delta_{x_{half}}$ distributions for the T1-T3 pair are obtained and divided by $\sqrt{3/2}$ to take into account the different drift gaps of T1 and T3. Figure 5.15 shows the spatial resolutions obtained using the centroid method and the μTPC method at five inclination angle configurations for data at B = 0 (a) and B = 0.2 T (b). The results can be easily understood considering that at B = 0.2 T the Lorentz angle θ_L is very close to 10°, so that the resolution profiles are shifted by this amount. At the singular configuration, the bad performance of the μTPC method is compensated by the good performance of the cluster centroid method, due to the very small cluster size. A combination algorithm can be applied to have a constant resolution through all configurations. Notice that the absolute values of the resolutions shown here are systematically larger than those in Section 5.4. This is not due to the presence of the magnetic field, but it is due simply to the fact that in this case the amplification was lower and this affects directly the resolution. The

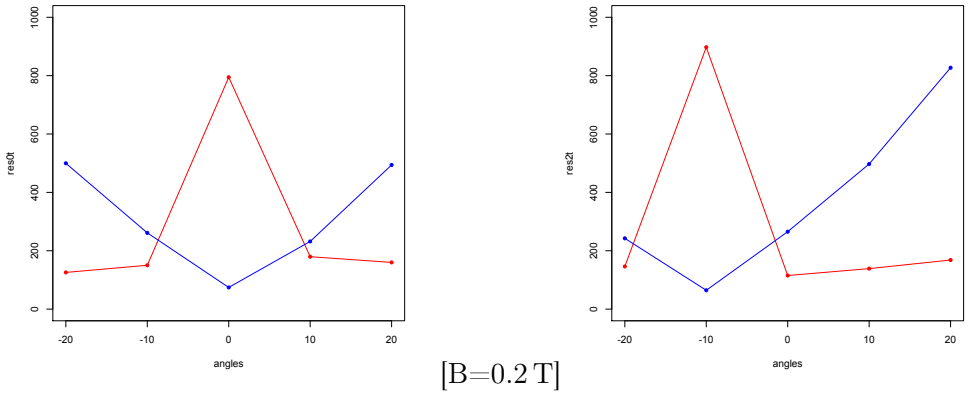

[B=0.2 T]

(a) B=0

Figure 5.15: Comparison of space resolutions obtained in the H2 test-beam using the centroid (red) and the μTPC (blue) methods.

systematic shifts of the reconstructed position due to the magnetic field can be corrected in two ways: i) by using the average point measured in a doublet in back-to-back configuration, which is systematic-free as demonstrated with simulations; ii) by measuring accurately the magnetic field on the NSW with an adequate number of magneic field sensors.

5.5 Aging studies on resistive micromegas detectors

The long-term radiation resistance of standard MM detectors have been shown elsewhere [32, 33]. However the introduction of the resistive coating technique with the addition of new materials required additional aging tests. In this section the first aging tests with this type of detectors using different types of highly ionizing radiations are presented. The complete studies with details can be found at [34–36].

Two identical prototypes built by the CERN workshop based on a resistive strips technology [37] with a 2-dimensional readout have been used for this study. These prototypes were built with materials and technology very similar to the ones to be used in the NSW detectors [5]. The two

[5]Copper X and Y readout strips. The top Y-strips insulated with a 60 μm thick coverlay film. The 35 μm thick

detectors were characterized in Ar:CO_2 mixture prior to any irradiation and showed comparable gains. One prototype (R17b) was kept unexposed as a reference while the other (R17a) was exposed to different types of radiation, listed below.

X-rays exposure. Assuming the expected rate at the HL-LHC muon chambers will be 14 kHz/cm^2, the total charge generated in five years of operation will be 45.2 mC/cm^2. The prototype under test was exposed to a high intensity X-ray flux for 21.3 days with a gain of 5000 and a gas flow of one renewal per hour. The current remained stable, proving the detector gain was not affected during the whole irradiation period for an integrated charge of 918 mC. This corresponds to five years of HL-LHC with a safety factor above five.

Neutron exposure. Neutron irradiation took place at the Orphée reactor [38] in CEA-Saclay using a line with a thermal neutron beam of about $8 \times 10^8\,\mathrm{cm^{-2}s^{-1}}$, (with energies in the range of 5-10 meV) within an area of a few cm^2. The total exposure time was more than 40 hours, accumulating a total amount of neutron flux equivalent to five years of operation at the HL-LHC with a safety factor well above seven. The gain was monitored before and after the neutron tests and is compatible. The performance of the detector showed no degradation with respect to measurements before the neutron irradiation.

Gamma exposure. The R17a detector was exposed to a ^{60}Co source, of about 500 mGy/h, emitting gammas at 1.17 MeV and 1.33 MeVat the COCASE [39] gamma facility in IRFU at CEA/Saclay. The highest activity for gammas in ATLAS muon spectrometer is recorded in the forward CSC region [40], with a flux below $\sim 1.8 \times 10^4\,\mathrm{cm^{-2}s^{-1}}$. For five years of HL-LHC, considering a factor five in luminosity increase, with a safety factor 3, the integrated gamma flux results to be $2.3 \times 10^{13}\,\mathrm{cm^{-2}}$. In our set-up conditions, the time required to reach five years of HL-LHC gamma exposure would be 16 days. The detector was exposed for more than 20 days and no change in gain behavior was observed. The mesh current was stable within 5%, a variation which can be perfectly attributed to environmental effects[6].

Alpha exposure. Additional tests were carried out by using an ^{241}Am source emitting alphas at 5.5 MeV. The source was placed inside the detector chamber, just on top of the metallic mesh defining the drift field. A first alpha measurement took place at low gain (around 100), determining the alpha decay rate observed by the detector. Considering that the estimated number of primaries produced by an ^{241}Am alpha is between 30000 and 60000 for a 5 mm conversion gap in Ar:CO_2 90:10, gains above 3000 will exceed the Raether limit [26] producing a spark almost on every alpha. Therefore, the gain was increased well above this value to about G = 7000. The alpha source stayed inside for a period of 66 hours leading to a mesh current above 100 nA. After the alpha irradiation (which was localized at the center of the detector) the gain behavior was remeasured and no change was observed.

Beam test performance after irradiation. After the completion of the above described exposures, the R17a and R17b prototypes were installed in the H6 CERN-SPS beam line (120 GeV pion beam) to measure and compare efficiencies and spatial resolutions. No visible degradation effects were observed in these measurements.

5.5.1 Micromegas in ATLAS

In order to test the MM detectors under realistic LHC conditions six small MM chambers were installed in the ATLAS detector in February 2012. Two MM detectors (named MBT03 and MBT04) with an active area of 9×4.5 cm^2 were installed in the high-rate environment in front of

resistive strips placed above this layer parallel to the X strips. 250 µm pitch and 150 µm width for both resistive and copper strips. 35-50 MΩ cm^{-1} resistivity along strips and 60-140 MΩ boundary resistance.

[6]The COCASE facility is kept at constant temperature with pressure and humidity variations within 5%.

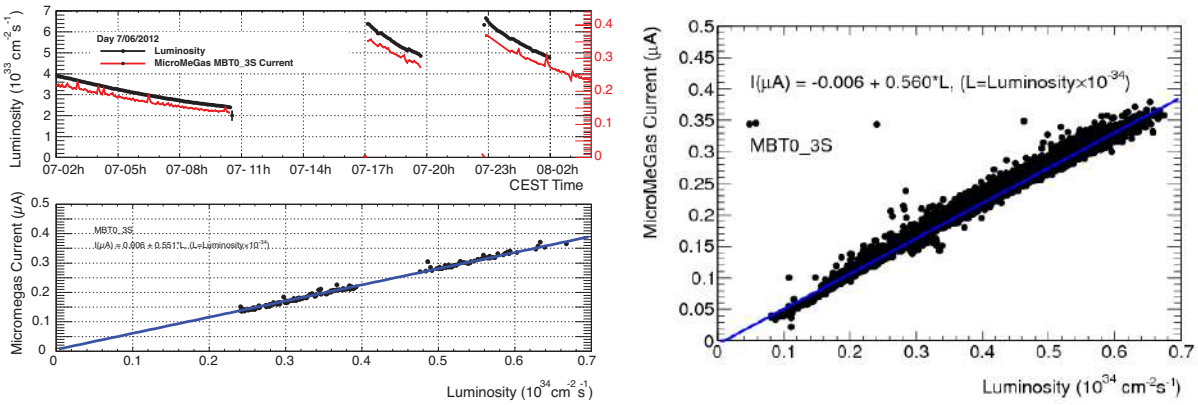

Figure 5.16: The top left plot shows the MM current (red) and the luminosity as measured by ATLAS (black) for three short fills. In the lower left plot the MM current is plotted versus luminosity for the same data. The right plot shows the correlation of the MM current and the luminosity as measured in the ATLAS for the full data set.

the electromagnetic end-cap calorimeter, 3.5 m from the interaction point in the z direction, at a radius r$\sim$1 m. The other four detectors were installed on the Small Wheel at 1.8 m distance from the beam pipe.

The MBT chambers have a drift gap of 4.5 mm and two-dimensional readout with 500 μm pitch of the x strips (in ϕ-direction) and 1.5 mm pitch of the v strips which are inclined with respect to the x strips by 30°. The hit rate measured in the MBT chambers is about 70 kHz/cm^2 for a luminosity of $5 \times 10^{33}\,\mathrm{cm}^{-2}\mathrm{s}^{-1}$, with about 90% of the hits being correlated in both chambers. The hit rate in the chambers on the Small Wheel is more than two orders of magnitude lower, with most of the hits being uncorrelated.

All chambers were operated with an Ar:CO_2 93:7 gas mixture. They were continuously operational except for a few weeks after the September 2012 technical stop[7]. The HV was kept on the same value independent of the LHC beam conditions. The detector currents were continuously monitored.

The left plots of Fig. 5.16 show an example of the current of the MBT03 chamber recorded during three short fills on 7 June 2012. The MM current follows nicely the ATLAS luminosity measurement. In the right plot, the MBT03 current is plotted against the ATLAS luminosity for a large number of fills. The data points are fitted with a linear slope of $0.560\,\mu\mathrm{A}/10^{34}\mathrm{cm}^{-2}\mathrm{s}^{-1}$, indicating a stable response of the detectors up to approximately 100 kHz/cm^2 (at $\mathcal{L} = 7 \times 10^{33}\,\mathrm{cm}^{-2}\,\mathrm{s}^{-1}$).

Using this correlation, together with the integrated LHC luminosity of 23.3 fb^{-1} (minus 10%), it is estimated that the total charge accumulated by the MBT03 chamber during the run adds up to about 1.2 C or 0.03 C/cm^2. This figure should be compared to the accumulated charge of 0.005 C/cm^2/year that is expected in the MM operating at a gas gain of 10^4 at a rate of 10 kHz/cm^2, the highest counting rate expected on the Small Wheel. In other words, the one year long exposure of the MBT chambers located on the front face of the electromagnetic calorimeter is equivalent to six years of operating the MM on the New Small Wheel at $\mathcal{L} = 5 \times 10^{34}\,\mathrm{cm}^{-2}\,\mathrm{s}^{-1}$. No degradation of the detector operation was observed after this exposure.

[7]It is estimated that less than 10% of the luminosity delivered by the LHC was not seen by the MM.

6 New Small Wheel performance

In this chapter, the performance of the NSW as an integrated unit is presented, assuming the nominal layout described in Section 3. The emphasis is on use of the precision bending-plane measurements of the MM for offline tracking and the fast response and versatility of the sTGC design for triggering.

6.1 Simulation of the NSW

The implementation of the NSW simulation infrastructure can be broken down into three steps:

1. **Geometry:** New detectors must be integrated seamlessly into the existing infrastructure and co-exist with the current detector description chain keeping a certain level of flexibility needed to accommodate new features and layouts
2. **Hit deposition:** Information about physics processes and energy deposition in the sensitive layers must be gathered and stored in appropriate objects to be used later in the data processing chain
3. **Detector response/digitization:** Hits and energy deposits must be processed in order to simulate the detector response and the electronics chain must be accurately modeled to reproduce the functions of an active detector.

Detector layers and multiplets are described in substantial detail in terms of material distribution and components, but lacking are a few distinctive features such as frames or spacers, which affect detector acceptance. These inefficiencies are instead currently taken into account at the digitization level, where also readout elements (such as strips and pads) are introduced. Because of the demanding precision design criteria, a detailed material description is needed in order to simulate the performance of the NSW. It was therefore decided to implement from the beginning the NSW support structures (these are not implemented for the small wheel in the current simulation).

For each event, the location where the generated particles, including all the muon-related secondaries (e.g. $e^{\pm}$), cross the active volume boundaries is saved. Particles that do not interact with the detectors or that fall outside of the geometric acceptance are ignored. Low energy secondary particles (kinetic energy below 50 MeV) are also removed. The detailed detector response to the passage of particles through the active detector material, i.e. 'full digitization,' is not yet implemented. A simplified approach has been adopted which is sufficient to evaluate the performance of NSW muon reconstruction.

- **MM:** The particle trajectory is extrapolated to the detector readout plane to determine the hit position. The hit position is then smeared along the precision axis with a Gaussian distribution centered on the hit position, to take into account detector resolution. The angular dependence of the hit resolution is modeled by varying the standard deviation of the Gaussian using the formula $\sigma = (-0.333\theta + 93.3)\,\mu\text{m}$, where θ is the angle of the incoming particle, in degrees. A linear dependence between the resolution and the incoming angle of the particle is assumed, as observed in test beam studies, such that the spatial resolution of a single MM detector will be 90 µm for a track with $\theta = 10°$, and 80 µm for $\theta = 40°$.

- **sTGC:** Digitization is performed for hits on sTGC pads, strips and wires (wires only for sTGC modules 2 and 3, following the hardware design). To produce strip hits, the energy deposition must be least 0.52 keV, simulating the strip efficiency of 95% that was measured in test beam studies. For pads, a detection efficiency of 95% is used, as measured in the test beam, and includes energy threshold effects, readout timing effects and the effect of inactive areas inside the detector due to the support structure. The hit positions for pads, wires and strips is determined by extrapolating the track to the respective readout plane. The strip position error is sampled from a Gaussian distribution with an angle dependent width, $\sigma = (4.5\theta + 70)\,\mu\text{m}$, which varies from 115 µm to 205 µm over angles of incidence from 10° to 30°. The errors on the pad X and Y position and wire X position are set to the size of the detector element in that dimension divided by $\sqrt{12}$. Hence, the wire error is given by the pitch of the ganged wires divided by $\sqrt{12}$. The arrival time of the particle is smeared with an angular-dependent time jitter derived from test beam measurements to account for variations in arrival time of drift electrons. The bunch crossing (previous, current, or next) is tagged using the smeared arrival time.

6.2 Single muon performance

The NSW performance is measured from a simulated sample of dimuon events, with one muon per end-cap per event being generated. The sample comprises 5×10^5 generated events, with the muons evenly distributed in the ϕ coordinate and in transverse momentum, in the range $4 < p_{\text{T}} < 100$ GeV. Additional samples are simulated at higher p_{T} values, up to 1 TeV, primarily for studies of the p_{T} resolution. In the η coordinate they are flatly distributed as well, in the range $1.0 < |\eta| < 3.2$, which exceeds the NSW acceptance. Therefore, additional selection criteria are applied to study only those muons clearly passing through the NSW volume.

The NSW has been added into VP1, the ATLAS event display, for both geometry and hits. A VP1 event display for a representative dimuon event, showing all detector hits, MM strips and sTGC strips, pads and wires, is presented in Fig. 6.1.

6.2.1 Geometrical acceptance and reconstruction efficiency

The acceptance is measured at two stages of the simulation chain, once at the level of simulated hits and once after the fast digitization of those hits. In this context, 'simulated hit' refers to the space point recorded in a sensitive detector volume assigned to either of the two technologies, MM or sTGC. In the digitization, described in Section 6.1, those hits are translated into the expected signal response of the corresponding technology. These correspond to either a firing strip, in case of the MM, or a firing strip, wire or pad, in the case of the sTGC.

In the acceptance studies, only muons with $1.2 < |\eta| < 2.8$ at the entrance to the muon spectrometer volume are considered. Muons outside this η range are rejected because they are not expected to traverse the NSW. Thus, rare cases of muons experiencing large angle scattering or very high energy losses in the calorimeters and in consequence being bent into the NSW are excluded to avoid artificial features in the study. The entrance to the muon spectrometer volume is assumed to be a cylinder that extends to $|z| \approx 6.8\,\text{m}$ and has a radius of 4.3 m. As the shielding in front of the NSW is considered part of the spectrometer, any scattering taking place in this structure is included. Signals generated by secondary particles, such as photons originating from bremsstrahlung, or delta electrons, are not taken into account.

The acceptance of the NSW for digitized hits (total number of hits per single muon) is presented in Fig. 6.2 for both the MM and sTGC strips. As expected, muons are typically traversing 8

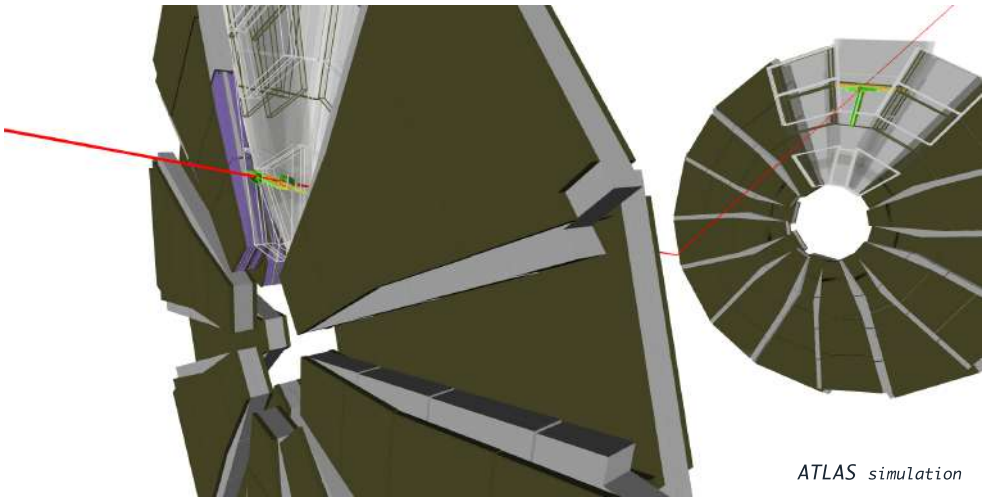

(a)

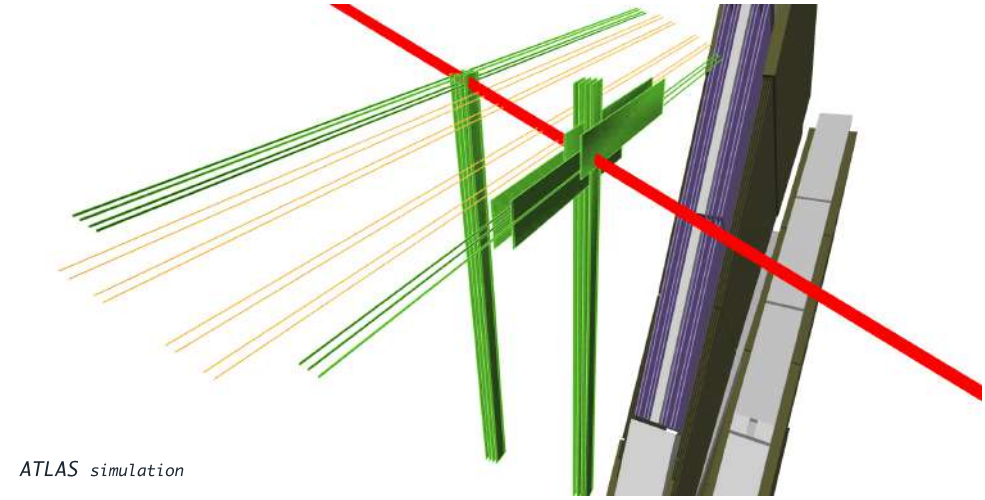

(b)

Figure 6.1: An event display of a dimuon event, with both muons passing through the NSW: (a) both muons, (b) zoomed in to display MM and sTGC hits for one of the muons ($p_{\mathrm{T}} = 65$ GeV, $\eta = -1.51$, $\phi = 1.62$). The MM strips are displayed in orange, while all sTGC elements are displayed in green (narrow strips for η measurements, rectangular 2-d pads and gangs of five wires for ϕ measurements). The displayed muon passes through the gap between the third and fourth sTGC modules of the multiplet furthest from the IP and does not fire pads there.

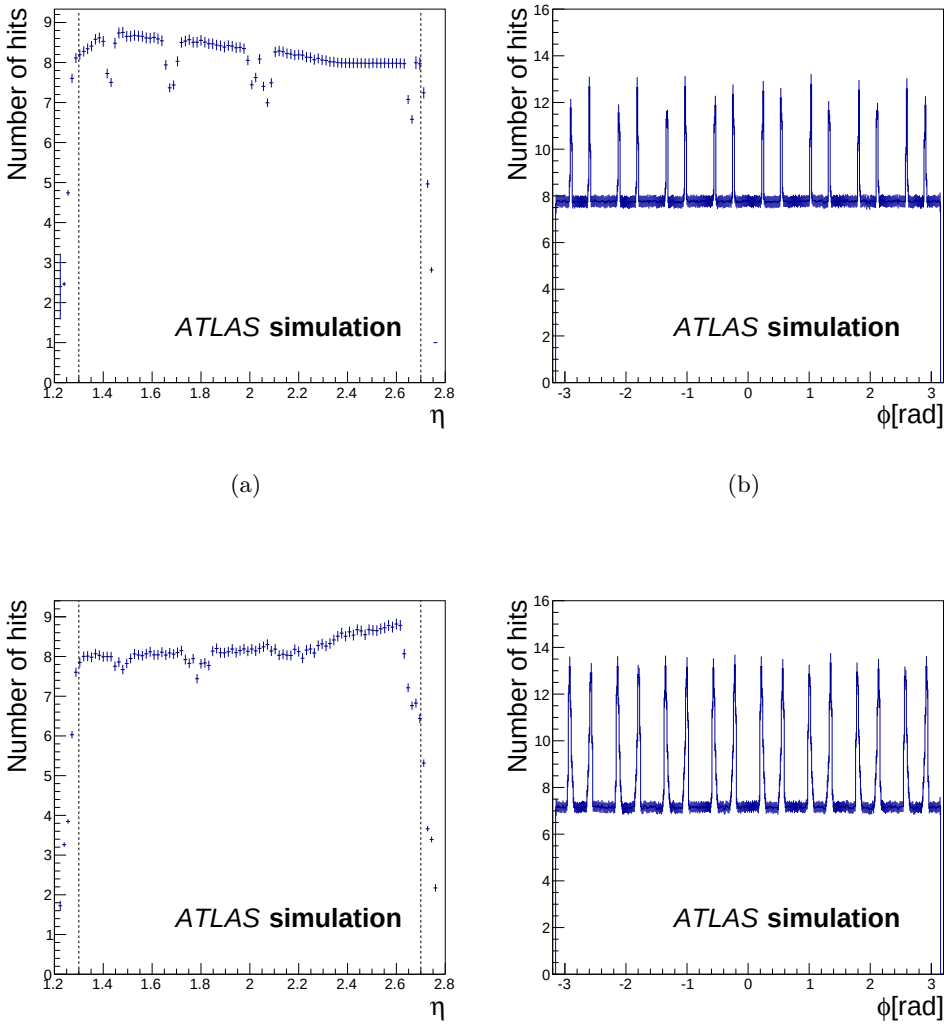

(a) (b)

(c) (d)

Figure 6.2: Number of digitized simulation hits of various types for a single muon traversing the NSW: (a) MM strips, as a function of $|\eta|$; (b) MM strips, as a function of ϕ; (c) sTGC strips, as a function of $|\eta|$; (d) sTGC strips, as a function of ϕ.

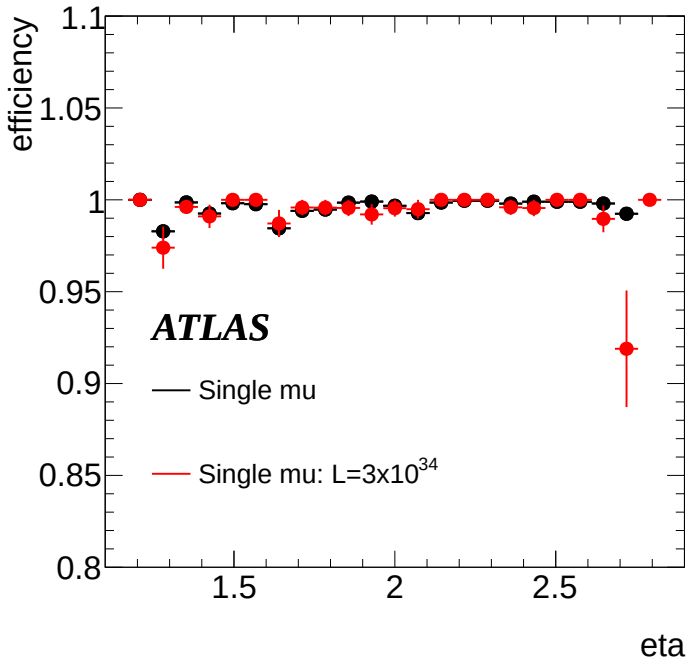

Figure 6.3: Efficiency to reconstruct segments in the NSW as a function of $|\eta|$, based on MC-simulated events. The red points represent the efficiency in the absence of background-related hits while the black points represent the efficiency with background included, at the rate expected at a luminosity of 3×10^{34} cm^{-2} s^{-1}.

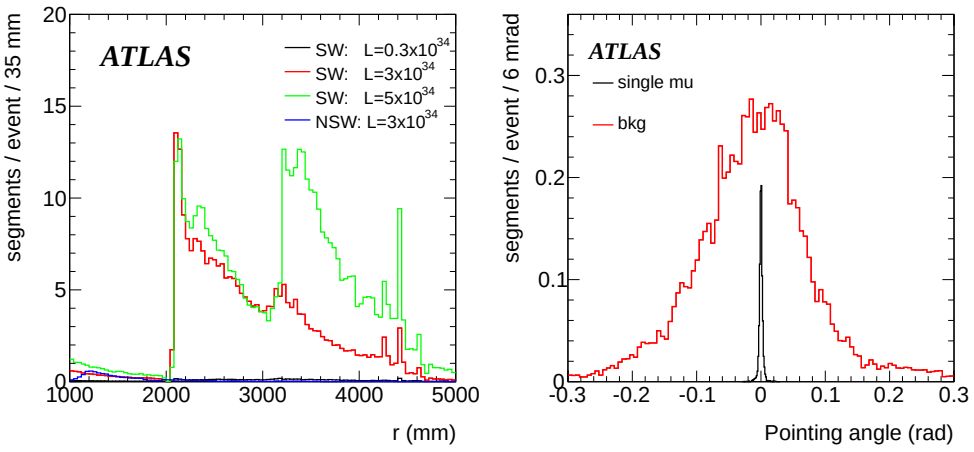

(a) (b)

Figure 6.4: (a) Fake NSW segments (not associated with a true muon) per event, as a function of radial distance (mm) from the beam axis; and (b) distribution of segment pointing angle. The background corresponds to the rate expected at a luminosity of 3×10^{34} cm^{-2} s^{-1}.

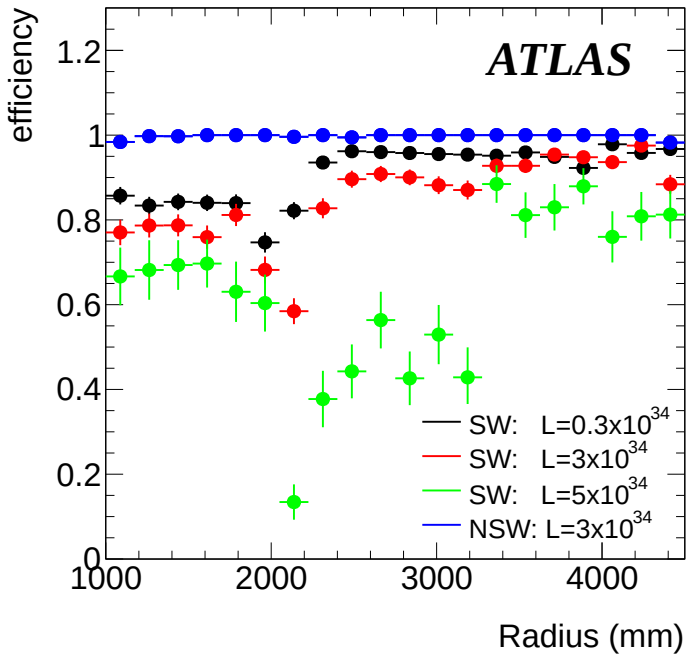

Figure 6.5: Segment-finding efficiency as a function of radial position, derived from a sample of simulated $Z' \to \mu^+\mu^-$ events, with a Z' mass of 2 TeV. Results are shown for the existing small wheel and nominal 2012 luminosity, 0.3×10^{34} cm^{-2} s^{-1}, as well as for factors of ten and twenty times larger, corresponding to luminosities of 3×10^{34} cm^{-2} s^{-1} and 5×10^{34} cm^{-2} s^{-1}, respectively. Results for the NSW are shown for a luminosity of 3×10^{34} cm^{-2} s^{-1}.

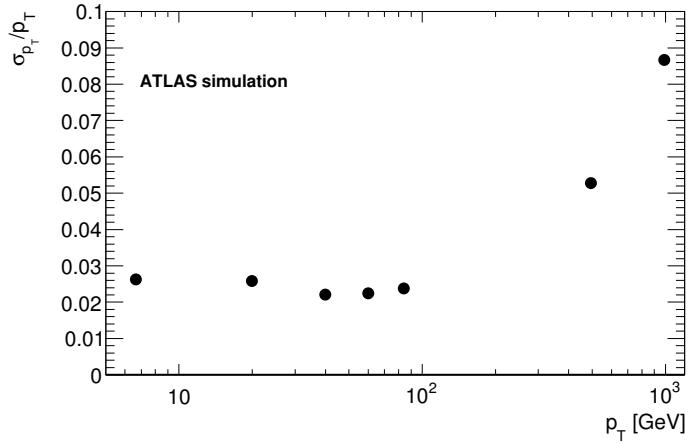

Figure 6.6: Reconstructed muon p_{T} resolution as a function of p_{T}, based on MC-simulated events.

active detector layers of a given technology, in a regular sector, while at the acceptance edges in η the efficiency drops rapidly. In the regions of overlapping large and small sectors, the number of volumes with recorded hits is as large as 16. Areas of reduced efficiency visible in the η distribution are due to the radial gaps between the four η stations, around $\eta = 1.43$, 1.68 and 2.05. For the

sTGC, the area of decreased efficiency due to the radial gaps is less sharp than for the MM because the distance in z between the two multiplets of a station is larger. For the area around $\eta = 2$, the staircase geometry of the sTGC results in a nearly complete recovery of the efficiency.

6.2.2 Segment and tracking performance

Candidate muon track reconstruction proceeds from simulation and digitization of the precision (η) and second-coordinate (ϕ) hits described in the previous section according to an algorithm modeled closely after the existing software that incorporates information from the inner (small wheel), middle (big wheel) and outer end-cap muon stations. The algorithms have not yet been tuned to optimize the balance between muon reconstruction efficiencies and fake rates, but are robust enough to evaluate the performance of the NSW. The bunch-crossing identification capabilities of the sTGC are exploited to reduce backgrounds, while the high granularity of the MM provides excellent separation of segments in the NSW.

The algorithm uses Hough transforms for both the precision and second coordinates. In the former case, hits from both the MM and sTGC are used, while in the latter case, only sTGC hits are used, as the current simulation of the NSW does not include MM stereo strips. The roads found by this procedure are then processed by an algorithm that defines segments in the NSW that are required to have a minimum of five hits, out of a maximum possible of 16, within 2 mm of the segment. Finally, segments found in the NSW are combined with those found in the BW and EO to form muon tracks.

For the simulation of background, particles are injected in the NSW using the fluxes measured from 2012 data scaled to the expected luminosity. Both the in-time (correlated to the BC) and out-of-time particles (uncorrelated to the BC) rates, including cavern background, are generated. The systematic uncertainty on the total rate is estimated to be about 50%.

The efficiency to reconstruct NSW segments as a function of $|\eta|$ is measured both with and without background, at rates expected at a luminosity of 3×10^{34} cm^{-2} s^{-1}, and is shown in Fig. 6.3. The efficiency for the no background case is on average 99.5%. The inclusion of background has a negligible effect on the efficiency. The segment position and angular resolutions in the precision coordinate are found to be approximately 29 µm and 0.27 mrad, respectively, within the specifications outlined in Chapter 2. These resolutions are without any detector mis-alignments considered and correspond to the width of the narrower, core Gaussian of double Gaussian fits to the distributions of position and angle residuals. Owing to the high granularity of the MM, no degradation of position or angular resolution is observed when background is included. For the trigger, the angular resolution after back extrapolation to the IP is important. It is estimated to be 2.2 mrad and is dominated by the multiple scattering of low p_{T} muons in the calorimeter material.

Another important parameter for the segment finding is the rate of reconstructed fake segments. These are defined as segments that do not match to a true (generated) muon. The radial distribution of number of segments per single muon event is shown in Fig. 6.4. The total rate in both end-caps is about 8.5 segments per event. Also shown in Fig. 6.4 is the pointing angle of the segments (difference between the direction of the reconstructed segment, extrapolated back to the IP, and the direction of the actual muon) for events with and without background included. By applying a loose requirement that the pointing angle be less than 50 mrad the segment rate is reduced by about a factor of two.

The segment-finding performance is also studied in a sample of simulated events of a typical benchmark signal of physics beyond the Standard Model, $Z' \to \mu^+\mu^-$, with a mass of 2 TeV. Figure 6.5 shows the segment-finding efficiency as a function of the radius in the end-cap small

wheel region for different levels of background. For the existing small wheel, a loss of 10% in efficiency is observed in the inner-most region for a factor of ten times the nominal 2012 background levels (corresponding to a luminosity of 3×10^{34} cm^{-2} s^{-1}). At twice that background level, an effective luminosity of 5×10^{34} cm^{-2} s^{-1}, the losses significantly increase: the efficiency in the range 2000-3300 mm drops below 50%. Also included in the figure is the expected performance of the NSW in background conditions corresponding to a luminosity of 3×10^{34} cm^{-2} s^{-1}. Unlike the case of the current small wheel, the segment finding is not affected by the background.

Displayed in Fig. 6.6 are the measured p_{T} resolutions for reconstructed muon tracks, after having combined NSW segments with those found in the BW and EO. For muons with $p_{\mathrm{T}} < 100$ GeV the p_{T} resolution is less than 3%, dominated by multiple scattering effects,[1] and for muons with $p_{\mathrm{T}} = 1$ TeV it is about 9%. These figures are obtained assuming perfect alignment. For each muon momentum the momentum resolution is fitted with two Gaussians. The width of the narrow Gaussian is presented. The efficiency to reconstruct muon tracks with segments in all three end-cap stations is approximately 97% over the full range of acceptance.

6.3 Level-1 sTGC trigger performance

The sTGC L1 is a two-step trigger system: an ultra-fast *pad trigger* to define regions-of-interest for selected muon candidates, followed by a precision muon track measurement with 1 mrad angular precision using sTGC *strips*. Trigger data is transmitted using the multi-GBit/s fast trigger data serializer (TDS).

In this section, studies of the sTGC L1 trigger performance at a luminosity of 3×10^{34} cm^{-2} s^{-1} are presented. They include simulation of the following backgrounds, where pileup events are taken from the standard ATLAS simulation:

- An average of 81 pileup events from the current BC, taken from generated minimum bias events and sampled from a Poisson distribution.
- Uncorrelated cavern background from BC in the range -4 to 3 (corresponding to $[-100, 100]$ ns in time), as described in Chapter 2, where the worst case is used.
- Correlated cavern background from BC in the range -4 to 3, as measured from straight tracks in the CSC detectors of the existing small wheel.

Figure 6.7 shows the beam background rates in the NSW as a function of radius. There is a significant contribution from pileup events. The sTGC hits are required to have a minimum energy deposition of 520 eV to simulate a 95% efficiency due to inactive regions inside the gas gaps. A 75 ns dead time is applied to each active readout channel, and a 30 ns time window is used to collect strip and pad signals within each bunch crossing.

6.3.1 sTGC Level-1 pad trigger

The NSW pad-trigger logic is implemented in two steps:

1. Single wedge pad trigger: trigger decision based on coincident hits in three out of four layers of a multiplet in each wedge, independently.
2. Pad trigger: trigger decision based on geometrical matching between the two wedge triggers, one from the pivot multiplet and one from the confirm multiplet.

[1] Tracks reconstructed in the muon spectrometer are ultimately combined with inner detector tracks, thereby improving significantly the resolution for muons with $p_{\mathrm{T}} < 100$ GeV.

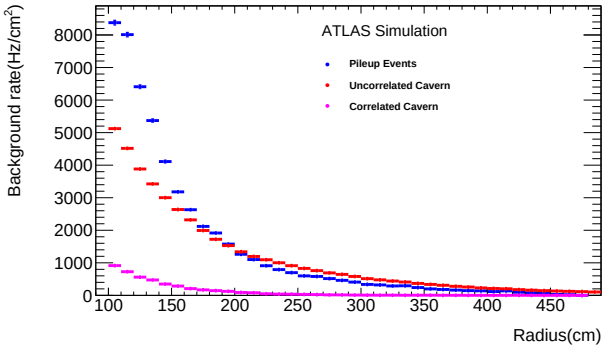

Figure 6.7: Beam background rates from different sources. The red, blue and pink points are rates from pileup events, uncorrelated cavern background and correlated cavern background, respectively.

An exception is made for the transition regions in η between the detectors. In this case, hits are required in all four layers of a single wedge.

The efficiencies presented in this section are estimated using the sample of simulated muons described in Section 6.2. The pad trigger efficiency for a single muon event, in the absence of any background, is shown as a function of η and ϕ in Fig. 6.8. The average pad trigger efficiency is 97%, with some loss of efficiency in the transition regions between the different modules. The difference in the pseudorapidity between the actual muon and that of the trigger candidate is also shown in Fig. 6.8, demonstrating that the trigger candidates correspond to the original muon.

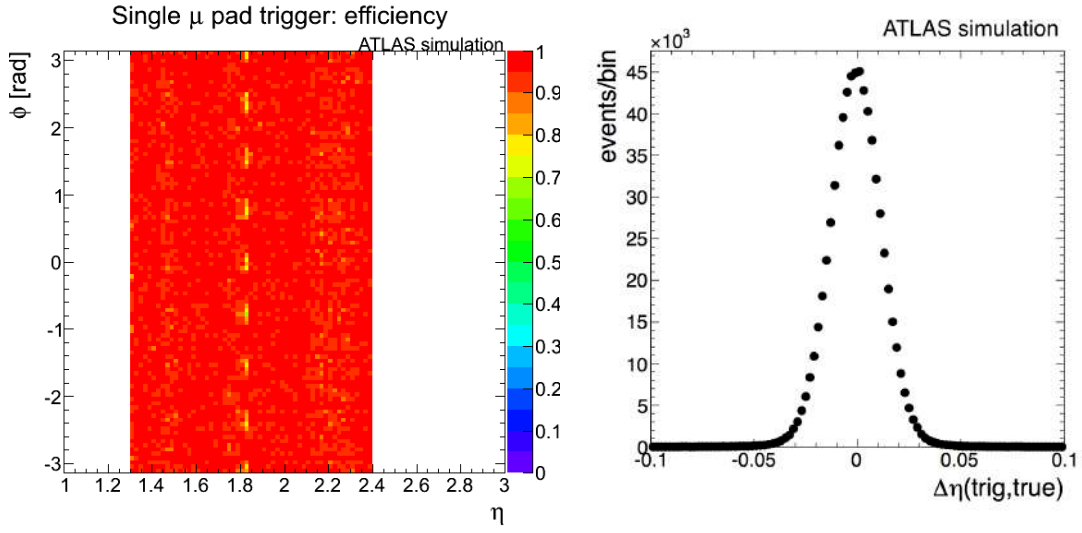

(a) (b)

Figure 6.8: (a) The sTGC pad trigger efficiency as a function of $|\eta|$ and ϕ. (b) The difference between the η of the true muon and the η of the trigger candidate.

The pad trigger rate and the single muon trigger efficiency in the presence of pileup and cavern background are estimated using single muon sample with cavern background and pileup overlaid.

On the one hand, random background hits arriving within the bunch crossing gate can compensate for lost signal hits and actually improve the trigger efficiency. On the other hand, a background hit in previous bunch crossings can prevent the detection of a signal hit due to readout channel dead time and degrades the efficiency. The pad-trigger efficiency for single muons, as a function of η, for the described set of parameters is shown in Fig. 6.9. The pad trigger efficiency in the presence of pileup events and cavern background is lower (average of 95%) compared to the efficiency in absence of these backgrounds (average of 97%). As the background rate is higher at larger values of η, the efficiency loss in this region is also larger.

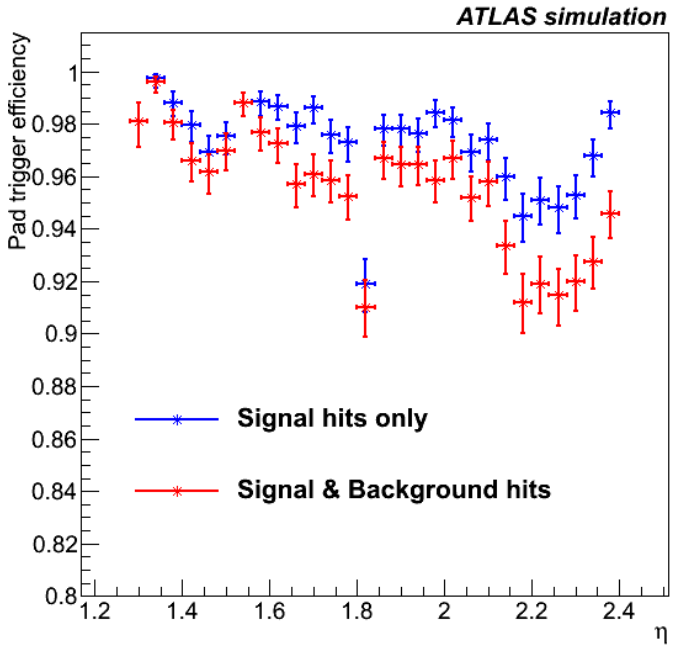

Figure 6.9: The sTGC pad trigger efficiency as a function of $|\eta|$, both with and without pileup and cavern backgrounds expected at a luminosity of 3×10^{34} cm^{-2} s^{-1}.

The expected number of trigger candidates per event, for the different background sources, and the number of trigger candidates per sector are both shown in Fig. 6.10. Non-correlated cavern background generates a negligible number of trigger candidates. However, the probability to measure at least one trigger candidate due to the correlated cavern background or pileup is nearly 100%. The resulting pad trigger rate is therefore of order 40 MHz. The fraction of events with more than three trigger candidates per sector is negligible, however, consistent with the design of the NSW trigger system.

6.3.2 sTGC Level-1 segments

Adjacent strip hits in the same layer are first grouped into a cluster, from which track segments are formed by using the road defined by the sTGC pads, These segments are used in the sector logic to confirm segments found in the Big Wheel and form muon candidates. Only clusters with fewer than six active strips are considered. The hit position within a layer is given by the layer

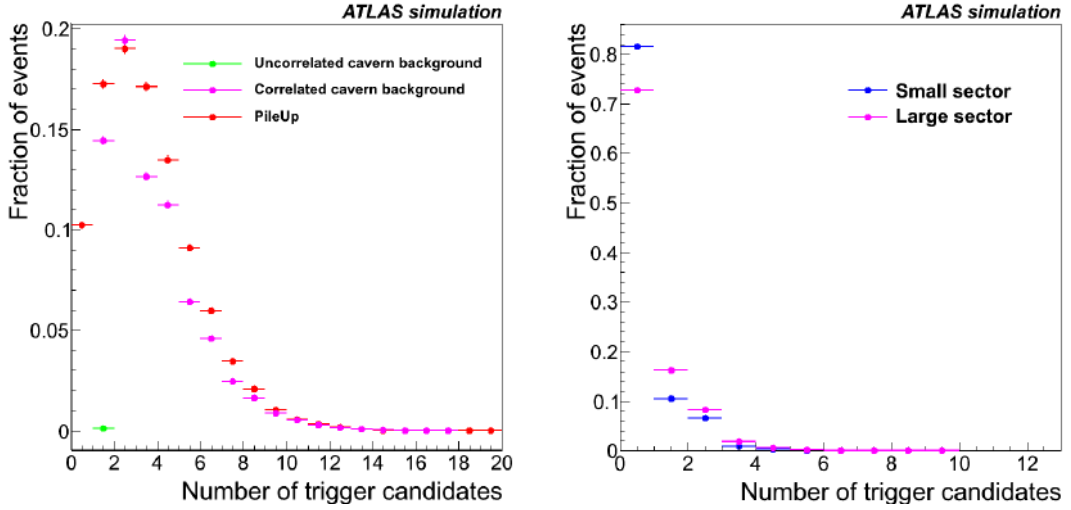

(a) (b)

Figure 6.10: (a) The number of sTGC pad trigger candidates per event expected from the different background sources. (b) The number of sTGC pad trigger candidates per sector, per event, expected from background, for both small (blue) and large (violet) sectors.

cluster centroid C, which is calculated from:

$$\mathrm{C} = \Delta + \frac{\sum_{n=1}^{5} n \times S_n}{\sum_{n=1}^{5} S_n}\,, \tag{6.1}$$

where Δ is an offset corresponding to the strip number of the edge of the cluster; n is the strip number within the cluster; and S_n is the ADC charge measurement of strip n. The cluster position is converted to physical coordinates in the measurement plane using the 3.2 mm strip width. The position resolution of the cluster is measured from the residual distribution, $Y_{\text{truth}} - Y_{\text{cluster}}$, where Y_{truth} and Y_{cluster} are the Y positions of the simulated and reconstructed clusters, respectively. As shown in Fig. 6.11, the position resolution is approximately 177 µm, uniformly throughout the NSW. The cluster efficiency, defined as the ratio of the number of clusters reconstructed in all sTGC layers over the number of true hits over a 520 eV threshold, is nearly 100%. The measured rate of sTGC clustering is found to be dominated by beam background, and hence has a distribution similar to beam background as shown in Fig. 6.7.

The layer cluster centroids are combined to form a quadruplet centroid (QC) which is computed when there are clusters found in a minimum of two out of the four layers of a confirm or pivot multiplets:

$$\mathrm{QC} = \frac{\sum_{n=1}^{N} C_n}{N}\,, \tag{6.2}$$

where N is the number of valid centroids at least 2 and C_n is the position of centroid n. Quadruplet centroids must be found in both the pivot and confirm multiplets within a trigger region-of-interest to form a trigger segment. The segment efficiency, including the pad efficiency, is estimated at 93%, averaged over the full η and ϕ range of the NSW, and without any region of significant

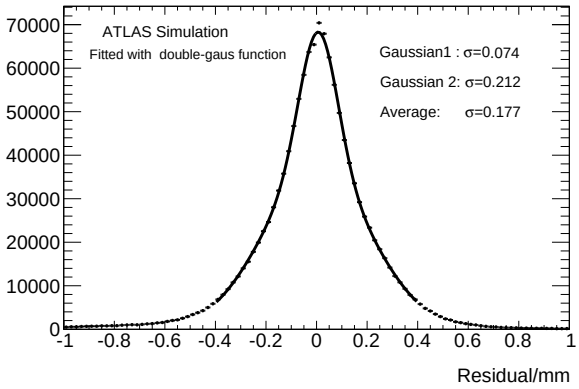

Figure 6.11: Residual distribution from sTGC clusters: $Y_{\text{truth}} - Y_{\text{cluster}}$, where Y_{truth} and Y_{cluster} are the positions of the simulated and reconstructed clusters, respectively, in the measurement plane. The quoted resolution is the weighted average of the widths of the two Gaussian distributions in the fit.

efficiency loss. The segment-finding efficiency drops to 89% when three hits are required in each multiplet. It is clear that a sTGC detector with 8 layers provides a robust L1 trigger with high segment-finding efficiency even in the presence of large background rates.

The segment angular resolution measured by sTGC strips is estimated by measuring the Gaussian width of the difference between the direction of the measured segment and that expected from simulation hits. Figure 6.12 shows the mean of the angular difference and the segment θ resolution over the entire NSW. The mean of the segment angular difference is close to zero, demonstrating that their is no bias in the reconstruction, and the average angular resolution is 0.54 mrad, assuming perfect detector alignment, well below the 1 mrad requirement for the L1 system. Beam background is observed to have a negligible effect on the segment angular resolution.

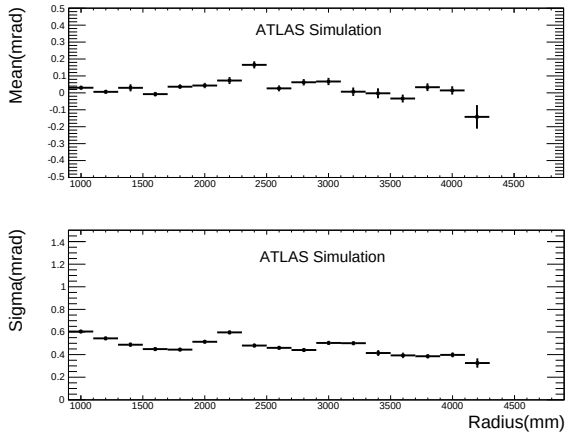

Figure 6.12: The (a) mean of the sTGC segment angular difference and (b) resolution, at different radii.

The effect of the B-field on the segment θ measurement is also found to be small: the angle is shifted by -0.12 mrad and 0.17 mrad for positively and negatively charged muons, respectively,

with $p_{\mathrm{T}} > 20$ GeV.

Finally, the rate of fake sTGC segments has been studied. Figure 6.13 shows the number of segments in simulated $\mathrm{Z} \to \mu^+\mu^-$ events, where the average is 2.9, dominated by beam background. The average number of segments is increased to 3.2 for events in which there is at least one muon inside the NSW acceptance. In the same figure, the average number of segments in the trigger region of interest at different radii shows a clearly reduced fake rate, where the average is a single segment per event.

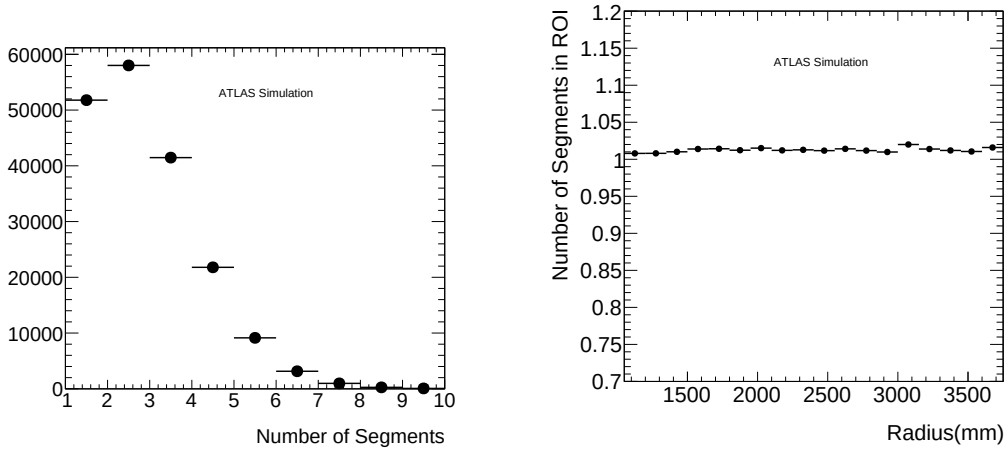

(a) (b)

Figure 6.13: (a) Number of segments in simulated $\mathrm{Z} \to \mu^+\mu^-$ events; (b) average number of segments in the trigger region of interest at different radii.

6.3.3 NSW sTGC Level-1 trigger

The final decision of the L1 muon trigger is from the combination of the NSW trigger segment with a muon Big Wheel TGC L1 trigger segment. Three different methods to study the L1 muon trigger turn-on curve are used. The first method is to use 8 TeV collision data with 25 ns bunch spacing. ATLAS data collected in December 2012 are used, from the enhanced-bias stream, where the angular resolution of the MDT segments is smeared from 0.3 mrad to 1.0 mrad to simulate the expected resolution of NSW segments matched to BW TGC L1 trigger segments. The second method is to apply a similar technique to fully-simulated $\sqrt{s} = 14$ TeV $\mathrm{Z} \to \mu^+\mu^-$ events. The third method entails matching NSW sTGC L1 trigger segments with BW TGC L1 trigger segments in fully-simulated $\sqrt{s} = 14$ TeV $\mathrm{Z} \to \mu^+\mu^-$ events. Two requirements must be satisfied to generate an L1 muon trigger: a) the NSW segment angle must be within 15 mrad of the vector pointing to the IP; b) the NSW segment η measurement must match the BW TGC MU20 trigger segment within 0.08 ($|\delta\eta|$). Figure 6.14 shows the L1_MU20 trigger efficiency curve for each of the three methods, where good agreement is obtained from all three methods, and the trigger efficiency at plateau is just above 87%, an approximately 5% trigger efficiency loss when requiring the NSW in the L1 trigger.

The L1 muon trigger rates have been studied assuming a luminosity of 3×10^{34} cm^{-2} s^{-1} with fully-simulated $\sqrt{s} = 14$ TeV MC samples of $c\bar{c}$, $b\bar{b}$ and $\mathrm{Z} \to \mu^+\mu^-$. Figure 6.15 gives the

L1_MU20 trigger rates as a function of muon p_{T} and η. The rate from real muons is dominated by heavy quark production, $b\bar{b}$ (7.5 kHz) and $c\bar{c}$ (4.1 kHz).

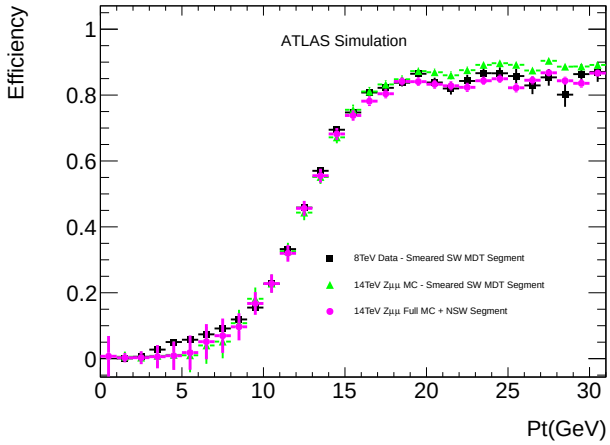

Figure 6.14: The L1_MU20 trigger efficiency as a function of p_{T} of the triggering muon. The three sets of points correspond to different techniques, described in the text.

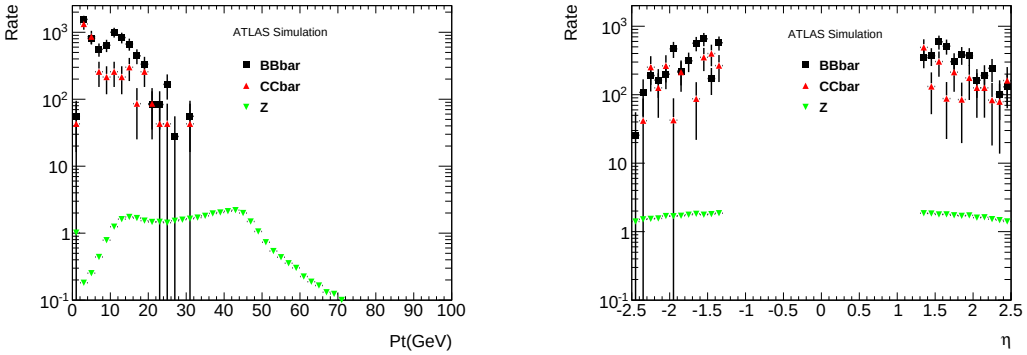

Figure 6.15: The L1_MU20 trigger rate (Hz) as a function of (a) p_{T} and (b) η of the triggering muon.

The proposed NSW layout and design of the trigger system provide full trigger coverage in the region $1.3 < |\eta| < 2.4$ with an 87% L1 muon ($p_{\mathrm{T}} > 20$ GeV) trigger efficiency, consistent with the requirements. Approximately 95% pad trigger efficiency is demonstrated for muons with $p_{\mathrm{T}} \geq 5$ GeV, also consistent with the requirements. The effect of non-correlated cavern background on the total trigger rate is insignificant. Trigger candidate from correlated cavern background and pileup are expected at high event rate, but nevertheless well below the limitation of the designed NSW trigger system.

7 sTGC construction

7.1 Introduction

The construction procedure described, constitutes a complete version on how the sTGC can be constructed at the various production sites. It is based on the experience gained in the construction of the ATLAS-TGC [41–43] with the necessary expected modifications needed to achieve the 40 μm positioning in the four strip planes that constitute the basic quadruplet structure, as well as the procedure to achieve the precise spacing of 70 μm between the four planes. The various steps related to the construction of the present ATLAS-TGC are not described in detail, and only the relevant figures are shown, while the steps needed to achieve the new precision requirements are described in detail, as well as the new quality control procedures to achieve the required uniformity.

Section 7.2 presents the pad arrangement with the pad surface area increasing as the fake rate decreases. The pads (half overlapping in both η and ϕ in every second layer to define a logical pad, used in the trigger definition of Region Of Interest, ROI) have, however, the same size in η while increasing size in ϕ. This allows the same number of selected strips to be readout for the Level-1 trigger and furthermore allows a first selection on quasi-pointing muon tracks while rejecting low momentum protons from neutron interactions and high energy non-pointing e from the back of the calorimeter, both sources generally not pointing to the interaction point.

The basic philosophy in the construction procedure of the quadruplets, is to produce a high precision strip board that can be referenced from the outside for each plane and for each quadruplet. This is achieved by placing brass inserts in the strip boards that are machined together with the strips. These inserts protrude outside the detector volume and can always be positioned with respect to precision pins on a flat granite table. To ensure this precision, a stiff structure is required, which is not available as a single FR4 board. Consequently the positioning is performed only when a full single detector plane (including also wires and pads, which are positioned with a maximum deviation within the detector plane of 100 μm) is constructed. Such a structure has the needed stiffness to be pressed against the precision pins. The requirement of 70 μm maximal deviation between planes is hard to achieve due to the non-uniformity of the FR4 boards. This is alleviated by using paper-honeycomb fillers 40 μm thinner than their corresponding frames, which permits local deformations of up to 30 μm to be filled by the glue, while the cathodes are always attached to a flat surface through vacuum. The assembly of a quadruplet is made of two doublets; where each doublet is constructed as a symmetric structure, with the pads, that carry the wire planes, being always in the external side. This allows, not only for a symmetric structure from the point of view of forces, but also, since the strip and pad electronics are mounted alternatively on each side of the wedge, to have more space in the thickness of the quadruplet for their respective electrical connections. Furthermore, such an arrangement allows a slightly asymmetric (3 mm shift) ϕ pattern on the pad board, which by reversing its position in the second doublet, allows for a fuzziness in the limits of the logical pads. This fuzziness allows the logical pad logic to define tracks close to the edges and to reduce the number of trigger logic combinations. The fuzziness in η is achieved by the non-polar pointing of the pads. All positioning, from single detectors to construct a quadruplet, to the final positioning of the quadruplets on the support frames is performed by pressing the brass inserts placed in the strip boards against precision pins. The

relative position along z of the various planes is checked using precision brass balls inserted in the strip boards, whose positions are measured using an x-ray camera.

The main quality control operation is the exposure of single detectors planes and full quadruplets to a γ source in a scanning mode, at the production sites, with the detectors operating at two different HV settings (one above the plateau and one at half gain, while measuring the high voltage current at each point as a function of position). This is complemented by a scan of the efficiency and local position resolution using cosmic rays and a final irradiation test at CERN (GIF++) with an intense γ source.

7.2 Layout and construction facilities

The preliminary design of the NSW detectors is described in Chapter 3. Each sector contains three quadruplets of sTGC in the front and three behind the MicroMegas (MM) packages. The innermost quadruplets of sTGC are divided into two sets of chambers with three chambers always overlapping in their sensitive volume, to reduce the currents in the high rapidity region. Each chamber volume contains wire readout (wires are radially oriented) and two cathodes, one containing pads, with changing geometry according to the rapidity region, and one containing precision strips. The inner-most set of chambers do not provide readout of their wires. The arrangement of the pads is shown in Fig. 7.1.

The three quadruplets that constitute a sector wedge will be assembled at CERN into a glass fiber support structure (see Fig. 7.2) which will be glued at the transition between two quadruplets and along their external frame. This will make the wedge into a single stiff structure. The results of a Final Element Analysis calculations of the deformation of such structure, kinematically hanging in the NSW is shown in Fig. 7.3 for a large and a small wedge. The maximal deviation from planarity is less than 50 µm for both cases, consistent with NSW requirements.

To construct the basic quadruplets four to five clusters of institutions are being proposed (Israel, Canada, China, Chile and possibly Russia), where two of the clusters already have a large portion of the required equipment and two are in the process of a purchasing it. The basic equipment for

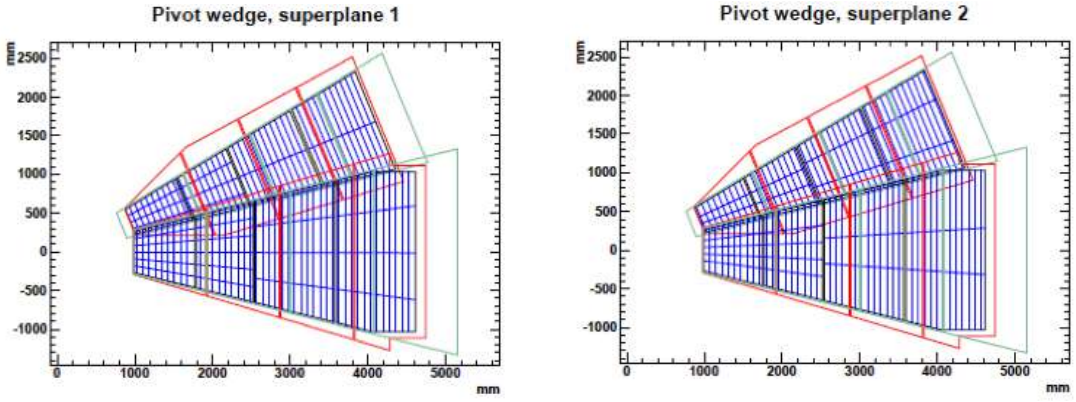

Figure 7.1: Pads arrangements in two alternating layer of a quadruplet for a small and a large sector. The ROI's are defined as the overlap between the two layers, obtained by a 3-out-of-4 coincidence. The green lines represent the projection of infinite momentum tracks traversing the large MUON Wheels, which give a 20 mm overlapping in the NSW, while the red lines show the available envelopes, where the sTGC frames, electronics and services are to be installed.

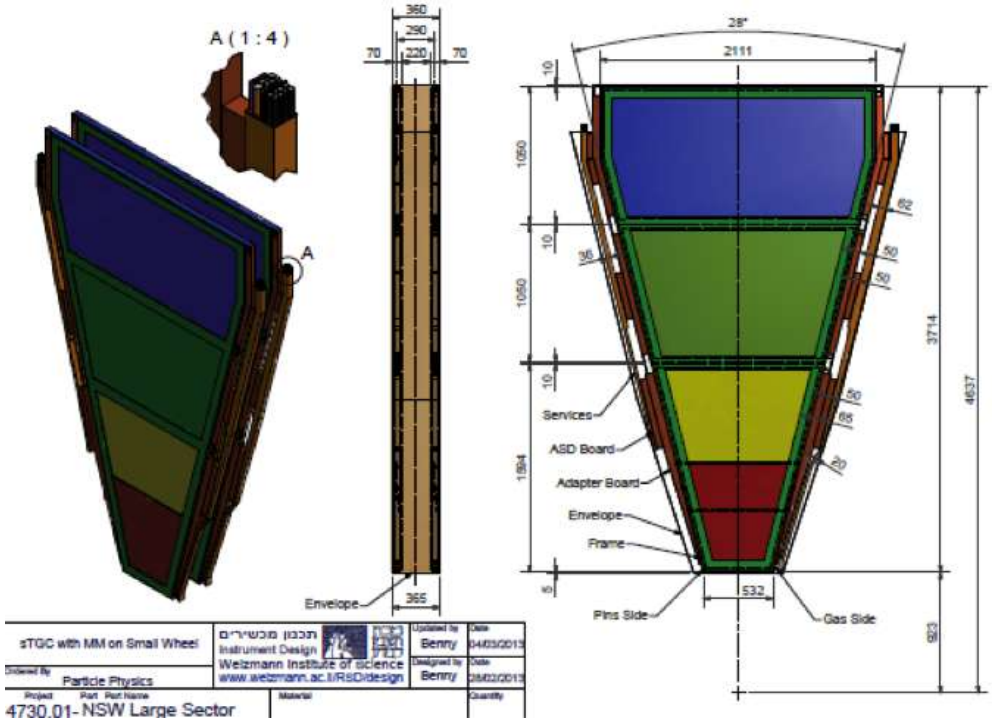

Figure 7.2: Large sector arrangement, including glass fibre frames, electronic channels adapter boards, front-end electronics and services.

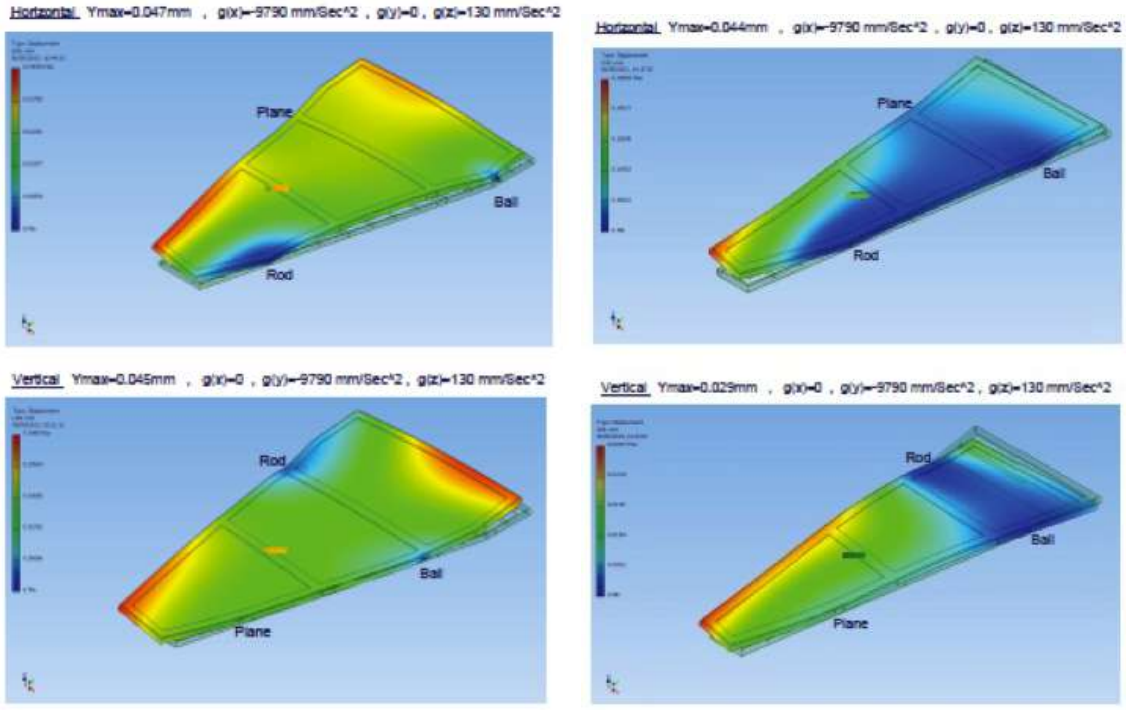

Figure 7.3: Calculated deformation of a Large (left) and a Small (right) wedges at 0.75° inclination. All deformations are bellow 50 µm for the wedges.

constructing and testing the detectors at each production site consists of:

- a resistive coating spraying system placed in a well-controlled environment facility with temperature 25° C and humidity $< 30\%$
- a set of 4-5 flat ($< 20\,\mu m$ deviation from flatness) granite tables, with at least one of them in a clean room, class 1000 (ISO 6), equipped with an overhead crane
- a vacuum system to be used as part of the granite tables
- a gas mixing system to test the detectors during the various phases of construction
- a winding machine, computer controlled, that can apply pre-tension (400 gr) during the winding of the gold-plated tungsten wire on two detectors
- a number of rotating carriages on which liquid glue can be applied to gas seal the single planes
- a set of x-ray cameras with the corresponding x-ray tubes to measure the relative position of each layer of a quadruplet
- a vertical x-y scanning device to perform an irradiation of single plane detectors to control its gas amplification uniformity
- various jigging devices for precision placement
- a complete set-up to scan the fully constructed quadruplets with cosmic rays, with full readout, to compute local efficiencies and position resolution

Once the individual quadruplets will be fully certified, by passing through an irradiation test in the new GIF++ facility to be constructed at CERN, they will have to be assembled in a designated area at CERN that contains the following infrastructure:

- a large ($3 \times 4\,m^2$) precision granite table with a vacuum system, installed in a temperature controlled clean room, class 10000 (ISO 7), equipped with an overhead crane
- an assembly area to install services and electronics on each wedge
- a testing area for testing individual fully equipped wedges with cosmic rays
- a testing facility, once the wedges are installed into the NSW structure

7.3 Material procurement and testing

Two types of cathode boards are used in the production of sTGC's, the pad boards, which require the standard production methods of multi-layer boards, and the strip boards. This requires the combination of a firm that performs the usual multilayer board operations, combined with a firm that performs accurate mechanical machining. Although the final supplier of the two (one for pads and one for strips that includes external alignment elements) have not been finalized, various firms have been contacted and have produced prototypes. The basic material for both boards is Class 3 FR-4. For the strip boards, the place for the positioning brass inserts are machined (using a jig and a special tool) and the brass pieces are inserted (see Fig. 7.4). The strip patterns are machined together with the inserts in a single operation, using a computerized milling machine (CNC) to achieve the necessary precision of the strips with respect to the external brass pieces. The pad boards are produced using standard multi-layer procedures (4 layers) with feed-through for the pad connections to the edges of the detector. The multi-layer press is always performed using Tedler paper between boards, to keep necessary porosity for gluing.

The internal inner frame is made out of FR-4 boards 1.4 mm thick boards. Two types of FR-4 boards are used, Type I with one-sided copper for etching the wire soldering pads and Type II for internal wire support and to cover the soldering pads.

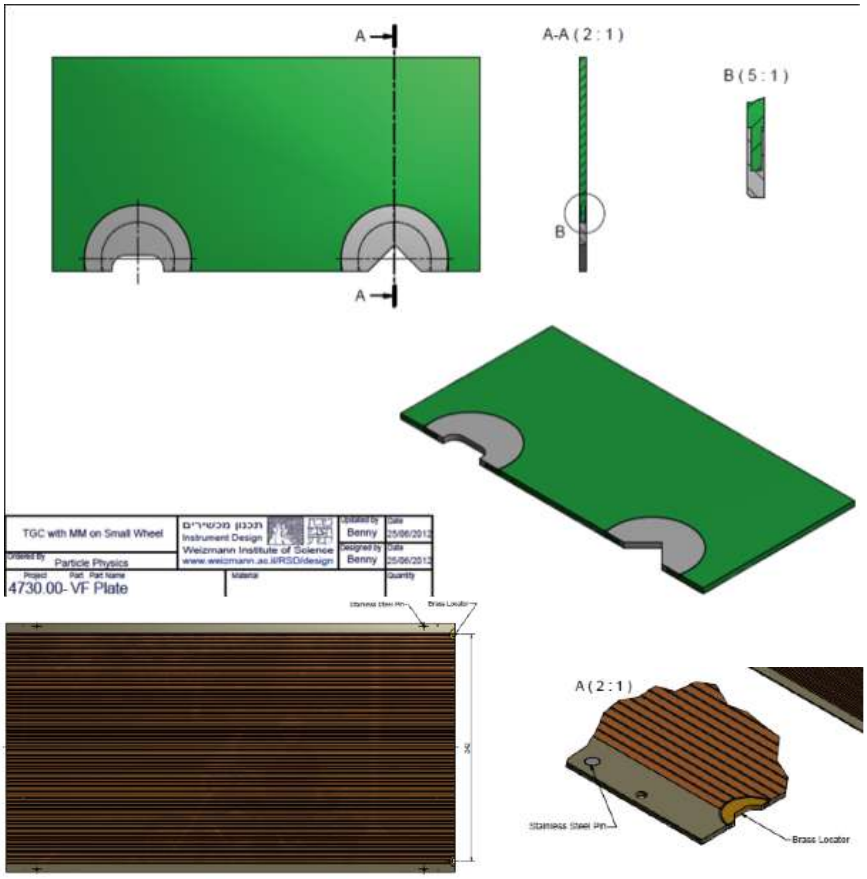

Figure 7.4: Schematics of the brass inserts to be glued to the strip cathode board as well as the stainless pin for x-ray positioning, to be machined together with the strips.

7.4 Single plane assembly

Some of the procedures to be used are partly described in [41]:

Masking for graphite spraying: as shown in Fig. 7.5.

Graphite Spraying: to be performed in all production sites (using Kontact Chemie-33) in an environmental controlled room (25±1° and less than 30% humidity), with the steps being shown in Figs. 7.6 and 7.7.

Polishing of the cathode boards: to achieve the required surface resistivity ranging between 90-110 kΩ/□.

Gluing of frames and wire supports on cathode boards: The operation is performed on granite tables, using precision jigs under vacuum. Glue used is Ciba-Geigy, Araldite 2011.

Anode plane wiring of two detectors: Two pad cathode planes with their corresponding support frames are wound by a rotating winding machine while applying a pre-tension. After soldering and cleaning, the uniformity of the wire tension is checked optically by releasing the cathode plane with the wires (see Fig. 7.8) and looking for non-uniformities in the wire plane.

Single detector closing: Unlike the TGC's presently operating in the ATLAS experiment, the high precision requirements on the spacing between detector planes and their respective planarity, impose new procedures. This is achieved for the single detector plane by placing the pad cathode, which includes the anode wires, on a flat granite table (20 µm deviation

Figure 7.5: Application of masking tape.

Figure 7.6: Filters and hanging rails for cathode boards

Figure 7.7: Graphite spraying. Right photograph shows graphite spray being completed for one board.

over the full surface) and applying vacuum from underneath. The cover cathode is attached through vacuum to a double honeycomb with a spacer frame between the two honeycomb plates (this allows to apply high vacuum to hold the cathode flat, while the final vacuum to perform the full gluing will not produce local deformations of the cathode). The arrangement is placed over the pad cathode using guiding pins (precision 100 μm) as shown in Fig. 7.9. The full assembly is covered by a silicon-rubber frame, which is then attached to the table. Low vacuum (-0.1 atm.) is applied to the volume under the silicon-rubber. Then gas (CO_2:n-pentane, 55:45) is injected into the detector inflating the silicon-rubber. The operation is repeated two to three times until 3.3 kV can be applied to the assembly (see Fig. 7.10).

The detector is left to operate half an hour at 3.3 kV and the HV current is recorded in the data-base. Following this test, glue (Ciba-Geigy Araldite 2011) is applied to the strip cathode frames and the procedure is repeated with the vacuum applied until the glue is cured, following which the flatness and thickness (which should be 6.3 ± 0.05 mm) of the assembly is checked. The single detector plane is then mounted into a special carriage (see Fig. 7.11) where it can be gas sealed.

Figure 7.8: 1/2 chamber after being released from the winding machine with the wires already soldered.

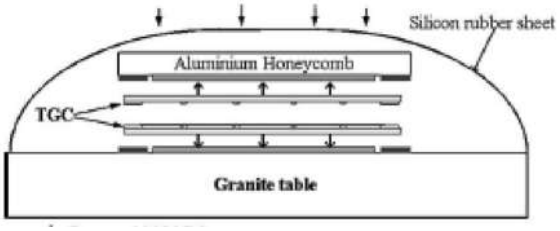

Figure 7.9: Above, a double Aluminum honeycomb cover is being placed before covering with the silicon rubber sheet. A drawing of the layering is shown below, left. Only the lower honeycomb and the granite table have full vacuum applied to it, to keep the surfaces flat, while the vacuum under the silicon rubber is -0.1 atm.

Figure 7.10: Filling the full volume with the operating gas.

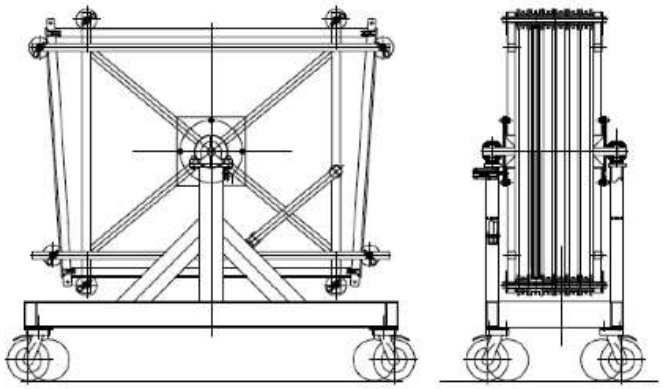

Figure 7.11: Rotating carriage to seal detectors and to perform work around the edges.

Gas sealing of the detectors: This is performed by applying heated epoxy on each edge for ten detectors at once. After completing the procedure on the four edges, the single plane detectors are tested for gas leaks.

Testing of a single detector plane: The detectors are operated at 500 V over the usual operating voltage for seven days. The carriage with ten detectors is then scanned with a γ source mounted in a precise X-Y table and the current in each plane is registered at each point of the scan, at two operating voltages (2.5 kV and 2.85 kV) to find possible defects and check the detector gain uniformity. Detectors that do not satisfy this requirement are rejected.

7.5 Quadruplet assembly

This operation is performed in two stages, by first building two doublets and then gluing them together. Each doublet is constructed with the pad planes towards the outside, in order to have a symmetric structure and to be immune to possible creeping of the glue.

Gluing of honeycomb 1/2 panel on the tested single plane detector: the operation is performed on a flat granite table (within 20 µm) where the detector is held with vacuum from underneath. The double honeycomb plate shown in Fig. 7.9 is also used here on top of the honeycomb to be glued but without any vacuum applied. The assembly is covered with silicon rubber and vacuum is applied from the edge of the granite table.

Gluing of a doublet: The single plane detector with its 1/2 honeycomb panel is then glued to a single plane detector using the same procedure. This is performed on a flat granite table (flat to within 20 μm). The table contains two thick precision machined pins attached to a jig (see Fig. 7.12) to align the two planes using the brass inserts of each of the strip planes. While the lower single plane detector is held flat by applying vacuum from underneath, the upper detector with its glued 1/2 panel honeycomb is kept flat by using the double honeycomb plate shown in Fig. 7.9 with vacuum applied. The silicon-rubber is brought in to cover the assembly and a low vacuum (-0.1 atm.) is applied until the glue between the honeycomb and the lower detector is cured. The assembly is then checked for planarity (it should be better than 50 μm) and thickness (it should be 18.0 ± 0.05).

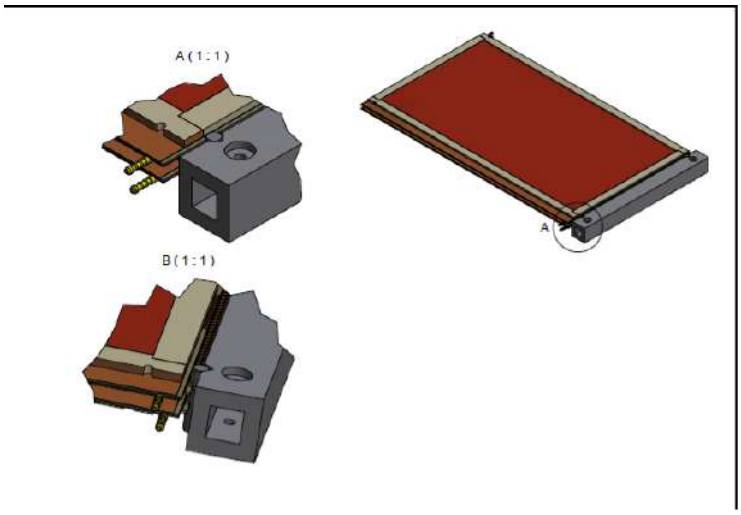

Figure 7.12: Schematic view of the attachment to the jig containing the precision pins.

Gluing of a quadruplet: the procedure is identical to the one used to construct a doublet, using the same alignment pins to define the relative position. After completing the gluing procedure, while the vacuum underneath is still applied, the X-ray cameras are installed on the granite table. The position of the precision brass balls in the strip boards is registered in 3-D (see Fig. 7.13) and cross checked with their expected position (it should be within 40 μm in x-y and within 50 μm in the vertical direction). The planarity of the upper surface is then checked again, and then placed on a carriage similar to the one shown in Fig. 7.11.

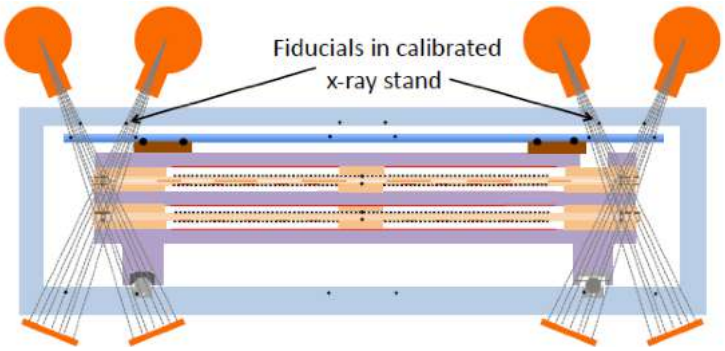

Figure 7.13: Possible measurement of the vertical position of the alignment brass pins using an x-ray camera set-up (taken from H. Wallenstein presentation).

Installation of the adapter boards and CO_2 channel: The adapter boards route the various signals (wire groups, pads and strips) to connectors where the readout electronics can be plugged. These adapters also allow making a gas channel around the quadruplet, where CO_2 will be flowed to dilute any possible leak of the flammable gas.

Testing of a quadruplet at the production sites: All quadruplets are tested using cosmic rays at the various production sites. A similar procedure has been described in [42]. The cosmic ray scan provides a full map of their efficiency and by reading the charge of each strip, a rough measurement of the position resolution (∼400 µm). The cosmic-ray set-up includes two precision chambers (TGC's) above and below the test volume. They track the cosmics through the quadruplets under test and provide the expected hit point. The pads of every detector plane are readout and if a hit is observed in the expected incident point, this is used for the calculation of the local efficiency.

A mapping of the detector efficiency for every point is produced (see for example Fig. 7.14, where such a scan is shown for one of the present ATLAS triplets). Furthermore, the charge in the strips of every plane is also readout and their centroids are calculated. Comparison of the position in two adjacent planes, gives the average resolution (within a given pad) to better than 400 µm. The efficiency maps and the average resolution for every pad on a given planes are recordered in the data-base. A quadruplet is considered acceptable if each of its planes has an efficiency exceeding 95% on 95% of its sensitive area.

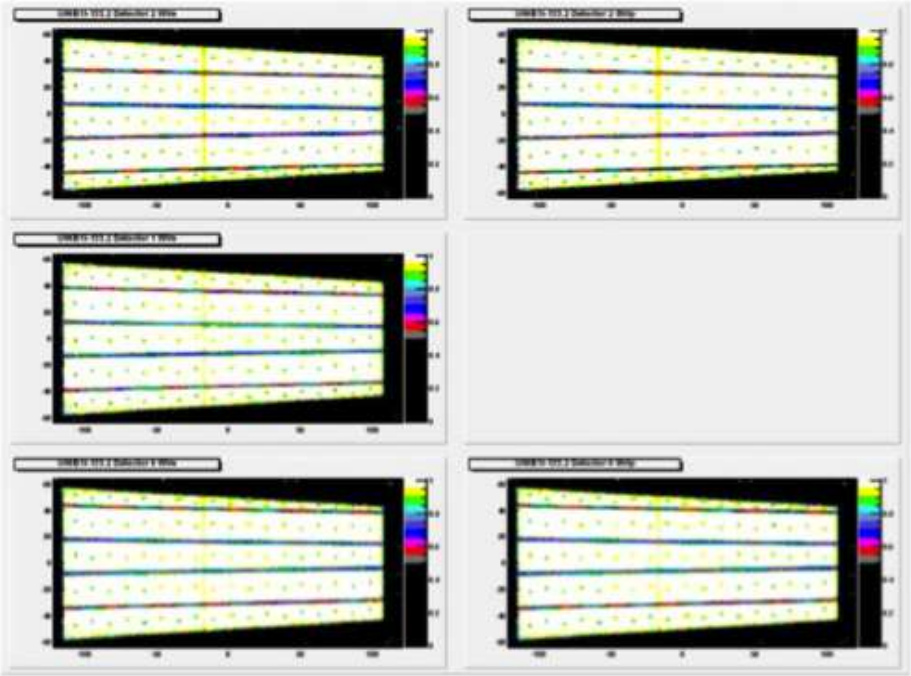

Figure 7.14: Example of a cosmic ray scan of an ATLAS triplet (two planes with strip readout and three planes with wire readout) where the wire support frames and buttons can be clearly seen as inefficient regions.

7.6 Construction achieved with present doublet

A first set of two $60 \times 40\,\mathrm{cm}^2$ doublets has been constructed using the procedure described above. The two doublets have been measured to be flat to within 50 µm and their overall thickness at the edges uniform to within 30 µm. The relative parallelism between the two strip layers has been measured using cosmic rays at two positions spaced by 45 cm. The difference between the two strip layers at the two positions was measured to be 20 ± 36 µm, consistent with the needed requirements.

7.7 Checks at CERN

Chambers will be mounted on palettes and be transported in air-conditioned containers. Upon arrival to CERN, each palette will be recorded in the data-base; it will be checked for any damage and the shock sensors will be checked. Any irregularity will be recorded in the data-base.

The palettes with their detectors will be transported to the GIF++ area, where they will be flushed with gas for 48 hours before being moved into the radiation area. There, they will be connected to readout electronics and HV. The general procedure is partly described in [15]. A HV of 2.9 kV is applied to all the detectors and the ground current of each one is entered into the data-base. The source is turned on to provide $20\,\mathrm{kHzcm}^2$ of detected photons in each plane and the current for every plane will be recorded. Data will be read from pads, strips and wires at a 10 Hz rate, to find any low efficiency or dead channel. The source is kept on for 1/2 hour, then it is switched off (no detector should have tripped, otherwise they are rejected). The HV current of each detector is entered into the data-base. It should not exceed the initial ground current by more than 1 μA The detectors will then be flushed for 12 hours with CO_2.

7.8 Installation into sectors at CERN

This operation requires a flat (within 20 µm) granite table of $5 \times 3\,\mathrm{m}^2$ where optical elements will be placed. The table also contains six machined pins that will match the inserts shown in Fig. 7.4 (see Fig. 7.15). The three fully-qualified quadruplets are brought into contact with the precision

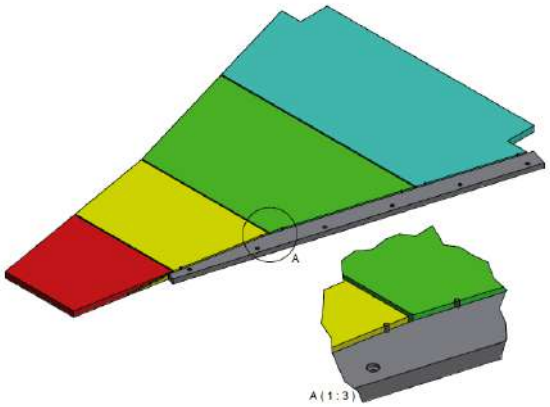

Figure 7.15: Schematic view of the placing of the modules against the precision pins.

alignment pins with pneumatic pressure while vacuum is applied from underneath. The glass-fibre external frame (manufactured with a precision of 150 µm) is then glued to the quadruplet assembly.

After curing for 12 hours, the assembly is lifted and turned around, to place it with the three quadruplets facing precision aluminum honeycomb planes in the regions free of the fiberglass frame, and then vacuum is applied from underneath. The second glass-fibre frame is then glued to the assembly. The glue is left to cure for 12 hours. The x-ray cameras are placed to measure the 3-D position of the brass balls. The crane attachment points are placed and the wedge is lifted.

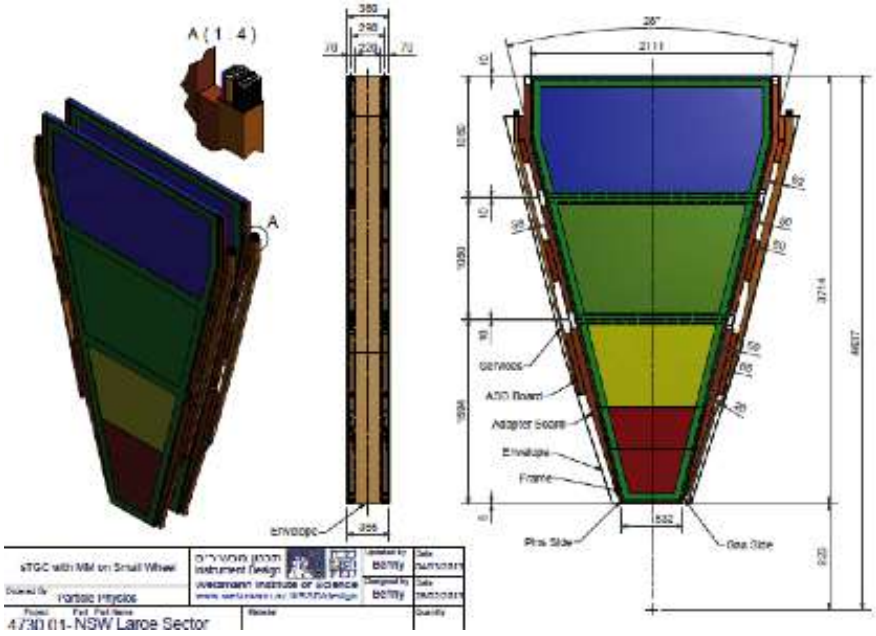

Figure 7.16: Design of a large wedge with all the services installed.

7.9 Completion of the sector wedge

The sector wedge can now be equipped with all the services. A design of such a wedge, fully equipped with its services is shown in Fig. 7.16. The equipped wedge can be tested with cosmic rays for long periods until it can be attached to the MM frame and incorporated into the NSW.

8 Micromegas construction

The construction of the MM detectors is planned to start in 2015 and will be completed by the end of 2016. The flow chart shown in Fig. 8.1 lists the main tasks. The detector construction will be a collaborative effort of the participating institutions and industry, the latter for the PCB production. Only the detector construction is covered here. The production of the electronics and services is described in chapter 12.

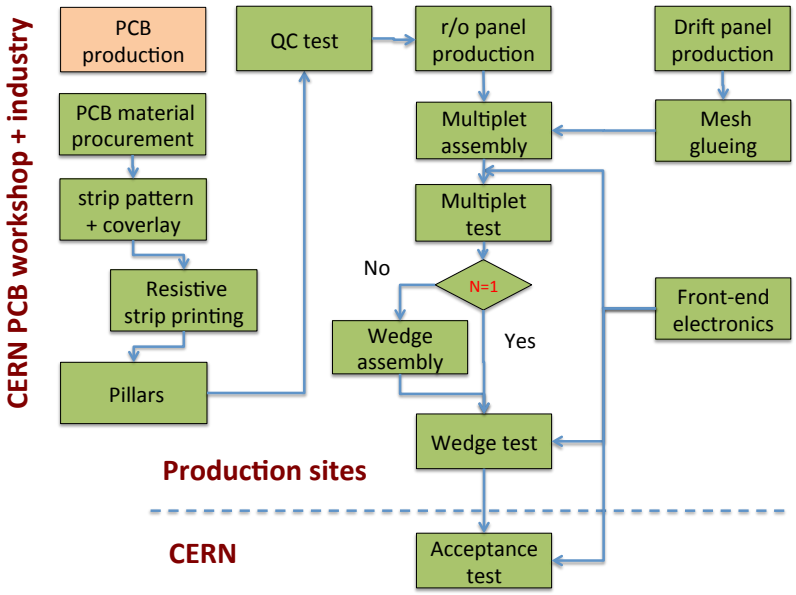

Figure 8.1: Flow chart of the MM detector construction.

The detector construction can be split into a number of separate steps that are discussed in the following sections.

8.1 PCBs and other raw material procurement

8.1.1 PCBs

The readout boards are the key element of the MM detectors. Their quality in terms of strip precision and electrical properties determine whether the detector will work properly or not. A reliable production of these boards is therefore of prime importance.

For a total of 256 detector planes, 2048 readout PCBs have to be produced with 32 different shapes and dimensions, varying from $2220\times511\,\mathrm{mm}^2$ to $460\times450\,\mathrm{mm}^2$. The number of pieces required per PCB type is 64.

Figure 8.2 shows the layout of a typical PCB, here the innermost PCB of the large sector with η strips. It comprises 1024 Cu readout strips, 17 μm thick, 325 μm wide, with a pitch of 0.425 mm. The readout strips are routed to both sides. The boards are made of 0.5 mm thick Cu clad FR4 with a Tg[1] of 170 °C or higher.

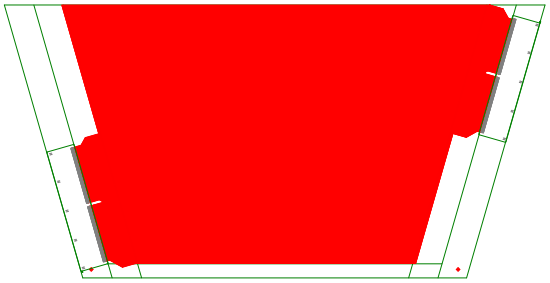

Figure 8.2: Layout of the innermost readout PCB of the large sector, indicating along the sides the location of the contacts for the connection to the front-end boards and the outline of the front-end boards together with the ground contact connectors.

The MM development for the NSW was done in close collaboration with the CERN PCB workshop. In consequence it is planned to charge the CERN PCB workshop to organize and follow the PCB production in industry.

With the choice to separate the amplification mesh from the MM readout board, the production of the latter is reduced only to processes that are commonly used in PCB industry. A number of PCB companies may produce these boards without having to invest in new equipment, as the width of the PCBs is limited to less than 600 mm.

The board production procedure has been validated on a number of boards that were used for the construction of the $2.2 \times 1\,\mathrm{m}^2$ prototype detectors and is considered mature. Figure 8.3 shows the measurement of the distance between the first and last strips of the four PCBs that were used in the second 2.2 $\times 1$ m^2 prototype detector along the length of the boards. The boards were produced at CERN.

The PCB production consists of the steps listed below:

PCB layout will be done by the MM Collaboration together with the CERN PCB workshop.

PCB material procurement either via CERN purchasing or directly by the production site.

Production of films three films per type of board are required, one for the PCB etching, one for the resistive-strip pattern, and one for the pillar deposition.

Etching of the readout pattern and plating of the contacts with a layer of nickel-gold.

Lamination of coverlay to produce an insulation layer between the readout strips and the resistive strips, curing.

Deposition of resistive strips: either by screen printing or sputtering that have both been proven to give excellent results; an interesting option is the printing or sputtering of the resistive strips on a polyimide film (Kapton) that is then press-glued to the PCB (in this way the previous step, lamination of coverlay, is not required).

[1]Tg means Glass Transition Temperature and defines the temperature at which the PCB changes from a solid to a rubbery consistency and becomes unstable.

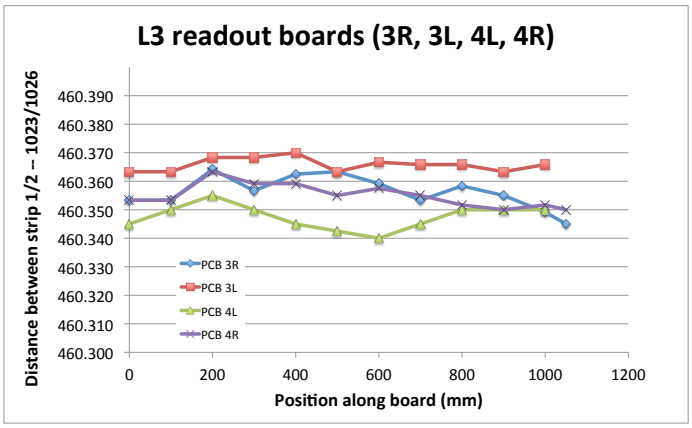

Figure 8.3: The distance (in mm) along the length of the boards between the first and last strips of the four PCBs that were used in the second 2.2 $\times$1 m^2 prototype detector.

Deposition of pillars: that define the distance between the amplification mesh and the resistive strips; it consists of laminating two layers of 64 μm thick photo-imageable coverlay to the PCB, exposing, and developing the pattern of the pillars.
Curing at 160 °C: to stabilize the pillars.
Finishing Cutting the board to size and drilling, if required.

During and after each of these steps, quality control will be essential to ensure a homogeneously good production quality. The films used for the patterning of the PCBs, resistive strips, and the pillars must be qualified before they are used in their respective processes. The first boards of each step and series must be controlled, as well as samples throughout the production.

The exact production process depends on the work flow in industry and needs to be agreed with them. Most likely a full set of PCBs of each type will be produced in one go. This avoids changing of tooling and setting up overheads. In total there are 32 different shapes of boards to be produced. The number of boards per batch is 64 pieces. Taking into account the potential need for additional boards during the full production and assembly chain, 10% of spare boards will be produced[2].

The mass production of the boards is estimated to take (probably much) less than one week per batch, including quality control. With a 50% safety factor, all boards can be produced in one year if they were produced in a single company. Two companies in Europe[3] have already been contacted. They have both already produced operational MM detectors and are familiar with the processes involved although they have not yet produced detector boards of the size required.

The production sequence should take the needs for module construction into account, i.e., all board types needed for a module shall be produced in series, then those for the next module type. Taking this into account the first module construction could start about three months after the

[2]The production of additional boards at a later time, using the original films, is always possible but creates overheads and additional costs that are probably higher than adding a few more boards to a series production.
[3]Cirea/Elvia, Coutance, France and Eltos, Arezzo, Italy.

start of PCB production[4]. The boards for the last type of modules will be available after about one year (single producer) or about six months (two producers).

To ensure good and homogeneous production quality, in particular if the boards are to be produced in two companies, the CERN PCB workshop (in collaboration with the industries involved) will draw up a production protocol that defines the production sequence, the conditions, including the quality control measures. The latter will be established by the PCB workshop together with the MM community. It will include test to ensure the mechanical precision of the boards as well as the electrical board integrity.

8.2 Single plane assembly

The assembly of the single planes will happen in the collaborating institutes. Depending on the final segmentation of the detector wedges into one or several modules three or more assembly sites may be set up. An assembly method that has been realized at CERN when constructing the 2.2×1 m^2 prototype chambers is described here. The final assembly scheme will be decided this summer after the mechanical prototype construction efforts currently under way in six assembly sites.

In order to assemble an operational detector two types of panels are needed, the readout panel, carrying the readout boards, described in the previous section, and the drift panel which comprises the drift electrode and the amplification mesh. This is schematically shown in figure 8.4.

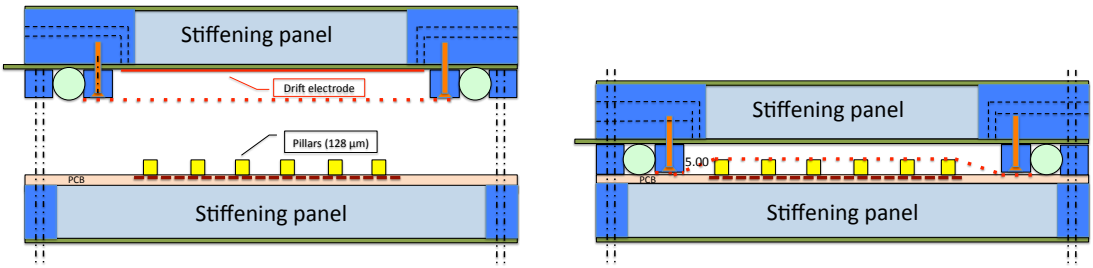

Figure 8.4: Schematics of a single MM plane assembly showing the drift and readout panels in open (left) and closed (right) position.

Readout and drift panels can be produced in the same or in different institutes. Both panels are expected to be rigid and need to be produced with adequate mechanical precision which, however, is not the same for the two panel types.

The tools used for the assembly of the two panels are very similar or identical. The assembly of the panels is done on a granite table equipped with a vacuum sucking system. The vacuum sucking system is made by a thin layer of a mesh fabric covered by a 175 μm thick mylar foil. The mylar foil is sealed against the granite table and carries a grid of small holes. The second tool is a stiff-back with a flat lower surface and provisions for vacuum sucking. In the second assembly step, see below, the positioning of the half-panel is controlled by the stiff-back, placed at fixed distance above the PCB on the granite table. For the 2.2×1 m^2 prototypes, a simplified stiff-back structure

[4]This assumes a full-sector module with eight PCBs per plane and all boards are done in the same company; should the module size be reduced or half of the board types used for a single module are produced by the second provider the delay is shorter.

was used, an assembly of aluminum bars equipped with sucking heads approximately every 25 cm. The bars span the width of the panel to be constructed and are spaced by about 25 cm in the other direction. The bars were precisely machined and glued together with longitudinal bars, stiff enough to keep their structural form after the curing of the glue. Thus forming a plane that matches the surface of the granite table.

The panel assembly method is schematically shown in Fig. 8.5.

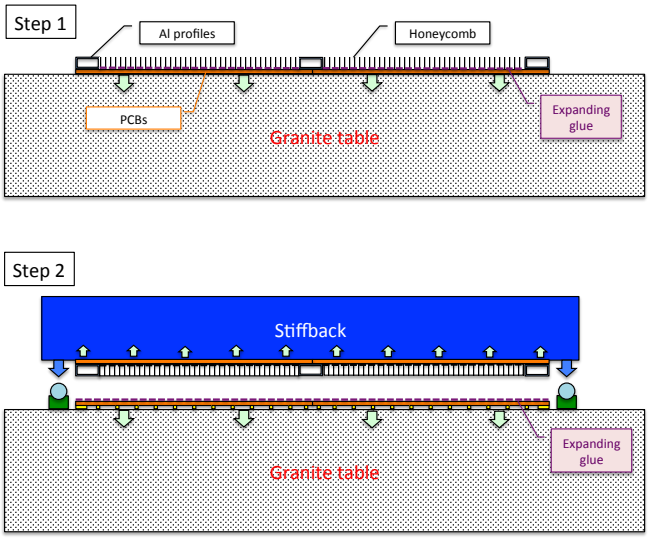

Figure 8.5: Schematics of the panel assembly method.

8.2.1 Readout panel assembly

The readout panels carry on both faces readout boards which must be parallel to each other within 50 μm. The readout boards constitute the skins of a honeycomb panel, reinforced by aluminum profiles around the rim and at the junctions of the PCBs. In the final detectors, custom-made extruded aluminum profiles will close the detector sides where the electronics is located. They will integrate channels for the cooling water and serve as cable trays.

The PCBs to be glued to the honeycomb are placed face down on the mylar foils and positioned to each other with the help of a jig and positioning holes in the PCBs. When the PCBs are in the correct position the gaps between the boards are closed by tape. Then the boards are sucked to the granite table and their relative position is controlled. Along the outer edges the readout boards are about 10 mm wider than their final width and the panel frame. The boards are taped along the edges to the granite table to prevent glue from creeping under the boards. The aluminum profiles are glued to the boards using Araldite 2011. The next step is to deposit the expanding glue that is used for the glueing of the honeycomb on the readout boards and to place the honeycomb. The glue used is a two-component resin foam[5] with an expansion coefficient of about four and a life time of about 30 minutes. It completely cures within 24 hours.

One day later the panel consisting of one skin reinforced by the honeycomb is turned and picked by the stiff-back. The second layer of readout boards is placed on the granite table and sucked

[5]PB250.DM03.0.66 and PB250.SD5604.0.95 in the proportion 100:90 in weight.

to it in exactly the same way as the first layer. A thin layer of the expanding glue is deposited on the readout boards and the stiff-back with the open panel side facing down is positioned at a defined distance above the readout boards leaving a glue gap of a few hundred microns. In the 2.2×1 m^2 prototype about 1.4 kg of glue for the complete panel has been used.

The relative alignment of the readout boards on the two faces of the panel has not been addressed yet. A set of jigs, fixed to the granite table, against which the precisely cut PCBs are brought in contact such that the x and y position of the boards is constrained should do the job.

Around two days are needed for the construction–glueing of each panel plus another day for the drilling and finishing. The granite table is occupied for two days per panel. It seems reasonable to assume that two panels per week can be glued on a single table.

The final steps are the mounting of the HV connectors and the soldering of the ground pins as well as the mounting of the cooling plates for the electronics, as described below.

For the full-wedge solution, a total of 64 readout panels for the large sectors and the same number for the small sectors need to be produced. This work could be achieved by two production sites in a single year. In the case of several modules per wedge, the number of readout panels will increase accordingly. Panel construction would have to proceed in more places or on more tables in parallel. The time estimate of one year for the full production of readout panels is also valid in this case.

8.2.2 Drift panel assembly

The assembly method of the drift panels follows the one of the readout panels. The same tools and glues are used. A small difference lies in the fact that the skins of the drift panels have flat surfaces, while the readout boards have the 128 μm high pillars.

Other differences are related to the different function of the drift panel: it serves as support of the amplification mesh and as gas distribution system.

As in the readout panels the skins of the drift panels are made of 0.5 mm thick FR4, however, not patterned. The outer frame structure differs from the one of the readout panels. Since the mesh is stretched with a force of about 10 N/cm it was decided to embed a solid profile into the frame to which the mesh support frame is screwed. In addition an open channel that serves as gas manifold is integrated into the drift panel frame. The solution adopted for the 2.2×1 m^2 prototype is shown in Fig.8.6. The gas channel is only present along the two shorter sides of the prototype panel where also the readout electronics is located. In the final panels the profiles will be replaced by custom-made extruded profiles. The extruded profiles along the sides where the readout electronics is located will incorporate the holders for the on-chamber electronics boards (that are connected to the readout board). It will however, opposite to the prototype, not include the gas channel which will be part of the profile along the other two sides.

Once the panel is glued, the drift electrode is added by either glueing a thin Cu film to the appropriate skin of the panel[6] or by applying a layer of conductive paint. Then the gas in- and outlet holes are drilled through the drift electrode and sealed, as well as the bolt holes in the outer panel frame. The next step is to add the drift panel spacers, see below, and the mesh support frame.

The mesh is glued to the mesh support frame with a tension of about 10 N/cm, either in-house, if the tooling for the mesh stretching is available, or in a specialized company[7]. For the glueing a

[6] An alternative is to use Cu clad skin material with the drift electrodes already patterned, as in the 2.2×1 m^2 prototype; the latter can be done by etching or machining.

[7] The same type of mesh is used for screen printing.

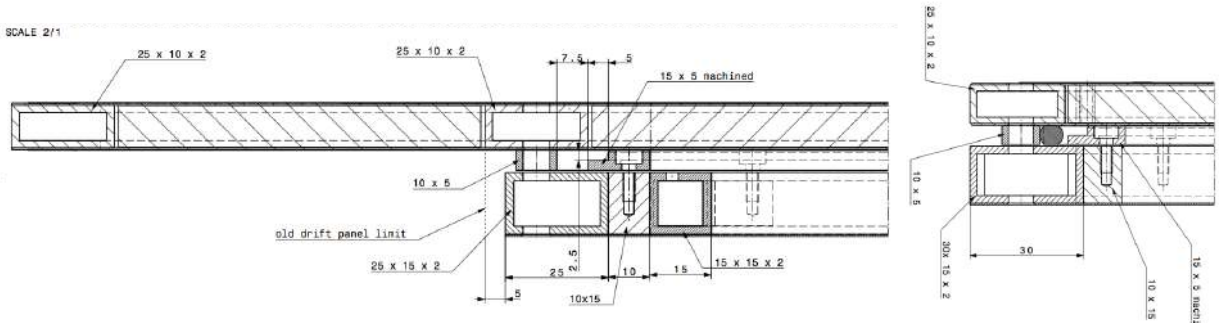

Figure 8.6: Cross-section through the frames of the readout and drift panels of the 2.2×1 m^2 prototype; in the left drawing the profiles along the readout side is shown, with the gas channel, in the right drawing the profiles along the long panel sides are shown. In both drawings the mesh frame is also shown.

cyanolit-based glue is used, and the mesh is secured with a second line of Araldite 2011. The mesh is also glued to the drift panel spacers, the latter have the same height as the mesh support frame.

The last step consists of cutting small openings into the mesh at the place of the drift panel spacers and to create the passages for the panel interconnects.

Around two days are needed for the construction–glueing of each panel, an additional day is needed for the drilling and making the drift electrode. Another day should be foreseen for the mesh glueing if done in-house. If the mesh glueing is done out of house then it is more efficient to do this in batches. Including some safety factor this leads to about one week per panel. Much of this time is waiting for glue curing. The granite table is occupied for two days per panel. It seems reasonable to assume that two panels per week can be glued on a single granite table.

Three drift panels are required per quadruplet. The two outer panels are identical, with a single drift electrode. The middle panel has drift electrodes (and gas channels) as well as the mesh on both sides. In total 192 drift panels need to be produced for the single-wedge option and 576 in the three-module-per-wedge option. It seems reasonable to assume that 64 panels/year can be produced in a single production site. Three sites would be able to do the full production in one year for the 192 panels. In the other option, parallel production or more sites will be required to complete the drift panel production in one year. Alternatively the panel production could be stretched over two years.

8.3 Quadruplet assembly and testing

A quadruplet consists of two doublets each of which comprises a two-sided readout panel and two drift panels. The gas tightness is achieved by O-rings between the flat surfaces of the drift- and readout panels[8].

The distance between the readout and the drift panels is maintained by 5 mm thick precisely machined bars plus a number of internal spacers. The bars and spacers define not only the drift space but, more importantly, they assure the co-planarity of the two readout doublets. The spacers consist of small peek inserts with an inner bore of a few millimetres that are placed between the mesh and the readout electrode. Holes in the readout panels with diameter of a few millimetres

[8]In the 2.2×1 m^2 prototype detectors a 6 mm diameter O-ring is used. Another option is a flat O-ring with rectangular cross-section.

permit the passage of an insulated threaded rod[9]. Three spacers between the panels have been realized in the second 2.2×1 m^2 prototype, the implementation is shown in Fig. 8.7.

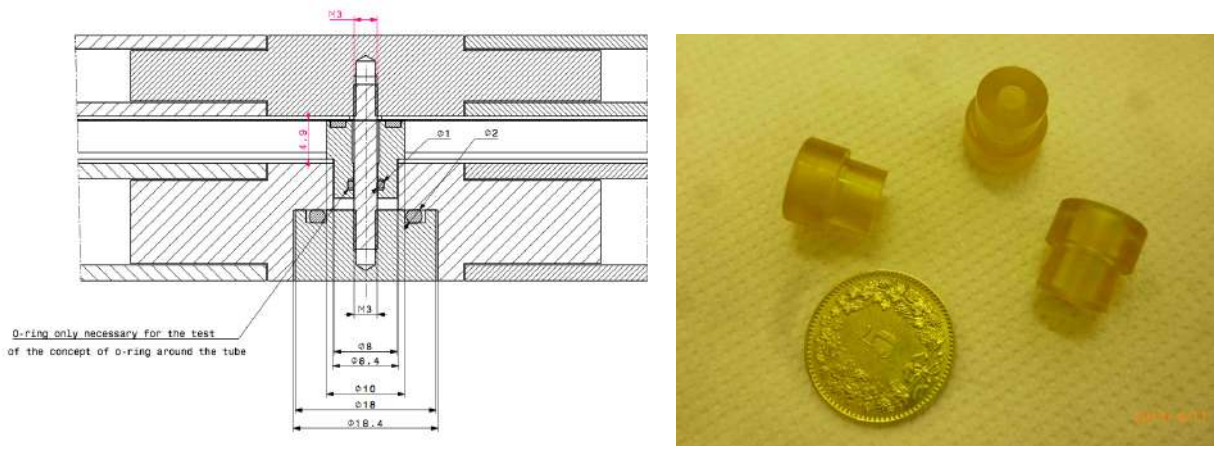

Figure 8.7: Spacer that defines and maintains the distance between the readout and drift panels; left: the solution implemented in the 2.2×1 m^2 prototype; right: the three peek inserts that were glued to the drift panel.

The quadruplet assembly is done on a flat surface with some positioning jigs. This is not necessarily a granite table given the stiffness of the individual panels. Each readout panel has a set of precision holes at defined positions with respect to the readout strips.The lateral positions of the two readout doublets will be aligned to each other using a simple but precise jig with a dowel pin, as shown in Fig. 8.8. The lateral positioning of the drift panels is not critical.

A critical element is the cleanliness during the assembly to avoid dust particles that can produce current bridges over the 128 μm distance between the mesh and the readout structure. The assembly should therefore be done in a temperature and humidity controlled clean room of class 10000 (ISO 7) or better. All parts need to be throughly cleaned before entering the room.

For the cleaning of the readout panel and the amplification mesh, a rotating brush combined with vacuum cleaning, followed by a passage with an adhesive roll works very efficiently.

The panels of a doublet are stacked first without O-rings and spacer bars. During this step the mesh frames, being about 50–100 μm thinner than the spacer bars, define the drift gap and the mesh is sitting on the pillars. In such a way the electrical integrity of the assembly can be checked by applying HV to the resistive strips in air. Experience shows that, if the current drawn between the resistive strips and the mesh is in the range of a few nA[10] the boards are functioning well and are free of dust particles. This procedure must be repeated for each gas gap. When the two gas gaps of a doublet are declared functional the O-rings are inserted from the sides and the boards are positioned with respect to each other using the alignment pins. This done, the spacer bars are inserted and the panels are bolted together.

The assembly itself is fast and takes less than two hours. The cleaning and HV testing is usually more time consuming. Typically one to two days per quadruplet should be counted for. The total number of quadruplets is 64 for the full-wedge option or 192 quadruplets otherwise. No experience has yet been gained in the assembly of full-wedge quadruplets. Probably there is no big difference

[9]In the readout boards for the ATLAS detectors the readout lines will be routed around the holes such that only the space taken by the inserts is inactive.

[10]The exact value depends on the humidity level and the detector area that is tested.

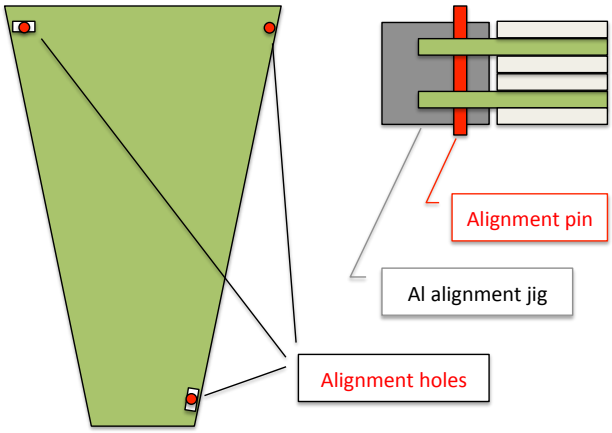

Figure 8.8: Schematics of the MM panel alignment showing in the left sketch the positions of the precise and elongated alignment holes and in the right drawing a sketch of the alignment jig.

time-wise between the two options, to be confirmed. In both cases the assembly of all quadruplets could be achieved in about one year in one or two assembly sites.

More time consuming will be the testing of the assembled quadruplets.

8.4 Quality control, final test and expedition

The quality control proceeds in steps, as to avoid the assembly of parts that are not qualified.

During the PCB production quality assurance procedures will include the control of PCB panel flatness, electrical integrity (no shorts), controlled resistivity in an acceptable range[11], strip precision, and the correct development of the pillars. The development of quality control procedures and (automatized) tools to check the PCB production will be one of the main issues over the next two years.

Only boards that fulfil the quality specifications are glued to the stiffening panels.

After the assembly of a doublet, the electrical integrity of the detector has to be qualified. The drift electrodes must not draw any current when polarized with negative HV up to 1000 V (the operating voltage is 300 V). The mesh must be properly connected to ground potential and the resistive strips are tested by applying HV in air and monitoring the current. The currents should not exceed a few nA at +900 V on the resistive strips.

After the assembly of quadruplets, the detectors must be tested for gas leaks and then with gas and HV. A test with (some) readout electronics and cosmic ray particles or/and photons from an X-ray source should follow.

Tests with a 30 kV X-ray tube demonstrate that all planes of a quadruplet can be qualified at once. Figure 8.9 shows the current recorded in a small MM detector as a function of the material traversed by the X-rays. The interaction rate is attenuated by a factor 30 between the amount of material corresponding to the first and the fourth MM but still results in a sizeable current. With a 40 or 50 kV X-ray tube there should be no problem to reach high penetration.

[11]The exact values of the resistivity are not very critical.

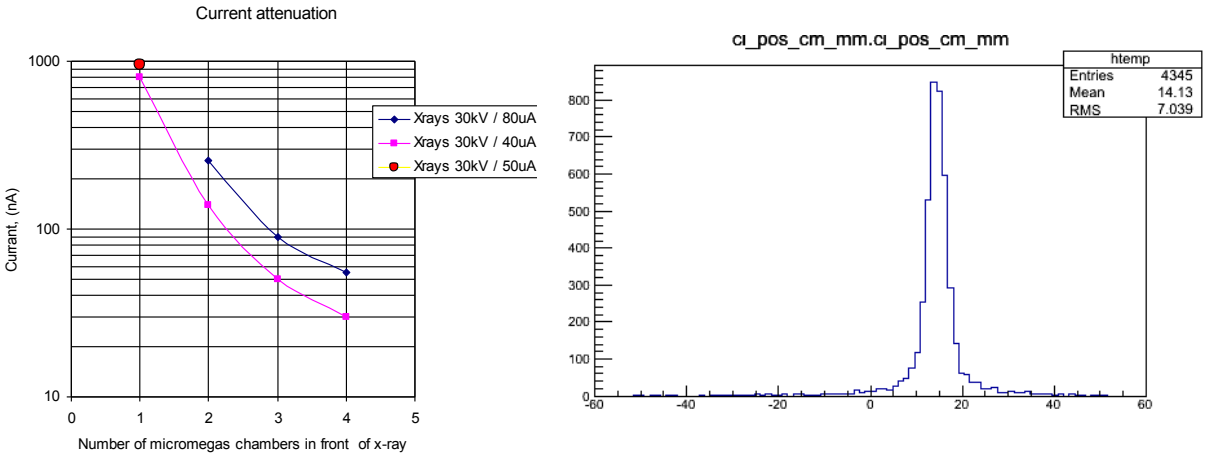

Figure 8.9: Left: current drawn by the MM detector as a function of the number of MM panels traversed by the X-rays; right: distribution of the X-rays as measured in the MM.

A relatively fast scan of a complete quadruplet without the need of readout electronics can take place by measuring the current. An effort to set up such a system with position encoding and current readout that scans a complete quadruplet has started.

For this measurement only a small fraction of the detector needs to be equipped with readout electronics.

The last step of testing before the installation of the detectors on the Small Wheel will be done once the quadruplets have been equipped with their final electronics. This will happen at CERN. With an exposure to comic ray particles non-functioning electronics cards and/or cabling errors may be identified. For this it is envisaged to refurbish the cosmic ray stand in BB5 that was heavily used during the testing of the ATLAS MDT and RPC chambers.

9 Integration and commissioning

9.1 Assembly of the New Small Wheels

The NSW will be assembled at the surface on the CERN site. During the first step of the detector integration, the sTGC and the MM detector units have to be assembled into sector sized objects. The subsequent step integrates these sector-sized objects onto the mechanical structure of the NSW detector wheel. Whether the new detector wheels will be integrated with the JD shielding at the assembly site depends on the installation scenario, see Chapter 11.

The assembly site, where the integration of the NSW takes place, must meet several requirements.

1. A bridge crane with a minimal load of 5 t and a minimum clearance of 15 m from the ground. Used during the assembly of any support structures, the mechanical wheel structure, and the integration of the NSW detector sectors with the mechanical wheel structure.
2. Empty floor and wall space of length × width × height of twice 10 m × 7 m × 15 m. Used for the assembly of the NSW and support structures.
3. A bridge crane with a minimal load of 160 t (80 t if the JD shielding is not part of the assembly) and a minimum clearance of 15 m from the ground. Used to lift a finished NSW in the transport frame onto the transport trailer.
4. A door of width times height of 8 m × 9.5 m. Provides access for the trucks and trailer needed for the transport of the NSW from the assembly site to Point 1.
5. Empty floor space of length × width × height of 15 m × 8 m × 15 m adjacent to the main door. Reserved area for the trailer during loading. In addition used for temporary storage of detectors during the assembly.

A likely location for the integration is building 191 at CERN where the original SWs were assembled and which fulfills all the above requirements.

9.1.1 Mechanical integration of sTGC and MM detectors

Starting from the MM chamber, the two sTGC wedges of each sector will be fixed to the MM spacer frame to form a sTGC–MM station. Subsequently, that integrated station will be mounted on the NSW structure, greatly speeding up the assembly of the wheels by having to install only 16 completed detector sectors per wheel already containing almost all of the services.

The sTGC wedges will be mounted force free on the MM spacer frame in 3 points using kinematic bearings. The two wedges will be connected by stiff bars to these three kinematic mounts, so that the adjustment of their relative positions within a few mm can be realized. Thus, a fixed geometric relationship will exist between the strips of all eight sTGC planes in each sector at all times—for the four planes in each wedge by construction, between the wedges by a one-time adjustment—simplifying any corrections for the geometry to be implemented in the trigger algorithms. The same three mount points on the MM spacer frame are used later on to mount the completed station to the NSW structure with a second set of kinematic bearings. The use of two separate kinematic bearings in the mount points decouples the MM chamber from the sTGC wedges as

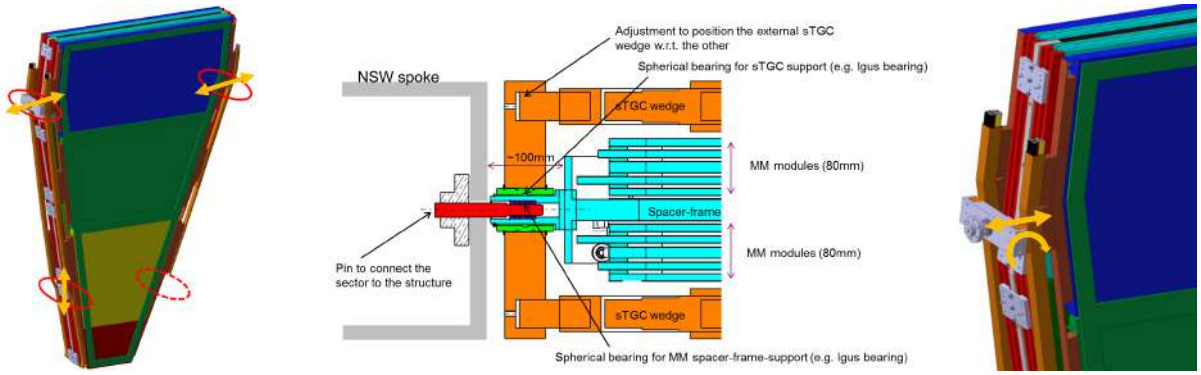

(a) (b) (c)

Figure 9.1: (a): integrated sTGC–MM sector. The four possible mount points are indicated by the red circles. The arrows give an example of the degrees of freedom of translations of the three used kinematic bearings. (b): cut though the sTGC–MM station at a kinematic double bearing. (c): detail of the sTGC mounted to the MM frame. Visible is the bar connecting the two sTGC wedges to the MM frame and the double kinematic bearing. The arrows indicate the possible adjustment of the sTGC wedges on the connecting bar.

the weight of the latter is transferred directly through the bearings to the NSW structure. The optimal locations and the choice of the degrees of freedom of each kinematic bearings depend on the orientation of the station in the NSW. To allow the use of only one type of MM spacer frame for either all small or all large sectors, regardless of where a station is being mounted, the frames will be equipped with four possible mount points. Of these four points the three most suitable ones are selected for each sector. Figure 9.1 shows a drawing of the double kinematic mounts with the sTGC wedges connected to the MM chamber.

The integration of the sTGC wedges with the MM chamber is foreseen to take place at a dedicated location to relieve the detector assembly sites from additional work and avoid problems due to the logistics in case of delays on the production schedule of either detector type. The sector assembly should take place as close as possible to the NSW integration site, to minimize possible damage due to transportation.

A possible integration procedure could be as given below.

1. The first sTGC is positioned upside down on a flat surface (e.g. a granite table). Precision pins on the flat surface at the locations of the externally available precision surfaces of the sTGC modules can be used for the placement;.
2. The double kinematic bearings and connection bars for the sTGC are mounted on the MM chamber.
3. the MM chamber is lifted by a support frame which connects to the external part of the double kinematic bearings. The frame allows the fine adjustment of the vertical position of the MM chamber at all mount points.
4. The MM chamber is lowered on the sTGC wedge and connected to the wedge after adjustment of its position.
5. Using the same precision pins as in (1) and the same support frame as in (3) the second sTGC wedge is positioned and connected to the MM chamber.

If necessary, the in-plane alignment systems of the sTGC wedges and the MM chamber (see Chapter 10) can be used to monitor adjustments. Additional mount points on the sTGC wedges and the MM spacer frame can be foreseen to simplify the handling. The estimated integration rate of sTGC and MM is 1 sector per day with 4 FTE of manpower.

Any detector unit scheduled for integration will have to pass a quality assurance test after its transport from the production site to CERN to ensure that only fully functional sectors are assembled. After a sector is integrated, it will be tested again. The quality assurance tests will be similar to those used during the assembly of the ATLAS muon spectrometer [44, 45]. If all quality assurance tests are passed, the sector will be transferred to a storage and transport frame in which it will be suspended, hanging vertically at two points with the long station axis horizontal.

9.1.2 Assembly of the New Small Wheel mechanical structure

The NSW mechanical structure consists of the hub and interconnected rectangular spokes between the sectors. While the hub consists of brass, the rest of the structure is foreseen to be built of aluminum. In case a greater tensile strength is needed in some parts of the structure to reduce overall deformations, these parts could be manufactured of stainless steel. To reinforce the structure, close to the hub the two spokes at the side of each large sector are closed by plates in the xy-plane to a tubular geometry. Cross bars interconnect the spokes further away from the hub. The spokes in sector 11 and 15 will deviate from the usual geometry to accommodate the feet of the JD shielding after transferring the detector wheel onto the JD plug. Due to the weaker structure in the feet region, the upper 225° will contribute most to the structural strength. The spokes in the large sectors (i.e. on the IP side of the detector wheel) and in the small sectors (HO side) are interconnected by bars arranged in circles coaxial with the z-axis. The spokes will contain the necessary cut-outs or holes for the optical alignment lines. Cable trays will be integrated at the outer rim of the NSW structure to distribute the services from the patch panels in sector 1, 9, and 13 around the wheel (see Chapter 13.4).

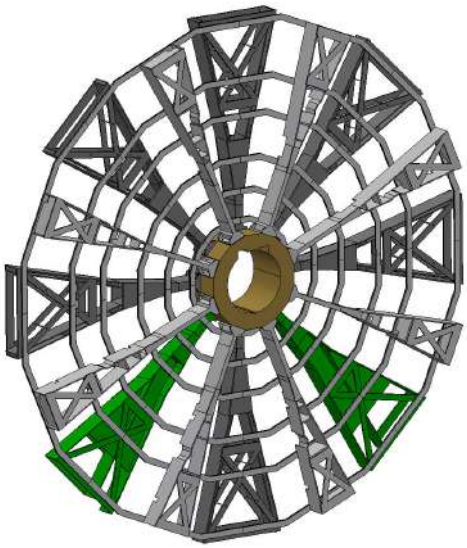

Figure 9.2: The NSW mechanical structure. View from the HO side.

To assemble the NSW mechanical structure a grid of girders mounted on a wall will be used (Fig. 9.3 (a)), similar to the HO structure in UX15 which supports the EO MDT chambers. This grid can be part of the transport structure later on, see section 9.1.5. Mounted in the middle of the grid is a stub which will serve as a fake JD plug to carry the NSW hub. The stub will be longer than the hub so that it may be matched to the JD plug during the later integration of the detector wheel with the JD shielding. The hub will have the same inclination from the vertical plane of $\sim 0.708°$ as the wheels in the experiment, to ensure that the weight distributions during the position adjustments of the detectors after assembly reflects the real case. The small sector spokes are mounted on the hub and fixed with adjustable supports to the grid (Fig. 9.3 (b)) Once the small sector part of the structure has been completed, the eight alignment bars located in the small sectors are added.

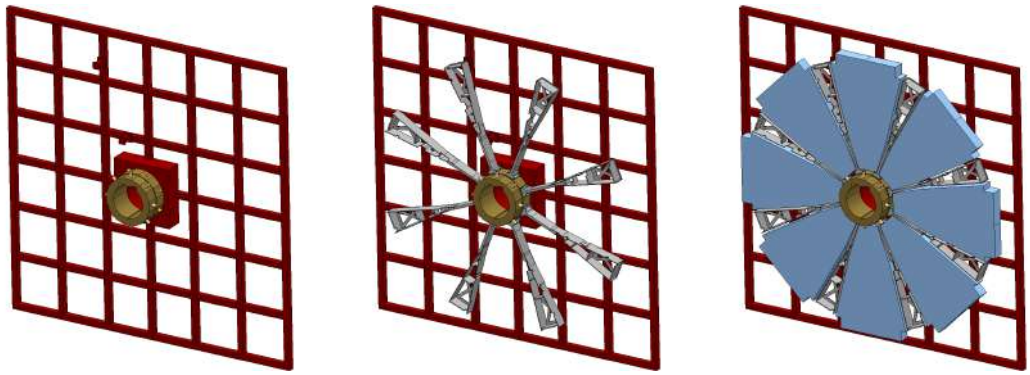

(a) The hub and the spoke mounts are attached to the support grid.

(b) The small sector spokes are added and fixed to the hub and support grid.

(c) The detectors in the large sectors and the alignment bars in the small sectors (not shown) are added.

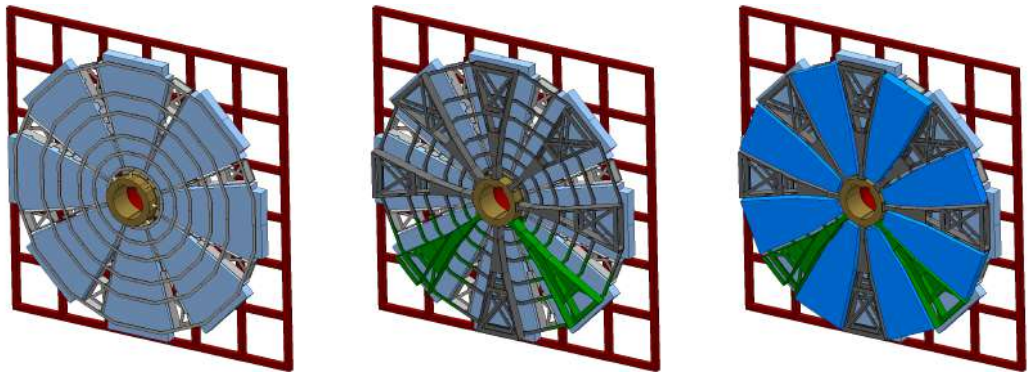

(d) The interconnecting arcs of the central plane of the support are mounted.

(e) The large sector spokes are added and fixed to hub and the arcs of the central plane. The mechanical support structure is now complete.

(f) The detectors in the small sectors and the alignment bars (not shown) in the large sectors are added. The detector wheel has been assembled.

Figure 9.3: A possible scenario for the assembly of the NSW mechanical structure and the integration of the detectors.

The large sector stations are then inserted [1] (Fig. 9.3 (c)). The sector interconnections (Fig. 9.3 (d)) and the large sector spokes (Fig. 9.3 (e)) are then mounted and connected to the existing half of the structure. The small sector stations are installed (Fig. 9.3 (f)), followed by the eight remaining alignment system bars of the large sectors and the services at the rim.

In case the described assembly of the NSW mechanical structure proves to be not feasible for any reason, an alternative scenario has been developed. A flat support table is used on which the NSW structure is assembled in a horizontal position. The table with the attached mechanical structure is then rotated with the help of a crane into an upright position. A cantilever arm,

[1] see Chapter 9.1.3 on the installation procedure

Figure 9.4: The chamber installation tooling used for the assembly of the present SW, the EE, and the EO MDT chambers. It allows the insertion of MDT chambers into vertical support structures. The tooling for the assembly of the NSW will be similar.

supported on one side, is coupled to the table and the structure is moved onto the cantilever. The detector integration can then take place from both sides of the mechanical structure. The use of this backup scenario entails the manufacturing of the support table, while the tooling for integrating the sectors on the mechanical structure remains unchanged.

The time for the assembly of the mechanical structure is estimated to be 5 weeks with a manpower of 3 FTE. This time includes the survey and adjustment, but not the production of the parts (estimated at 10 weeks with 3 FTE).

9.1.3 Integration of the detectors on the New Small Wheel mechanical structure

Once one half of the NSW structure is assembled on the support grid, the detectors of the adjacent sectors are mounted. A tooling similar to the one used for the end-cap MDT chamber installation will be employed, see Fig. 9.4. A sector may be picked up by this tool from the transport frame and rotated to the required angle for the installation in the structure, both, perpendicular to the sector plane and around the horizontal axis to match the $\sim 0.708°$ inclination of the support structure on the hub (see Chapter 9.1.2). An adjustable counter weight balances the tooling with the attached station. The forks of the tooling either grab the station at all four mount points—thus releasing one bearing after the other and to fix it to the structure—or at dedicated points on the MM spacer frame. The counterparts of the station mounts on the NSW structure are adjustable at a range of 20 mm to take into account (and compensate) their position due to the deformation of the structure under load. The deformations of the structure can be measured by photogrammetry, using targets on the mount points. After the second half of the structure has been assembled, the rest of the detectors are installed.

The NSW structure is then detached from its support points on the grid while the hub remains fixed. The structure is now supported as it would be in its final configuration in the experiment on the JD plug. It can deform freely and assumes its final shape. The stations are re-adjusted to match their theoretical positions within the achievable tolerance of 1–2 mm. After the position adjustment of the sectors, the structure is fixed again to the grid with the adjustable supports at their new positions.

A time of 4 weeks with 3 FTE manpower is estimated per wheel for the integration of the detectors and alignment bars in the mechanical structure.

9.1.4 Integration of services on the New Small Wheel mechanical structure

The NSW mechanical structure also carries part of the services required for the operation of the detectors and the alignment system. The other part will be routed on the rim of the JD shielding disk. Services arrive at the detector wheel at five points:

- Two patch panels in sector 1 for the flexible chains containing the gas and cooling pipes;
- two patch panels in sector 9 for the flexible chains containing the optical fibers, the alignment cables, and the HV cables and
- one patch panel in sector 13 to connect the LV cables.

Cable trays will be integrated into the mechanical structure at the outer rim at the middle plane between the small and large sector structure and filled once the necessary structural elements are available and the large sector detectors have been installed. The selected services will be routed from the patch panels around the rim in these cable trays for a maximum distance of half the circumference.

The service routing and access to the connection points of the wedges on the NSW rim is further detailed in Chapter 13. The time estimated for the integration of the services is 2 week per wheel with a manpower of 2 FTE (not including the preparation of the service).

9.1.5 Transport frame

The NSWs have to be transported from their assembly site to SX1 and subsequently lowered into the experimental cavern.

The grid structure used for the assembly of the wheels can be adapted as a transport structure by adding stabilizing parts on the side and the open face, thus resembling a cage. Alternatively, the existing transport frame of the present SW might be modified to accommodate the needs of the NSW. An additional lifting beam might be necessary in order to handle the frame by crane.

The transport and installation of the detector wheels in the experiments is described in Chapter 11.

9.1.6 Integration of the detector wheel with the JD Shielding

The integration of the detector wheel with the JD shielding is similar to the procedure that was used for the original SW. The part of the support structure or the transport frame carrying the hub is linked to the JD plug and the wheel is transferred via a rail onto the plug, see Fig. 9.5. The integration will take place only after the 1-year commissioning phase at the surface to provide the maximum time for access to the detectors. A cantilever arm, supported at its end point, can be used to move the detector wheel to open a gap to the grid structure if needed, similar to the mechanism to transfer the wheel to the JD plug.

The location of the integration with the JD shielding depends on the installation scenario of the NSW in the ATLAS experiment, see chapter 11.

9.1.7 Expected mechanical deformations of the mechanical structure

Definite calculations are not yet available as the FEM analysis will be made when the NSW mechanical structure is close to its final shape and design. Analytical calculations of the current

Figure 9.5: Integration of the detector wheel with the JD shielding in 2007. The wheel is transferred from the support structure (right) to the plug of the JD shielding (left) via a temporary rail (middle). The procedure used for the integration of the new detector wheels with the JD shieldings will be similar but the support structure and rail will differ.

baseline structure show that the overall deformation of the structure ranges between 10 mm and 15 mm, which is compatible with the amount of $x, y,$ and z adjustment range of the detector mounts. The present SW shows comparable deformations which proved to be no problem in neither the integration nor the installation.

9.2 Detector commissioning

To ensure that the NSW is operational immediately after the installation in the experiment, a full 1-year commissioning phase is foreseen at the surface, using cosmic rays to test its full functionality. It is mandatory that all necessary tooling, used during the integration process, is available during the commissioning. Therefore the best commissioning sites would be either the integration site at CERN or SX1.

The necessary infrastructure for the commissioning would include gas systems, power systems, and a DAQ system. Temporary cabling over distances of about 50 m has to be foreseen and cooling of the front-end electronics should be foreseen. This will be less demanding than in the experiment, as power dissipation into the environment can be allowed.

To limit the infrastructure and cost during the commissioning phase, only a smaller part (e.g. a quarter) of each wheel will be used for data taking at the same time. Nevertheless, other services like HV (and gas) would be kept on for as large a part as possible to condition the detectors even if the majority of those detectors are not used for data taking at that moment.

The NSW should be installed as soon as possible in the ATLAS experiment at the beginning of LS2. Full commissioning in-situ may take place once the final services have been connected.

10 Alignment system

10.1 Introduction

As in the present Small Wheel, an optical alignment system will be installed on the new Small Wheel, and be integrated as a part of the end-cap optical alignment system [46].

The current end-cap optical system is an absolute alignment system, meaning that the sensors provide the muon chamber positions at any given time without any external input like e.g. an initial alignment that was obtained (at an earlier time) using tracks. In other words, the alignment system is used as a real-time surveying system.[1] The optical system of the NSW should follow the same principle, i.e. it should again be an absolute system. Reverting to using such a system in relative mode is always possible as a fall-back solution.

Both types of NSW chambers, sTGC and MM, are supposed to be usable for precision track measurements. Therefore, both types will need to be integrated into the optical alignment system – in contrast to the TGC chambers of the current ATLAS detector which are only very loosely coupled to the MDT alignment system.

The optical absolute alignment system of the end-caps is designed such that the positions with respect to each other in the precision coordinate of any three chambers that can be traversed by a muon track can be determined with an accuracy of 40 µm. The position of any single chamber with respect to another one, on the other hand, can be determined only with a much lesser accuracy, around a few hundreds of micrometers.

The key prerequisite for an absolute alignment system is a knowledge at a level of typically 20 µm and 50 µrad of the positions and rotations of the optical sensor elements (CCDs, lenses, light sources) with respect to the active detector elements (wires, strips, etc.) of the chamber they are mounted on, i.e. their positions and rotations in the local chamber coordinate system.

It is often useful to divide this problem into two parts: (1) to determine the positions of the optical elements with respect to a mounting platform on the chamber which the sensor will be mounted on; and (2) to determine the position of this platform with respect to the active detector elements. The two steps are referred to as sensor calibration and mount calibration, respectively, and separating them makes it possible to calibrate sensors at a different place and time from chamber mounts, and to replace damaged or broken sensors during commissioning on surface or during shutdowns in the detector.

10.2 System requirements

The following criteria have to be fulfilled by any design for the NSW chambers:

- The internal geometry of the chamber needs to be under control at a level of about 40 µm while the chamber is being constructed. Internal geometry means the positions of the detector

[1] The opposite would be a relative alignment system, where the sensors are only used to follow chamber movements in time with respect to a set of initial chamber positions determined by a method other than optical sensors. This alignment scheme is used in the muon spectrometer barrel.

elements with respect to each other, both within one chamber layer and between different chamber layers.[2]

- There need to be mechanical objects, e.g. spheres or holes or other marks, on the outside of the assembled chamber that can later be used as a reference for determining the positions of the by then inaccessible active detector elements, or sensor mounts need to be mounted early enough in the chamber assembly process that other marks, e.g. on the assembly table, can be used.
- A procedure needs to be foreseen to measure the positions of the sensor mounts with respect to the reference points, either after the chamber is assembled or during the assembly process. The required accuracy of these sensor mount measurements is around 20 µm and 50 µrad.

In addition to sensors that are sensitive to chamber positions, sensors measuring the mechanical chamber deformations and their thermal and/or humidity expansion will also be required, unless chambers are small enough to neither deform nor expand by any significant (below 20 µm) amount. The in-plane RASNIKs of the MDT chambers may serve as a model; mechanically different chambers may however exhibit different deformation modes.

One important difference between wire chambers (MDT) and planar chambers (MM and sTGC) is that for the former it is sufficient to determine the endpoints of the wires, while for the latter deformations of the entire PCB plane affect the track measurement and thus have to be measured by the alignment system. In MDTs the thermal expansion is measured indirectly by temperature sensors; this is not the only possibility: thermal expansion may also be measured by a length measurement with optical sensors, which actually has the advantage that humidity expansion is measured at the same time too.

Whatever the final arrangement of deformation and expansion sensors is, it must be sufficient to measure all degrees of freedom of a chamber, including, for example, out-of-plane deformations due to gas overpressure in the gas gap.

For what concerns integrating NSW chambers with the existing alignment system, at least eight NSW alignment bars per wheel will be the interface between old and new components. Polar BCAMs, viewing existing other polar BCAMs on other wheels, will provide the positions of the NSW bars with respect to the rest of the end-caps. Azimuthal BCAMs, or equivalent devices, will provide the NSW bar positions with respect to each other within the wheel, and sensors on the NSW chambers will be used to determine chamber positions with respect to alignment bars.

Most of the parameters of the alignment bar geometry may be slightly changed to accommodate the NSW chamber geometry, like the positions of the bars and their diameter and length. One could e.g. consider extending the NSW bars towards smaller radii, and in this way improving the accuracy of the alignment system for chambers in the region currently occupied by CSC chambers, where all sensors are located at the outer edge of the chambers, somewhat limiting the precision near their inner edge.

A few parameters can, however, not be modified: the positions of the NSW polar BCAMs (in global ATLAS coordinates) cannot change, or only by less than about 10 mm in x and y, since the existing polar BCAMs on other wheels are pointing to their current locations, and since there is a

[2] As it turns out, the accuracy of the chamber geometry affects the momentum (sagitta) measurement by different amounts in different layers (EI-EM-EO); the historical 20 µm requirement for MDT chambers was driven by the EM layer which contributes most to the sagitta accuracy. For NSW chambers, being the EI station, this requirement can be relaxed to 40 µm with only a negligible deterioration of the final momentum resolution. Strictly speaking, these 40 µm correspond to the accuracy in the bending direction, i.e. a linear combination of the radial direction and the beam direction in ATLAS. The radial direction being the dominant contribution to the sagitta measurement, the chamber construction accuracy has to be higher in the radial than in the beam direction.

complicated and carefully tuned arrangement of BCAMs along the polar lines to ensure visibility between many different pairs of BCAMs. Note that this does not imply that the alignment bar positions cannot change: keeping a BCAM in place and displacing a bar is always possible by designing a different mounting platform (or extension arm) under the BCAM; arms with lengths up to about 200 mm are currently in use in the end-caps and do not exhibit any particular problems.

The design of the NSW alignment system depends crucially on the chamber layout, more precisely on the question what the 'smallest alignable unit' will be. An alignable unit means a 3-dimensional body whose location in space is defined by the usual six degrees of freedom for position and rotation, plus a reasonably small number of additional parameters describing changes in shape (deformation) and size (thermal or humidity expansion) with respect to the nominal values. In the MDT case, the MDT chamber is the smallest alignable unit – not e.g. the multilayer, since the two multilayers are rigidly connected by the spacer frame, ensuring that they move and deform coherently.

From the alignment system point of view it would be preferable to link (glue or bolt) sTGC and MM quadruplets and wedges in such a way that they move and deform together, in which case an alignment system for aligning a single layer or quadruplet would again be sufficient. This is, however, not the current NSW design. A tentative alignment system layout for independent quadruplets or wedges is presented below. For generality, an alignment scheme for N independent quadruplets in radial direction (so $4N$ quadruplets of MM and sTGC per sector in total) will be discussed. This scheme can accommodate any reasonable value of N; for $N = 1$ it turns into a scheme for independent wedges.

10.3 Alignment system layout

10.3.1 Alignment bars

As shown in Fig. 10.1, in the current layout the eight alignment bars are located in-between the large (EIL) chambers, overlapping in ϕ with the small (EIS) chambers. In such a layout, adding new sensors on the bars that view targets on all the quadruplets at different global z is easy for quadruplets in large sectors, but impossible in small sectors.

A solution is to make the alignment system layout symmetric by doubling the number of alignment bars, adding eight new bars[3] in-between small chambers and overlapping in ϕ with the large chambers. Old/new bars will be refered to as S-bars/L-bars occasionally, where S and L denote their location in small and large sectors, respectively.

These eight new alignment bars in large sectors have to be connected to the polar lines, which are located in small sectors. It is impossible to link them directly, because this would require extension arms of several meters length. Instead, they will be linked indirectly, by connecting with high accuracy (30 µm) the new bars with the old ones. Currently, bars in a wheel are linked by azimuthal lines: each line consists of a pair of BCAMs on two neighboring bars, viewing each other, and there are at least two azimuthal lines between two neighboring bars in a wheel. With this layout, the position of one bar with respect to its neighbor is determined to not better than a few hundreds of micrometers. To reach a higher accuracy, the pairs of azimuthal BCAMs will have to be turned into triplets, with three BCAMs mounted on three neighboring bars (L-S-L and/or S-L-S), and each BCAM in the triplet viewing the other two (Fig. 10.2). This resembles the layout of polar lines, where triplets of BCAMs link e.g. the EI-EM-EO bars in one sector to

[3] 'New bars' means: bars in new places, places where no bars are installed on the current Small Wheel. All bars for the new Small Wheel will be 'new', of course, in the sense that they will be designed, built, and calibrated from scratch.

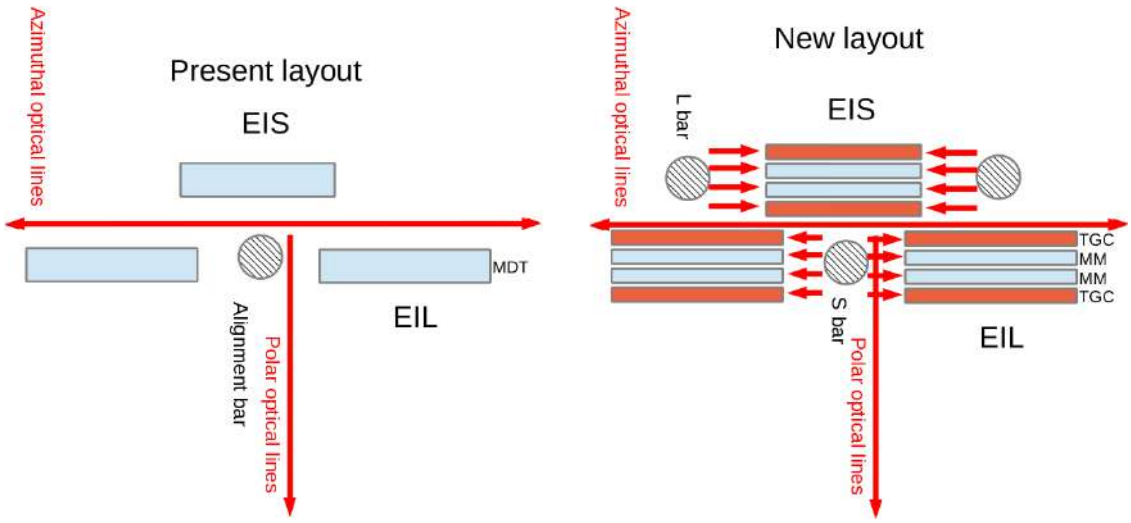

(a) (b)

Figure 10.1: (a): Old layout of alignment bars in a wheel (viewed from the outer rim to the center of the wheel) with alignment bars placed between large chambers, overlapping with small chambers; (b): proposed new layout with alignment bars added between small chambers, overlapping with large chambers.

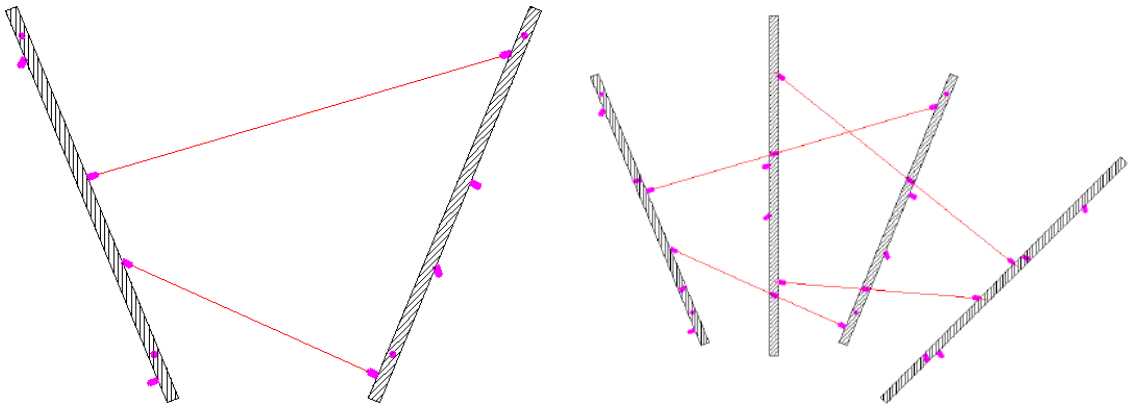

(a) (b)

Figure 10.2: (a): Old layout of the azimuthal system with pairs of BCAMs; (b): layout of the system with eight new alignment bars added on top of the existing eight old ones, using triplets of BCAMs.

each other. In such a layout the position of an L-bar with respect to its two S-bar neighbors (and thus the polar lines) is determined to several tens of micrometers in the precision coordinate.

10.3.2 Chamber deformations

The deformations of the individual quadruplets need to be measured by alignment sensors. The in-plane deformations of planar detectors are expected to be small, but the out-of-plane deformations may be relevant and moreover they have to be determined over the entire surface of the plane.

One possible way to measure quadruplet deformations follows the concept of the MDT in-plane RASNIKs: CCDs, lenses, and RASNIK masks forming a grid of parallel and diagonal RASNIK lines across the quadruplets (Fig. 10.3). The layout could be rotated in the plane by 90° if the resulting locations of CCDs and masks were more desirable.

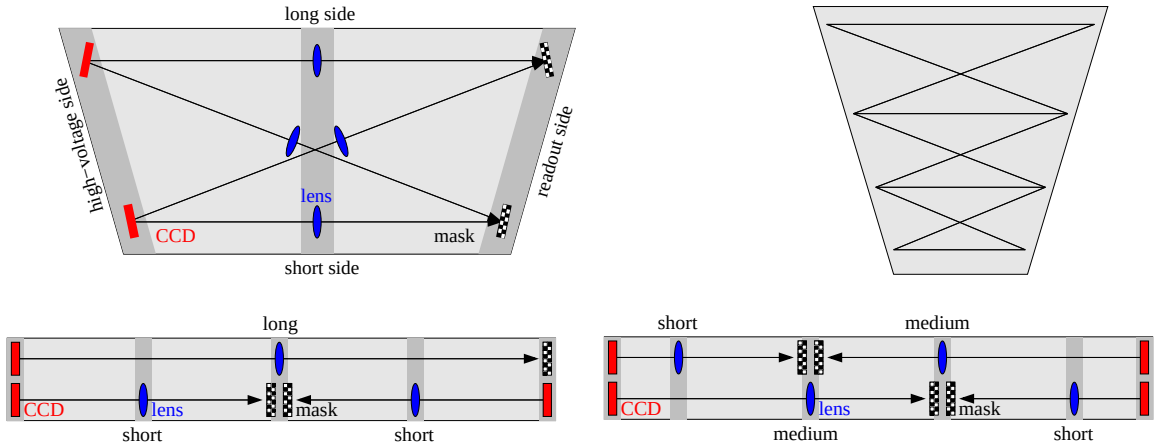

Figure 10.3: Top left: the current layout of the end-cap MDT chamber in-plane RASNIK system. Two CCDs view two RASNIK masks through four lenses, resulting in four measurements of the chamber deformation. Top right: extension of the scheme to a full wedge, at the same time being an option if a closer spacing between elements is required in the radial coordinate. Bottom: a closer spacing between elements in the azimuthal coordinate can be obtained by interleaved RASNIKs, like in the end-cap alignment bars.

The spacing of RASNIK elements needs to be matched to the expected 'wavelength' of the deformations: shorter wavelengths require more elements at shorter distances, so that the interpolation of the deformation in-between elements becomes more accurate. It would be desirable to design detectors such that deformations can be interpolated accurately enough by simple functions like second- or third-order polynomials. This can be achieved by making the detectors as rigid as possible, or by making their mechanical structure sufficiently simple and symmetric, or by a combination of the two.

In the radial direction, varying the spacing between RASNIK elements is trivial, by just compressing the pattern of parallel and diagonal lines and duplicating it multiple times. Along the second coordinate, varying the spacing is done by adding interleaved RASNIKs with different (shorter) CCD-lens-mask distances, where some but not all of the added elements are placed close to already existing ones.

In-plane RASNIK elements would be glued onto the surfaces of quadruplets at the end of the construction process, when the quadruplets are still perfectly flat on a granite table. By reading out all RASNIKs at this time one obtains the 'zero' measurement corresponding to a flat quadruplet. An attractive feature of this scheme is that the RASNIK elements can be glued without high accuracy, at the millimeter level, since the zero measurement serves as a full calibration.

10.3.3 Chamber-to-bar alignment

For linking quadruplets to alignment bars, presumably the easiest solution are cameras on alignment bars viewing targets (point-like light sources, e.g. laser diodes, or RASNIK masks) mounted for instance, but not necessarily, near the four quadruplet corners, either on the quadruplet surface or on the side faces. Cameras on L-bars view targets on small chambers, and cameras on S-bars view targets on large chambers (Fig. 10.4a).

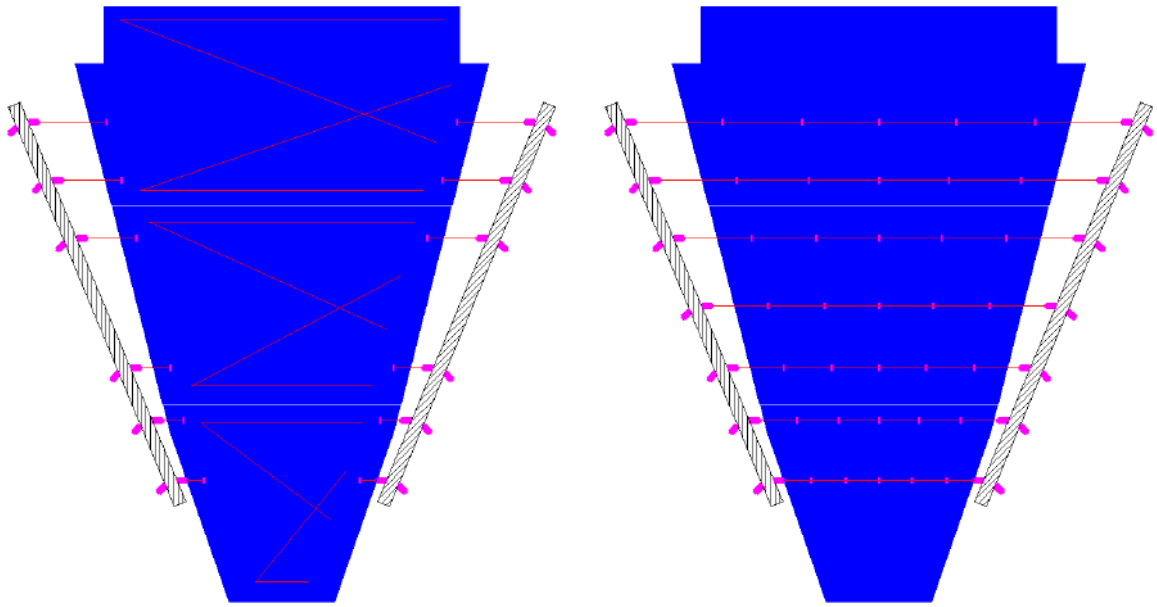

(a) (b)

Figure 10.4: (a): Conceptual layout of the chamber-to-bar alignment in the option of a dedicated in-plane RASNIK system monitoring chamber deformations; (b): layout in the option with additional light sources on the chambers, integrating chamber-to-bar alignment with chamber deformation monitoring.

The quadruplet at the smallest radius has to overlap in radial direction with the alignment bars over at least a third, better one half of its radial size in order to give sufficient lever arm to the alignment sensors linking the quadruplet to the bars. A variation of this scheme is to distribute additional light sources across the surface of each quadruplet, with each camera now viewing several such sources on a line, as well as a partner camera on the next bar. In such a scheme the added light sources can be used to measure quadruplet deformations in addition to positions, making a dedicated in-plane RASNIK system unnecessary (Fig. 10.4b).

A potential challenge here is the calibration of the added light sources – the position of each light source with respect to the active detector elements needs to be determined with high accuracy, which may be difficult to achieve all across the quadruplet surface. Another complication is that this variation of the scheme requires the alignment bars to cover the full length of the NSW chambers in the radial direction. Extending alignment bars towards smaller radii (compared to the existing ones) is difficult because of the space needed by the bars. A hybrid of in-plane RASNIKs at small radii and on-quadruplet light sources at larger radii could solve this problem.

10.4 Alignment sensors

From the layout studies performed so far it seems that the sensor size will be an important issue, in particular in layouts with floating quadruplets or wedges: there is very little space foreseen between chambers. While optical sensors can, a priori, be built to rather small size, the sensor mount will at some point become a limiting factor: for e.g. a 3-ball mount to be reasonably robust, the balls must have some minimal diameter and spacing, otherwise even a mild shock to the sensor will cause the balls to make dents in the sensor mounting surfaces, thus destroying the calibration. If this is perceived as an unacceptable limitation, the concept of mounting sensors on sensor mounts, rather than gluing them directly on chambers, may have to be abandoned.

Another important issue is radiation hardness. For radiation (and other) reasons, the CSC sensors in the current Small Wheel are located at the outermost radius of the CSCs, and the inner endpoint of the alignment bars is at that same radius. Radiation levels on the NSW will be much higher, making it challenging to put sensors in this region.

A cheap and versatile way to make light sources effectively radiation-hard is to position the actual source of light, e.g. an LED or a laser diode, in a low-radiation region and to use radiation-hard optical fibers to transmit the light from there to the high-radiation region where the alignment sensor light source is located.

10.5 Data acquisition and analysis

The NSW alignment sensors will be read out by the existing long-wire data acquisition (LWDAQ) system of the end-cap alignment sensors. Some components (on-sensor electronics and multiplexers) will have to be radiation-hardened. Compatibility between the current and the new LWDAQ components is a requirement since some sensors (polar BCAMs) will have to be read out in combinations between current and new versions: e.g. a polar BCAM on an NSW alignment bar taking an image of another polar BCAM on an EM or EO bar, and vice versa.

10.6 Alignment performance

Any alignment system design has to be validated by Monte Carlo simulations, using e.g. the alignment reconstruction and simulation software used in the ATLAS muon end-caps, ARAMyS. The simulation starts from an implementation of the foreseen network of sensors. Sensor readout values are computed as the expected measurements for nominal positions of all chambers, and are randomly smeared by an amount that reflects the intrinsic resolution and mounting accuracy of the individual sensor. The alignment is then reconstructed by using these simulated measurements, and a figure of merit is computed from the difference between true (nominal) and reconstructed chamber positions. For the ATLAS muon spectrometer, the figure of merit is the width of the false sagitta distribution (the false sagitta is the reconstructed deviation from straightness of a straight truth track traversing a triplet of MDT chambers). The ARAMyS simulation of the current end-cap geometry predicts a mildly position-dependent false sagitta width in the range of 30–55 µm over the full end-cap, in line with the original 40 µm specification. A well-designed alignment system layout for the NSW should have a similar performance. Another aspect to be verified by simulations is redundancy, i.e. how the performance degrades when single alignment sensors break. Graceful degradation is a required feature of a well-designed system.

11 Installation sequence and procedures in the ATLAS experiment

The installation of the NSWs will be based on the procedures [47] and the experience gained with the original SWs.

11.1 Factors affecting the installation procedure

The installation procedure of the NSWs is subject to several constraints.

1. **Safety**: The JD shielding, especially the inner part of the plug shielding around the beam pipe, and the detector material will be activated from the previous LHC run. Radiation-protection measures have to be taken to minimize the exposure of personnel working on and around the shielding and the old detectors.
2. **Space**: Temporary storage space for the NSW has to be available at the surface hall SX1. Contrary to the situation at the time of the installation of the original SWs, the buffer zone in the middle of the hall will not be free, but will be mostly blocked by elements of the forward shielding of the ATLAS experiment. This not only affects the temporary storage of the NSW in SX1, but also the installation of the NSW on side A, which has to pass from the entrance area on side C through the buffer zone to the shaft on side A.

   After the original SWs have been dismantled, the old detector wheels, trigger chambers, and services have to be stored as a backup at least until the full functionality of the NSW has been proven after their installation in the experiment.
3. **Weight**: The weight of the detector wheels will increase from about 17 t to 25–30 t. This poses no problem if only the detector wheels have to be lowered into the experiment. However, together with the JD shielding and the lifting frame the weight of a complete NSW will be around 150 t, well above the load limit of 140 t of a single hook of the bridge crane in SX1. While the possibility exists to link the two 140 t hooks of the crane for the lowering of a NSW into the cavern, this severely limits the accessible area underground (see Fig. 11.1), making the operation extremely difficult as several steps are necessary to navigate around obstacles like shielding or other detector parts with clearances of only about 30 cm, compare [48, 49].
4. **Time**: The shutdown period LS2—in which the NSW will be installed—is foreseen to last only about 12 month. An optimized schedule has to be prepared to quickly de-install the present SW at the beginning of the shutdown and install the NSW in the experiment as soon as possible to maximize the time for their final commissioning.

   Blocking resources in UX15 and SX1 for extended periods of time will affect other upgrade projects.

In view of the limiting factors several installation scenarios have been developed.

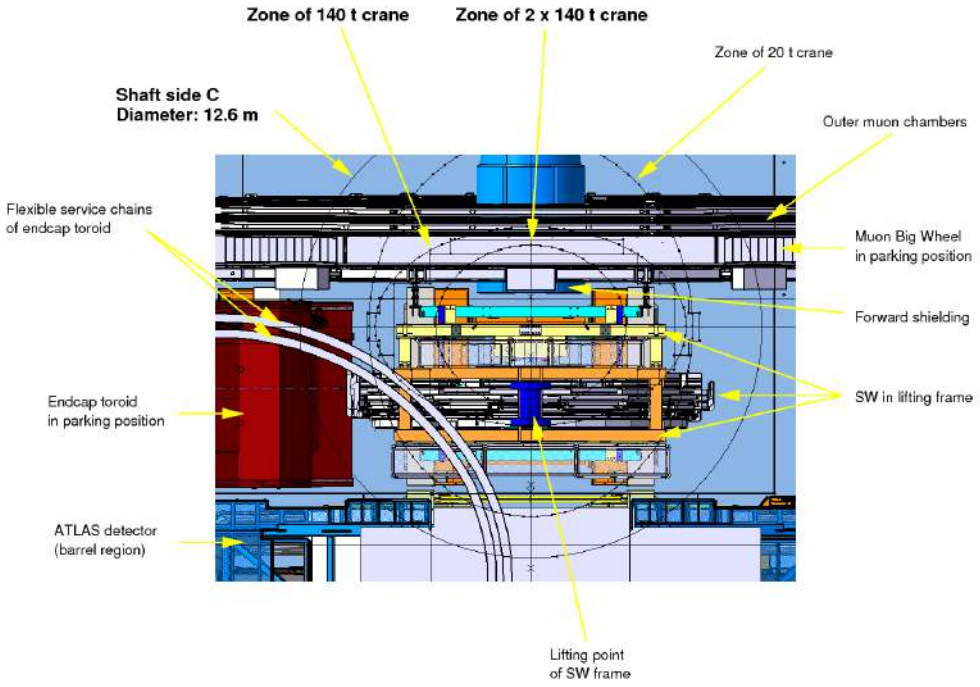

Figure 11.1: Accessible area of the surface cranes in SX1 in the underground cavern UX15.

Table 11.1: Expected dose rates at different positions in the vicinity of the SW at the beginning of LS2 in 2017. A cool-down time of 56 days is assumed. Upright numbers: closed configuration with the detector wheel adjacent to the JD disk. Boldface numbers: open configuration with the detector wheel at 100 cmdistance to the JD disk. Negative numbers denote distances from the IP side, positive from the HO side. All distances are given in cm, all dose rates in µSv/h.

Radial distance	Distance to detectors											
from plug	-100		-50		-0		+0		40		100	
0	—	**20**	—	**14**	—	**8**	12	**9**	8	**3**	7	**1**
40	—	**3**	—	**0.1**	—	**3**	2	**11**	2	**3**	2	**1**
100	—	**0.2**	—	**0.3**	—	**1**	1	**7**	1	**4**	1	**2**
>100	—	**<1**	—	**<1**	—	**<1**	<1	**<2**	<1	**<2**	<1	**<2**
Radial distance	Distance to face of JD plug											
from beam pipe	-100		-40		-0		+0		40		100	
0	65		116		706		378		62		11	

11.2 De-installation and dis-assembly of the present Small Wheels

In order be able to re-use the JD shielding, the present SW detectors have to be removed first; this includes not only the detector wheel but the TGC trigger detectors and all services mounted directly on the shielding disk as well. The present SW should therefore be de-installed at the beginning of the LS2, once the end-cap toroids have been moved from the beam line to their parking positions and the beam pipe has been opened.

The expected radiation dose rates in the vicinity of the SWs at the beginning of LS2 have

been simulated—with the beam pipe and end-cap toroid removed, and the end-cap calorimeter at a distance of 120 cm from the IP side of the JD disk—for an assumed cool-down time of 56 days. The simulation has been validated with the currently available measurements. The results a summarized in Table 11.1. The grid points are defined as follows: negative distances are measured from the IP side of the detector wheel (located at -0 cm) to the JD disk (at -100 cm). Positive distances are measured from the HO side of the detector wheel (at +0 cm). Radial distances are always measured from the surface of the plug (at 0 cm). The last row in Table 11.1 lists the expected dose rates on the IP and HO side of the JD plug faces, measured from the surface of the plug at the height of the beam line.

The problematic areas are the two faces of the JD plug close to the beam line, which a highly activated. The expected dose rates reach about 400–700 μSv/h at contact and are still high up to distance of about 1 m. For work around the JD plug or for a transport of the SWs, the bores should be shielded by additional plates, as it was done for the lifting of the SW of side C in LS1. The rest of the surface of the shielding shows no high activation and can be declared as a supervised or a simple controlled area, according to the CERN rules [50]. Of the detector wheel, only the hub is activated, but the expected dose rates at contact are below 15 μSv/h, allowing again the declaration as only a supervised zone.

The de-installation and dis-assembly will follow the ALARA principle and radiation-protection recommendations.

Three different de-installation scenarios can be envisaged:

1. The detector wheels of the SWs are decoupled from the JD shieldings in UX15. The JD shielding remains in UX15.
2. The two SWs are lifted to the surface, the JD shieldings then remains at SX1.
3. The two SWs are transported to the NSW assembly site and di-assembled there.

For the scenarios 2 and 3, a procedure has been defined and partial experience has been gained by the lifting of the SW of side C to the surface at the beginning of LS1 in 2013 [49].

All scenarios require the construction of new storage and transport frames for the SW detector wheels. For the first scenario it might be necessary to build a new lifting tool if the present one cannot be adapted to handle only the detector wheel.

Scenario 1 is the preferred scenario, but requires time-consuming operations in UX15 which might be incompatible with the schedule of the LS2 shutdown. The decoupling of a detector wheel from the JD shielding has never been attempted underground. In addition, the limited space around the SW will require special access platforms to be manufactured for the removal of the services.

Scenario 2 suffers from possible space constraints in SX1. Scenarios 3 has the disadvantage that a large mass of activated material has to be transported through public space. The radiation of the plug surfaces can be reduced with additional shielding during a transport. As the plug will be at a height of at least 6 m [47], the dose rates at ground level should then be negligible. The risk of contamination of the environment in the case of an accident during the transport is almost non-existent, as the activated material consists of solid pieces of metal and form a single object.

The MDT/CSC detector wheel has to be separated from the JD shielding and transferred to the transport and storage frames. The procedure would be similar, but reverse, to the one used in the assembly of the SW detectors with the JD shielding. A cantilever rail couples the JD plug to the frame and the detector wheel is then transferred (see e.g. [51] for the principle of operation). Once the detector wheels have been removed, the TGC detectors mounted on the JD disk, and remaining services and cable trays on the rim of the shielding can then be dismantled.

11.3 Modifications of the JD shielding

The conical shielding in the CSC region of the JD disk has to be replaced by a new disk-shaped shielding to follow the planar detector geometry. No major difficulties are foreseen for this work as the conical shielding consists of several petals which are fixed with screws to the JD disk and the activation is low with an expected maximum dose rate of <15 µSv at contact (after 56 days of cool down). In addition, modifications of the two rails of the JD plug—on which the hub of the NSW moves—might be necessary due to the increased weight of the new detector wheels. An exchange of the rails against a reinforced type is possible without machining. The expected dose rates on the surface of the JD plug are below <20 µSv at contact (after 56 days cool-down) and the cool-down time can be increased to at least 100 days before the work. The maintenance scenario of the NSW involves the coupling of a pair of extension rails to the JD plug to be able to open a gap between the detector wheel and the shielding disk (see Chapter 14). No modification of the plug is necessary for this arrangement as existing holes on the plug face can be used to guide and attach the required extensions.

11.4 Transport to Point 1

The transport of a single wheel from the assembly site at CERN to SX1 will be similar to the transport of an original SW [47], using two trucks with a special heavy load trailer. The wheel will be protected by a tent-like structure during the transport which can be heated by fans if necessary. The NSW is unloaded from the trailer at the C side of the SX1 hall. To illustrate the procedure, figures 11.2 shows the transport of one of the present Small Wheels in 2008 from its assembly site, building 191 at CERN, to the ATLAS surface hall SX1.

The unloading procedure of the NSWs from the trailer will be similar to that of the original SWs [47, 52], using special hydraulics as the crane in SX1 does not have the necessary clearance in height. The crane will only be able to pick up a NSW once it has been maneuvered into a special trench in SX1.

After unloading, the NSW can be either stored temporarily between the entrance and the shaft on side C or in the buffer zone in the middle of the hall (Fig. 11.2 (d)). The storage in the buffer zone might not be possible in 2018, depending on its use for other material at that time.

Before being lowered into the underground cavern, the NSW has to be rotated around the vertical axis to be aligned for its position in the experiment. A rotation in UX15 itself is impossible due to the limited space. In case both 140 t hooks of the crane in SX1 are necessary for manipulating a NSW due to its weight, a rotation around the vertical axis on the crane is not possible due to the geometrical position of the hooks. This implies that the buffer zone has to be cleared before the NSW of side A can traverse it, as the full width is then needed. Otherwise, with only one 140 t hook, a rotation of the NSW above the shaft of side A is possible and the NSW can pass the buffer zone if a path along the middle has been cleared.

11.5 Installation scenarios

The installation scenario to be used depends on the location of the JD shieldings. As described in Chapter 11.2 above, there are three possible locations, UX15, SX1, and the NSW assembly site.

The next sections describe a scenario for each of these cases[1]. After an NSW has been lowered

[1] The first scenario is strongly preferred considering the limitations imposed by having to use both 140 t crane hooks for the other two scenarios due to the weight of the assembly of the JD shielding with the detector wheel.

(a) Loading of a Small Wheel

(b) Transport to Point 1.

(c) Arrival at the ATLAS surface hall SX1.

(d) Temporary storage of one of the Small Wheels in the buffer zone.

Figure 11.2: Transport of the present Small Wheel from the assembly site (building 191 at CERN) to the ATLAS surface hall SX1 in 2008.

onto the HF truck and in case of the first scenario has been integrated with the JD shielding, it is moved onto the barrel rails inside the ATLAS detector and is connected to the flexible chains and other services. The commissioning of the NSW in the experiment can then start.

Scenario 1 – JD shielding in UX15: The NSW will be lowered into the experimental cavern within its transport and support frame using one 140 t crane. The frame is positioned on the HF truck and is secured to the rails. The front face of the frame facing towards the IP is then removed. All mounts fixing the detector wheel on the support structure are released and the wheel is only supported by the hub sitting on the stub of the support frame. The JD shielding is moved towards the detector wheel, the JD plug is mated to the stub carrying the hub, and the detector wheel is transferred to the JD plug.

Scenario 2 – JD shielding in SX1: The scenario to transfer the detector wheel from the transport and support frame to the JD plug is similar to scenario 1. Contrary to that scenario the transfer takes place at the surface in SX1. To align the JD shielding and the detector wheel in the transport frame a rail system on part of the floor of SX1 and a smooth surface layer on top of the concrete is necessary so that the airpad system to move the JD shielding can be used. After the transfer, the transport frame is removed and is replaced by a lifting frame (whether the current lifting tooling has enough safety margin to be used with the NSW has to be determined). The completed NSW is then lowered onto the HF truck in UX15 using both 140 t cranes in SX1.

Scenario 3 – JD shielding at the assembly site: The complete NSW (detector wheel and JD shielding) is assembled and then transported to SX1. The buffer zone in the middle of SX1

(a) A SW being picked up by the overhead crane at the surface in SX1.

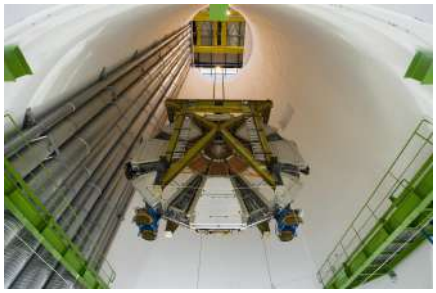

(b) Lowering of the SW in one of the two the access shafts to UX15.

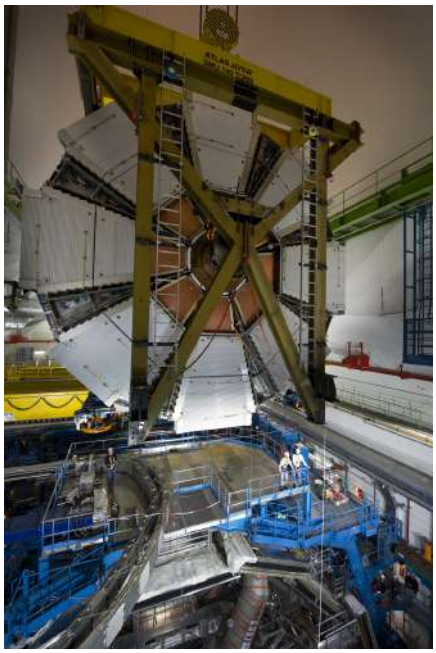

(c) Arrival in the experimental cavern. At the bottom, part of the ATLAS detector is visible.

(d) Positioning of the SW on the HF-truck. The truck connects to the ATLAS barrel rail system.

Figure 11.3: Installation of the present Small Wheels in the ATLAS detector in 2008.

has to be cleared for the installation of the wheel of side A. The NSW is lowered in its transport frame (whether the current lifting tooling has enough safety margin to be used with the NSW has to be determined) onto the HF truck in UX15 using both 140 t cranes in SX1. The transport frame is then removed.

The process of lowering the NSW into the experimental cavern will be very similar—albeit using a different or modified transport frame for the new wheels—to the installation of the present SW in 2008. Figure 11.3 shows the lowering of a SW from the surface at SX1 to the truck connecting to the ATLAS barrel rail system in UX15. The wheel is subsequently moved on the rails to its final position inside the ATLAS detector.

12 Trigger, data acquisition and detector control

12.1 System overview

The NSW trigger will enable to drastically reduce the trigger rate in the end-cap by reducing fake triggers coming from non-pointing tracks, as shown in Fig. 12.1. The trigger is based on track segments produced online by the sTGC and MM detector. The NSW trigger system provides candidate muon track segments to the new TGC Sector Logic which uses them to corroborate trigger candidates from the Big Wheel TGC chambers. The Sector Logic then sends Level-1 trigger candidates to the ATLAS Muon Central Trigger logic.

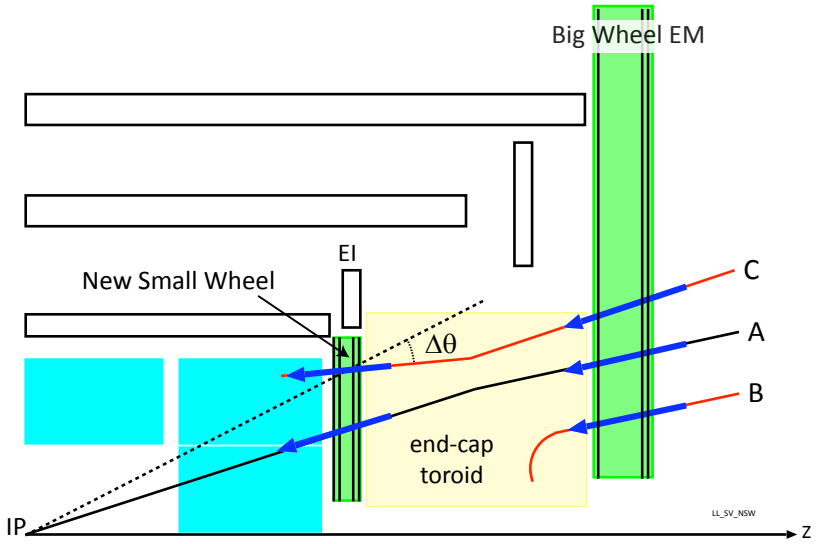

Figure 12.1: Schematic of the Muon End-cap trigger. The existing Big Wheel trigger accepts all three tracks shown. With the NSW enhancement of the Muon End-cap trigger only track 'A', the desired track, which is confirmed by both the Big Wheel and the New Small Wheel, will be accepted. Track 'B' will be rejected because the NSW does not find a track coming from the interaction that matches the Big Wheel candidate. 'C' will be rejected because the NSW track does not point to the interaction point. The NSW logic requires that $\Delta\theta$ be less than ± 7 mrad.

Table 12.1 summarizes some sTGC and MM parameters. The NSW measures the radial coordinate in two planes, the azimuthal, ϕ, coordinate and the angle $\Delta\theta$ of track segments inside the wheel. $\Delta\theta$ is the angle of the segment with respect to an 'infinite momentum track', i.e. a line from the interaction point to the segment's radial position in the NSW. The radial coordinate is measured by high precision strips. For sTGC, ϕ is determined by the triggering tower of sTGC pads and for MM, by small angle stereo strips. The angle $\Delta\theta$ inside the Small Wheel, i.e. before the end-cap toroid, is measured to an accuracy of <1 mrad by calculating the track position in

two virtual planes within the NSW. Corroboration with the Big Wheel is done by projecting the 'infinite momentum track' through the R-ϕ point of the segment in the NSW onto the Big Wheel's R-ϕ array of Regions-of-Interest (RoI).The Sector Logic attempts to match this projected point to an active RoI in the Big Wheel. Confirmed hits become Level-1 candidates sent to the Muon Central Trigger Interface. The NSW trigger logic rejects track segments with $\Delta\theta > \pm 7.5$ mrad.

For sTGC, each of the two radial coordinates is calculated by averaging up to four centroids of strip signals from four sTGC detectors in each multi-layer. The centroids are calculated by the sum of strip charges weighted by position. The azimuthal coordinate, ϕ, is defined by the pad tower that provided the sTGC trigger. For MM, the 0.5 mm strip pitch allows the use of the strip address of the earliest arriving hit within one front-end ASIC in a given bunch crossing to obtain the radial coordinate with sufficient resolution in each plane to calculate a position and polar angle. The ϕ coordinate is obtained by a lookup table addressed by the strip addresses of two small angle stereo views. A stereo angle of just 3° is sufficient to determine the ϕ coordinate with the required precision.

Table 12.1: Some sTGC and MM parameters

	sTGC	MM
strip width	3.2mm	0.5mm
strips/layer	∼1050	8,192
strips/octant	17,260	131,072
triggering pads/octant at $\|\eta\|$ <2.4	2,362	–
All pads/octant	2,738	–
wires/octant	736	–
channels/octant	20,734	131,072
channels/two end-caps	331,744	2,097,152
VMM chips/octant	384	2,048
MM trigger elements	–	32,768

The angle $\Delta\theta$ is passed to the Sector Logic, but is not used in Phase-I. In Phase-II, the Big Wheel trigger will measure the angle of the track in the Big Wheel with better precision, which, in combination with the precision angle measurement in the NSW, will improve the trigger p_{T} threshold sharpness.

The sTGC NSW trigger logic uses pad tower triggers to drastically reduce the amount of sTGC data to be processed on each bunch crossing for the Level-1 trigger (a factor of 60 to 100). Three-out-of-four coincidences are made in pad towers, separately in the pivot and confirmation quadruplets; these are then combined to choose a band of strips in each of the eight sTGC layers to be read out into the trigger processors in USA15. The details are described in Section 12.3.1.

There are no plans to use the wires in the sTGC trigger, but they are read out in response to a Level-1 Accept and are therefore available to the Level-2 trigger. Only the outer two modules have wire readout. For the inner, the pad segmentation provides a fine enough ϕ coordinate.

The NSW electronics has several difficult overall constraints: For Phase-I, the trigger processing must be completed in 1025 ns from the interaction time (including 450 ns for fibre to USA15) to be in time with the Big Wheel signals at the Sector Logic. Phase-II will allow a longer latency. The front-end electronics must be actively cooled so power consumption must be minimized. Access to the front-end electronics after installation is extremely limited. Electronics on the wheel rim is more accessible, however space for cables to the rim is limited. The front-end electronics must withstand moderate radiation and operate in a magnetic field. Use of FPGAs is possible only on the rim and only if SEU mitigation techniques are employed. All NSW TDAQ systems must be compatible with Phase-II.

12.1.1 Background radiation and radiation tolerance

The background radiation levels at the NSW, although not as high as those encountered in the Inner Tracker, are sufficiently high that they affect the design of the on-detector electronics as well as the choice and radiation certification of custom and off-the-shelf components (COTS).

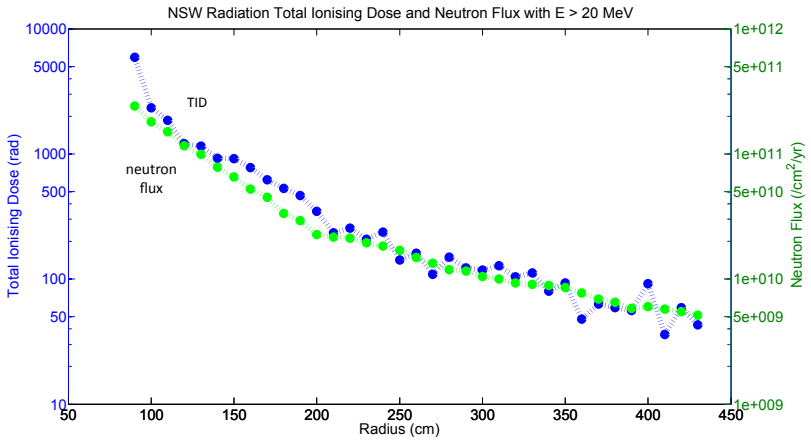

Figure 12.2: Total, per year, Ionizing Dose (TID) and neutron fluence ($E > 20\,\text{MeV}$) vs. radius at the NSW for luminosity 10^{34} (from the 2005 Radiation Task Force Summary report)

Fig. 2.2(a) shows the incoherent background rate in the cavern at the NSW. Fig. 12.2 shows the Total Ionizing Dose (TID) and the fluence of neutrons with energy greater than 20 MeV for luminosity 10^{34} and for one year of LHC operation. Extrapolating to the expected luminosity of 5×10^{34} and for 10 years of operation, the TID at the highest pseudo-rapidity region of the NSW will be of the order of 0.5 Mrad (with some uncertainty factored in). Modern deep sub-micron CMOS processes are generally sufficiently radiation tolerant at such levels. Nevertheless a radiation certification program of the VMM and the companion ASICs is planned using the ^{60}Co source at Brookhaven National Laboratory. The single event effects (SEE) induced by energetic neutrons are of greater concern, especially since they preclude placing most common FPGAs on-chamber. The VMM front-end ASIC as well as the custom companion ASICs will include SEE mitigation features. A certification program using suitable hadron sources is also planned for all custom and COTS components.

12.2 Shared building blocks

Wherever possible the two technologies, sTGC and MM, use the same building blocks to construct their systems. This section describes these building blocks. The details of their use are described in the dedicated sTGC and MM trigger sections below. The readout system is the most unified and Section 12.4 describes the system used for both.

12.2.1 Front-end readout ASIC

In the fall of 2009 an effort was launched to develop a custom front-end Application Specific Integrated Circuit (ASIC) that could be used to read both the sTGC and the MM detectors of the ATLAS new Small Wheels (NSW). The ASIC is named "VMM". Both NSW detectors require precision amplitude measurement for position determination by charge interpolation.

In addition, in order to mitigate the deterioration of the spatial resolution for inclined tracks in the MM technology these detectors will be operated as a so-called μTPC where the track is reconstructed by measuring the drift time of charges arriving on individual strips as is done in large Time Projection Chambers (TPC). Therefore, time measurement with precision of 2 ns, in addition to the amplitude measurement, is needed. The ASIC provides both.

The ASIC provides the peak amplitude and time with respect to the bunch crossing clock, or other trigger signal, in a data driven mode. Fig. 12.3 shows a block diagram of the 64 channel VMM. Each channel is equipped with a fast comparator with an individually adjustable threshold. When a signal crosses a set threshold a peak detection circuit is enabled. Neighbour-enable logic allows setting the threshold relatively high and yet recording very small amplitudes. At the peak, a time-to-amplitude converter is started and then stopped by the next bunch crossing. The two amplitudes are digitized and stored in a de-randomizing buffer and read out serially with a smart token passing scheme that only reads out the amplitude, timing, and addresses of the active channels, thus dramatically reducing the data bandwidth required and resulting in a very simple readout architecture. Sufficient memory is provided to store the expected number of hits in the 20 µs Phase-II latency. See [53] and [54] for more information.

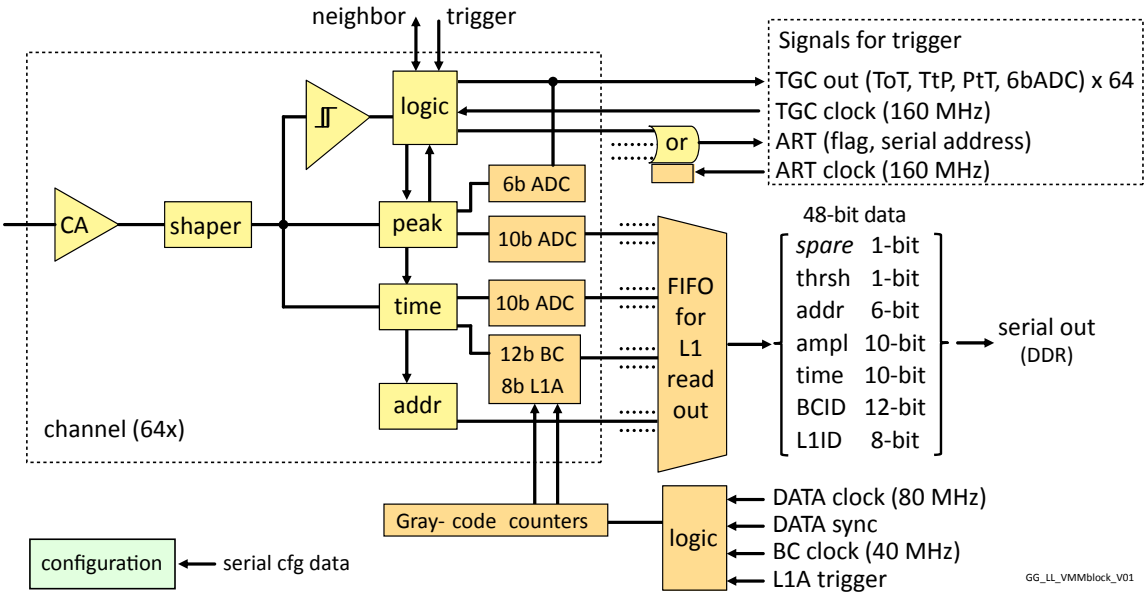

Figure 12.3: Block diagram of the VMM ASIC

Much of the functionality of the VMM front-end needed for the two detector technologies is identical. Thus the same firmware and software for the readout and control of the ASICs can be used. The differences are primarily in the trigger-related primitives provided by the VMM. The following features are required specifically for the MM technology:

- The trigger primitive is provided by the 6-bit address of the hit with the earliest arrival time in the chip within a given bunch crossing. This address is output as a serial differential LVDS stream clocked by both phases of a 160 MHz clock. The stream consists of a flag bit sent at the time of the amplitude peak followed by the 6-bit address.
- The time of the amplitude peak with respect to the event BC is recorded in order to use the µTPC mode of operation of the MM detectors for the offline track reconstruction.

The features required specifically for the sTGC are:

- 6-bit flash ADC value of the channel peak value: for strips, one LVDS output per channel: This value is output as a serial stream clocked by both phases of a 160 MHz clock. The stream consists of a flag bit followed by the 6-bit ADC value. The value is used by the trigger processor to calculate the centroid of the strips for a precision coordinate of the track.
- Time-over-Threshold: for pads, one LVDS output per channel (the same line as used for the flash ADC value): This pulse is latched externally by the next BC and the pad signal

is assigned to that BC for use in the pad tower trigger. A timing edge at the peak is also available, it has less time walk, but longer latency.

The ASIC is designed in the radiation tolerant IBM 130 nm process. In addition to the main properties mentioned above it includes a plethora of features that significantly increase its versatility. These include selectable polarity, gain (0.5, 1.0, 3.0, 9.0 mV/fC), integration time (25, 50, 100, 200 ns), adjustable maximum drift time measurement (150, 250, 500, 1000 ns) and individually adjustable thresholds. The first design was completed and submitted for fabrication in November 2011. Prototypes were received in mid-March 2012. This first version included all the analog circuitry and sufficient configuration, readout, and control logic to be successfully used by both sTGC and MM in beam and cosmic ray tests. All essential features work with relatively minor issues to be addressed in the next version. In addition, extensive lab tests were done. Fig. 12.4 shows pileup and the double pulse resolution of VMM1.

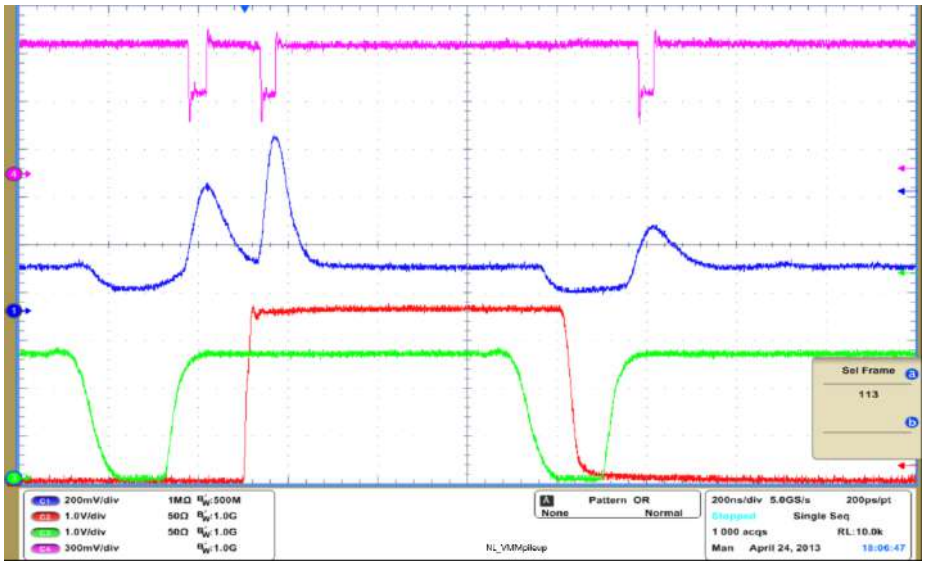

Figure 12.4: Example of pileup and the resolution of the VMM Threshold-to-Peak logic output. Detector wires were pulsed via a capacitor by two unsynchronized pulsers, 300 kHz and 1 MHz, bottom traces (2) and (3). The middle trace (1) is the VMM analog output; the top trace (4) is the TtP output. The TtP pulses are about 30 ns wide.

Some subtle problems were identified (e.g. stability at large capacitance that affects peaking time and gain) which are also being addressed by the second prototype. For more details of these tests and all identified issues, see [55].

VMM Calibration

The CMOS VMM ASIC inherently has small channel-to-channel variations. Accurately calculating centroids requires knowing the relative (neighbouring channels) gain to <2%. The VMM's built-in calibration capacitors and programmable pulser system enables such a calibration. For MM the critical calibration is time, not amplitude. This can also be calibrated using the built-in pulser. Channel thresholds should be calibrated accurately in order to be set just above the noise. To ensure the discriminator fires at the same threshold for all channels, each individual channel threshold can be trimmed by approximately 0–15 mV. Procedures have been developed and successfully performed in test beam to calibrate the VMM ASIC.

12.2.2 GBT, SCA, TTC and optical-electrical converters

High speed serial data transmission has become the norm in data acquisition systems of HEP experiments following the development of commercial high-speed serial protocols such as PCIexpress, 10G Ethernet, Infiniband, etc. Serializers and deserializers are the key components of such systems. Off the shelf components (COTS) are typically not sufficiently radiation resistant and, in particular, quite susceptible to single event upsets (SEU) caused by energetic ($E > 20\,MeV$) hadrons. For this reason the CERN microelectronics group has been developing a radiation hard chipset, the GigaBit Transceiver (GBT) [56]. The GBT chipset consists of a 4.8 Gb/s serializer/deserializer ASIC, a versatile optical transceiver along with a laser driver IC and a pin diode receiver IC and a Slow Controls Adaptor (SCA). This separation of functions allows different combinations of transceivers, optical drivers, laser sources, and photodiodes to be used according to the needs of a particular application. Event data, Timing, Trigger and Control signals, front-end configuration, and DCS data can be exchanged via a single fibre pair between the front-end and USA15 using the GBT. It is assumed that the USA15 end is implemented in an FPGA rather than a GBT ASIC.

Gigabit transmission (GBT) ASIC The GBT can be viewed as multiplexing a number of serial links, called e-links, with 80, 160, or 320 Mb/s rates onto one fibre by transferring 2, 4, or 8 bits per e-link via an 80-bit word (optionally 116 bits) every 25 ns, for an aggregate GBT bandwidth of 3.2 Gb/s. The e-links, consisting of serial in, serial out and clock lines, can directly connect to other ASICs.

Slow Control Adapter (SCA) ASIC The Slow Control Adapter (SCA) ASIC [57], as shown in Fig. 12.5, provides an interface to several protocols needed for front-end configuration and monitoring. Both MM and sTGC place an SCA on each front-end board. Although this results in a substantial number of SCAs, it is far more reliable, more compact and less expensive than connectors and cables to a more central location.

TTC distribution Any e-link can be used to send TTC information since the GBT clock is the BC clock. Either the raw TTC A and B channels in a 2-bit wide e-link, or decoded TTC signals in a wider e-link can be sent. The destination chip must determine the alignment of the

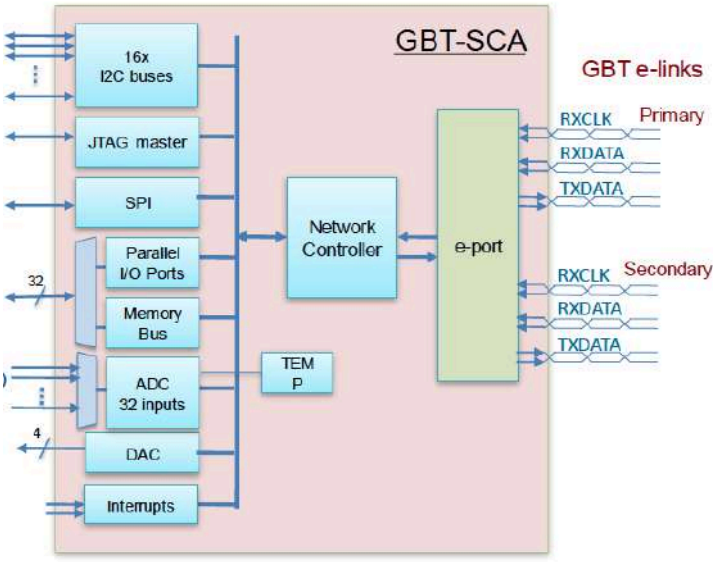

Figure 12.5: Block diagram of the SCA ASIC (Slow Control Adapter)

e-link bits to the 40 MHz beam crossing clock. The GBTx does provide eight external user clocks with programmable frequency and phase.

Electro-optical converter The Versatile Link Project [58] has produced a family of radiation tolerant, 5 Gb/s electro-optical components for the on-detector part of LHC experiments. Two form factors are available: a transmit–receive pair used for the readout and a dual transmitter used by the trigger.

12.2.3 Front-end companion ASIC

Both MM and sTGC require 'companion' ASICs near the VMM front-end chip for serializing data off the detectors and other support functions. The support functions include:

- TTC signal decoding from a GBT e-link and its distribution to VMM.
- Generating the appropriate clocks for the VMM (e.g. 80 and 160 MHz).
- Programmable delays for the bunch crossing clocks and TTC signals delivered to the VMM to compensate for their distance from the GBT and interaction point.
- Interfacing the serial data flow of the VMM data read out on Level-1 Accept to conform to e-link requirements. This may include 8b/10b encoding and header insertion.

In addition, specialized functions for the trigger are required to select and serialize: MM address in real time (ART) data, sTGC strip trigger data, and sTGC pad trigger data. A fourth case, the MM readout, requires only the shared support functions. The four cases may be implemented as separate ASICs or different operating modes of a single ASIC. Design of the various function modules will be shared across the MM and sTGC communities. The ASIC technology used by the VMM will be adopted so that the VMM and companion chips can be produced on a single silicon wafer. The three different trigger functions of the companion chips, the Trigger Data Serializers (TDS), are described in the appropriate trigger sections, Sections 12.3.1 and 12.3.2.

12.2.4 On-chamber power converters and power distribution system

The on-chamber power for the MM detector components is shown in Table 12.2. The main electronics power load is the front-end VMM chip, dissipating 8 mW per channel at 1.2 V. The total VMM power per MM sector is 524 W. The addition of trigger, readout, and control functions ($\times 1.3$) and a realistic transmission efficiency (64% see below) roughly doubles the total power required, shown in the rightmost column. The sTGC power demand is described in detail for a wedge (large and small are almost identical) and scaled to the system in Table 12.3. The final column contains the effect of the transmission efficiency. The total power for each sector is 1.1 kW for MM and 0.5 kW for TGC.

To deliver locally high currents at low voltage within the severe service constraints of the NSW, point-of-load (POL) power distribution will be employed using DC-DC converters. Similar schemes are being investigated for the Phase-II Inner Tracker upgrades at ATLAS and CMS [59, 60]. A commercial power system in UX15 transmits power to the sectors at 24 V. The 24 V is distributed separately to each front-end board where DC-DC converters step it down to 1.5 V, and linear regulators then convert it to 1.2 V for the VMM.

Each step incurs an efficiency loss; an overall efficiency of 64% is assumed. Considering current delivery, for the MM, transmission at 24 V will require 44 A per sector or 5.5 A per layer, minimizing cable cross-section in the crowded service spaces.

The DC-DC converters must have good efficiency ($> 85\%$), low noise, and operate in magnetic and radiation fields. A test programme described in [61] identified several potentially suitable 24 V devices, and we are beginning a broad survey of additional new products. The Linear Technologies

Table 12.2: MM power

MM Unit	Contains	VMM Power	Total Power
channel		8 mW	
VMM chip	64 channels	512 mW	
FE-card	8 chips	4.096 W	8.3 W
plane	16 FE-cards	66 W	133 W
doublet	2 planes	131 W	266 W
quadruplet	2 doublets	262 W	532 W
sector	2 quadruplets	524 W	1.1 kW
wheel	16 sectors	8.39 kW	17.0 kW
NSW	2 wheels	16.8 kW	34.1 kW

Table 12.3: sTGC power

TGC Unit	Contains	Unit Power	All Units	Total Power
Wedge FE	24 FE cards			
	96 VMM	0.512 W	49 W	
	48 TDS	1 W	48 W	
	6 GBT	3 W	18 W	
	24 SCA	0.25 W	6 W	
	Wedge total		121 W	189 W
Sector	2 wedges		242 kW	378 W
	1 router		58 kW	91 W
	pad trigger		10 kW	16 W
	Sector total		310 kW	485 W
Wheel	16 sectors		5.0 kW	7.8 kW
NSW	2 wheels		10.0 kW	15.6 kW

LTM4619 survived a 350 kRad exposure. The device performance specifications and a program to test in magnetic and radiation fields will be established to qualify all of the front-end components, including the linear regulators. Work will go on together with the Inner Detector power groups at ATLAS and CMS to tap existing expertise and also understand possible custom fallbacks if a commercial solution is not viable.

12.2.5 On-chamber electronics cooling

For the MM, a design for cooling each doublet of planes is considered. The electronics heat is carried away by a cooling channel running down between the front-end cards of the doublet on one side of the sector, across the narrow inner wall, and out between the cooling cards on the other side. Working with a temperature change of the cooling liquid of 3° C the required water flow in one channel is 21.5 mℓ/s or 77.4 ℓ/h. The heat will be transported from the chip surface to the cooling channel by a thermally conductive ceramic foam pad (Raychem HeatPath). It is a rather soft pad material with a thermal conductivity of about 1 W/m K. A 1 mm thick pad will result in a temperature drop of 4 K over a chip surface of 1.3 cm^2. Starting with a cooling water temperature of 17° C which gets warmed up to 20° C this design will keep the temperature of the front-end chips safely below 30° C, the maximum tolerable temperature.

As shown in Fig. 12.6 the cooling channel is planned to be made from a drawn copper profile which contains a bore for the cooling liquid and also a channel for cables and optical fibres that are to be connected to the front-end cards. Clips apply a small force on the gap pads to ensure

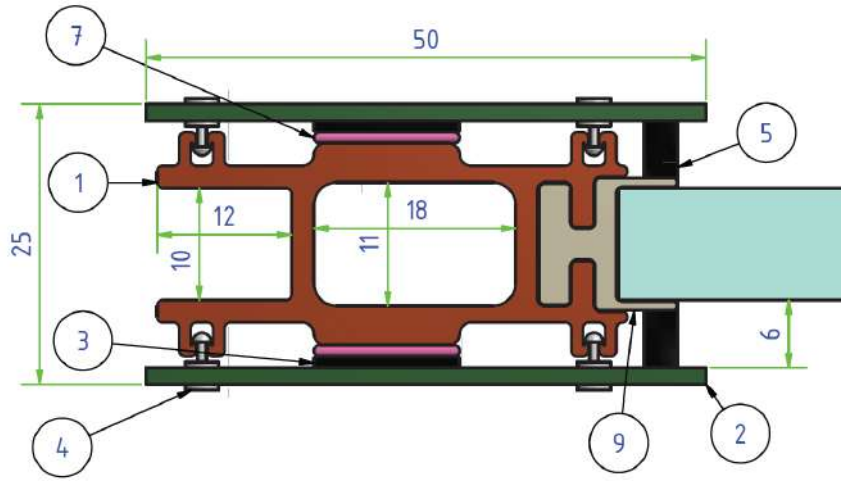

Figure 12.6: Conceptual MM cooling channel design, looking down a sector edge. (1) Cooling profile (2) Electronics PCB (3) VMM (4) Clip (5) Zebra connector (7) Pad (9) Fixation to MM chamber (blue)

good thermal contact between the front-end chips and the cooling channel.

Fig. 12.7 shows a TGC cooling station consisting of two pad and two strip front-end cards at the edge of each module. The component sides of one pad and one strip board face each other and are joined by a layer of HeatPath padding, distributing the heat of the chips into the strip PC board, which is thermally coupled to a water-cooled aluminum plate. The strip-pad pairing is repeated on both sides of the plate to cool all four boards. The system is encased in a copper box that provides compression for the board/pad/plate coupling and also serves as a Faraday cage. The total power to be removed is 18 W per station on the outer and middle, and 24 W in the inner modules; total cooling load on the side of each wedge is 60 W. In each sector, the cooling pipes also run through the router/pad trigger station where a similar scheme is employed.

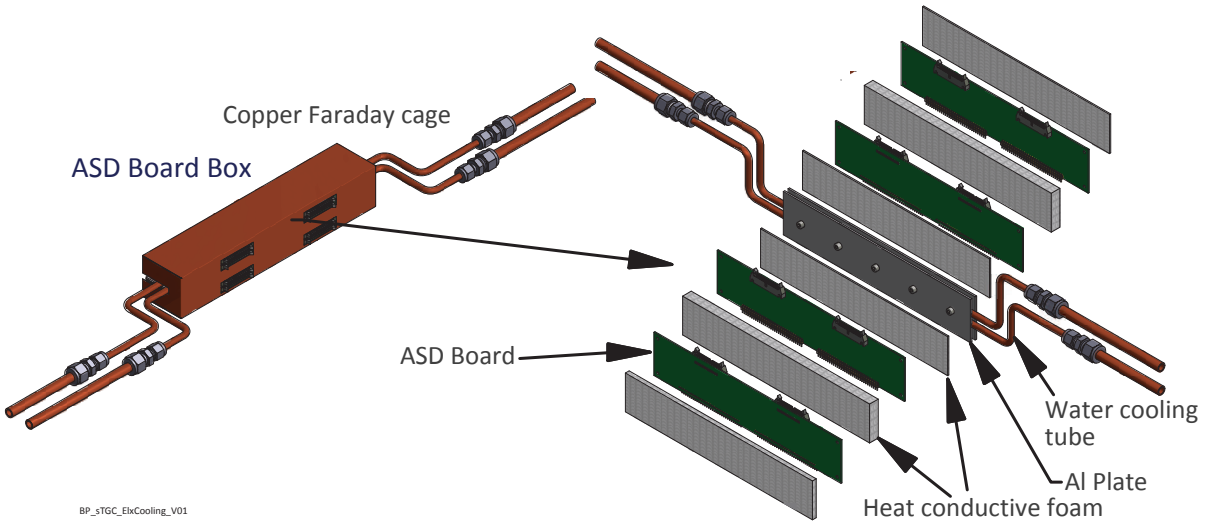

Figure 12.7: Cooling system for one station on one sTGC module. Exploded view shows Front-end boards sandwiched in thermally conductive foam, and two boards in full area contact with the cold plate.

12.2.6 Trigger processor modules and crates in USA15

It is intended that the two technologies will use the same trigger processor cards in the ATCA standard as the platform for their trigger logic in USA15, but with different firmware and numbers of input links. An example ATCA card, commercialized by the Scalable Readout System, SRS, project is shown in Fig. 12.8. This card exists and can be used for prototyping the trigger logic.

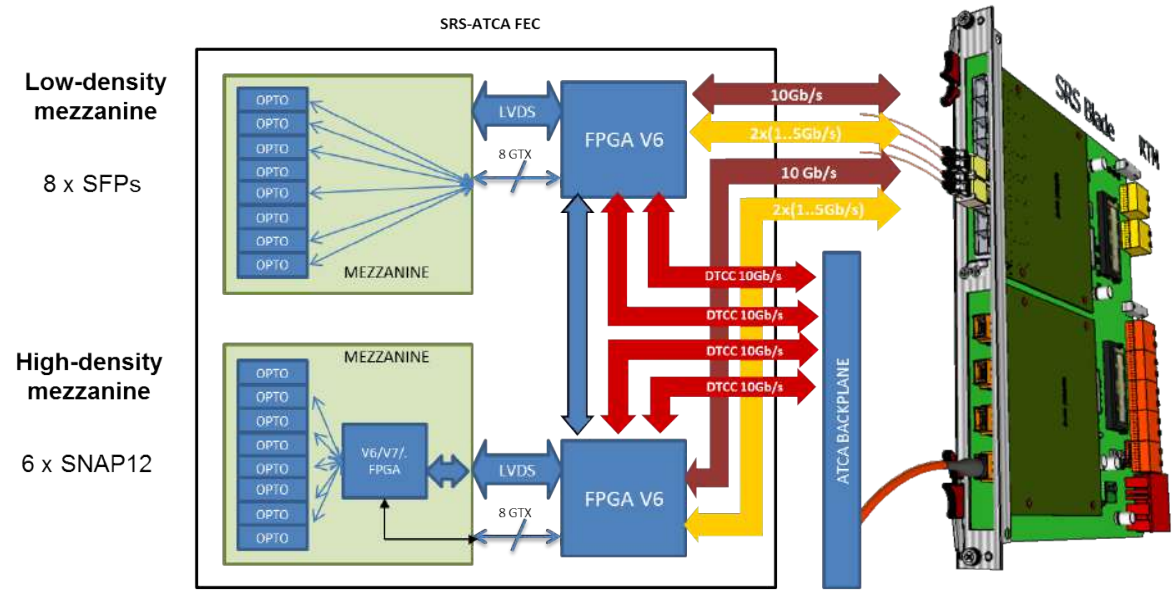

Figure 12.8: An example FPGA board (from the SRS project) for prototyping the trigger logic in USA15 contains two FPGAs, each connected to a mezzanine card and one memory socket. The total data bandwidth of each mezzanine-FPGA connection is about 90 Gb/s, split between 8 high-speed serial and 48 low-latency LVDS connections.

An ATCA card is also being developed for the LAr calorimeter which could also be a suitable prototyping platform. A full-size ATCA chassis contains 12 cards. Mezzanine cards and/or rear transition modules (RTMs) can support a large number of serial optical links; one crate per End-cap with four cards for MM and four for sTGC is possible. The MM and sTGC cards can exchange data with each other using the high-speed, full-mesh ATCA crate backplane; see Section 12.3.3.

12.3 Trigger systems and Front-end boards

12.3.1 sTGC trigger system

At each bunch crossing, the sTGC trigger electronics finds local tracks that point, with <1 mrad precision, to the Big Wheel to corroborate its coincidences. In order to place the track finding and extrapolation logic off-detector, a 3-out-of-4 coincidence of pads in each of the 4-layer quadruplets is used to choose the relevant bands of strips to be sent off-detector. This substantially reduces both the required bandwidth and the amount of centroid and track finding logic. To reduce the number of pad channels, the layers are staggered by half a pad in both directions to make logical towers one quarter the area of a pad. An example pad division, that of Pivot Layer 1, is shown

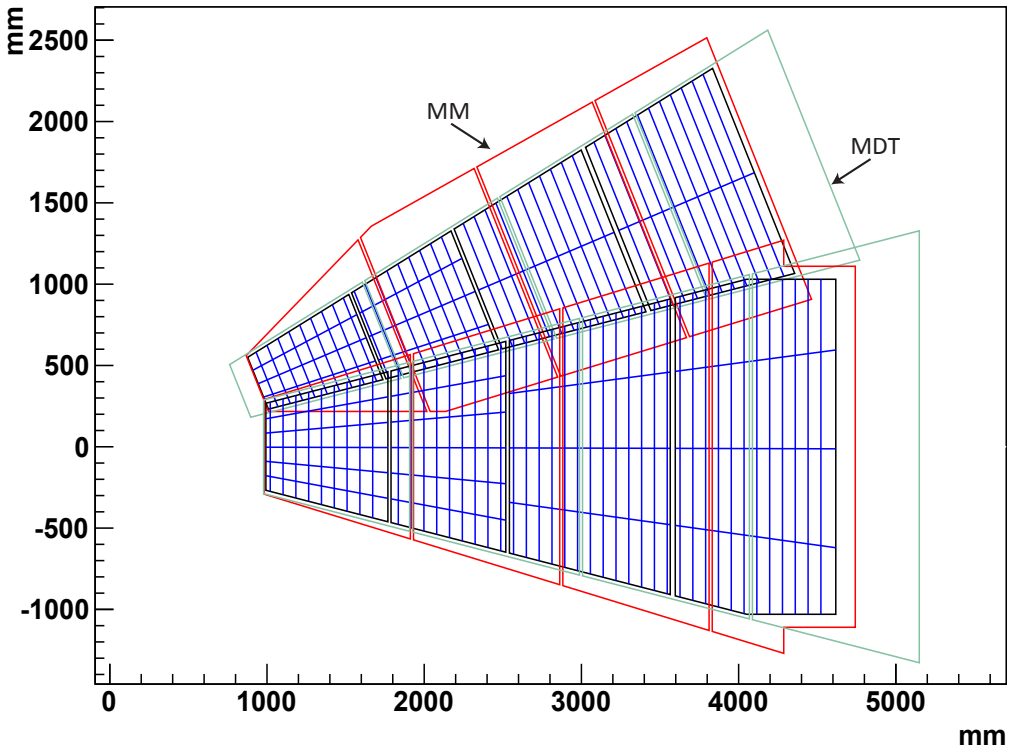

Figure 12.9: The pad division of a octant (small sector plus large sector) in Pivot Layer 1.

in Fig. 12.9. The width of the pads in ϕ decreases with lower radius to handle the increased background rate.

The block diagram of the trigger logic for one layer of a $1/16^{\text{th}}$ sector is shown in Fig. 12.10. The figure shows the signal flow from chamber to the track finding and extrapolation logic in USA15. On detecting a peak in the signal from a strip, the VMM digitizes the peak amplitude to a 6-bit value which is immediately sent serially over one line per channel, to the strip Trigger Data Serializer, TDS, in the companion ASIC. (See also Section 12.2.3.) There all active strips are saved and tagged with the BCID, awaiting possible selection by the pad tower trigger for transmission off-detector. The Time-over-Threshold pulse of each pad is latched in the pad TDS by the next BC. The pad 'hit' bits from all channels are serialized and sent within one BC to the pad trigger on the rim of the NSW. The pad coincidence logic, running in parallel with the strip data collection, then selects the band of strips in each layer that passes through the tower generating the pad coincidence. Up to three such towers per $1/16^{\text{th}}$ sector per beam crossing, one per Inner/Middle/Outer region, are envisioned. That this is sufficient will be verified by simulation. It may be possible to provide three towers per beam crossing without regard to radial regions.

The IDs of the bands that are selected and the BCID are distributed to the TDS chips. The TDS in each layer that holds the selected band for the selected BCID transmits its 'strip charges' on a fast serial copper twinax to a router on the periphery of the wheel. The data transmitted include the Bunch Crossing ID, band-ID, ϕ-ID and the strip charges. 128 bits must be transmitted in 25 nsec, necessitating a link with 5.1 Gb/sec payload. 8b/10b encoding would require a 6.4 Gb/s link. The ASIC design for this rate may prove challenging and may require running at 3.2 Gb/s either over two lanes or taking two bunch crossings. The Router then sends the data from the active TDS ASICs to the centroid finding and track extrapolation logic in USA15 via optical fibre.

In USA15 the active strips selected by the pad trigger are used to compute centroids and then

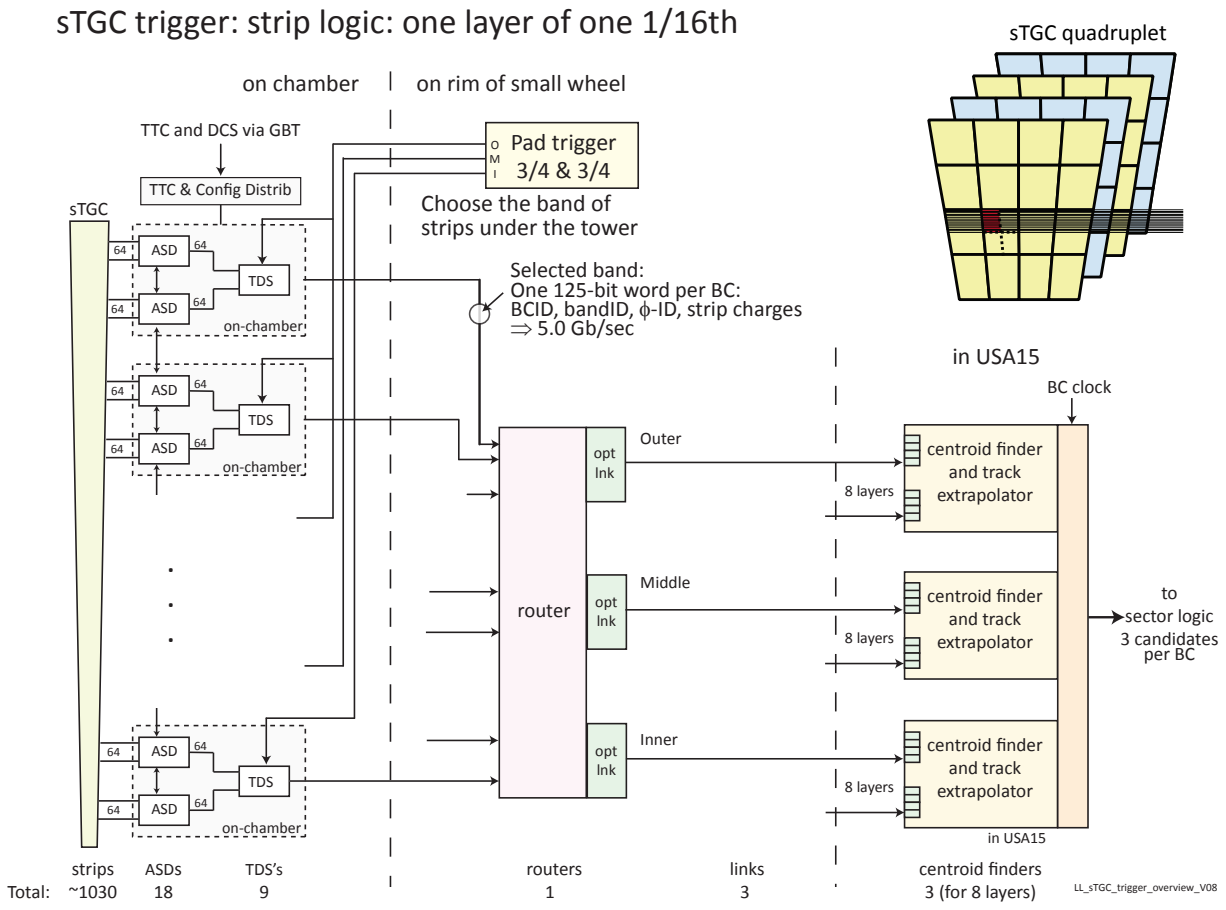

Figure 12.10: Block diagram of the trigger logic for one layer (of eight layers per side) of a $1/16^{\text{th}}$ sector

track segments that point to the Big Wheel. These candidates are then sent via fast serial links to the Sector Logic to be combined with Big Wheel candidates. The whole process repeats every bunch crossing with a fixed latency (See Table 12.6). Details of the sTGC trigger components are elaborated in the following sections.

Pad tower trigger

The pad tower trigger tags a bunch crossing and the band of strips passing through the triggered tower in each layer that must be selected for readout by the Trigger Data Serializer ASIC (TDS). Its inputs are all the ~ 1300 (~ 1200) pads of all 8 layers in a large (small) $1/16^{\text{th}}$ sector, up to $|\eta| < 2.4$. It is located on the periphery of the Small Wheel and must be implemented in radiation tolerant electronics. The $1/16^{\text{th}}$ sector is divided into regions in radius (currently three, without regard to physical gas volumes) of roughly balanced trigger rate. Pad tower triggers are produced independently in each region so that one candidate from each region can be sent to the Big Wheel Sector Logic. The BCID and ϕ of the triggering pad tower are also sent to the selected strip TDS and flow downstream along with the selected digitized strip charges. It is the pad trigger that defines to which bunch crossing the strip signals belong. The logic is as follows:

- Try to make a 3-out-of-4 coincidence for every tower in each quadruplet.
- Try to make a coincidence between the 3-out-of-4 coincidences in the two quadruplets.
- Choose up to one coincidence per Inner / Middle / Outer region.

The pad trigger electronics are on the rim of the small wheel. To avoid using one cable for each of the ~ 1300 pads, the pad companion ASIC assigns pad hits to bunch crossings and sends, for every 32 pads, a 32-bit hit map serially to the Pad Logic within one bunch crossing. This reduces the number of cables to approximately 64 per sector and preserves the flexibility of doing the pad tower coincidence logic in accessible programmable logic.

Random trigger rates and simple pad tower trigger simulation

In order to verify the sTGC trigger algorithm and to evaluate its efficiencies and fake rates, a fast simulation program has been developed. Its main features are:

Detector and pad geometry: The exact geometry taken from the parameter book. In particular the pads staggering and displacement is faithfully reproduced.

Magnetic field and multiple scattering: An angle distributed with a Gaussian distribution with $\sigma_\eta, \sigma_\phi = 5, 20\,\text{mrad}$ is conservatively assumed.

Incoherent Background: The η-dependent incoherent rate is from Fig. 2.2, scaled to $\mathcal{L} = 5 \times 10^{34}$.

Coherent Background: The 'standard' coherent background is not yet simulated.

Cathode charge distribution: The charge is spread in two dimensions over the neighbouring pads with a Gaussian distribution, $\sigma = 3\,\text{mm}$.

Efficiency: An efficiency of 1 for a charge deposit $> 0.5\,\text{mip}$ is assumed. For a deposit $< 0.2\,\text{mip}$ the efficiency is 0, and increases linearly between these two values.

It should be noted that each of the above features with its parameters can be switched on or off and parameterized. Once energy deposition and digitization have been performed, all 3-out-of-4 hit coincidences in pad towers in each wedge and the combined coincidence of the two 3-out-of-4 hit wedge coincidences are found. Table 12.4 summarizes the results. Note that the sector trigger rate depends on the 6^{th} power of the individual rate.

Table 12.4: Results of the simple pad trigger simulation

	Small Sector			Large Sector				Total		
	Pivot	Confirm	Total	Pivot	Confirm	Total		octant	side	2 sides
Hits per BC	7.0	7.4	14.5	9.4	9.8	19.3		33.7	269.7	539.3
Hits per BC for $\lvert\eta\rvert < 2.4$	6.0	5.9	11.9	7.9	8.5	16.4		28.3	226.4	452.7
Pad occupancy per BC	1.0%	1.0%	1.0%	1.1%	1.3%	1.2%		1.1%	1.1%	1.1%
3-out-of-4 wedge rate, kHz	2043	2213	4256	3008	3166	6175	MHz	10.4	83.4	166.9
Sector trigger rate, Hz			364.0			645.4	kHz	1.0	8.1	16.1

sTGC Front-end board for trigger and readout

Strips and pads signals cannot all be easily extracted from the same edge of a chamber. Front-end boards are therefore placed on both edges of a chamber to avoid cables crossing between edges and to balance heat. Wires are brought out from the outer radius end of the wires on a flex-PCB to the edge. (The wires of the innermost module are not read out.) Strips are brought to one edge, pads and wires to the other; the side alternates with even and odd layers. One Front-end board per layer serves a complete detector. The number of VMMs on the different types of Front-end boards is shown in Table 12.5. There are 48 Front-end boards and a total of 192 VMM ASICs in a large sector (190 for a small sector). There is a 'TDS' companion ASIC for each two VMMs and a Slow Control Adapter (SCA) ASIC on each Front-end board for configuration of the VMM and TDS ASICs, and environmental monitoring, which is described in Section 12.5. Ideally there is one GBT on each edge of each of the three modules in a wedge, resulting in six GBTs per wedge – in total, 384 GBTs for the whole sTGC. The number of channels and their occupancy only require a fraction of the bandwidth provided by these two GBTs per module. However, with this arrangement each module can be readout and tested at its construction site, before it is sent to CERN for assembly with the other two. Fig. 12.19 shows the SCA-related connections for configuration, calibration and environmental monitoring.

Table 12.5: The number of VMM ASICs on the different types of Front-end boards of a layer.

FEB type	Left edge	Right edge
Outer, even	5 strip	1 pad, 1 wire
Outer, odd	1 pad, 1 wire	5 strip
Middle, even	5 strip	1 pad, 1 wire
Middle, odd	1 pad, 1 wire	5 strip
Inner, even	8 strip	2 pad
Inner, odd	2 pad	8 strip

Router

The Router is a custom packet router located on the periphery of the Small Wheel. On every beam crossing it routes one of its inputs, the one from the active TDS chosen by the pad trigger, to the trigger processor in USA15. The Router does not alter the packets in any way. Packets are fixed length, 160 bits (including 8b/10b encoding), taking one beam crossing to transmit at 6.4 Gbits/sec. To reduce latency, packet transmission can begin immediately after the start-of packet symbol is received. Radiation levels on the rim are low enough to allow implementation by FPGAs.

The Trigger Processor: Calculating centroids and track segment parameters

Centroid finding, averaging and extrapolation to the Big Wheel will be done in a conventional FPGA in USA15. Pipelined DSP (Digital Signal Processor) blocks are used. The centroid finder demonstrator calculates the centroid from the charge on up to five strips. Centroids are included in the average only if the number of strips above threshold is below a certain maximum value (e.g. five) in order to exclude δ-rays and conversions. Fig. 12.11 shows a block diagram of an sTGC trigger processing. Fig. 12.12 shows the details of the pipelined centroid finding and averaging calculation.

The identification of the track in the NSW with a RoI at the Big Wheel is done using Look-up-Tables (LUTs) for the radius, R, and azimuth, ϕ, coordinates. The LUT input for R is the centroid average in the pivot plane; the LUT input for ϕ is the column of the triggering pad tower. The algorithm also provides the Sector Logic with the angle, $\Delta\theta$, between the track segment in the NSW and an infinite momentum track from the interaction point, calculated from the two centroid averages in the two quadruplets.

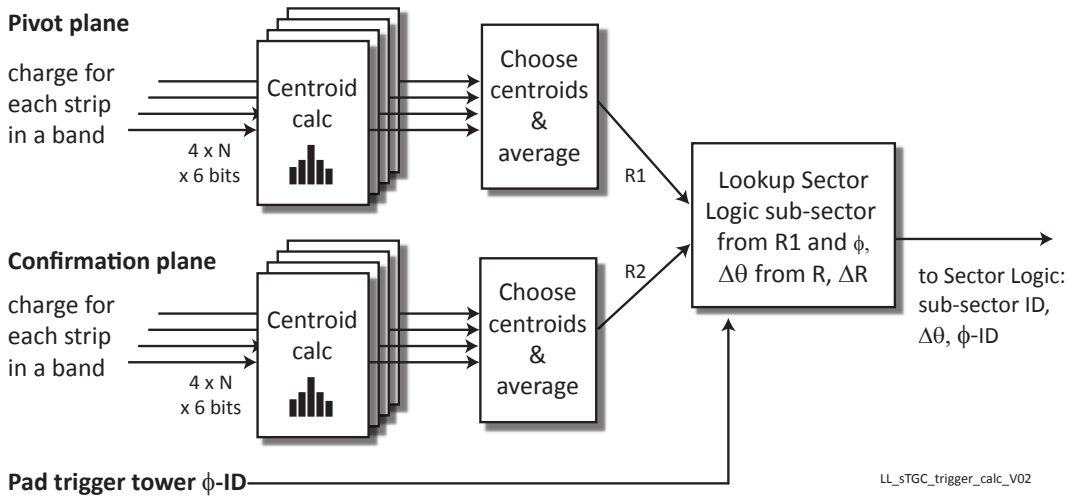

Figure 12.11: Block diagram of an sTGC trigger processor showing the centroid calculation, centroid averaging and extrapolation to the Region-of-Interest, RoI, in the Big Wheel.

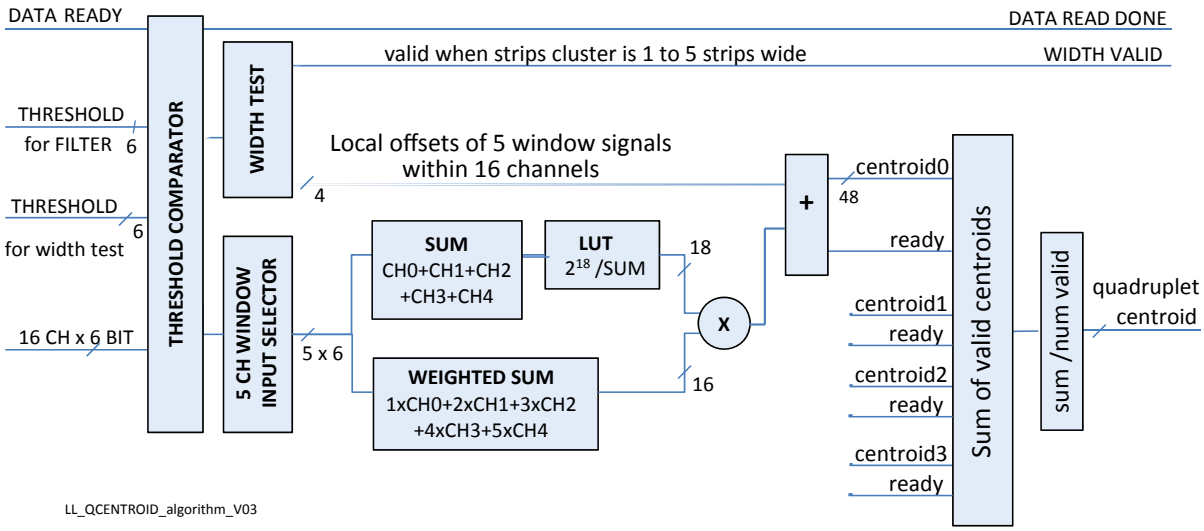

Figure 12.12: Details of the centroid finding and averaging algorithm

Currently up to three candidates per sTGC $1/16^{\text{th}}$ sector are envisioned to be sent to the Sector Logic for combining with the Big Wheel coincidences – one from each of the Outer, Middle, Inner regions of the Small Wheel. The number of candidates, i.e. the number of regions, and the region boundaries will be optimized by simulations. It is likely that the three output links could each serve a complete $1/16^{\text{th}}$ sector and so up to three candidates from anywhere in the sector may be sent.

Finally the Trigger Processor synchronizes its output to the correct bunch crossing for the Sector Logic. Although data has passed through elements that operate independently of the BC clock, the TDS companion ASIC has tagged the strip data with the BCID determined by the Pad Trigger. This BCID is used to correctly align the output.

sTGC trigger path demonstrator

Two sTGC demonstrators were built to study (1) the centroid finding algorithm, particularly to determine if a viable algorithm could be performed within the very limited latency budget, and (2) to measure realistic latencies of a serial link of the type needed for the trigger path to USA15. Fig. 12.13 shows the results of the centroid finder and averager for a cosmic ray triggering a pad tower as it passes through four sTGC layers. The first demonstrator, Demo-0, is connected to the strips and pads of an sTGC quadruplet via ASDs used in the TGC Big Wheel; the second, Demo-1, via the VMM1 prototype front-end ASIC. Both use Time-over-Threshold (ToT) as the estimation of strip charge. The peak value, as will be digitized by the next VMM prototype's Flash ADC, is more linear with charge and will be used in future. Since the VMM1 does not incorporate the FADC, the demonstrators do not attempt to demonstrate the accuracy of the centroids found, only the latency. This will be done with the next prototype.

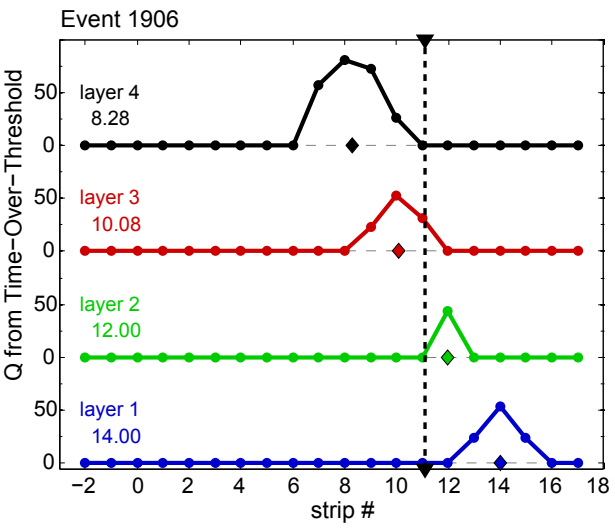

Figure 12.13: A cosmic ray passing at an angle through a quadruplet. The ⋄'s are the calculated centroids (values on the left). The vertical dashed line is the calculated average.

The Demo-0 used a commercial FPGA evaluation board; it demonstrated only the centroid calculation and track segment finding. It is able to handle four layers of 16 strips each, plus the 44 pads needed to form towers covering a single band of strips.

Demo-1 is a custom PCB built from two FPGAs connected by serial and parallel links. One FPGA executes the pad trigger and centroid logic. The second FPGA is intended to emulate the 'TDS' front-end companion ASIC. It receives the pad trigger via LVDS lines and sends the 'charge' values of the strips selected by the pad trigger over a 6.25 Gb/s copper twinax serial link to the centroid/segment logic in the other FPGA. Additional links allow the trigger data to be sent to a second identical board and for that board to return its strip data to the centroid logic on the master board. Each Demo-1 board can handle four layers of 64 strips, 512 strips for two boards. 148 pads cover the strips with towers. Hardware and software capable of configuring the 44 VMM ASICs was also built. The measured latencies for the centroid and segment calculation and the link latency are included in Table 12.6.

sTGC latency

The total latency of the trigger system must comply with the existing Sector Logic timing which allows a total of 41 bunch crossings, 1025 ns. Table 12.6 shows the latency budget of the system. It is within the allowed time, but without much margin. Note that the pad path is longer than the strip path, which is not shown.

Table 12.6: Latency from the interaction point, through the sTGC trigger logic for the NSW to the Sector Logic in USA-15. All times are estimates, except for the centroid finder, the VMM1 latency and the FPGA ser/deserializer latency which have been measured.

	min (ns)	max (ns)	Notes
TOF from interaction point to NSW (z=7.8 m)	29	31	to periphery of NSW @R=5m
pad signal jitter in chamber	25	25	worst case due to tracks midway between wires
pad ASD (VMM)	30	40	VMM1 latency
serialize 32 pads @2 GHz	16	20	
TDS to pad trigger on rim, max 4 m	15	20	3-4 m @ 5 ns/m
up- to down-stream package (50 cm)	3	3	
pad trigger (incl de-skew)	15	25	strip charge values are pipelined
pad trigger to on-chamber TDS ASIC	15	20	3-4 m @ 5 nsec/m
TDS: Trigger Data Serializer	10	20	until pad trigger arrives
On chamber cabling to Router	15	20	5 nsec/m, 3 to 4 m
TDS-to-Router ser/deserializer	15	25	
Router	6	10	switch
Router to Centroid ser/deserializer	60	80	Xilinx GTX @6.4Gb/s, measured optimizaton still in progress
Wait for last bit from deserializer	25	25	for a 160 bit frame
fibre to Centroid card in USA15 90 m	450	450	5 nsec/m
find valid centroids and averages	32.5	52	8 layers done in parallel, measured to be 13 clocks
difference of centroid averages	2.5	4	
lookup sub-ROI pointed to at BW	5	5	
resynch to BC clock driving the output serializer	6.25	6.25	90° phase chosen to best match pipeline length
centroid to Sector Logic serializer	5	15	The deserializer is on the Sector Logic latency budget
Total	780	896	

12.3.2 MicroMegas trigger system

Both the sTGC and MM chamber technologies will contribute to the formation of the Level-1 muon end-cap trigger. The primary chamber technology that provides the trigger is the sTGC but the MM technology will also be capable, thereby forming a very powerful, redundant trigger system.

MM detectors with a pitch of 500 µm provide excellent spatial and double track resolution. Exploiting this capability, however, requires a large number of electronics channels, about two million for an eight layer detector. The electronics of the NSW must provide both a high resolution vector, in real time, to be used in the formation of the muon Level-1 trigger in addition to the amplitude and time information provided on the reception of a Level-1 Accept.

In order to reduce the number of trigger channels the design takes advantage of the MM detector's fine readout pitch to reduce the number of channels by a factor of 64. This is accomplished by considering only the first arriving hit in each 64-channel front-end IC for a given bunch crossing, resulting in a system with granularity of 32 mm (64×0.5 mm) but having spatial resolution better than half a millimetre by simply recording the address of the strip with the earliest arrival. This immensely simplifies the task by reducing the number of channels by almost two orders of

magnitude while not requiring any processing of the raw signals to determine the hit coordinate with the precision required for a 1 mrad resolution. The address of the channel with the earliest hit per bunch crossing is sufficient. At every bunch crossing (BC) each of the 64-channel front-end ASICs outputs serially the 6-bit address of the channel with the first detected amplitude above a set threshold. This, in effect, results in a total channel count for the trigger logic of about 30,000.

The efficiency loss due to a second hit in a given ASIC over the processing time (about 5 BCs) is about 1% even in the highest pseudo-rapidity region. Because of ionization fluctuations, the earliest arriving hits have a distribution that spans approximately three bunch crossings; about 90% of them are within two. Therefore a rolling window of the current, plus one (or two) subsequent, BCs is used to find a track segment in a given BC. Fig. 12.14(a) shows the results of a Monte Carlo simulation of the efficiency of such a trigger (right scale) and the pointing resolution as a function of the size (in BC units) of the rolling window. At least 5 of the 8 planes are required to define a track segment. Already with a 2 BC window the required resolution is achieved with an efficiency better than 95%. With a window of 3 BC the system is fully efficient. The lever arm was 20 cm. The actual available space may not be enough for such a lever arm because in the baseline configuration the MM detectors are inside the sTGC planes. The pointing resolution would be degraded accordingly. These results were compared with measurements in a test beam in the Summer of 2012. A set of 8 small MM detectors were arranged parallel to each other and at varying angles with respect to the 120 GeV pion beam at the H6 line of the SPS. The address of the first signal arrival from each detector was recorded and the track was reconstructed offline. The VMM ASIC provided the Address in Real Time (ART) either at the threshold crossing or at the peak detection. The results are shown in Fig. 12.14(b) as a function of incident angle. The lever arm in the test beam setup was about 50 cm. The results are within a factor of less than two from the simulation. The limitations of the first version of the ASIC, as discussed in Section 12.2.1 could account for this difference.

MicroMegas Front-end board for trigger and readout

The MM front-end boards (MMFE's) utilize the VMM ASIC described above to provide the zero-suppressed readout of the address, amplitude, and time of all MM hits that are read out in response to a Level-1 trigger, and the Address in Real Time (ART) data that is used to form the Level-1 trigger. The MMFE's must also provide a configuration path for the VMM ASIC's and distribute TTC (Timing, Trigger and Control) signals to each VMM. The MMFE has eight VMM ASIC's and a companion ASIC. The MMFE's are equipped with external input protection against sparks that safeguards the inputs to the eight VMM's. Flexible high density Zebra connectors are used to connect the MM signal traces to the MMFE. The Front-end boards also support the calibration of the VMM and the monitoring of chip and board voltages and temperatures (see Section 12.5). Fig. 12.15 is a block diagram of a MM Front-end board.

Level-1 data readout

The companion ASIC is used as an interface between the VMMs and the GBT e-links used for Level-1 readout. Each MM detector plane will be read out by four MMFE's and there are 4096 MMFEs for the entire MM system. The companion ASIC formats and sequences the Level-1 readout data from its eight VMMs and sends the data via an 80 Mb/s e-link to a GBT on a Level-1 Data Driver Card (L1DDC) that is near the MMFE. The opposite direction of the e-link is used to bring the TTC signals to the companion ASIC. A second bi-directional e-link is used for

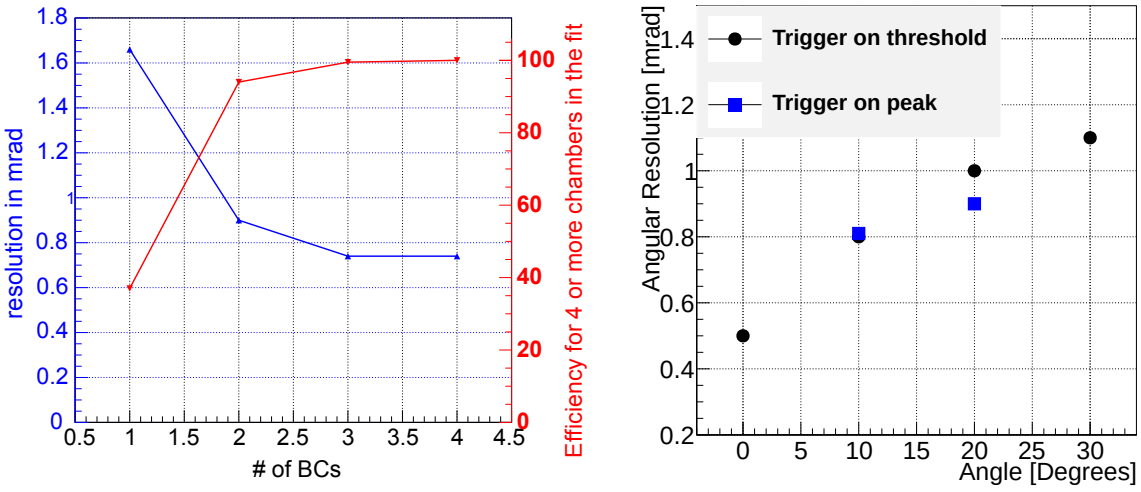

(a) (b)

Figure 12.14: (a) Simulation results; efficiency (right scale), and angular resolution as a function of the size of the rolling BC window requiring five or more planes.
(b) Angular resolution measured in a test beam as a function of incident angle. The dots use the Address in Real time at threshold crossing while the square use the ART at amplitude peak. The lever arm was 50 cm.

configuration, calibration and monitoring. There are 256 Level-1 DDC's in the MM system; each serves 16 MMFE's. Eight of the 40 available e-links remain unused and can be used for DCS.

For service modularity concerns, a Level-1 Data Driver Card serves four layers in the same MM multiplet. The MM $1/16^{\text{th}}$ sectors are divided into four radial stations, each with a separate Level-1 Data Driver Card and fibre pair on each of two edges.

A detailed hit rate table was used to examine the actual data rates on the links for different regions of the detector. Given the requirement that the NSW must operate through the Phase-II era, the hit rate used for the bandwidth estimate is extrapolated from $\mathcal{L} = 1 \times 10^{34}\,\text{cm}^{-2}\,\text{s}^{-1}$ to $\mathcal{L} = 5 \times 10^{34}\,\text{cm}^{-2}\,\text{s}^{-1}$ and another $\times 1.4$ safety factor imposed. The MM readout system will be designed with this conservative rate 'headroom'.

ART data driver card (ADDC)

The scheme for readout of trigger data is shown in the block diagram in Fig. 12.15. The Address-in-Real-Time words are sent to the trigger processor in USA15 via optical links in two steps. First, the ART from each of 32 front-end VMMs (four MMFE's) is serially transmitted, point-to-point, to a companion digital ASIC on the trigger data driver card; from there it is sent to USA15. The ASIC performs the following functions (See Fig. 12.16):

- Deserialize the ART stream and phase align the hits to the BC clock.
- Identify the strip addresses of up to six hits by means of cascaded priority encoders.
- Append the 5-bit geographical VMM ASIC address to the strip address of each hit.
- Send the 11-bit addresses and the 12-bit BCID to a GBT configured to operate in parallel mode without Forward Error Correction (FEC).

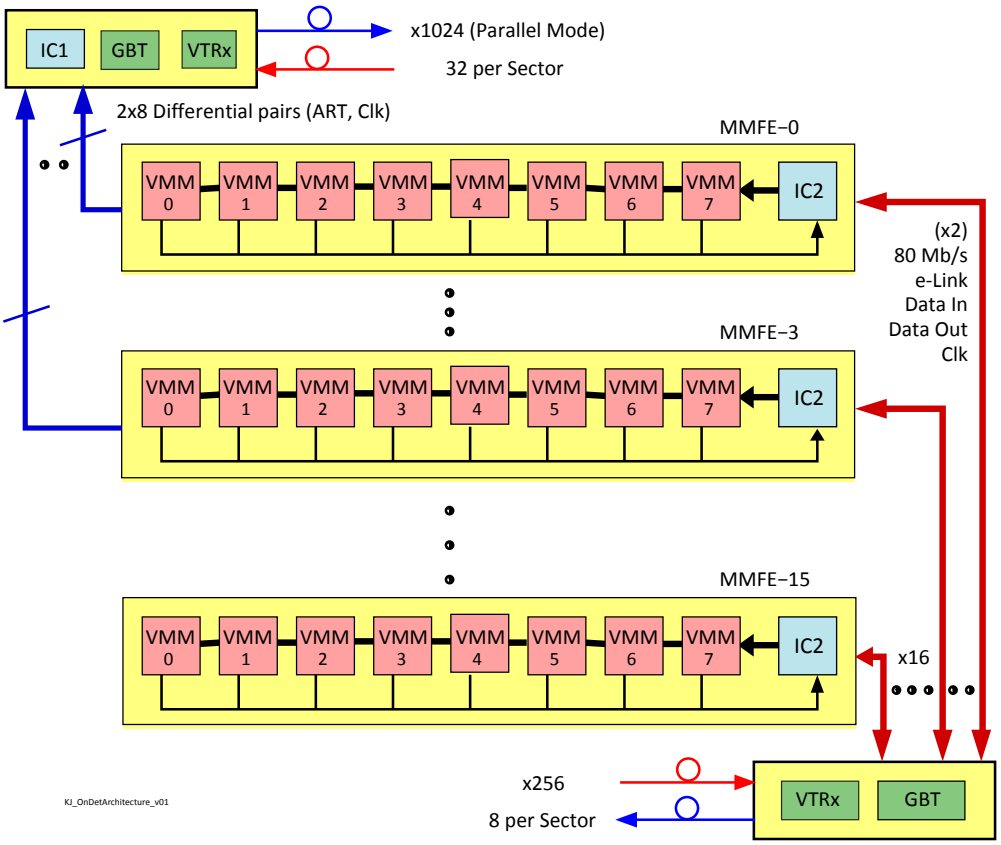

Figure 12.15: Block diagram of MM Front-end Level-1 data and trigger readout out boards. There are three different boards: the Front-end card housing eight VMM ASICs, one trigger data driver card receiving from four Front-end cards (top), one Level-1 readout data driver card receiving from 16 Front-end cards (bottom). IC1 is the ART companion; IC2 is the readout-only companion ASIC.

There are a total of 1024 ART data driver cards. Their latency is about 2 BC.

Using the dual Versatile Transmitter (VTTx) significantly reduces the cost per link. The absence of the downlink, however, requires that the ART ASIC receive its TTC and clock signals from the Level-1 event readout downlink and that the ART GBT transmitter also be configured via that downlink.

MicroMegas Trigger Processor

The MM trigger processors located in USA15 and are housed in the same ATCA crates as the sTGC logic. They are implemented by conventional FPGAs. Mezzanine cards on each of several ATCA blades receive and deserialize the ART data from the on-detector drivers. The stereo pair in the down stream end of the detectors is designated as the pivot pair. Lookup memories addressed directly by the ART data of the pivot planes determine the R, ϕ coordinates at the pivot location. In addition the same addresses define the regions in the remaining planes where a hit should be found for a track originating at the interaction point. This scheme serves as a 'firmware pad tower'. The appropriate lookup space is searched in parallel for all the remaining planes. The tables provide R, ϕ pairs which are averaged in the two multilayers and subsequently determine the R, ϕ, $\Delta\theta$ of a track candidate which is sent to the Sector Logic.

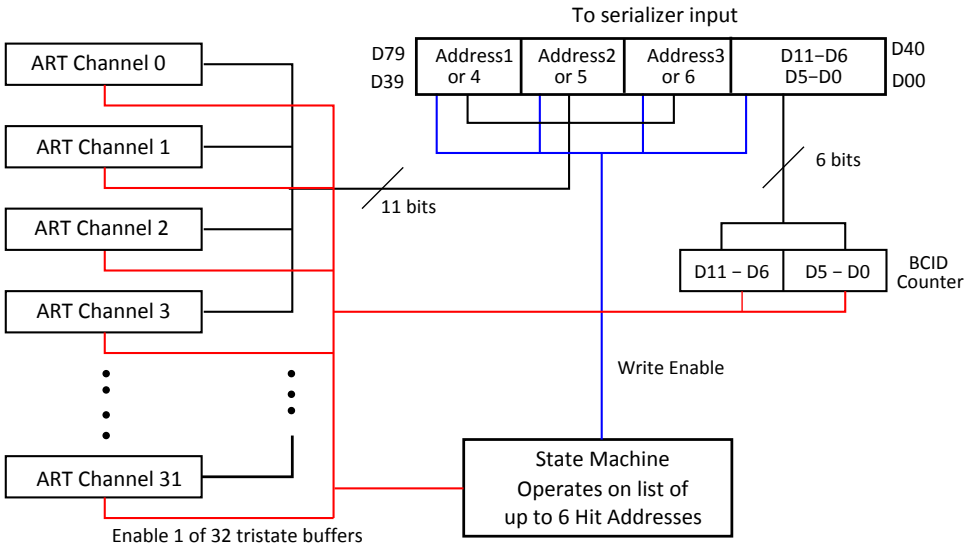

Figure 12.16: Block diagram showing the identification of up to six ART signals per VMM augmented by the 5-bit geographical address, and the loading of these addresses along with the 12-bit BCID on the GBT bus.

The total latency of the trigger system must comply with the existing Sector Logic timing which allows a total of 41 bunch crossings. Table 12.7 shows the latency budget of the system. It is within the allowed time, but without much margin. If, while implementing the trigger, it turns out that more time is needed serializers with lower latency will be considered.

Table 12.7: Latency from the interaction point, through the MM trigger logic for the NSW to the Sector Logic in USA-15. All times are estimates. The maximum allowed latency is 1025 ns.

	min (ns)	max (ns)	Notes
TOF from interaction point to NSW (z=7.8 m)	29	31	to periphery of NSW @R=5m
earliest arriving hit	50	75	depends onsite of rolling window (2 or 3 BC)
shaper response	60	80	VMM1 latency + time-to-peak
trigger driver latency	40	50	
GBT serializer+deserializer latency	100	150	
fibre to AMC card in USA15 90 m	450	450	5 nsec/m
lookup R,ϕ of pivot layer	5	10	
lookup R in rest of layers	30	40	
average R in the 2 multilayers	2.5	4	
difference of R averages	2.5	4	
lookup sub-ROI pointed to at BW	5	5	
resynch to BC clock driving the output serializer	6.25	6.25	90° phase chosen to best match pipeline length
centroid to Sector Logic serializer	5	15	The deserializer is on the Sector Logic latency budget
Total	785	920	

12.3.3 Combining sTGC and MM trigger data

As a baseline, the MM and sTGC will independently compute track vectors. Both sTGC and MM trigger modules belonging to a $1/16^{\text{th}}$ sector will be in the same ATCA trigger crate which has a fully interconnected backplane, i.e. all modules are connected to every other module by several high-speed, low latency differential pairs. In this way MM vectors will be sent to a final merging stage of the sTGC trigger and vice versa. The output of the merging stage is sent to the Sector Logic (see Section 12.3.4). Since both merging stages would output the same merged list of vectors, only one must actually be connected to the Sector Logic. This provides redundancy in the case of failure of one of the modules. Each vector sent to the merging stage is tagged with a 'quality' flag that is used by the merging logic to select the best vectors. For example, if the vector was produced from only one of the two four-layer modules of the sTGC because the track passed through a support in the second module, it would have a lower quality because its resolution is much poorer. Because both sTGC and MM trigger modules are in the same ATCA crate with high bandwidth connectivity, it may be possible to merge hits and then find vectors. Handling the details of the detector differences at the hit level may require more processing time than is available in the Phase-I latency budget. Any improvement of the vectors' accuracy from such an algorithm may not be needed, at least for Phase-I, and the added complexity may not be justified.

12.3.4 Sector Logic for the New Small Wheel

Track vector information from the New Small Wheel (NSW) is combined with results from the current Level-1 muon trigger system based on the TGC Big Wheel (TGC-BW) by the new Sector Logic board. A block diagram of the new Sector Logic board for the Phase-I upgrade is shown in Fig. 12.17.

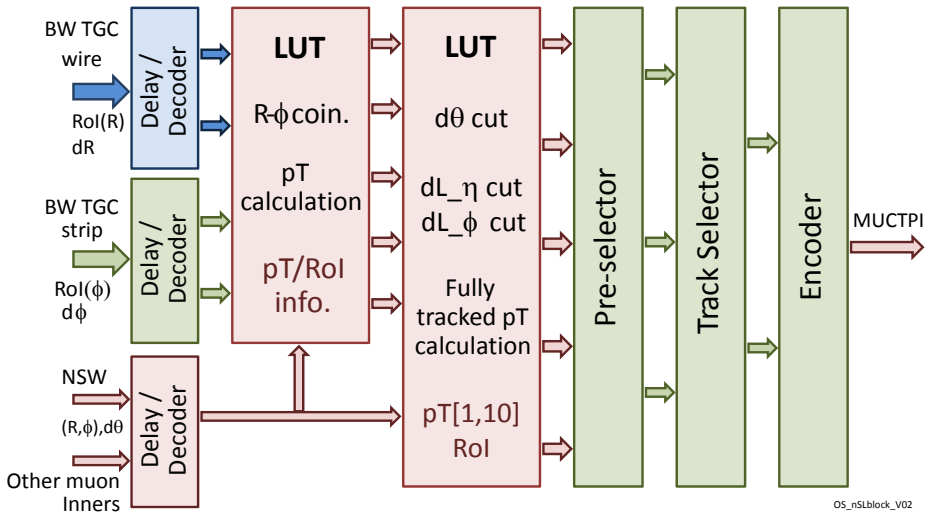

Figure 12.17: Block diagram of the new Sector Logic board

The partitioning of the Trigger Sectors and granularities of Region-of-Interest (RoI) for the new Sector Logic board remain the same as in the present scheme. Exactly the same hardware (optical links) and data formats are used for signals from the TGC-BW. Additional input ports are introduced to receive track information for the NSW and other muon inner detectors. The input from the sTGC and MM trigger processors to the Sector Logic will be via optical fibres. Each

connection will run at 6.4Gb/s, 128 bits, 8b/10b encoded, per BC clock. Up to four candidates, 24 bits each, a 16-bit header and a 16-bit trailer containing the BCID can be transferred every beam crossing. The format of a track candidate (24-bits) is shown here (The valid bits indicate the source and quality of the candidate.):

Field:	sTGC valid	MM valid	θ (mrad)	ϕ index	R index	*spare*
Num of bits:	2	2	5	6	8	1

Signals from TGC-BW and muon inner detectors are aligned with the LHC bunch crossing clock and decoded at the first stage of the Sector Logic board. In the first Look-Up-Table (LUT), coincidence is made between wire and strip signals from the TGC-BW, then RoI and p_{T} information of the track candidates are provided to the second LUT. The second LUT is used for requiring a track-vector in the muon inner detectors. Position matching between RoI's of the TGC-BW and track-vectors in the Muon inner detectors, as well as, angle consistency between the two tracks are required. The p_{T} value of track candidates is re-calculated with about 10 sets of p_{T} thresholds. Up to the two highest p_{T} muon tracks are selected; their p_{T} value, RoI and a quality flag of coincidences among muon detector stations are transmitted to the MuCTPI (Muon to Central Trigger Processor Interface). Input signals from both TGC-BW and Inner muon detectors are delivered to the Sector Logic board 44 BC clocks after every *pp* collision. The estimated latency of the signal processing is 10 BC clocks excluding the de-serialization time of optical links. The Sector Logic input deserializer is expected to take three BC clocks. If so, the NSW must deliver its output to the Sector Logic front panel at 41 BC clocks, equal to 1025 nsec.

The Sector Logic provides its input and output data to be read out every Level-1 Accept via an Ethernet connection per end-cap.

12.4 Readout system

12.4.1 Readout from GBT to ROS

The off-detector readout chain of the ATLAS detectors presently consists of sub-detector specific custom ReadOut Drivers (RODs), usually FPGA-based, which output event fragments to the ReadOut System (ROS) via the ReadOut Links (ROLs) [62]. The ROLs are point-to-point custom optical links that cross the boundary between the sub-detector domains and the TDAQ domain. The Readout Architecture Upgrade Working Group, with representatives from all detectors and TDAQ, is considering a new architecture for Phase-II that better promises to take advantage of future advances in electronics and information technology. The new architecture (see Fig. 12.18), proposed by members of the NSW collaboration, reduces the amount of custom electronics and links in favour of industry standard equipment. The ROD functionality becomes split in two:

- The front-end links connecting the detectors to the off-chamber readout electronics will be interfaced to a general purpose COTS network with a stateless, non-detector-specific and high-availability interface, called FELIX (Front End LInk eXchange) [63].

- The ROD data processing and other functions will operate on data delivered by an industry standard network. The ROD's output will also be via an industry standard network. Eventually such a ROD could be implemented in an industry standard server PC.

The Working Group is currently evaluating the architecture based on FELIX and the existing architecture based on RODs connected directly to the Front-end links. It is expected that a recommendation will be made by early summer. The NSW must be compatible with Phase-II and will adopt the readout architecture recommended by the Working Group.

The front-end links for the NSW and also, for Phase-II, for many other detectors will be CERN GBT links, which, in addition to event data, will transfer TTC, DCS, and front-end configuration information. According to detector-defined routing tables, FELIX will route these multiple logical data streams within a single GBT link to different network endpoints. Since DCS must operate irrespective of the TDAQ state, FELIX operation must not depend on the TDAQ state. Also, altering or depending on detector-specific data should be avoided.

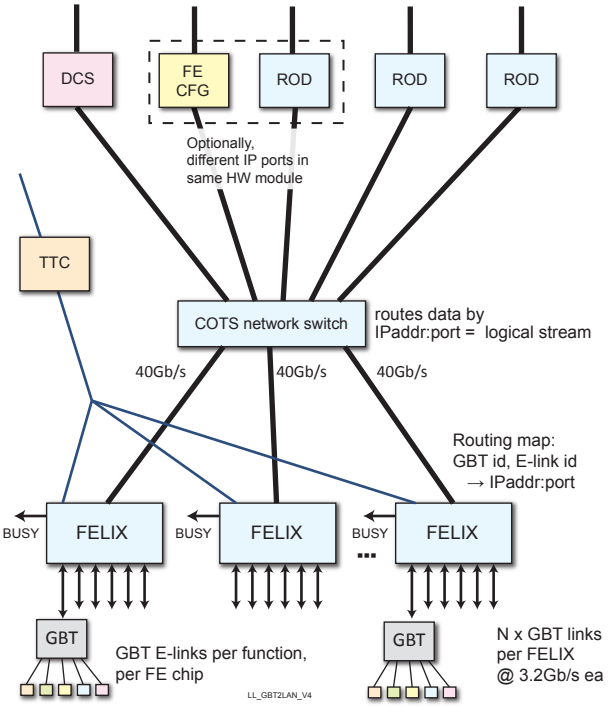

Figure 12.18: Front-end link, FELIX and ROD connections

FELIX will be implemented with FPGAs for interfacing to the GBT links and for extracting the various data streams. Event data is routed to RODs performing the classic ROD functions: fragment building and associated error detection, data checking and transformation and monitoring. RODs may be server PCs, or, similar to current RODs, FPGA-based hardware in an ATCA environment. The SLAC Generation 3 RCE/COB [64, 65], planned to be the Muon CSC RODs for the next run, is a natural candidate for the latter. The RCE/COB can also implement the current architecture with direct connections to the front-end links.

The ROD output fragments may be forwarded to server PCs implementing the ROS functionality or alternatively the ROS functionality may also be implemented in the same hardware as used for the ROD functions. DCS and front-end configuration interact with the on-chamber systems via the general purpose network and FELIX.

Two important advantages of the architecture based on FELIX are: 1) minimization of the amount of special-purpose detector-specific hardware and associated firmware and therefore the flexibility of general purpose, industry standard equipment, and 2) the ability to easily scale in power and be upgraded with new technologies to meet future needs. On the time scale of installation 40 or 100Gb/s network technology can be expected to be available at reasonable cost, so that the data from 10 to 25 fully utilized GBT links can be concentrated on a single network link. ROD data can then be distributed over as many RODs as required to provide the traditional ROD functionality. The use of PC technology, perhaps augmented by coprocessors such as GPUs and the Intel Xeon Phi, and a COTS network (including the output to the ROS) will make it possible to purchase the hardware relatively late, benefiting from further evolution of the technology. Test beam work and testing NSW detectors at construction sites will be possible with less performant network and server nodes than needed for the final system.

By adopting the architecture recommended by the Readout Upgrade Working Group, the NSW readout architecture will be Phase-II compatible with respect to functionality. More and/or faster

hardware may need to be added to cope with Phase-II data. The interface to the TTC system needs to be implemented using mezzanine cards, to be replaced for Phase-II running by other mezzanine cards interfacing to the Phase-II TTC system. NSW collaborators are part of a wider collaboration defining and developing the Phase-II off-detector front-end readout.

The FELIX approach is foreseen to be demonstrated without building hardware, using a PC server outfitted with a commercial FPGA PCIe card and a high performance 10G network PCIe card. Existing GBT interface firmware will be combined with firmware developed to extract the logical streams and transfer them to PC memory. PC software then routes the data streams onto the network.

In addition to the front-end ASIC data, the Readout system also reads out the inputs and outputs of the Pad Tower trigger, the Trigger Processors and the Sector Logic.

12.4.2 Data acquisition software and event-based data monitoring

Configuration software at start-up of the off-detector readout system will, for example, configure the type of frame format, width of e-links, etc. of the GBT. Counters for monitoring errors and statistics will be initialized and periodically read out. Fragment building, data integrity checking, error detection and handling of any errors, data transformation (e.g. compression or decompression, channel mapping) and formatting in the ATLAS standard format will be implemented in software if server PCs perform of these tasks. The ATLAS ROD Crate DAQ (RCD) [66] functionality will control the handling of the event data, marshal states, enable/disable portions of the detector and report errors.

Event-based data monitoring can take place in server PCs handling fragment building and the tasks associated with it. Data samples will be routed to PCs dedicated to monitoring if not enough computation resources are available for this task, or if fragment building is done in dedicated hardware.

12.5 Configuration and monitoring

12.5.1 Configuration and monitoring of the front-end electronics

Configuration of on-chamber electronics will be done by one or more server PCs via the network and the FELIX system, using the appropriate e-links connecting to GBT-SCA and companion chips, see Fig. 12.5 and [57]. Also the on-detector GBT chips need to be configured, for each GBT link a dedicated e-link is reserved. The server PCs doing configuration may be driven either by the DCS or by the DAQ system or by both.

Environmental parameters can be read out via the GBT-SCA chips and passed by appropriate e-links via the GBT links and FELIX to server PCs. The GBT-SCA chip can autonomously send messages upon external interrupts (signalling, for example, that a temperature is too high).

On the front-end, the GBT connects to the GBT-SCAs via e-links. The GBT-SCA then connects to several other chips in the system. This architecture assumes that the control is done by sending data packets (messages) to the respective SCA channels, which interpret the messages as commands, execute them on their external interfaces (for example just a read or write operation to a memory bus) and return a status reply to the GBT via another message.

Each Front-end readout board connected to MM or sTGC chambers will carry from two up to eight VMM ASIC chips. This comes from the radial segmentation of the wedge in sTGC pads, sTGC strips and MM strips shown in Chapters 7 and 8. Each ASIC has to be configured independently through its I^2C bus port. Each Front-end board will include an SCA chip that has

16 I^2C buses for control and 32 multiplexed ADC inputs for monitoring. For every VMM ASIC, a dedicated I^2C connection will be used. The monitor output of each VMM will be connected to one of the SCA's ADC inputs. The VMM ASIC's internal reference voltages, its temperature, and the peak value of any channel can be selected for output to this monitor. The selection is controlled via I^2C. A connection diagram is shown in Fig. 12.19.

Furthermore, the SCA will provide I^2C connections to the front-end companion chip, the MM trigger companion chip, the control of the uni-directional GBT trigger links and ADC inputs for board temperature and power supply voltages. The SCA will also read out ambient air (∼20 per $1/16^{\text{th}}$ sector) and cooling water inlet and outlet temperature sensors (∼12–16 per $1/16^{\text{th}}$ sector). B-field sensors (five per $1/16^{\text{th}}$ sector) will also be read out.

A major advantage of putting an SCA chip on every front-end board is that the SCA concentrates many on-board connections onto a single e-link (3-pairs) and so reduces the number of cables and connectors. 4096 SCA's are needed by MM and 1536 by sTGC.

The SCA features dual redundant e-link ports which run at 80 Mb/s. A primary e-link is connected to the on-board GBT. A secondary link can be connected to a neighbouring GBT and can be activated in case of failure of the primary e-link.

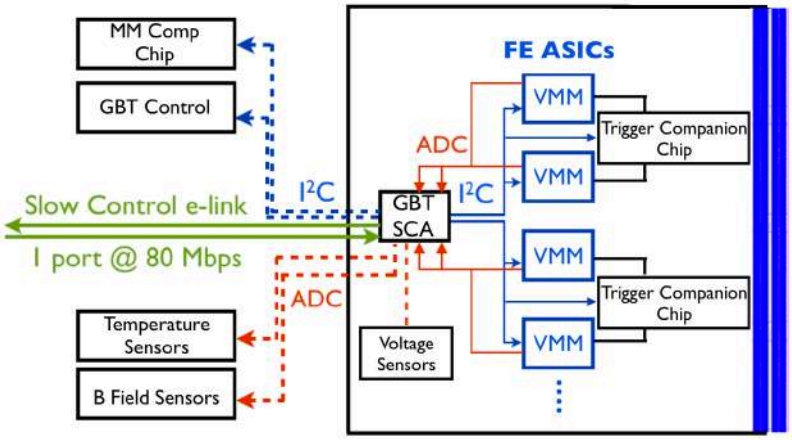

Figure 12.19: The SCA and its connections to VMM ASICs, companion ASICs and environmental sensors on the Front-end readout board

12.5.2 Back-end detector control and configuration system

The back-end detector control system is assumed to be the current SIMATIC WinCC Open Architecture system (previously known as PVSS) [67] [68]. Currently the system communicates via the OPC middleware with dedicated controllers; this can also be done for the communication with the GBT-SCA chips. An OPC UA [69] server will need to be available for this purpose and could be running on a dedicated server PC.

13 Services and infrastructure

This chapter describes the services and infrastructure needed to operate the NSW detectors. Only the service distribution from outside of the detector up to the patch panels at the NSW rim is discussed; for the distribution on the detector wedges see chapter 7 and 8.

13.1 Power systems

13.1.1 LV power system

The sTGC and MM detectors will share a common LV system and distribution, as the front-end electronics of both detectors will use the same ASIC.

The LV system needs to supply 50 kW of DC power to the detector front-end electronics of both wheels, see Tables 12.2 and 12.3 on page 126. This amount of power cannot be supplied directly at the voltage of 1.2–1.5 V required on the front-end electronics as it would entail a total current of about 35 kA, leading to an unmanageable total cable cross-section or a high power loss during transmission.

In order to reduce the total current, the LV distribution is foreseen to use a DC voltage of 24 V for the transmission from the power supplies to the NSW rim. Point of load DC-DC voltage converters at the rim of the NSW and/or on the front-end cards reduce the transmission voltage to the required voltages. Depending on the exact scheme either a reduction in one or two steps is foreseen.

To estimate the necessary amount of rack space and cabling, a segmentation of the LV distribution of one channel per wedge, i.e. 4 channels per sector will be assumed[1]. This translates to a current of 10.1 A at 24 V for a sTGC wedge and 22.2 A at 24 V for a MM wedge.

Table 13.1: LV system parameters.

Parameter	Value
Output voltage (V)	24
Max. output current (A)	30
Voltage resolution (V)	0.05
Current resolution (A)	0.1
Total number of channels	128
Channel per module	2
Total number of modules	64
Single module width (U)	4
Total number of crates	13
Total number of rack space (U)	52
Total number of racks	1.6
Conductor area — sTGC (mm^2)	4
Cable outer diameter — sTGC (mm)	13
Number of cables† — sTGC	32
Conductor area — MM (mm^2)	8
Cable outer diameter — MM (mm)	13
Number of cables† — MM	64

†The cables have 4 leads of $4mm^2$ each

The preferred location of the 24 V power supplies would be UX15 to minimize the cable lengths to the NSW. This location requires the power supplies to be moderately radiation and magnetic field tolerant. Alternative locations would be either USA15 or US15 for which the cable length increases by a factor of 3.

[1]To improve the redundancy and minimize losses of acceptance in case of failures, the same amount of channels could connect to only two layers in each wedge, but in two adjacent sectors.

Table 13.1 summarizes the parameters of the LV system. The conductor area of the cables assumes a routing length of 50 m and a maximum of 10% power loss in the cables. The module width and the rack space is given in units (U). A crate is 20 U wide, a rack is 41 U high (of which 34 U are available). The number of racks is given as a fractional number as the remaining space inside them can be otherwise used.

13.1.2 HV power systems

The HV system for the sTGC will be based on the existing system used for the present TGC detectors in ATLAS. The HV system of the MM detectors will be a new design, as they do not resemble any detector system currently used in the experiment and have different requirements on the supplied voltages and currents limits.

The sTGC detectors are operated with a single positive high voltage, applied to the anode wires of a plane. The maximum current at the highest LHC luminosities for a single plane is expected to be 100 µA. Including a safety factor of 5, the HV modules used should be able to supply at least 500 µA. The nominal operating voltage of the sTGC detectors is 2800 V. The modules should be able supply a maximum voltage of 3200 V for detector conditioning. For monitoring purposes and to detect discharges in the detectors a current resolution of 0.1 µA and voltage resolution of 0.5 V of the HV modules is desirable.

Table 13.2: sTGC HV system parameters.

Parameter	Value
Max. output voltage (V)	+3200
Max. output current (µA)	500
Voltage resolution (V)	0.5
Current resolution (µA)	0.1
Total number of channels	1024
Channel per module	32
Total number of modules	32
Single module width (U)	4
Total number of crates	8
Total number of rack space (U)	48
Total number of racks	1.4
Cable diameter (mm)	3.2
Number of cables	1024

The sTGC HV system will be based on the modular CAEN EASY3000 system [70], using either currently available modules if they are still in production or their replacements. The 2-channel CAEN AC/DC converters of type CAEN A3485 [71] will be located in US15 and drive with a 48 V DC voltage the radiation-hard and magnetic-field tolerant CAEN HV 32-channel modules A3535 [72] located in the EASY3000 crates of the racks on the HS structure in UX15 on the USA side. The system is controlled by CAEN branch controllers A1676A [70] housed in a SY1527 [70] mainframe in the service area USA15.

Each sTGC plane is connected with a dedicated HV cable to a separate channel of the HV system, so that an individual anode voltage and individual current limits can be set depending on the size and position of the detector. At the same time the impact of failures of the power system are minimized and localized to small parts of the detector. Per side of the experiment, a total of 512 channels will thus be necessary, corresponding to 16 CAEN A3525 HV modules. The modules can be housed in four CAEN EASY3000 crates, in one rack per side.

Table 13.2 summarizes the requirements and parameters of the sTGC HV system and lists the number of necessary modules, the required rack space, and the number and diameter of cables from the racks to the NSW rim.

The HV system of the MM detectors needs to supply two different voltages to each detector plane, a positive voltage for the signal amplification between the readout plane and the mesh and a negative voltage to the drift electrode. The mesh itself is serving as the ground plane for both potentials. Only the amplification channel needs to drive a sizable currents, the maximum current at

the highest LHC luminosities for a single plane is expected to be $\leq 0.5\,\mathrm{nA/cm^2}$. Including a safety factor of 5, the HV module used for the amplification gap should be able to supply at least 10 µA. For the drift gap a maximum current of about 1 µA is sufficient. Both the amplification and the drift gap voltage are in the range of a few hundreds of Volts. Thus, power supply modules with a maximum output voltage of ±1000 V are sufficient. For monitoring purposes and to detect discharges in the detectors a current resolution of 2 nA and voltage resolution of 0.5 V of the HV modules is desirable.

Currently, there is no HV power supply unit available which would suit the MM purposes. With the rather low HV requirements and the thus easier insulation between channels, a highly integrated module with 32 channels could be envisaged. The power supply channels for the positive and negative voltages could be housed in common unit with a selectable channel polarity, simplifying the cabling to the detector. If the requirement of the current measurement proves too difficult to achieve in a multi-channel commercial unit, the measurement could use a dedicated system of ADC modules, similar to the gap current monitoring of the ATLAS RPC HV system [73]. This latter approach would of course increase the required rack space. The cabling of the MM HV foresees the use of multi-channel cables with 23 separate channels of which 18 are used[2].

Table 13.3: MM HV system parameters.

Parameter	Value (min./max.)
Max. output voltage (V)	+1000
Max. output current (µA)	10
Voltage resolution (V)	0.5
Current resolution (µA)	0.02
Total number of channels	1024
Channel per module	32
Total number of modules	32
Single module width (U)	4
Max. output voltage (V)	-1000
Max. output current (µA)	1
Voltage resolution (V)	0.5
Current resolution (µA)	0.002
Total number of channels	256 / 1024
Channel per module	32
Total number of modules	8 / 32
Single module width (U)	4
Total number of crates	8 / 13
Total number of rack space (U)	48 / 78
Total number of racks	1.6 / 2.6
Cable outer diameter (mm)	11.1
Number of cables	64

Table 13.3 summarizes the requirements and parameters of the MM HV system and lists the number of necessary modules, rack space, and the number and diameter of cables from the racks to the NSW rim.

13.1.3 Operation and control

The control, monitoring, and alert handling of the LV and HV power systems will be implemented in the ATLAS DCS FSM as sub-nodes of the respective detector systems inside the muon tree.

Automatic actions are foreseen to trigger a state transition of the HV systems between a safe standby state with reduced voltage to a ready state at the nominal voltages for data taking, depending on the state of the LHC.

For detector safety reasons, hardware limits are set to limit the maximum output voltages and the maximum output currents, in addition to the programmable software limits.

Automatic actions on the power system in case abnormal conditions in the experiment are observed will be implemented via the DSS system.

[2]The remaining channels serve as spares.

Table 13.4: sTGC and MM gas system parameters.

Item	sTGC	MM
Gas System Type	open (n-pentane recovery)	open
Gas Mixture	n-pentane/CO_2 = 45/55	Ar/CO_2 = 93/7
Gas Pressure (mbar)	atmospheric + ≤ 4	atmospheric + ≤ 2
Detector Volume (nl)	3400	6000
Nominal volume exchange rate (vol d^{-1})	5	24
Nominal Flow (nl h^{-1} m^{-2})	1.5	5
Nominal total flow (nl h^{-1})	1280	6000

13.2 Cooling

As for the LV system, the sTGC and MM detectors will share a common cooling system and distribution to the NSW. In addition to ensure the FE chips are operated within their temperature limits, the cooling has to remove any power dissipated at the NSW which would otherwise contribute to heating up the upper sectors of the muon spectrometer, in particular the temperature-sensitive RPC trigger detectors. As the total power dissipation on the NSW is high, a water cooling system is foreseen.

Assuming a maximum allowed temperature increase of $\Delta T = 3\,K$ (see Chapter 12) between the input and output of the cooling loops, a water flow of 120 l/min per wheel will be required.

With a spare capacity of currently about 200 l/min each, the two existing cooling stations of the muon spectrometer can be used without the need for refurbishment.

Each NSW will be connected to one of the cooling stations by two cooling loops, serving the eight top and the eight bottom sectors, sector 1–8 and 9–16, respectively. The routing of the cooling pipes to the NSW will be in the flexible chains in sector 1 on either side.

13.3 Gas systems

The gas systems for the NSW detectors will use or re-use existing infrastructure, especially the mixing facilities at the surface building SGX1 connected to the primary ATLAS gas supplies and distribution racks in UX15 with local flow and pressure control. The sTGC detectors will be using the same gas mixture and pressure as the already installed TGC detectors and will be connected to the same gas system. The MM detectors will use an Ar/CO_2 mixture at atmospheric pressure, similar to the present CSC. Hence the CSC gas system may be re-used. For both detector systems only minimal modifications will be necessary.

The activation of the gas flowing through the detector has to studied and to be taken into account in the design of the gas systems. However, with the composition of the gas[3] and the foreseen high volume exchange rates it is expected to be negligible.

The requirements and parameters of the sTGC and MM gas systems are summarized in table 13.4. Both systems will be designed to handle a maximum flow rate of 5–10 times the nominal flow rate in case an increase of the gas flow proves necessary.

The sTGC gas system will be part of the TGC recirculating gas system [6, pp. 325–331]. It will thus be connected to the existing mixer, purifier, pump, and liquifier modules in SGX1. The gas distribution in UX15 to the detector re-uses the existing two TGC distribution racks on the

[3] Production of radio-active isotopes of H, C, O, Ar is unlikely and the half-lives, except for ^{3}H and ^{14}C, are in the millisecond to minute range. Only spallation products might contribute to an activation.

HS structure on level 4 on US side. The racks supply the drift gas as well as the CO_2 of the safety envelope around the detectors, as the n-pentane/CO_2 mixture used in the TGC/sTGC is flammable. Each NSW on either side is supplied from one distribution rack. The number of currently 4 drift gas lines and 2 lines for the CO_2 envelope per rack should be increased to 16 drift gas lines and 4 lines for the envelope. The distribution racks have sufficient space and free control and monitor channels for these modifications. For all channels the input and output flows will be monitored, with a shared pressure regulation, in each distribution rack. An overpressure control by a bubbler will vent the gas safely to avoid damage to the detectors in case of blocked gas flow. Each gas channel can be individually switched off by a remote-controlled valve. At the rim of the NSW each drift gas input pipe is connected to a manifold which distributes the gas flow in parallel to a single plane in either the eight lower or the eight upper sectors. A similar manifold on the output side collects the return gas of the same planes and connects to an output line. The CO_2 envelope lines each serve in parallel a full wedge of the upper or lower eight sectors via 2 input and 2 output manifolds for each half wheel.

The MM gas system will re-use the existing infrastructure of the former CSC detectors [6, pp. 210–213]. The MM system will be open loop, i.e. the gas is vented into an exhaust after it has passed the detectors as it contains neither flammable nor expensive gas components. The existing mixer module in SGX1 can provide the required flow rate, the primary ATLAS Ar and CO_2 gas supplies will be used as inputs to the mixer. The gas distribution in UX15 to the detector re-uses the existing two CSC distribution racks on the HS structure on level 4 US side. The detectors of each NSW are supplied by one rack, using the 16 input and 16 output channels already in place. Each line will be split at the rim of the NSW to connect to the multiplets of two wedges in adjacent small and large sectors. If necessary for further redundancy, a scheme with 32 input and output lines could be implemented, with a dedicated gas channel for the multiplets of a single wedge. For all channels the input and output flows will be monitored, with a shared pressure regulation, in each distribution rack. An overpressure control by a bubbler will vent the gas to avoid damage to the detectors in case of blocked gas flow. Each gas channel can be individually switched off by a remote controlled valve.

For both systems the splitters to distribute the gas flow will be placed on the NSW rim at accessible locations in the large sector. In case of a catastrophic gas leak on either detector system, a small part of the detector containing the leak can be disconnected from the distribution system during an ultra-short access, thus minimizing the impact of the leak on the detector operation.

The gas system control and monitoring is to be integrated into the ATLAS GCS via a WinCC [68] system provided by the CERN EN-ICE division. The system allows the remote control of the complete gas systems down to a minimum granularity of a single gas channel in a distribution rack. In addition an automatized handling of failures or abnormal conditions is implemented via alarm levels on all monitored parameters.

Additional monitoring and alert handling for the shift crew in the ATLAS control room will be implemented in the ATLAS DCS FSM, with the data transfer from the GCS application handled via DIP, similar to the existing gas systems.

Automatic actions on the gas systems in case abnormal conditions in the experiment are observed which affect the safety of either the personnel or the detectors will be implemented via the DSS system.

13.4 Service routing

13.4.1 Flexible Chains in Sector 1

The two flexible chains in sector 1 to either SW have a size of 350 mm × 110 mm (upper chain) and 370 mm × 140 mm (lower chain). The gas and the cooling pipes for both detector systems will be routed through these chains. All pipes will be flexible and made of stainless steel. The gas pipes will have an inner diameter of 10 mm (input) or 12 mm (output) to avoid pressure drops in the lines. A calculation of the total cross-section of all services was made, including an additional packing factor of 2.6 to account for line bends and space for the pipes to move relative to each other. All foreseen services fit into the flexible chains, with the upper chain filled to 60% and the lower chain to 50%.

With the currently foreseen segmentation and number of pipes, all gas and cooling lines would fit into the lower flexible chain of sector 1. This would free up the upper flexible chain for the use of the LV cabling, which otherwise has to be routed through sector 13. The possibility of combining the gas and cooling pipes into one flexible chain will be investigated.

13.4.2 Flexible Chains in Sector 9

The two flexible chains in sector 9 to either SW have a size of 300 mm × 160 mm (upper chain) and 370 mm × 160 mm (lower chain). The HV cables, optical readout fibers, and the alignment cables will be routed through these chains.

A careful calculation of the total cross-section of all services was made, including an additional packing factor of 2.6 to account for line bends and space for the cables to move relative to each other. All foreseen service fit into the flexible chains, with the upper chain filled to 90% and the lower chain to 80%.

13.4.3 Sector 13

As in the present SW, the LV cables are foreseen to be routed through sector 13 to a patch panel at the bottom of each wheel, as their volume is too large for the flexible chains. The LV cables will have to be disconnected before the NSW can be moved during the detector opening as it is currently the case as well.

A calculation of the total cross-section of the LV cables was made. Two scenarios were considered, a routing to the racks on UX15 with a cable length of 50 m and a routing to racks either located in USA15 or US15 with a cable length of 150 m. A maximum power loss of 10% was assumed for the calculation of the required cable conductor diameters. All calculations included an additional packing factor of 2.6 to account for line bends and a less than dense packing in the cable trays. The cable trays from the racks to the ATLAS detector and inside the experiment offer enough space for all cables in both scenarios.

13.4.4 Service routing on the NSW

Services arriving at the patch panels of the flexible chains in sector 1 and 9 and at the bottom of the wheel in sector 13 have to be further distributed around the wheel to the connection points for the detectors in each sector. The requirement of being able to move the detectors wheel on the JD plug to gain access to the detectors on the IP side for maintenance complicates the service distribution. As many services as possible should move together with the detector wheel, to avoid time consuming and error prone reconnecting after maintenance. Cable trays on the outer edge of

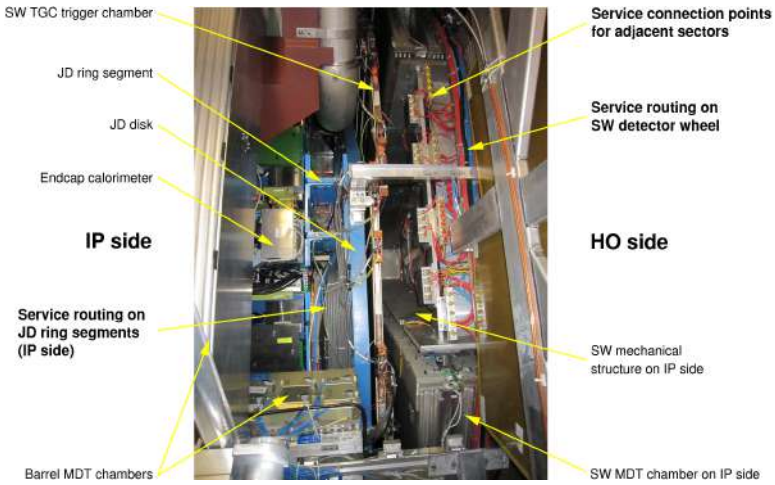

Figure 13.1: Service routing of the present SW in sector A07.

the mechanical support structure, located in the middle plane to stay inside the allowed outer envelopes of the NSW, can carry the gas manifolds, the alignment cables, the sensitive fibers, and part of the HV cabling, see Fig. 13.1 which shows the service routing of the present SW. A second set of cable trays, carrying the LV cabling and the remaining part of the HV cabling, can be mounted on the IP side of the JD disk where 31 steel ring segments serve as magnetic field returns of the inner detector solenoid field to the tile calorimeter (see Fig. 3.6 on page 28). These segments are located 280 mm inward from the outer rim of the JD disk and have a minimum free width in the z-direction of 215 mm (nominal: 270 mm). The available space is more than sufficient to accommodate the LV cables and the remaining HV cables and can also be used for trigger electronics. Fig. 13.1 shows the service routing on the JD disk for the TGC detectors of the present SW.

13.5 Logistics

The infrastructure and the services required in UX15 for the NSW can be pre-installed and commissioned up to the patch panels of the flexible chains or in sector 13 in the experiment independent of the NSW itself. The service distribution on the NSW itself will have been thoroughly tested during the integration of the NSW and the one-year commissioning phase at the surface.

Routing of new cables, fibers, and pipes from their endpoints in US15, USA15 and UX15 should begin immediately after the present SWs have been removed from the detector in LS2. Power supply units and electronic modules can be installed in the electronics racks at the start of LS2, subject to their availability. All services must be in place before the NSW is lowered into the cavern to allow a rapid connection and hence maximize the commissioning time in the cavern after installation.

The time scale for the final service connections to the NSW is about two weeks per side with a manpower of 4 FTE, followed by a commissioning period of the newly installed NSW.

Any components—power supply modules, cables, connectors, gas pipes, fittings—to be used will have to undergo a certification process which entails a long-term test of a reasonable sample of each production batch under operating conditions to show their suitability. A test of the radiation hardness is mandatory, as is the fulfillment of all rules regarding the use of plastic and non-metallic materials at CERN [74].

14 Detector maintenance

The NSW is designed with built-in redundancy featuring two detector technologies and a large number of measurement planes. Failures of the services, front-end electronics and detectors during data taking will affect only a small portion of the NSW and will have only negligible impact on the physics performance. Nevertheless, maintenance scenarios have been developed for repairing or exchanging components.

14.1 Safety

To ensure the safety of the personnel and the experiment any service will be disconnected by an automatic action if certain limits are exceeded or emergency conditions are met. Actions will be either implemented via the DSS or via the DCS. During scheduled accesses the LV and HV of all affected detector parts will be switched off and interlocked. The standard ATLAS rules for grounding equipment [14, p. 409] will be followed for all detector parts and services.

The placement of the services and the access scenarios follow the ALARA (as low as reasonably achievable) principle for work in a radiation environment, to ensure fastest and most easy access while minimizing the exposure to radiation for the personnel:

- Readout and alignment system back-end electronics are located in the service cavern USA15 .
- Racks for the distribution of power and gas will be located on the HS structure in the experimental cavern UX15.
- Any service distribution which is necessary for the recovery of larger detector parts in case of failures will be located at the rim of the NSW, preferably in the large sectors which are easily accessible.

All access scenarios will have to pass a risk analysis before approval.

14.2 Access during LHC operation

The access scenarios to maintain services in USA15, US15, or in UX15 on the HS structure follow the standard ATLAS access rules and are similar to other detectors in case of failures. Maintenance of the service distributions at the rim of the NSW requires access to the toroid area, with the additional complication of a possible sizable magnetic field strength during the intervention. The rim of the large sectors of the NSW is accessible from the standard muon spectrometer platforms at the level of the innermost muon stations (BI level) inside the detector. The central parts of the small sectors are inaccessible due to the barrel toroid coils, only the edges of these sectors may be accessed from the nearby large sectors.

Figure 14.1 visualizes the access paths to the different large sectors of the SW.

The access path to the NSW for sectors 3, 5, and 7 start at the detector entrance on top of the detector at $z = 0$ in sector 5, down the ladders along the radial direction to the BI level platforms, then outwards along the platforms in z-direction to the end of the barrel and the NSW. Sectors 3

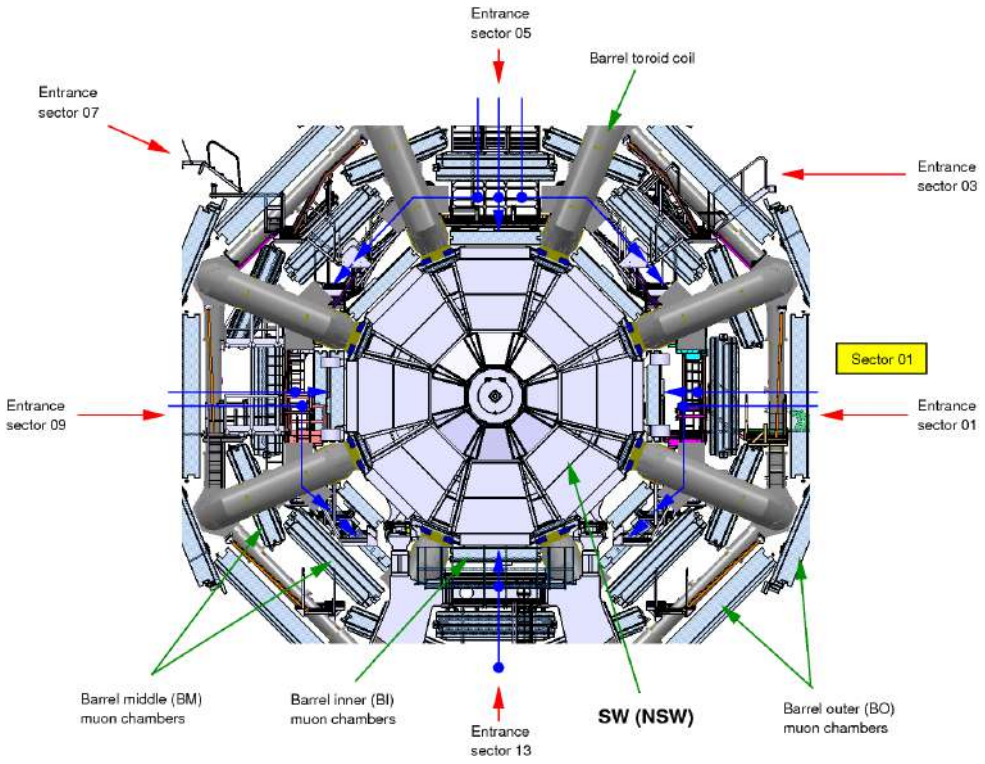

Figure 14.1: Visualization of the access paths to the large SW sectors. The drawing shows a cut through the detector in the xy-plane, with the muon access platforms inside the toroid area. All entrances to the toroid area are located at $z = 0$, except for the entrances of sector 13 which are located at the face of the barrel on either detector side. The blue lines mark movements in the xy-plane, the filled blue circles movements in the z-direction to reach respective the SW sectors. The top and bottom of the barrel region are not visible, and part of the BI muon chambers are hidden behind the Small Wheel.

and 7 are accessed by inclined ladders at the end of the barrel region. The access to sectors 1 and 15 starts at the entrance to the detector on level 4 of the HS structure on the US side at $z = 0$ in sector 1, inwards along the radial direction until the BI level is reached, then outwards along the z-direction to the end of the barrel and the NSW. The BI platforms in sector 15 can be reached by a ladder from sector 1 and the platform of sector 16. A similar path exists on the other side of the detector for sector 9 and 11 (entrance on the level 4 of the HS structure on the USA side at sector 9). The access to sector 13 uses the entrance at the face of the barrel in the trench on either side of the experiment. Ladders at the elevator shafts in sector 13 lead to the platforms at the BI level, next to the NSW.

While the rim of the NSW is directly accessible from the BI level platforms for most of the large sectors, it is hidden below the platform for sector 5. A possible solution is the installation of a trap door to avoid the need to remove floor boards for access.

Fig. 14.2 (a) shows a schematic of the access platforms and the muon chambers in sector A01, Fig. 14.2 (b) a photograph taken from the access platform in sector A01 near the SW.

In the years of detector operation since the start-up of the LHC in 2008, the experience necessary to minimize the time of interventions and the exposure to both, radiation and magnetic fields, has already been gained and procedures have been defined. The maintenance of the NSW will not be different from the maintenance of the rest of the muon spectrometer.

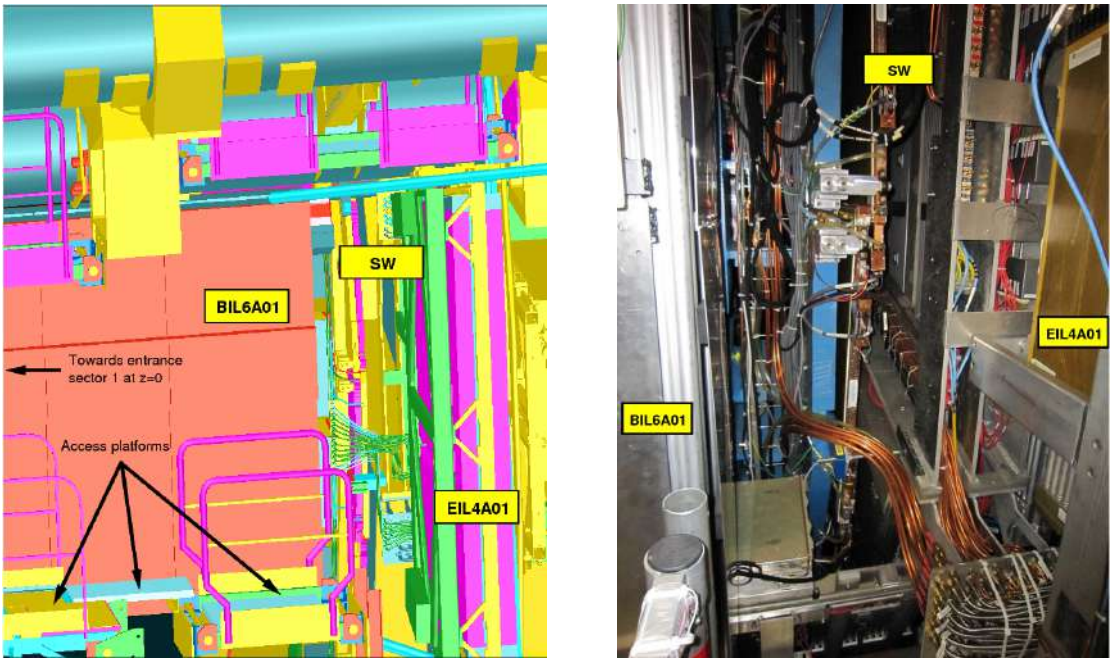

(a) (b)

Figure 14.2: Access to the SW in sector 1 on side A. (a) Visualization of the access platforms in sector 1 in the vicinity of the SW. (b) Photograph of the SW taken from the access platform. The end of one of the flexible chains in sector 1 is visible close to the lower right corner. BIL6A01 and EIL4A01 are the location identifiers of a barrel and an end-cap muon chamber.

14.3 Detector opening and movement of the NSW

The opening [75] of the ATLAS experiment during the annual and long shutdowns of the LHC foresee the movement of the SW on the barrel detector rail system to provide access to the end-cap calorimeters. For the present SW, a pair of airpads is mounted on either side of the JD shielding feet and the SW is lifted pneumatically from the rails and moved by a hydraulic system attached again the to JD feet. The movement of the NSW will use the same system, as the JD shielding will be re-used. However, the increased weight of the detectors will move the center-of-gravity of the NSW from above the middle between the airpads to (almost) the center of the outer airpad. Due to its inertia and the drag of the flexible chains for the services, the NSW might thus become unstable during its movement along the rails. Two possible approaches exist to stabilize the NSW during its movement:

1. The NSW is coupled to and moved together with either the end-cap calorimeter or the end-cap toroid.
2. An extensions with rollers is mounted on the HO side of the JD feet after the end-cap toroid has been moved to support the NSW on the barrel detector rails. The center-of-gravity of the NSW is then safely between the innermost airpad and the rollers of the extension.

Both solutions entail additional steps during the opening of the experiment, leading to a increase of the time required for the opening and therefore to an increased exposure of personnel to radiation

as well. The second approach is by far more flexible and less time consuming, but has the drawback that a minimum distance between the NSW and the end-cap toroid of about 1 m has to be kept free for the extensions at all times of the opening. It thus reduces the space available for access between the end-cap calorimeter and the JD shielding, leading to an increase of the radiation dose rate in that region due to the closer distance of the JD plug. Before a decision for either scenario can be made the implications have to be evaluated under the ALARA principles.

14.4 Access to detectors during LHC shutdown periods

The access to the NSW detectors is only possible after the ATLAS experiment has been partially opened. For the annual shutdowns, due to the time needed and due to radiation-protection concerns, maintenance on the detectors themselves is only foreseen in case of severe failures which affect the performance of the NSW, e.g. the loss of the trigger or tracking capability over a full sector, but not for individual FE-electronics cards. The situation is different for the long shutdowns during which maintenance on the NSW detectors can be accommodated in the schedule.

For the detectors on the HO side of the NSW (i.e. the large sectors), the standard opening scenario with the end-cap toroid on the small truck foresees access once a scaffolding has been erected between the NSW and the end-cap toroid. Experience for this maintenance scenario has already been gained in the four shutdown periods since the LHC start-up in 2008.

To reach the detectors on the IP side of the NSW, a gap has to opened between the detector wheel and the JD shielding. To stabilize the NSW during this opening due to the shift of the center-of-gravity and to provide sufficient space for access, two beams are coupled to the JD plug, supported by an arch fixed to the barrel rails on the HO side of the NSW.

The movement of the detector wheel itself is similar to the reverse motion of the installation, using threaded rods to slide the detector wheel on the rails of the plug and partially onto the additional beams. With such an arrangement an opening of up to 1200 mm between the JD disk and the detector wheel is feasible. If the arch has a small enough thickness (300–350 mm) it can be lowered to the barrel rails between the gap of the outermost barrel MDT chamber (BOL6) in sector 5 and the end-cap toroid on the small truck, thus allowing the use of this scenario in the standard ATLAS opening scheme without requiring the removal of the end-cap toroid from the beam line or the removal of the beam pipe itself. The two support beams (of a length of about 1500 mm) would be mounted to the arch with a pivot point and are rotated into place by 90° once the arch has been lowered to barrel rails. The arch itself is supported on rollers on the barrel rails to permit the movement for coupling to the NSW. Figure 14.3 shows the concept of the NSW opening scenario. While this opening scenario of the NSW is in principle possible in each winter shutdown, time constraints and the maintenance of other detector systems of the ATLAS experiment might dictate to use it only in long shutdowns.

The major concern of accessing the detectors on the NSW is the radiation dose any personnel working in this vicinity will be exposed to. Especially the erection of the scaffolding required to reach the detectors is a lengthy process of at least 1 day of work for several technicians.

The maximum allowed dose rate limits for personnel and the area classifications according to the CERN radiation-protection rules [50] are listed in Table 14.1.

The expected radiation dose rates in the vicinity of the SW at the beginning of LS3 (2022) have been simulated, using the present shielding and detector geometry. They will be updated once the final layout and materials of the NSW are known. The simulation has been validated with the currently available measurements.

Two different scenarios were studied:

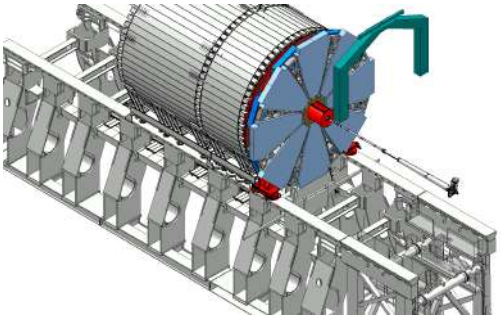

(a) Lowering of the arc by the UX15 bridge crane inside the detector. The position of the lowering along the barrel rails is shown at an arbitrary location.

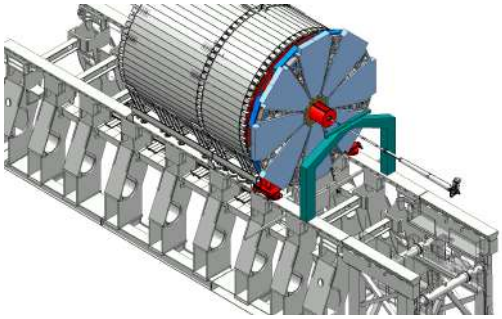

(b) Positioning and movement of the arc on the barrel rails towards the NSW.

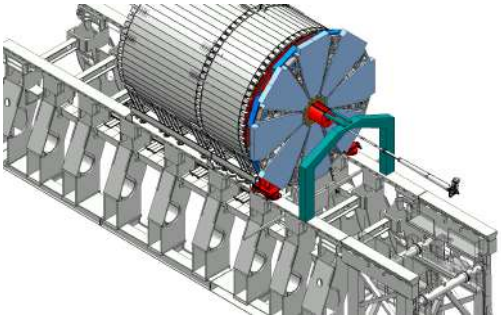

(c) Pivoting and connection of the extension beams.

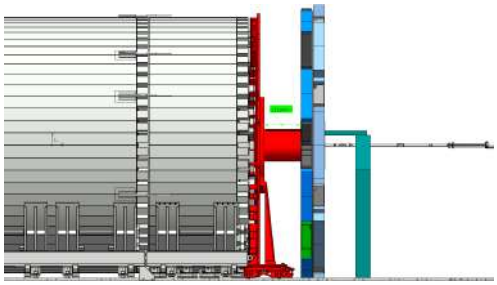

(d) View in the y-z plane in the final open configuration. The detector wheel has been moved onto the edge of the plug and onto the extension rails.

Figure 14.3: Opening scenario of the NSW. The detector wheel is moved on the plug of the JD shielding and, if necessary, further on the extension beams. During the whole process of opening, accessing, and closing, the NSW is stabilized by the arch fixed to the barrel rails. The NSW detectors are depicted in blue, the JD shielding in red. In addition, the barrel rails and part of the calorimeter are shown.

1. SW in closed configuration during 3-month shutdown

   The experiment has been opened to the standard maintenance configuration [76]: The beam pipe remains in place, the end-cap toroid has been moved on the HF truck (Fig. 14.4 (b))

   Access only to the SW detectors on the HO side

2. SW in open configuration during 3-month shutdown

   The beam pipe remains in place, the end-cap toroid has been moved on the HF truck. The end-cap calorimeter is at its nominal run position, as is the SW. The detector wheel of the SW has been moved about 1 m away from the disk shielding on the plug. (Fig. 14.4 (c))

   Access to the SW detectors on both sides, HO and IP, sides

Table 14.1: Radiation area classification and dose rate limits at CERN [50]. The third column lists the allowed dose rates at regular daily work places, the fourth column for areas which are only entered on a non-regular basis for interventions (like the NSW vicinity for maintenance).

Area	Dose limit per year	Ambient dose equivalent rate	
		Work place	Low-occupancy
Non-designated	1 mSv	<0.5 µSv/h	<2.5 µSv/h
Supervised	6 mSv	<3 µSv/h	<15 µSv/h
Simple	20 mSv	<10 µSv/h	<50 µSv/h
Limited Stay	20 mSv	n.a.	<2 mSv/h
High Radiation	20 mSv	n.a.	<100 mSv/h
Prohibited	20 mSv	n.a.	>100 mSv/h

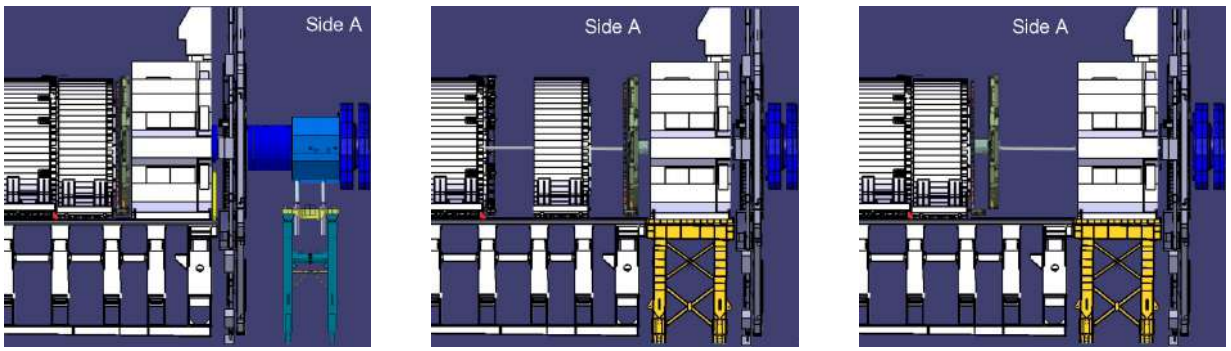

(a) Run positions. (b) Scenario 1. (c) Scenario 2.

Figure 14.4: The positions of the endcap calorimeter, the SW, and the endcap toroid of the ATLAS experiment. Only side A is shown. (a) Data taking, (b) and (c) SW maintenance during shutdowns.

A third scenario, with the detector wheel moved by about 1 m away from the disk shielding on the plug during a long shutdown, can be envisioned: In this case the beam pipe will be removed and the end-cap toroid will be moved away from the beam line to its parking position on the USA side of the cavern. The end-cap calorimeter and the SW will be moved to their positions in the standard maintenance configuration [76], or even further. Compared to scenario 2, the dose rates should be reduced on the HO side of the detector wheel due to the absence of the beam pipe and the end-cap toroid and the plug faces can be more easily closed by additional shielding as well. The dose rates between the JD disk shielding and the detectors will remain more or less unchanged compared to scenario 2.

For both scenarios, a cool-down time of 56 days after the stop of the LHC has been assumed, compatible the schedule of the standard opening scenario for the ATLAS detector (compare e.g. [77]).

The expected dose rate are listed in Table 14.2; they can also serve as an estimate for the values during the earlier annual shutdowns of 2015 and 2016. The grid points are defined as follows: negative distances are measured from the IP side of the detector wheel (located at -0 cm) to the

JD disk (at -100 cm). Positive distances are measured from the HO side of the detector wheel (at +0 cm). Radial distances are always measured from the surface of the plug (at 0 cm). The last row in Table 14.2 gives the expected dose rates on the HO side of the JD plug, measured from the surface of the plug at the height of the beam line.

The area in front of the bore of the JD plug close to the beam pipe has expected dose rates of almost 1 mSv/h up to about 1 m from the face of the plug and has to be declared a limited stay zone. To minimize the dose rates, additional shielding should be installed at the face of the plug for at least the innermost 30 cm of radius.

At the NSW detectors the expected dose rates are moderate and are not prohibitive for short-term work in the area. Most of the area can be declared as a supervised zone[1], except for the surface of the JD plug at which dose rates of 20–30 μSv/h will be reached. However, the latter area is of no interest for the maintenance as the NSW is only instrumented outside of the hub, with a minimum distance of a least 30 cm to the JD plug.

To further minimize the exposure, any scaffolding required to access the NSW detectors should leave a gap of at least 30 cm to the JD plug surface and should not extend in front of the plug.

Any maintenance work of the NSW will be scrutinized under the ALARA principles. Personnel foreseen to work on the NSW will receive special training to be aware of the risks and the procedures will be trained and tested before any intervention to minimize the time needed to complete them.

Table 14.2: Expected dose rates at different positions in the vicinity of the SW at the beginning of LS3 in 2021. A cool-down time of 56 days is assumed. Scenario 1: upright numbers. Scenario 2: boldface numbers. Negative numbers denote distances from the IP side, positive from the HO side. All distances are given in cm, all dose rates in μSv/h.

Radial distance	Distance to detectors											
from plug	-100		-50		-0		+0		40		100	
0	—	**39**	—	**31**	—	**20**	22	**16**	17	**23**	16	**17**
40	—	**5**	—	**2**	—	**8**	4	**2**	6	**9**	4	**11**
100	—	**2**	—	**2**	—	**1**	2	**1**	2	**4**	2	**6**
>100	—	**<2**	—	**<2**	—	**<2**	<2	**<6**	<2	**<6**	<2	**<6**
Radial distance	Distance to face of JD plug											
from beam pipe	-100		-40		-0		+0		40		100	
0	—	—	—	—	—	—	765	**808**	126	**286**	22	**74**

[1]This is anyway the case for the ATLAS cavern.

15 Requirements for compatibility with ATLAS Phase-II upgrade

15.1 The ATLAS Level-1 trigger in Phase-II

The ATLAS trigger system in Phase-II has to maintain a high level of selectivity for the relevant physics signatures in the presence of instantaneous peak luminosities of up to $7 \times 10^{34}\,\mathrm{cm}^{-2}\,\mathrm{s}^{-1}$. Simulation work has shown that Level-1 trigger rates can not be kept inside the present maximum of 100 kHz but have to be raised to at least 500 kHz, if the physics goals at the HL-LHC are to be maintained. Table 15.1 summarizes the minimum rate requirements for the main trigger channels[1].

Table 15.1: Requirements for Level-1 trigger rates in Phase-II, based on simulation studies, see [4].

Trigger	Estimated Level-1 Rate (kHz)
EM_20 GeV	200
MU_20 GeV	>40
TAU_50 GeV	50
di-lepton	100
JET + MET	∼100
Total	∼500

Level-1 trigger rates cannot be raised significantly beyond 100 kHz due to technical limitations of the readout systems in most ATLAS subdetectors. A widespread upgrade program has therefore been initiated to improve the performance of the ATLAS readout electronics. Even with these improvements the trigger rates in Table 15.1 can only be kept below the quoted limits, if the selectivity for the different signatures will be substantially improved.

This requires performance improvements at the level of detector parameters like spatial resolution and calorimeter granularity as well as technical parameters like buffer storage capacity and readout bandwidth. The main fields of hardware upgrade in the ATLAS subdetectors are as follows:

- The Level-1 Track trigger (ITK), generated by the Inner Detector (ID), will identify high-p_{T} track candidates, found in the RoIs defined by the Calorimeter and Muon trigger (RoI-seeded method). The availability of ID trigger information will be a new feature in Phase-II and will help, e.g., to discriminate electron against γ-showers in the LAr calorimeter.

- The L1Calo trigger will have access to the full calorimeter granularity. The fine-grained calorimeter information will improve the quality of the electro-magnetic triggers, which will be essential in order to maintain reasonably low thresholds for photons. The positions

[1] A detailed presentation of the Level-1 rate requirements of the different physics channels is given in the Letter of Intent for Phase II [4].

Table 15.2: Anticipated constraints on Level-1 rate and total latency from the proposed Phase-II readout of MDT, Liquid-Argon calorimeter (LAr), Hadron Tile calorimeter (TileCal) and Inner Tracking system (ITK).

Detector	Max. Rate (kHz)	Max. Latency (μs)
MDT	∼200	∼20
LAr	any	any
TileCal	>300	any
ITK	>200	<500

of electrons, for example, could be determined more precisely, which would improve the matching with track segments from the ITK.

- A L1Muon trigger will introduce the monitored-drift-tubes (MDT) of the muon spectrometer in the muon trigger. This enables a precise momentum reconstruction, providing better rejection against low momentum muons.

- The new Central Trigger Processor (CTP) will form the final Level-1 accept based on the Regions of Interest (RoI) supplied by the L1Calo, L1Muon and L1Track triggers.

Table 15.2 shows the maximum acceptable Level-1 rates which can be sustained by the main trigger systems after installation of new readout electronics. The maximum acceptable Level-1 latency, also being due to limitations of the readout electronics, are also shown in the same table.

As can be seen from Table 15.2, the tightest limits for both, rate and latency, are imposed by the MDT. This is due to the fact that a substantial fraction of MDT front-end readout cards ('mezzanine cards') in the barrel can not be reached for replacement or repair, and the existing readout electronics must therefore be used without change in Phase-II. In the readout electronics of these chambers the depth of the front-end data buffers limits the latency, while the available bandwidth for data readout limits the trigger rate, both values being a function of the expected occupancy of the MDT tubes at Phase-II luminosity.[2]

To assure sufficient latency for the selection of interesting physics events, it has been decided to partition the Level-1 trigger in two stages, the first, called Level-0, running at a rate of about 500 kHz with a latency of 6–7 μs, and the second, the final Level-1 trigger, running at 200 kHz with an additional latency in the range 15–25 μs. Due to the extra latency available after Level-0, the CTP may collect detailed information from the subdetectors and apply more refined algorithms for the event selection ('topological trigger'). This results in a reduction of the Level-1 rate down to the target value of 200 kHz. The increase of the first trigger latency from 2.6 to 6.4 μs gives more time to the sub-detectors to transfer detailed information to the CTP. The early occurrence of Level-0, compared to Level-1, strongly reduces the data storage needs at the detector front-ends. Data *not* flagged by a Level-0 can immediately be discarded from the buffer memories. Only events with a Level-0 trigger have to be kept up to Level-1.

[2]The derivation of the maximum acceptable Level-1 latency of approximately 20μs was originally based on a set of quite conservative assumptions. A more realistic evaluation revealed that latencies of up to 30 μs could be accepted without significant loss of information. One could, for example, ignore the trailing edge of the amplifier output without loss of efficiency or spatial resolution, all while reducing the date rate by nearly a factor 2. A detailed derivation of the acceptable latency is given in [4], section 5.1.

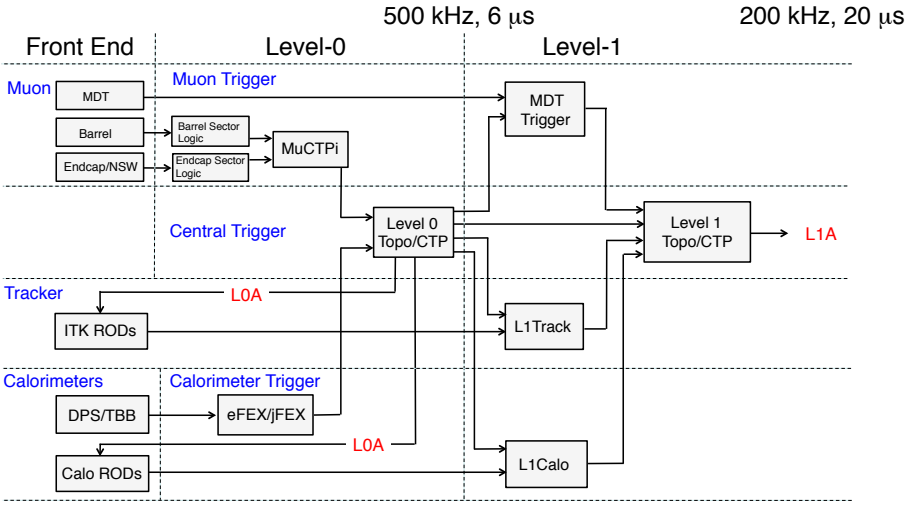

Figure 15.1: A block diagram of the architecture of the split Level-0/Level-1 hardware trigger proposed for the Phase-II upgrade (DPS = Digital Processing system, TBB = Tower Builder Board, FEX = Feature Extraction).

Figure 15.1 illustrates the data flow for the generation of Level-0 and Level-1 as foreseen for Phase-II. The trigger structure up to Level-0 closely corresponds to the trigger architecture in Phase-0 and Phase-1, where the Level-1 rate is limited to 100 kHz and the latency to 2.6 μs. Instead of one CTP in the present system, there are now two separate CTPs at Level-0 and Level-1, each performing topological processing.

In the new scheme, following a Level-0 trigger, additional information from sub-detectors like MDT, ITK and calorimeters is requested and processed for a refinement of the Level-1 trigger decision. The red arrows, marked L0A, are requests issued to specific sub-detectors before Level-0, asking for more information about the Level-1 candidate, as e.g. full granularity information from specific regions of the calorimeters, information on straight radial tracks from the ITK or precise coordinate information about a triggering muon from the MDT. In the case of the MDT, it has not yet been decided, whether the MDT information will be merged into the trigger decision at Level-0 or only at Level-1, the latter possibility being assumed in the diagram.

15.2 NSW readout compatibility with Phase-II

15.2.1 Requirements to cope with the Phase-II trigger scheme

An extensive upgrade of the ATLAS trigger and detector performance, capable to match the luminosity increase of up to $7 \times 10^{34}\,\mathrm{cm}^{-2}\,\mathrm{s}^{-1}$ is foreseen for Phase-II, when many of the stringent hardware limitations for the detector upgrade will be gone. The trigger and readout architecture developed for the high luminosity operation mode has been described above.

The readout of the NSW must be prepared to smoothly interface to the new trigger and readout scheme, as described above, and must keep options open for those features of the Phase-II readout, which have not yet arrived at a final decision.

The NSW readout has to deliver information about trigger and event data at different stages of the trigger and data acquisition cycle. The main requirements for the NSW readout to be prepared for Phase-II are:

Table 15.3: Summary of the signal traffic in the end-cap of the muon spectrometer in Phase-II (SL = Sector Logic).

Time	Source	Destination	Comment
BX ⇒ L0	TGC/NSW	SL	Hit information R,ϕ, dθ
40 MHz	MM/NSW	SL	Hit information R,ϕ, dθ
	TGC/BW	SL	L0 generation
	SL	CTP for L0	High-p_{T} candidates
BX ⇒ L0	SL	Tower module	RoI of high-p_{T} candidate
MDT based	TM	SL	MDT hits in the RoI
trigger	MDT in BW	SL	All MDT hits in the BW
BX ⇒ L0	Event data	Primary	Event related data to be stored
40 MHz		buffers	at 40 MHz rate during L0-latency
L0 ⇒ L1	Primary	Secondary	Store data during L1-latency
500 kHz	buffers	buffers	*(On average ∼ 60 events)*
L1-accept	Secondary	ROD	'Slow' readout of all data
200 kHz	buffers		

- Being an important element of the muon trigger in the end-cap, the NSW has to confirm high-p_{T} candidates as detected by the primary trigger logic of the TGC in the Big Wheel (BW). As already required in Phase-I, the NSW trigger logic has to certify, among others, that the candidate track is pointing to the primary vertex. In Phase-II, however, more information about the coordinates R, ϕ and the slope θ in NSW and BW must be supplied to the L0-CTP (cf. Fig. 15.1). This is important input for the Level-0 trigger decision, which at Phase-II will take topological criteria, like the isolation between a muon track and a jet, into account. The extra transfer time due to the additional data is no problem due to the increased Level-0 latency.

- In Phase-II an interface is needed between the end-cap trigger logic and the MDT readout in order to support the trigger option of the MDT. In the case of the RoI-seeded method, the coordinate in the bending direction r must be supplied from the SL to the Tower Module (TM) to define a RoI. The RoI predicts the track position in the tubes of the MDT chambers to within 1–2 tube diameters, limiting the data to be read out to a narrow road along the RoI and ignoring the large majority of data not related to the triggering track. In the case of the self-seeded method, the information from the TGC trigger and the MDT track finding logic will be combined at the level of the SL. A detailed discussion of the two methods is given in section 15.2.2.

- All data in NSW and BW, including the large majority of data not related to a triggering track, must be stored in a primary buffer during the Level-0 latency (256 BX). After a Level-0 accept, data must be transferred from the primary to a secondary buffer, waiting for an accept or reject at Level-1. With a Level-1 latency of 30 μs and a Level-0 rate of 500 kHz the average occupancy of the secondary buffer is 15 events, so an actual depth of 32 seems to leave a safe margin for rate fluctuations. Alternatively to the double-buffer scheme, the use of a single buffer could also be envisaged. In this case, data from all BX during the Level-1 latency, will have to be stored, requiring a buffer depth of $40 \times 30 = 1200$ events.

Table 15.4: Spatial and angular resolution of the TGC and MDT in the Big Wheel. The second column gives the width of the ganged wire groups in the TGC at the inner and outer boundary of the BW. In the case of the MDT it is the average drift distance during one clock cycle of 25 ns.

Chamb. Type	LSB error (mm)	RMS error (mm)	Lever arm (mm)	RMS slope (mrad)
TGC, R ∼2 m	11	3.1	1713	1.8
TGC, R ∼9 m	56	16.1	1713	9.5
MDT R ∼2–9 m	0.5	0.15	252	0.6

- At the time of writing of this report, the exact protocol for the Level-0/Level-1 trigger broadcasts has not yet been decided. During Phase-I the present scheme, where the Level-1 trigger is distributed via the TTC network, will remain in operation. This means that the readout of the NSW must be designed to support the TTC as well as the future trigger distribution scheme.

Table 15.3 presents a summary of the data traffic expected for the end-cap of the muon spectrometer in Phase-II. The main data transfer activities in the periods between BX and Level-0 trigger (BX ⇒ L0) and between Level-0 and Level-1 (L0 ⇒ L1) are shown.

15.2.2 The NSW readout and the MDT high-p_T trigger in Phase-II

The use of MDT precision coordinates for the refinement of the high-p_T threshold is an efficient tool to keep the muon contribution to the Level-1 trigger rate inside the 40 kHz budget foreseen for Phase-II (cf. Table 15.1). In the case of the end-cap the spatial resolution along r in the BW is decisive for the p_T-measurement of the triggering track. The p_T-resolution depends mainly on the difference of the track's slope in front and behind the EC toroidal magnet. While the NSW trigger will determine the θ angle with an accuracy < 1 mrad, the TGC in the BW will only achieve an angular resolution in the range 2–9 mrad, due to the pattern of wire ganging along R used in the TGC (see [2], section 8.2.2.2). The two MDT multilayers in the BW, being located between TGC1 and TGC2, have a lever arm of 252 mm between multilayers for measuring θ, compared to 1700 mm between TGC1 and TGC3. Due to their superior spatial resolution, however, they achieve an angular resolution of about 0,6 mrad[3]. With an angular resolution below 1 mrad, the MDT in the BW matches the angular resolution of the NSW and thus provides important input for sharpening the high-p_T threshold. Table 15.4 gives a summary of the numbers relevant for the slope resolution in the BW.

Two methods have been proposed to use MDT tracking capabilities for an improvement of the p_T determination, leading to the rejection of a large fraction of below-threshold track candidates. In the RoI-seeded method, see Fig. 15.2, only those regions of the MDT are considered, where the trigger chambers have already identified a high-p_T candidate. In the self-seeded method *all* hits from all MDT in each sector are transferred via high speed links to the Sector Logic (SL), where they are processed for track candidates pointing to the IP. Track candidates without a match in the trigger chambers are subsequently discarded, removing fake triggers.

[3]This value is based on the BX clock frequency of 40 MHz. While there is no technical obstacle, to also consider higher clock frequencies, the gain for the angular resolution resulting from a frequency increase would have to be justified by a more detailed evaluation.

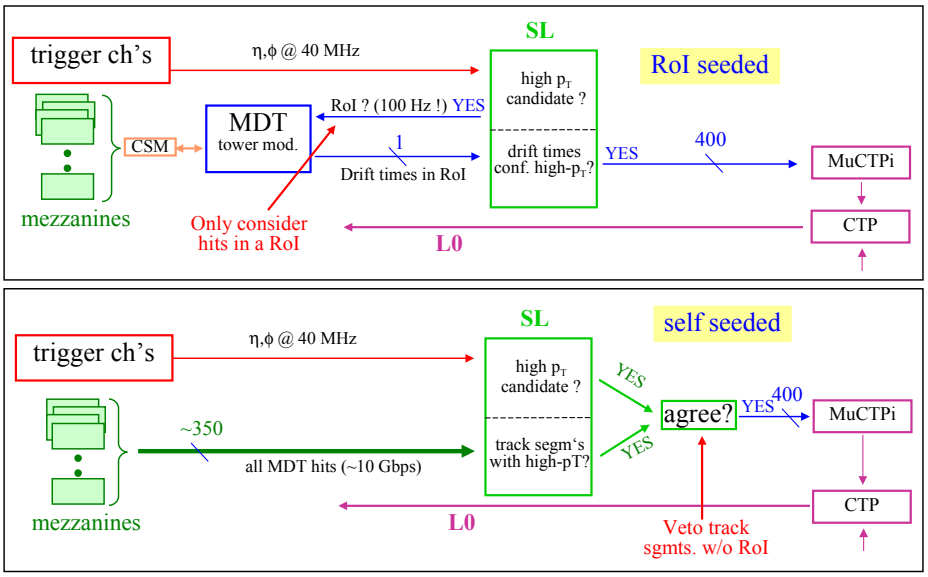

Figure 15.2: Flow diagram of the MDT Based L0-trigger for the RoI-seeded (top) and the self-seeded approach (bottom). The numbers of fibers before the Sector Logic (SL) are given per trigger tower. There are about 400 trigger towers in the muon spectrometer. The RoI-seeded method needs a back channel from the SL to the Tower Module (TM), identifying the RoI of the triggering track.

The rate of fake tracks found with the self-seeded method strongly depends on the background hit rate. Random hit patterns may generate fake trigger candidates, while background hits may mask valid hits. This comes in addition to other sources of inefficiencies of the MDT, like δ-rays or particles passing through dead material, which makes the recognition of tracks less reliable. It must also be kept in mind that the MDT in the end-cap are only equipped with 2×3 tube layers, providing little redundancy for track recognition in the case of inefficiencies or random hits.

The necessity of transferring *all* MDT hits to the processors in USA15 in the case of the self-seeded method leads to bandwidth requirements of about 5–10 Gbit/s for each group of 24 tubes. Consequently, each mezzanine card has to be equipped with an optical link, resulting in approximately 5000 links for the Big and Outer Wheels. In the self-seeded method, the MDT does not require feedback about the RoIs from the trigger logic and less latency is needed compared to the RoI–seeded method. Timing estimates lead to a latency of $< 2.55\,\mu$s, compatible with the Level-1 latency of $2.6\,\mu$s in Phase-I. In Phase-II, however, a short latency is no longer an important parameter.

15.3 Decisions to be taken for compatibility with Phase-II

The architecture of the NSW readout needs to take the specific features of the Phase-II trigger and readout concept into account, in order to guarantee a smooth transition from Phase-I to Phase-II. Main issues are compatibility with the Level-0/Level-1 trigger concept, the new trigger distribution scheme (replacing the present TTC system) and, finally, the design of an interface to the MDT for the inclusion of precision coordinates into the trigger decision.

16 Project organization and management

The NSW will be built by a group of ATLAS institutions, which commit to develop, design, construct and commission the NSW system. The group includes both institutes which were already involved in building of the current muon spectrometer as well as new institutions. While the NSW is an upgrade project of a part of the muon spectrometer, the NSW project will have a dedicated organization and management structure. The resources will also be handled separately from the muon spectrometer. After the completion, the NSW will become a part of the muon spectrometer. The point in time for this step is with the completion of the NSW assembly and surface commissioning.

Close collaboration between the NSW management and the muon spectrometer management will be crucial throughout the NSW project, from its earliest phase on: it will be ensured in particular by frequent exchanges between task conveners, a common institute board and by many collaborators and participating institutes being involved both in NSW and the current muon system.

16.1 Institute board

All institutions and institutes participating in the NSW project are members of the muon institute board (IB) which is the body for both the NSW project and the ATLAS muon spectrometer. Participation of a new institute to the NSW project therefore requires the institute to become a member of the muon IB. The process by which new institutes are admitted to becoming members of the muon IB is the one set out by ATLAS as standard procedure, in particular, if an institute is already involved in ATLAS in a subsystem other than muons, it should be ensured by discussions on EB and CB level that no holes are created in the activities of the system the institute so far contributed to and that responsibilities remain covered.

16.2 Management structure

The management structure of the NSW project is shown schematically in figure 16.1.

16.2.1 NSW project leader

The NSW project is led by a project leader (PL), elected by the muon IB. The PL is responsible for overseeing the design, construction and surface commissioning of the NSW. His or her mandate starts with the completion and approval of the TDR and ends with the completion of the surface commissioning phase of the NSW, at which point the NSW will be part of the muon system overall and its organization.

The NSW PL first term of office is two years, with periodic reelections as prescribed by the ATLAS collaboration.

The NSW PL forms a management board which is responsible for executing the project, including overseeing resources and ensuring the timely completion of milestones. The PL regularly communicates the status of the project to ATLAS management and to the muon IB.

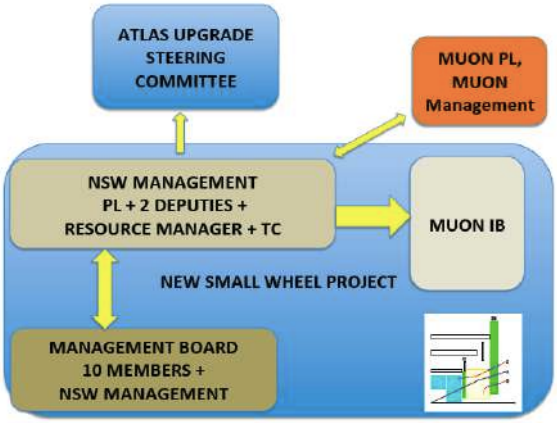

Figure 16.1: Organization of the NSW project.

16.2.2 Management board

The NSW management board will be the core body to coordinate and oversee the various aspects of the NSW project. The PL shall appoint two deputies, one from the MM, one from the sTGC community who will be responsible for following the progress, planning and technical details within detector design and construction, for the respective technology. The PL deputies will be endorsed by the muon IB. In addition to the PL deputies, the following responsibilities are foreseen within the management board:

Resource manager.

Layout and Mechanics: The responsible shall lead the NSW layout group, closely working with technical coordination and chamber construction experts. Core tasks are all aspects associated with the mechanical structure of the NSW, as well as installation and handling procedures.

Services: The responsible will follow and take responsible for developing the detailed services architecture for the NSW, including powering, cooling, gas and routing of services. The services responsible shall work closely with the layout and mechanics coordinator, and with technical coordination. A core task shall be to ensure from the early state on the smooth integration of the NSW into the existing muon spectrometer infrastructure.

Alignment: The alignment task responsible will take care an efficient alignment strategy for the NSW chambers is implemented, including overseeing appropriate alignment devices are part of the design. He/she will closely collaborate with both MM and sTGC communities as well as with the Layout and Mechanics responsible.

Production and quality assurance: The responsible will be in charge of implementing and overseeing systematic quality control procedures, as well as play a leading role in organizing production site reviews. In the second stage of the project, his/her tasks will extend to organizing and coordinating the testing of assembled sectors and surface commissioning at CERN.

Logistics.

Software: The responsible shall oversee, lead and coordinate the activities related to integrating the NSW within the software, in particular within reconstruction and detector description. Another core task within the field of software will be the Simulation, which shall be coordinated by a dedicated responsible.

Electronics: The responsible will coordinate the design, development and production in particular of the common front end electronics components. He/she will work closely with both the MM and

sTGC communities.
DAQ: The responsible will ensure the NSW can be smoothly integrated with the rest of the ATLAS TDAQ system.
Control system: The responsible will coordinate and oversee activities related to controls and DCS aspects of the NSW, including ensuring compatibility with the existing muon system
Trigger: The responsible will coordinate and overview all aspects related to the trigger functionality of the NSW, including the close liaison to the ATLAS trigger community. He/she will work closely with both MM and sTGC teams.

16.2.3 The NSW institutes

The NSW institutes have shown their intention of commitment to the NSW project, and many of them have already been working on the developments in the various areas of the project. Table 16.1 and 16.2 summarizes the present status of the NSW institutes and their corresponding area of interests. Detail of responsibility and sharing will be defined in the MoU for NSW construction.

16.3 Cost estimate

Earlier cost estimate of the NSW was shown in the phase-1 letter of intent (LoI) [3], calculated for one of the three technology options discussed there. As the final layout presented here is different and that is made of a combination of the detector technologies considered, the cost is updated and the CORE cost is shown here in table 16.3 with the highest level cost breakdown, based on the layout presented in this document and reflecting the progress of detector developments by now.

In general the cost of individual items are calculated based on a unit price and an estimate of the quantity required. The quantity is the number of items actually installed on the detector. In addition, cost of some items such as tooling essential for constructing the detector and quality control procedures are included in the cost. The cost for spares are not included in general.

In the case of ASIC production, the quoted CORE cost does not include the cost for prototyping. Only the cost for the final version (including NRE) are counted.

The accuracy of the cost estimate varies from item to item: some are based on close to the final design and cost information from the venders, whereas some are based on less mature design or the material cost based on limited experiences within prototype production. In all cases, the estimated cost of items are, where there are uncertainties, considered to be conservative. However it should be understood that there can be possible changes of the cost in future arising from effects such as cost increase of some materials and influence of currency rate changes. The cost of the optical alignment system depends on the detail of the final mechanical design of the detector, its mechanical properties, and the way how they are supported, requiring further design work and testing. The number of required precision alignment device (the alignment bars) may be either 8 or 16. The cost quoted in table 16.3 is for the configuration of 8 alginment bars (the same as the present system), while additional cost for possible increase to 16 is shown separately in the 'possible additions' column.

The total estimated cost is 11.4 MCHF of CORE value. A part of the mechanics are shown separately as common items, which include the cost of detector support structure, radiation shielding and installation tooling. The costs for the NSW trigger processors in USA15 (Sections 12.3.1 and 12.3.2), amounting to 315 kCHF for sTGC, 357 kCHF for MM and 21 kCHF for shared items (crates), as well as the sector logic (Section 12.3.4) are not included here, but it will be counted a part of the ATLAS TDAQ upgrade project (TDR in preparation). Note that the DAQ cost may also be treated as a TDAQ project depending on the detail of the DAQ scheme.

Table 16.1: List of participating institutes and area of interest (I)

		1	2	3	4	5	6	7	8	9	10	11	12	
		sTGC construction and tests	MM construction and tests	Alignment system	Mechanics, tooling, shielding	FE ASIC	FE electronics	Trigger electronics	DAQ, configuration	DCS system	HV, LV	On-detector services	Simulation, reconstruction	Integration, commissioning
Carleton cluster	Canada	x											x	x
McGill cluster		x												
TRIUMF cluster		x												x
Chile cluster	Chile	x				x								x
Chinese cluster	China	x				x		x					x	
Saclay CEA	France		x	x				x	x				x	x
Freiburg	Germany			x	x					x		x		
Mainz			x				x						x	
Munich LMU			x										x	x
Wurzburg													x	x
U. Atehns	Greece						x						x	x
NTUA			x				x	x	x	x			x	x
Tessaloniki			x				x	x	x				x	x
Technion	Israel	x					x	x	x	x		x	x	x
Tel-Aviv		x					x	x	x				x	x
Weizmann		x			x		x	x	x			x	x	x
Bologna	Italy							x					x	
Cosenza			x										x	
Frascati			x		x							x	x	x
Lecce			x											x
Napoli			x					x						x
Pavia			x								x	x	x	x
Roma I			x					x					x	x
Roma 2								x						
Roma Tre			x										x	x
Kobe	Japan		x											
Kyoto		x												
Tokyo ICEPP			x					x					x	x
Amsterdam	Netherland			x					x			x		
Mijmegen				x					x			x		
NIKHEF				x					x			x		
Bucharest cluster	Romania				x	x		x	x	x			x	x
Dubna	Russia	x	x									x	x	x
Moscow cluster		x	x										x	x
Petersburg NPI		x					x	x						
CERN	Switzerland		x		x							x	x	x
Taipei AS	Taiwan						x	x						

Table 16.2: List of participating institutes and area of interest (II)

		1	2	3	4	5	6	7	8	9	10	11	12	
		sTGC construction and tests	MM construction and tests	Alignment system	Mechanics, tooling, shielding	FE ASIC	FE electronics	Trigger electronics	DAQ, configuration	DCS system	HV, LV	On-detector services	Simulation, reconstruction	Integration, commissioning
Arizona	USA					x	x	x						x
Boston			x				x	x						x
Brandeis			x	x										x
BNL						x	x	x						x
Harvard			x					x						x
Illinois									x				x	x
UC Irvine								x	x				x	x
Massachusetts			x										x	x
Michigan						x	x	x			x	x	x	x
MIT			x											x
Oklahoma State					x								x	x
SLAC									x				x	x
SMU						x		x						x
Tufts													x	x
UT Austin													x	x

1 sTGC production, QC, engineering, assembly, testing at various stages
2 MM production, QC, engineering, assembly, testing at various stages
3 Alignment system
4 wheel structure, hub, disk shielding, installation tooling,
5 VMM, VMM companion, TDS,
6 FE cards, on-detector electronics (pad logic, router, …)
7 USA15 trigger logic
8 Readout system, FE configuration, data monitoring, ..
9 DCS system, including associated sonsors, etc.
10 HV, LV, powring
11 Cooling, gas distribution, ….
12 Simulation, reconstruction, performance studies

Carleton cluster	Carleton, Alberta, Toronto
McGill cluster	McGill, Montreal
TRIUMF cluster	TRIUMF, Victoria, SFU
Chinese cluster	Shanghai, Shandong, NTSC
Chilean cluster	UTFSM/CCTVAL, PUC
Bucharest cluster	IFIN-HH, ITIM
Moscow cluster	MEPhi, Lebedev, Lomonosov

Table 16.3: NSW cost table.

Item	CORE (kCHF)	Possible addition	Common item	2013	2014	CORE 2015	2016	2017	2018
sTGC detector	2,419			385	962	874	173	25	
MM detector	2,804			15	430	2,070	289		
Alignment system	610	132				59	474	77	
Mechanics, integration	150		1,558			60	60	30	
FE ASIC	1,049					682	367		
FE electronics	2,206				149	829	1,227		
DAQ(*), configuration	267						19	248	
DCS system	87				32		55		
HV, LV	1,600					500	500	600	
On-detector services	181					60	100	21	
Total	11,373	132	1,558	400	1,573	5,134	3,265	1,001	

16.4 Resources

The cost of the project is planned to be covered by all institutions participating the NSW project. Discussion among the institutions and the funding agencies are on-going in order to define the detailed list of deliverables, responsibility and the sharing of the project cost. The commitments of each funding agencies will be formulated in the MoU of NSW construction. Common items will be handled separately (CERN-RRB-2012-078, CERN-RRB-2012-07), and will not be included in the MoU.

16.5 Planning and milestones

The NSW project consists of R&D of detector technology and electronics, evaluation of required and expected performance using ATLAS data and simulation, prototyping and construction of the final system including various steps of quality control. The project schedule is shown in figure 16.2.

The important timing which determines the schedule is the installation in ATLAS in 2018. This process is a major operation including the removal of the existing small wheels from ATLAS and disassembling the detector from the JD shielding to prepare for mounting of the NSW. Modification of radiation shielding is also included in this process.

Before the installation, it is planned that the completed wheels are fully tested on surface during 2017 for about one year. In that way sufficient time for the commissioning of the detector is available, including possible repair or replacement, and for tests of the electronics system as well as for the preparation and testing of readout, control and monitoring software, with the complete detector system serving as a test bed. Based on the experience gained for the current Small Wheel commissioning and installation, commissioning on surface should be fast. For contingency this time is expanded to one year. In order to match the above schedule, the production of the chamber multiplets, which is expected to take at maximum two years, should start from 2015. Year 2014 will be devoted to the production of module-0 and its qualification. Finalization of the chamber construction procedure, preparation of the tooling and infrastructure for qualification should proceed in parallel during this period.

Delivery of the final front-end boards should ideally start in time for the production of sTGC and MM multiplets at the construction sites and the tests of the detectors with the final front-end

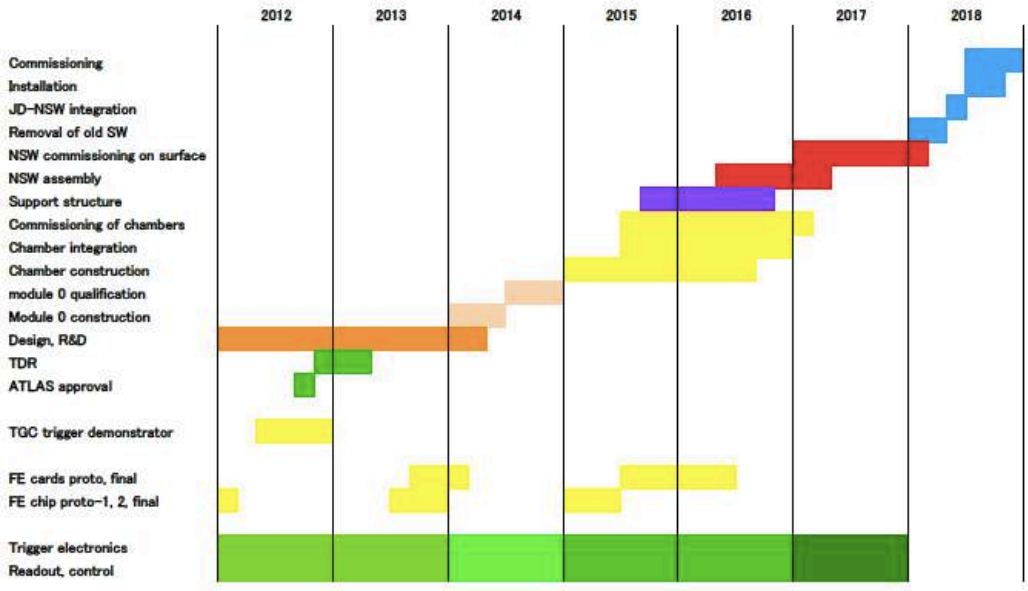

Figure 16.2: Time-line of the NSW project.

Table 16.4: List of major milestones.

Milestone	Due
Submission of VMM ASIC prototype 1	Beginning 2012 (done)
Submission of VMM ASIC prototype 2	August 2013
Submission of final FE ASIC	2015
Construction of module-0	First half of 2014
Start chambers production	January 2015
Start assembly of sectors	Mid 2015
NSW Assembly	Mid 2016
Installation	2018

boards integrated. However the currently estimated time of the ASIC production will be middle of 2015. In this case, a sufficient number of the front-end boards will be produced using the second prototype, VMM2, and can be made available for the testing.

Development of trigger, readout and powering system will also be done in parallel and to be completed for commissioning by 2017.

A crucial element of the detector is the common front-end ASIC. The first prototype (VMM1) has successfully been produced and evaluated during 2012. The second prototype, VMM2, that will have almost all of the functions as the final version, is expected to be submitted during the second half of 2013. Delivery of the production version should start in 2015 in order to be in time for the sector assembly and testing.

A list of major milestones is presented in Table 16.4.

A Naming conventions

A naming scheme has been developed to so that a single detector elements within the experiment and in the online and offline software may be identified. Naming actually refers to three different schemes:

Object type : Predefined name such 'plane', 'module', etc... Objects of the same type are further differentiated by their **subtype**, depending on their final location.

Location : Place to be filled by an object of the corresponding type. Identifiers used by the online and offline programs actually refer to locations.

Physical object : Type or subtype with its serial number; this identifier is used for construction, certification and installation. The object name should **not** reflect a particular location since a given object can be mounted in several locations while several physical (spare) objects can be mounted at a given location.

A.1 Object types

Several object types have been defined. Depending on the final layout of the New Small Wheel some of these types may never be used; however they are listed here for completeness. An effort has been made to use the same names across technologies; this is why the ambiguous terms 'detector' and 'unit' are not defined on purpose. Figure A.1 shows a typical breakdown of the objects in types.

Plane : Single detector gas gap. The smallest working detector element of a given technology.

Multiplet : Assembly of n planes of a single technology (sTGC or MM) in $z-$direction ($n = 4$ in the current design).

Module : The assembly of m multiplets ($m \geq 1$) in $r-$direction which constitute a single independent object produced as a unit. In the current design, only the sTGC modules at small r are made of more than one multiplets.

Chamber : The assembly of two modules of a single technology (sTGC or MM) in the z direction and one or more modules in the r direction which constitute a single independent object. A chamber might include an internal or external spacer frame between the modules in the z direction. Note that this object type might not exist, depending on the final choice for MM and sTGC assembly

Station : The assembly of two sTGC modules and two MM modules in the z direction and one or more modules of each type in the r direction which is aligned as a single object.

Wedge : The assembly of modules of a single technology type (sTGC or MM) covering a sector in the $r - \phi$ plane. Note that a wedge is equivalent to the 'supermodule' described below.

Sector : $1/16^{th}$ of the NSW on side A or C (corresponding to a large or small geometric sector), comprised of two sTGC wedges and two MM wedges.

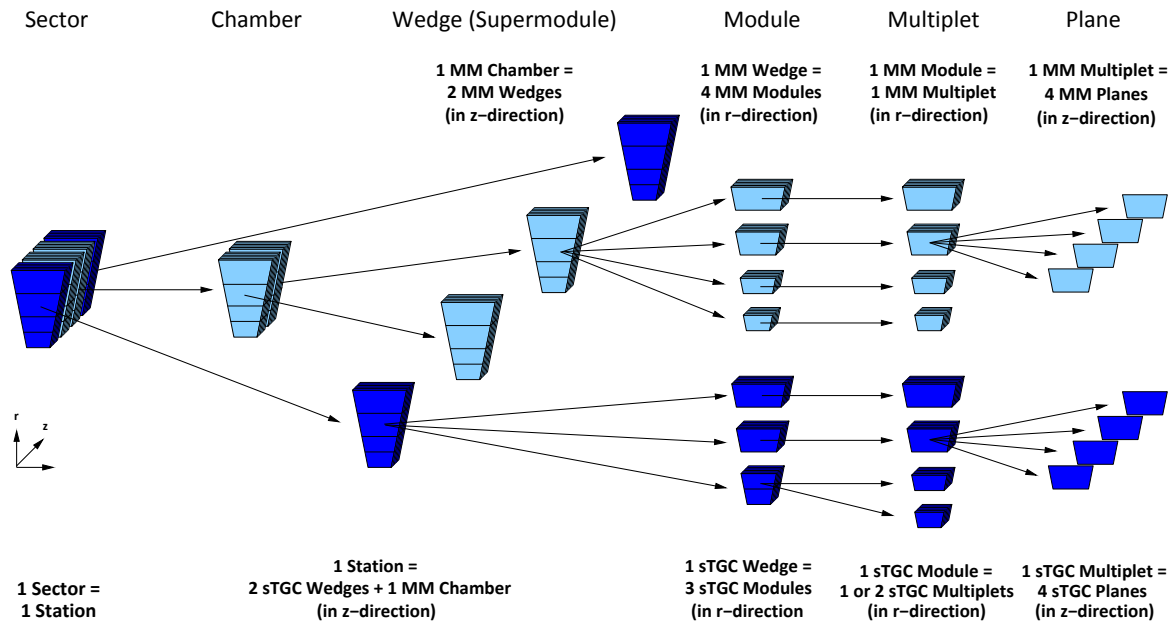

Figure A.1: Breakdown of object types. The number of objects of each type is only representative, see text for object deinitions.

'Super Object' —In order to refer to a virtual or real object consisting of similar components at various r, the prefix 'super' can the used. Uses of this modifier include

Super Plane : Virtual assembly of planes at the same Z; in the sTGC context, it is the basic object used by the trigger finders.

Super Module : Homonym for 'Wedge'.

A.2 Locations

The location identifier specifies in a unique fashion the position of a detector element in the ATLAS experiment. For the NSW a scheme similar to the current MDT location identifier scheme is used: like that elements in different detector regions, sectors, and different locations in the radial coordinate can be distinguished. The generic name for a location is:

{EI}[LS]{x}{w{p}}[AC]yz

Only one character of a set enclosed in brackets can be used in a given identifier, and characters enclosed in curly braces are only specified when needed: for example, indices x,w, and o is omitted in the location of a complete sector.

EI : Denotes the End-cap Inner region, the location of the NSW.

LS : Distinguishes between locations in a large and small sector, respectively. Note that denoting large and small sectors is redundant, as the odd sectors are always large and the even sectors always small. This is kept for compatibility with the MDT location scheme.

x : Index (≥ 1) identifying the position in increasing radial distance from the beam line. If a range of four identifiers is needed, x is in the range ($0 \leq x \leq 3$) to avoid clashes with the existing EIL4 MDT station location identifier.

AC : Distinguishes between locations on side A and C of the ATLAS experiment, respectively.

yz : Denotes the sector, ranging from 01,02,..,16, i.e. including a leading 0 if necessary.

w : Denotes the wedge index, in $|z|$.

p : Denotes the plane number. Currently $1 \leq p \leq 4$.

Note that an effort was made to follow the *enumeration rule* for layer, whenever possible, r division, channel numbers:

- Enumerations for the human eye should start at **1**. However an exception to this rule had to be made for sTGC multilayers and planes, for which the r division index runs from 0 to 3.
- Internal arrays in computer codes should start at **0**.

A.3 Physical objects and subtypes

Physical objects are identified by their technology, their type (preferably their subtype), and a serial number. Subtypes are named according the generic location they can fit in. For example:

(NSWSECTOR) EIS : small NSW sector.
(MMMODULE) EIS3A : a MM module for the outermost (in radius) location in small sector of side A
(STGCPLANE) EIS324A : a sTGC plane, the last one in the outermost (in radius) module of second wedge in sector 4 of side A

It is proposed to keep the same system and rules as presented in the ATLAS Muon Technical Design Report [6].

B Glossary

ALARA **A**s **L**ow **A**s **R**easonably **A**chievable. A radiation safety principle for minimizing the radiation dose by employing all reasonable methods. A requirement to be analysed and fulfilled for all interventions on the detector or its services.

APV25 The front-end chip historically used for evaluation studies of the MM technology.

ARAMyS **A**lignment **R**econstruction for the **A**TLAS **M**uon **S**pectrometer, the software that computes chamber displacements and rotations from alignment sensor measurements.

ATLAS **A** **T**oroidal **L**HC **A**pparatu**S**. A multipurpose detector at the LHC.

BCAM **B**randeis **C**CD **A**ngular **M**onitor, an alignment sensor consisting of a CCD camera and a pair of laser diodes; in ATLAS, polar BCAMs link alignment bars between wheels, azimuthal BCAMs link alignment bars in the same wheel.

CSC **C**athode **S**trip **C**hamber. A multiwire wire proportional chamber with readout of the induced charge on the cathode strips. Used in the ATLAS experiment in the innermost region of the end-caps of the original SW.

EI End-cap inner. Used to specify the location of a muon chamber.

EM End-cap middle. Used to specify the location of a muon chamber.

EO End-cap outer. Used to specify the location of a muon chamber.

FELIX Front-end LInk eXchange, is a Front-end Interface that aggregates and integrates several GBT links onto a higher bandwidth, industry standard network technology, e.g. Ethernet or Infiniband, from where standard network switches and protocols can be used to route data to and from the appropriate off-detector end-points.

FEM **F**inite **E**lement **M**ethod. A numerical technique to find an approximate solution to boundary values problems.

HF truck A movable support which can be coupled to the barrel rails in the ATLAS experiment at the face of the barrel region, extending the rails and allowing to move parts of the ATLAS detector to the outside.

HO side The side of a detector facing towards the HO structure, i.e. facing away from the interaction point.

IP The proton-proton **i**nteraction **p**oint within the ATLAS spectrometer.

IP side The side of a detector facing towards the interaction point.

L1Calo The ATLAS Level-1 trigger based on the calorimeter information.

L1Muon The ATLAS Level-1 trigger based on the detectors of the muon spectrometer.

L1Track The ATLAS Level-1 trigger based on the tracking detectors.

Level-1 The ATLAS Level-1 trigger system.

LHC The **L**arg **H**adron **C**ollider. The high energy pp collider at CERN.

LWDAQ **L**ong-**W**ire **D**ata **a**c**q**uisition system for reading out the alignment sensors of the MDT end-cap alignment system.

MDT **M**onitored **D**rift **T**ube chamber. A precision tracking detector consisting of densely packed layers of drift tubes on a spacer frame. Deformations of the chamber geometry are monitored by optical sensors. MDT chambers are the primary tracking detectors of the ATLAS muon spectrometer.

MM Detector used for the New Small Wheel project based on the **M**icro**M**egas technology.

Module Assembly of ≥ 1 multiplets in $r-$direction which constitute a single independent object produced as a unit.

Multiplet Assembly of n detector planes of a single technology (sTGC or MM) in $z-$direction.

NSW **N**ew **S**mall **W**heel Detector as part of the ATLAS Muon spectrometer (upgrade of the current end-cap Small Wheel detector).

PCB **P**rinted **C**ircuit **B**oard..

Plane Single detector gas gap. The smallest working detector element of a given technology.

RASNIK **R**ed **A**lignment **S**ystem of **NIK**HEF, an alignment sensor using an illuminated mask with a modified chessboard pattern; used in ATLAS for instance as the inplane system monitoring MDT chamber deformations.

RPC **R**resistive **P**late **C**hamber. Narrow gap gaseous detector formed by two parallel resistive bakelite plates. RPC chambers are used in the barrel part of the ATLAS muon spectrometer for trigger purposes due to their very fine time resolution (a few ns).

Sector $1/16^{th}$ of the NSW on side A or C, corresponding to a large or small geometric sector.

sTGC Detector used for the New Small Wheel project based on the **s**mall **T**hin **G**ap **C**hamber technology.

Super Plane Virtual assembly of detector planes at the same z.

TGC **T**hin **G**ap **C**hamber. A multiwire wire chamber with 2-dimensional readout of the wire and of the induced charge on the cathode strips perpendicular to the anode wires. Used in the ATLAS experiment as trigger chamber in end-caps of the muon spectrometer.

US side The side of the experimental cavern UX15 which is closest to the service cavern US15.

USA side The side of the experimental cavern UX15 which is closest to the service cavern USA15.

VMM The VMM is a configurable, radiation hard front-end ASIC, developed for both the MM and sTGC detectors, that incorporates the analog circuitry for reading out particle detectors, time and amplitude digitizers and digital logic for buffering the data and transmitting it out on-demand..

Wedge Assembly of modules of a single technology type (sTGC or MM) covering a sector in the $r - \phi$ plane.

The ATLAS collaboration

Argentina
Buenos Aires
M.L. Gonzalez Silva, G. Otero y Garzon, R. Piegaia, G. Romeo

La Plata
M.J. Alconada Verzini, F. Alonso, X.S. Anduaga, M.T. Dova, F. Monticelli, M.F. Tripiana

Armenia
Yerevan
H. Hakobyan

Australia
Adelaide
P. Jackson, N. Soni

Melbourne
E.L. Barberio, S. Diglio, K. Hamano, D. Jennens, T. Kubota, A. Limosani, G. Nunes Hanninger, Q.T. Shao, K.G. Tan, G.N. Taylor, W.M. Thong, M. Volpi, M.J. White

Sydney
A. Bangert, C.W. Black, C. Cuthbert, G.-Y. Jeng, N.D. Patel, A.F. Saavedra, M. Scarcella, K.E. Varvell, I.J. Watson, B. Yabsley

Austria
Innsbruck
S. Franz, P. Jussel, E. Kneringer, W. Lukas, K. Nagai, E. Ritsch, A. Usanova

Azerbaijan
Baku
O. Abdinov, F. Ahmadov, N. Huseynov, F. Khalil-zada

Brazil
Rio de Janeiro UF
Y. Amaral Coutinho, L.P. Caloba, C. Maidantchik, F. Marroquim, A.A. Nepomuceno, J.M. Seixas

UFJF
A.S. Cerqueira, L. Manhaes de Andrade Filho

UFSJ
M.A.B. do Vale

USP
M. Donadelli, M.A.L. Leite

Canada

Alberta

A.I. Butt, K. Chan, D.M. Gingrich, R.W. Moore, J.L. Pinfold, A. Saddique, A. Sbrizzi, HS. Subramania, F. Vives Vaque

Carleton

A. Bellerive, G. Cree, D. Di Valentino, T. Koffas, J. Lacey, J.F. Marchand, T.G. McCarthy, F.G. Oakham, F. Tarrade, R. Ueno, M.G. Vincter, K. Whalen

McGill

C. Belanger-Champagne, B. Chapleau, S. Cheatham, F. Corriveau, R. Mantifel, S.H. Robertson, M.C. Stockton, M. Stoebe, B. Vachon, K. Wang, A. Warburton

Montreal

J-F. Arguin, N. Asbah, G. Azuelos, J. Bouchami, F. Dallaire, M. Davies, L. Gauthier, M. Giunta, C. Leroy, R. Rezvani, P. Soueid

Simon Fraser Burnaby

E. Dawe, J. Godfrey, J. Kvita, D.C. O'Neil, M. Petteni, B. Stelzer, A.J. Tanasijczuk, H. Torres, M. Trottier-McDonald, J. Van Nieuwkoop, M.C. Vetterli

TRIUMF

G. Azuelos, A. Canepa, S.V. Chekulaev, D. Fortin, D.M. Gingrich, A. Koutsman, F.G. Oakham, E. Perez Codina, P. Savard, D. Schouten, R. Seuster, O. Stelzer-Chilton, R. Tafirout, I.M. Trigger, M.C. Vetterli

Toronto

O.S. AbouZeid, B. Brelier, T. Farooque, B. Fatholahzadeh, N. Ilic, J. Keung, P. Krieger, G. Mc Goldrick, R.S. Orr, R. Polifka, M.S. Rudolph, P. Savard, S. Schramm, P. Sinervo, T. Spreitzer, J. Taenzer, R.J. Teuscher, P.D. Thompson, W. Trischuk, N. Venturi

Vancouver UBC

W. Fedorko, C. Gay, Z. Gecse, S.B. King, A. Lister, C.W. Loh, W.J. Mills, S. Swedish, S. Viel

Victoria

J. Albert, V. Bansal, F. Berghaus, F.U. Bernlochner, L. Courneyea, C. David, M. Fincke-Keeler, R. Keeler, R. Kowalewski, M. Lefebvre, J-R. Lessard, C.P. Marino, A.C. Martyniuk, R.A. McPherson, E.A. Ouellette, J. Pearce, R. Sobie

York

J.A. Benitez Garcia, A.C. Florez Bustos, G. Palacino, W. Taylor

Chile

Santiago

E. Carquin, G. Cottin, M.A. Diaz

Valparaiso

W.K. Brooks, S. Kuleshov, R. Pezoa, F. Prokoshin, R. White

China

Beijing

Y. Bai, Y. Fang, S. Jin, F. Lu, Q. Ouyang, L.Y. Shan, J. Wang, D. Xu, L. Yao, X. Zhuang

Hefei

J. Gao, L. Han, Y. Jiang, B. Li, J.B. Liu, K. Liu, M. Liu, Y. Liu, H. Peng, C. Xu, L. Xu, Z. Zhao, Y. Zhu

Nanjing
S. Chen

Shandong
C. Feng, P. Ge, L.L. Ma, X. Zhang, C.G. Zhu

Shanghai
H. Yang

Colombia
UAN Bogota
M. Losada, L. Mendoza Navas, G. Navarro, C. Sandoval

Czech Republic
Olomouc
P. Hamal, M. Hrabovsky, L. Nozka

Prague AS
J. Chudoba, J. Hejbal, T. Jakoubek, O. Kepka, A. Kupco, V. Kus, M. Lokajicek, R. Lysak, M. Marcisovsky, M. Mikestikova, M. Myska, S. Nemecek, D. Roda Dos Santos, P. Ruzicka, P. Sicho, P. Staroba, M. Svatos, M. Tasevsky, T. Tic, V. Vrba

Prague CTU
K. Augsten, P. Gallus, J. Gunther, J. Jakubek, Z. Kohout, V. Kral, S. Pospisil, V. Simak, T. Slavicek, K. Smolek, M. Solar, J. Solc, B. Sopko, V. Sopko, M. Suk, D. Turecek, V. Vacek, M. Vlasak, P. Vokac, Z. Vykydal, M. Zeman

Prague CU
P. Balek, P. Berta, I. Chalupkova, T. Davidek, J. Dolejsi, Z. Dolezal, E. Fullana Torregrosa, P. Kodys, R. Leitner, J. Novakova, V. Pleskot, M. Rybar, M. Spousta, T. Sykora, P. Tas, S. Todorova-Nova, S. Valkar, V. Vorobel

Denmark
Copenhagen NBI
A. Alonso, N. Boelaert, M. Dam, G. Galster, K. Gregersen, J.B. Hansen, J.D. Hansen, J.R. Hansen, P.H. Hansen, S. Heisterkamp, S. Jakobsen, M.D. Joergensen, P. Kadlecik, A.E. Loevschall-Jensen, S. Mehlhase, J. Monk, T.C. Petersen, A. Pingel, M. Simonyan, L.A. Thomsen, C. Wiglesworth, S. Xella

France
Annecy LAPP
N. Berger, M. Delmastro, L. Di Ciaccio, T.K.O. Doan, S. Elles, C. Goy, T. Hryn'ova, S. Jézéquel, H. Keoshkerian, R. Lafaye, J. Levêque, V.P. Lombardo, N. Massol, E. Petit, H. Przysiezniak, E. Sauvan, M. Schwoerer, O. Simard, T. Todorov, I. Wingerter-Seez

Clermont - Ferrand
D. Boumediene, E. Busato, D. Calvet, S. Calvet, J. Donini, E. Dubreuil, N. Ghodbane, Ph. Gris, C. Guicheney, H. Liao, D. Pallin, D. Paredes Hernandez, F. Podlyski, C. Santoni, T. Theveneaux-Pelzer, L. Valery, F. Vazeille

FR-CCIN2P3 Tier-1
G. Rahal

Grenoble LPSC
S. Albrand, J. Brown, Q. Buat, B. Clement, J. Collot, S. Crépé-Renaudin, B. Dechenaux, T. Delemontex, P.A. Delsart, C. Gabaldon, M.H. Genest, J-Y. Hostachy, E. Laisne, B.T. Le, F. Ledroit-Guillon, A. Lleres, A. Lucotte, F. Malek, C. Monini, J. Stark, X. Sun, B. Trocmé

LPNHE-Paris
T. Beau, M. Bomben, S. Bordoni, G. Calderini, F. Crescioli, O. Davignon, S. De Cecco, A. Demilly, F. Derue, M.W. Krasny, D. Lacour, B. Laforge, S. Laplace, O. Le Dortz, G. Lefebvre, K. Liu, B. Malaescu, G. Marchiori, I. Nikolic-Audit, J. Ocariz, C. Rangel-Smith, M. Ridel, L. Roos, S. Trincaz-Duvoid, F. Vannucci

Marseille CPPM
L. Alio, M. Barbero, C.P. Bee, C. Bertella, N. Bousson, J.C. Clemens, Y. Coadou, F. Djama, L. Feligioni, J. Gao, D. Hoffmann, F. Hubaut, E.B.F.G. Knoops, E. Le Guirriec, B. Li, J. Maurer, E. Monnier, Y. Nagai, J. Odier, P. Pralavorio, A. Rozanov, T. Serre, M. Talby, N. Tannoury, E. Tiouchichine, S. Tisserant, J. Toth, F. Touchard, M. Ughetto, L. Vacavant

Orsay LAL
S. Abdel Khalek, A. Bassalat, S. Binet, C. Bourdarios, J.B. De Vivie De Regie, L. Duflot, M. Escalier, L. Fayard, D. Fournier, J.-F. Grivaz, T. Guillemin, S. Henrot-Versille, J. Hrivnac, L. Iconomidou-Fayard, J. Idarraga, M. Kado, N. Lorenzo Martinez, A. Lounis, N. Makovec, L. Poggioli, P. Puzo, A. Renaud, D. Rousseau, G. Rybkin, J.B. Sauvan, J. Schaarschmidt, A.C. Schaffer, E. Scifo, L. Serin, S. Simion, R. Tanaka, H.L. Tran, D. Zerwas, Z. Zhang

Saclay CEA
H. Abreu, H. Bachacou, F. Balli, F. Bauer, N. Besson, J.-B. Blanchard, N.M. Bolnet, M. Boonekamp, L. Chevalier, F. Deliot, J. Ernwein, A.I. Etienvre, E. Ferrer Ribas, A. Formica, J. Galan, P.F. Giraud, H.M.X. Grabas, P. Graffin, C. Guyot, S. Hassani, F. Jeanneau, W. Kozanecki, E. Lançon, J.F. Laporte, C. Maiani, P. Mal, J.A. Manjarres Ramos, B. Mansoulie, H. Martinez, N. Meric, J-P. Meyer, L. Mijović, E. Mountricha, V. Nguyen Thi Hong, R. Nicolaidou, A. Ouraou, A. Peyaud, P. Ponsot, E. Protopapadaki, B. Resende, C.R. Royon, L. Schoeffel, Ph. Schune, Ph. Schwemling, J. Schwindling, D. Tsionou, N. Vranjes, M. Xiao, C. Xu

Georgia
Tbilisi IP
E.G. Tskhadadze

Tbilisi SU
T. Djobava, J. Khubua, G. Mchedlidze, M. Mosidze

Germany
Berlin HU
M. Aliev, E. Bergeaas Kuutmann, F.M. Giorgi, S. Grancagnolo, G.H. Herbert, R. Herrberg-Schubert, I. Hristova, O. Kind, H. Kolanoski, R. Kwee, H. Lacker, M. Leyton, T. Lohse, A. Nikiforov, P. Rieck, H. Schulz, D. Wendland, M. zur Nedden

Bonn
T. Abajyan, O. Arslan, M. Backhaus, P. Bechtle, I. Brock, M. Cristinziani, W. Davey, K. Desch, J. Dingfelder, W. Ehrenfeld, G. Gaycken, Ch. Geich-Gimbel, J. Glatzer, L. Gonella, P. Haefner,

S. Hageboeck, M. Havranek, D. Hellmich, S. Hillert, F. Huegging, J. Janssen, G. Khoriauli, P. Koevesarki, V.V. Kostyukhin, J.K. Kraus, J. Kroseberg, H. Krüger, C. Lapoire, M. Lehmacher, A.M. Leyko, J. Liebal, C. Limbach, T. Loddenkoetter, S. Mergelmeyer, K. Mueller, G. Nanava, T. Nattermann, A.-E. Nuncio-Quiroz, D. Pohl, S. Psoroulas, B. Sarrazin, S. Schaepe, M.J. Schultens, T. Schwindt, F. Scutti, J.A. Stillings, J. Therhaag, J.-W. Tsung, K. Uchida, M. Uhlenbrock, P. Urquijo, A. Vogel, E. von Toerne, P. Wagner, T. Wang, N. Wermes, P. Wienemann, L.A.M. Wiik-Fuchs, K.H. Yau Wong, R. Zimmermann, S. Zimmermann

DESY
S. Argyropoulos, I. Bloch, S. Borroni, J.A. Dassoulas, J. Dietrich, V. Ferrara, M. Filipuzzi, C. Friedrich, A. Glazov, L.S. Gomez Fajardo, J. Goncalves Pinto Firmino Da Costa, K-J. Grahn, I.M. Gregor, A. Grohsjean, K.H. Hiller, A. Huettmann, M. Jimenez Belenguer, J. Katzy, T. Kono, T. Kuhl, C. Lange, M. Lisovyi, E. Lobodzinska, D. Ludwig, M. Medinnis, S. Mättig, K. Mönig, T. Naumann, T. Perez Cavalcanti, R.F.Y. Peters, S.M. Piec, V. Radescu, I. Rubinskiy, G. Sedov, S. Shushkevich, D. South, M. Stanescu-Bellu, M.M. Stanitzki, P. Starovoitov, N.A. Styles, K. Tackmann, P. Vankov, M. Viti, C. Wasicki, M.A. Wildt, E. Yatsenko, E. Yildirim, H. Zhu

Dortmund
M. Bunse, I. Burmeister, H. Esch, C. Gössling, J. Jentzsch, C.A. Jung, R. Klingenberg, I. Reisinger, T. Wittig

Dresden
P. Anger, P. Czodrowski, F. Friedrich, J.P. Grohs, C. Gumpert, M. Kobel, K. Leonhardt, W.F. Mader, M. Morgenstern, X. Prudent, C. Rudolph, U. Schnoor, F. Seifert, P. Steinbach, A. Straessner, A. Vest, S. Wahrmund

Freiburg
G. Aad, S. Amoroso, T. Barber, R. Bernhard, M. Boehler, R. Bruneliere, F. Buehrer, V. Consorti, A. Di Simone, M. Fehling-Kaschek, M. Flechl, C. Giuliani, G. Herten, K. Jakobs, P. Jenni, A.K. Kopp, S. Kuehn, K. Köneke, S. Lai, U. Landgraf, K. Lohwasser, R. Madar, K. Mahboubi, U. Parzefall, M. Rammensee, T.C. Rave, Z. Rurikova, N. Ruthmann, C. Schillo, E. Schmidt, M. Schumacher, F. Siegert, K. Stoerig, J.E. Sundermann, K.K. Temming, S. Thoma, V. Tsiskaridze, F.C. Ungaro, M. Venturi, I. Vivarelli, H. von Radziewski, T. Vu Anh, C. Weiser, M. Werner, S. Winkelmann, S. Zimmermann

Giessen
M. Düren, K. Kreutzfeldt, H. Stenzel

Goettingen
K. Bierwagen, U. Blumenschein, O. Brandt, D. Evangelakou, M. George, L. Graber, J. Grosse-Knetter, M. Hamer, C. Hensel, G. Kawamura, M. Keil, A. Knue, F. Kohn, N. Krieger, K. Kroeninger, B. Lemmer, E. Magradze, J. Meyer, J. Morel, O. Nackenhorst, S. Pashapour, R.F.Y. Peters, A. Quadt, A. Roe, A.L.S. Schorlemmer, L. Serkin, E. Shabalina, T. Vazquez Schroeder, J. Weingarten

Heidelberg KIP
G. Anders, V. Andrei, Y. Davygora, T.A. Dietzsch, M. Dunford, P. Hanke, J.I. Hofmann, E.-E. Kluge, H. Laier, V.S. Lang, K. Meier, F. Mueller, S. Poddar, V. Scharf, H.-C. Schultz-Coulon, R. Stamen, M. Wessels

Heidelberg PI
C.F. Anders, G. Kasieczka, R. Narayan, S. Schaetzel, S. Schmitt, A. Schoening

Heidelberg ZITI
T. Colombo, A. Kugel, N. Schroer

Mainz
O. Arnaez, W. Blum, V. Büscher, R. Caputo, F. Ellinghaus, O.C. Endner, E. Ertel, F. Fiedler, C. Goeringer, C. Handel, T. Heck, M. Hohlfeld, P.J. Hsu, T.A. Hülsing, W. Ji, M. Karnevskiy, K. Kleinknecht, S. Koenig, L. Köpke, M. Lungwitz, L. Masetti, J. Mattmann, C. Meyer, D. Moreno, S. Moritz, T. Mueller, A. Neusiedl, R. Poettgen, H.G. Sander, C. Schmitt, M. Schott, C. Schroeder, N. Schuh, U. Schäfer, E. Simioni, S. Tapprogge, S.J. Wollstadt, C. Zimmermann

Munich LMU
S. Adomeit, S. Beale, S. Becker, O. Biebel, J. Bortfeldt, P. Calfayan, B.K.B. Chow, J. de Graat, G. Duckeck, J. Ebke, J. Elmsheuser, A. Engl, C. Galea, C. Heller, R. Hertenberger, F. Legger, J. Lorenz, A. Mann, C. Meineck, T. Nunnemann, L.B. Oakes, F. Rauscher, P. Reznicek, A. Ruschke, M.P. Sanders, D. Schaile, J. Schieck, C. Schmitt, D. Vladoiu, R. Walker, J.Z. Will, J. Wittkowski, A. Zibell

Munich MPI
T. Barillari, S. Bethke, B. Bittner, J. Bronner, G. Compostella, G. Cortiana, M.J. Flowerdew, P. Giovannini, M. Goblirsch-kolb, T. Ince, A.E. Kiryunin, S. Kluth, O. Kortner, S. Kortner, H. Kroha, A. Macchiolo, A. Manfredini, S. Menke, H.G. Moser, M. Nagel, R. Nisius, H. Oberlack, C. Pahl, R. Richter, D. Salihagic, R. Sandstroem, P. Schacht, Ph. Schwegler, F. Sforza, S. Stern, S. Stonjek, S. Terzo, M. Vanadia, H. von der Schmitt, P. Weigell, A. Wildauer, D. Zanzi

Siegen
N.B. Atlay, P. Buchholz, H. Czirr, I. Fleck, B. Gaur, K. Grybel, I. Ibragimov, K. Ikematsu, M. Rammes, O. Rosenthal, V. Sipica, W. Walkowiak, M. Ziolkowski

Wuerzburg
P. Fleischmann, A. Redelbach, M. Schreyer, G. Siragusa, R. Ströhmer, J.Y.C. Tam, T. Trefzger, S.W. Weber

Wuppertal
M. Barisonzi, K. Becker, T.A. Beermann, J. Boek, T.T. Boek, T. Cornelissen, D. Duda, G. Ernis, J. Fischer, S. Fleischmann, T. Flick, K. Hamacher, T. Harenberg, D. Hirschbuehl, S. Kalinin, S. Kersten, A. Khoroshilov, S. Kohlmann, M. Mechtel, P. Mättig, M. Neumann, S. Pataraia, M. Sandhoff, G. Sartisohn, P. Sturm, W. Wagner, C. Zeitnitz

Greece
Athens
S. Angelidakis, A. Antonaki, S. Chouridou, D. Fassouliotis, N. Giokaris, P. Ioannou, K. Iordanidou, C. Kourkoumelis, A. Manousakis-Katsikakis

Athens NTU
T. Alexopoulos, M. Byszewski, M. Dris, E.N. Gazis, G. Iakovidis, K. Karakostas, N Karastathis, S. Leontsinis, S. Maltezos, E. Mountricha, K. Ntekas, E. Panagiotopoulou, Th.D. Papadopoulou, G. Tsipolitis, S. Vlachos

Thessaloniki
K. Bachas, I. Gkialas, D. Iliadis, K. Kordas, V. Kouskoura, I. Nomidis, K. Papageorgiou, C. Petridou, D. Sampsonidis

Israel
Technion Haifa
A. Di Mattia, R. Kopeliansky, E. Musto, Y. Rozen, S. Tarem

Tel-Aviv
H. Abramowicz, G. Alexander, N. Amram, A. Ashkenazi, G. Bella, O. Benary, Y. Benhammou, E. Etzion, A. Gershon, O. Gueta, N. Guttman, Y. Munwes, Y. Oren, I. Sadeh, Y. Silver, A. Soffer, N. Taiblum

Weizmann Rehovot
R. Alon, L. Barak, S. Bressler, Z.H. Citron, E. Duchovni, O. Gabizon, E. Gross, J. Groth-Jensen, D. Lellouch, L.J. Levinson, G. Mikenberg, A. Milov, D. Milstein, I. Roth, M. Shoa, O. Silbert, V. Smakhtin, O. Vitells

Italy
Bologna
L. Bellagamba, M. Bindi, D. Boscherini, A. Bruni, G. Bruni, M. Bruschi, D. Caforio, M. Corradi, S. De Castro, R. Di Sipio, L. Fabbri, M. Franchini, A. Gabrielli, B. Giacobbe, P. Grafström, M.K. Jha, I. Massa, A. Mengarelli, S. Monzani, M. Negrini, M. Piccinini, A. Polini, L. Rinaldi, M. Romano, C. Sbarra, N. Semprini-Cesari, R. Spighi, S.A. Tupputi, S. Valentinetti, M. Villa, A. Zoccoli

Cosenza
M. Capua, G. Crosetti, L. La Rotonda, V. Lavorini, A. Mastroberardino, A. Policicchio, D. Salvatore, M. Schioppa, E. Tassi

Frascati
A. Annovi, M. Antonelli, H. Bilokon, C. Capoccia, V. Chiarella, M. Curatolo, R. Di Nardo, B. Esposito, C. Gatti, S. Lauciani, P. Laurelli, G. Maccarrone, G. Pileggi, B. Ponzio, A. Sansoni, M. Testa, E. Vilucchi, G. Volpi

Genova
D. Barberis, G. Darbo, A. Favareto, A. Ferretto Parodi, G. Gagliardi, C. Gemme, E. Guido, P. Morettini, B. Osculati, F. Parodi, S. Passaggio, L.P. Rossi, C. Schiavi

Lecce
G. Chiodini, E. Gorini, N. Orlando, M. Primavera, S. Spagnolo, A. Ventura

Milano
G. Alimonti, A. Andreazza, M.I. Besana, L. Carminati, D. Cavalli, S.M. Consonni, G. Costa, M. Fanti, D. Giugni, I. Koletsou, T. Lari, L. Mandelli, F. Meloni, C. Meroni, L. Perini, C. Pizio, F. Ragusa, S. Resconi, R. Simoniello, G.F. Tartarelli, C. Troncon, R. Turra

Napoli
A. Aloisio, M.G. Alviggi, V. Canale, G. Carlino, G. Chiefari, F. Conventi, R. de Asmundis, M. Della Pietra, D. della Volpe, C. Di Donato, A. Doria, R. Giordano, P. Iengo, V. Izzo, L. Merola, S. Patricelli, E. Rossi, A. Sanchez, G. Sekhniaidze, G. Zurzolo

Pavia
D. Calabro, R. Ferrari, M. Fraternali, A. Freddi, G. Gaudio, A. Lanza, M. Livan, A. Negri, G. Polesello, D.M. Rebuzzi, A. Rimoldi, C. Scagliotti, F. Vercellati, V. Vercesi

Pisa
F. Bertolucci, V. Cavasinni, T. Del Prete, S. Donati, P. Giannetti, C. Roda, Z. Zinonos

Roma I
F. Anulli, G. Artoni, P. Bagiacchi, P. Bagnaia, C. Bini, A. D'Orazio, D. De Pedis, A. De Salvo, C. Dionisi, S. Falciano, A. Gabrielli, S. Gentile, S. Giagu, V. Ippolito, M. Kuna, F. Lacava, F. Lo Sterzo, C. Luci, L. Luminari, A. Messina, A. Nisati, E. Pasqualucci, E. Petrolo, L. Pontecorvo, M. Rescigno, S. Rosati, F. Safai Tehrani, A. Sidoti, E. Solfaroli Camillocci, R. Vari, S. Veneziano, A. Zullo

Roma II
G. Aielli, R. Cardarelli, G. Cattani, A. Di Ciaccio, B. Liberti, F. Marchese, L. Mazzaferro, A. Salamon, R. Santonico

Roma Tre
A. Baroncelli, M. Biglietti, V. Bortolotto, F. Ceradini, B. Di Micco, A. Farilla, E. Graziani, M. Iodice, D. Orestano, F. Petrucci, C. Stanescu, M. Trovatelli

Trieste ICTP
B.S. Acharya

Udine
M. Alhroob, S.F. Brazzale, M. Cobal, U. De Sanctis, M.P. Giordani, M. Pinamonti, K. Shaw, R. Soualah

Udine cluster
B.S. Acharya, M. Alhroob, S.F. Brazzale, M. Cobal, U. De Sanctis, M. Pinamonti, K. Shaw, R. Soualah

Japan
Hiroshima IT
Y. Nagasaka

KEK
Y. Arai, Y. Ikegami, M. Ikeno, H. Iwasaki, J. Kanzaki, T. Kohriki, T. Kondo, Y. Makida, S. Mitsui, K. Nagano, K. Nakamura, M. Nozaki, S. Odaka, O. Sasaki, Y. Suzuki, Y. Takubo, S. Tanaka, S. Terada, K. Tokushuku, S. Tsuno, Y. Unno, M. Yamada, A. Yamamoto, Y. Yasu

Kobe
Y. Inamaru, M. King, T. Kishimoto, T. Kitamura, H. Kurashige, R. Kurumida, T. Matsushita, A. Ochi, S. Shimizu, H. Takeda, K. Tani, I. Watanabe, Y. Yamazaki, L. Yuan

Kyoto
M. Ishino, T. Sumida, T. Tashiro

Kyoto UE
R. Takashima

Kyushu
K. Kawagoe, S. Oda, H. Otono, J. Tojo

Nagasaki
M. Shimojima

Nagoya
M. Aoki, S. Hasegawa, L. Morvaj, T. Ohshima, Y. Takahashi, M. Tomoto, J. Wakabayashi, K. Yamauchi

Okayama
I. Nakano

Osaka
K. Hanagaki, M. Hirose, J.S.H. Lee, M. Nomachi, W. Okamura, Y. Sugaya

Shinshu
Y. Hasegawa, T. Takeshita

Tokyo ICEPP
G. Akimoto, S. Asai, Y. Azuma, T. Dohmae, Y. Enari, K. Hanawa, N. Kanaya, Y. Kataoka, T. Kawamoto, S. Kazama, K. Kessoku, T. Kobayashi, Y. Komori, T. Mashimo, T. Masubuchi, H. Matsunaga, T. Nakamura, Y. Ninomiya, T. Okuyama, H. Sakamoto, Y. Sasaki, J. Tanaka, K. Terashi, I. Ueda, H. Yamaguchi, Y. Yamaguchi, S. Yamamoto, T. Yamamura, T. Yamanaka, K. Yoshihara

Tokyo MU
U. Bratzler, C. Fukunaga

Tokyo Tech
M. Ishitsuka, O. Jinnouchi, T. Kanno, M. Kuze, R. Nagai, T. Nobe

Tsukuba
K. Hara, T. Hayashi, S.H. Kim, K. Kiuchi, M. Kurata, F. Ukegawa

Waseda
T. Iizawa, N. Kimura, T. Mitani, Y. Sakurai, K. Yorita

Morocco
CNESTEN Rabat

Casablanca
D. Benchekroun, A. Chafaq, M. Gouighri, A. Hoummada, S. Lablak

Marrakesh
M. El Kacimi, D. Goujdami

Oujda
S. Boutouil, J.E. Derkaoui, M. Ouchrif, Y. Tayalati

Rabat
R. Cherkaoui El Moursli

Netherlands
Nijmegen
G.J. Besjes, S. Caron, V. Dao, N. De Groot, F. Filthaut, P.F. Klok, A.C. König, A. Salvucci

Nikhef
R. Aben, L.J. Beemster, S. Bentvelsen, E. Berglund, G.J. Bobbink, K. Bos, H. Boterenbrood, A. Castelli, A.P. Colijn, P. de Jong, C. Deluca, L. De Nooij, P.O. Deviveiros, S. Dhaliwal, P. Ferrari, S. Gadatsch, D.A.A. Geerts, F. Hartjes, N.P. Hessey, N. Hod, O. Igonkina, P. Kluit, E. Koffeman, H. Lee, T. Lenz, F. Linde, J. Mahlstedt, J. Mechnich, I. Mussche, J.P. Ottersbach, K.P. Oussoren, P. Pani, N. Ruckstuhl, N. Valencic, P.C. Van Der Deijl, R. van der Geer, H. van der Graaf, R. Van Der Leeuw, I. van Vulpen, W. Verkerke, J.C. Vermeulen, M. Vranjes Milosavljevic, M. Vreeswijk, H. Weits

Norway
Bergen
T. Buanes, T. Burgess, G. Eigen, A. Kastanas, W. Liebig, A. Lipniacka, P.L. Rosendahl, H. Sandaker, T.B. Sjursen, B. Stugu, M. Ugland

Oslo
L. Bugge, D. Cameron, B.K. Gjelsten, E. Gramstad, F. Ould-Saada, K. Pajchel, M. Pedersen, A.L. Read, O. Røhne, L. Smestad, S. Stapnes, A. Strandlie

Poland
Cracow AGH-UST
L. Adamczyk, T. Bold, W. Dabrowski, M. Dwuznik, I. Grabowska-Bold, D. Kisielewska, S. Koperny, T.Z. Kowalski, B. Mindur, M. Przybycien

Cracow IFJ PAN
E. Banas, P.A. Bruckman de Renstrom, D. Derendarz, E. Gornicki, W. Iwanski, A. Kaczmarska, K. Korcyl, Pa. Malecki, A. Olszewski, J. Olszowska, E. Stanecka, R. Staszewski, M. Trzebinski, A. Trzupek, M.W. Wolter, B.K. Wosiek, K.W. Wozniak, B. Zabinski, A. Zemla

Jagiellonian

Portugal
Portugal LIP
J.A. Aguilar-Saavedra, S.P. Amor Dos Santos, A. Amorim, N. Anjos, J. Carvalho, N.F. Castro, P. Conde Muiño, M.J. Da Cunha Sargedas De Sousa, M.C.N. Fiolhais, B. Galhardo, A. Gomes, P.M. Jorge, L. Lopes, J. Machado Miguens, A. Maio, J. Maneira, M. Oliveira, A. Onofre, A. Palma, B. Pinto, H. Santos, J.G. Saraiva, J. Silva, A. Tavares Delgado, F. Veloso, H. Wolters

Republic of Belarus
Minsk AC
S. Harkusha, Y. Kulchitsky, Y.A. Kurochkin, P.V. Tsiareshka

Minsk NC
S. Yanush

Romania
Bucharest IFIN-HH
C. Alexa, E. Badescu, S.I. Buda, I. Caprini, M. Caprini, A. Chitan, M. Ciubancan, S. Constantinescu, C.-M. Cuciuc, P. Dita, S. Dita, A. Olariu, D. Pantea, M. Rotaru, G. Stoicea, A. Tudorache, V. Tudorache

ITIM
G.A. Popeneciu

Politehnica Bucharest
G.L. Darlea

Timisoara WU

Russia
JINR Dubna
F. Ahmadov, I.N. Aleksandrov, V.A. Bednyakov, I.R. Boyko, I.A. Budagov, G.A. Chelkov, A. Cheplakov, M.V. Chizhov, D.V. Dedovich, M. Demichev, G.L. Glonti, M.I. Gostkin,

N. Huseynov, S.N. Karpov, M.Y. Kazarinov, D. Kharchenko, E. Khramov, V.M. Kotov, U. Kruchonak, Z.V. Krumshteyn, V. Kukhtin, E. Ladygin, I.A. Minashvili, M. Mineev, V.D. Peshekhonov, E. Plotnikova, I.N. Potrap, V. Pozdnyakov, N.A. Rusakovich, R. Sadykov, A. Sapronov, M. Shiyakova, V.B. Vinogradov, A. Zhemchugov, N.I. Zimin

Moscow FIAN
A.V. Akimov, I.L. Gavrilenko, A.A. Komar, R. Mashinistov, P.Yu. Nechaeva, A. Shmeleva, A.A. Snesarev, V.V. Sulin, V.O. Tikhomirov

Moscow ITEP
A. Artamonov, P.A. Gorbounov, V. Khovanskiy, P.B. Shatalov, I.I. Tsukerman

Moscow MEPhI
A. Antonov, K. Belotskiy, O. Bulekov, V.A. Kantserov, A. Khodinov, A. Romaniouk, E. Shulga, S.Yu. Smirnov, Y. Smirnov, E.Yu. Soldatov, S. Timoshenko

Moscow SU
A.S. Boldyrev, L.K. Gladilin, Y.V. Grishkevich, V.A. Kramarenko, V.I. Rud, S.Yu. Sivoklokov, L.N. Smirnova, S. Turchikhin

Novosibirsk BINP
A.V. Anisenkov, O.L. Beloborodova, V.S. Bobrovnikov, A.G. Bogdanchikov, V.F. Kazanin, A.A. Korol, V.M. Malyshev, A.L. Maslennikov, D.A. Maximov, S.V. Peleganchuk, K.Yu. Skovpen, A.M. Soukharev, A.A. Talyshev, Yu.A. Tikhonov

Petersburg NPI
O.L. Fedin, V. Gratchev, O.G. Grebenyuk, V.P. Maleev, Y.F. Ryabov, V.A. Schegelsky, E. Sedykh, D.M. Seliverstov, V. Solovyev

Protvino IHEP
A. Borisov, S.P. Denisov, R.M. Fakhrutdinov, A.B. Fenyuk, D. Golubkov, A.V. Ivashin, A.N. Karyukhin, V.A. Korotkov, A.S. Kozhin, A.A. Minaenko, A.G. Myagkov, V. Nikolaenko, A.A. Solodkov, O.V. Solovyanov, E.A. Starchenko, A.M. Zaitsev, O. Zenin

Serbia
Belgrade IP
J. Krstic, D.S. Popovic, Dj. Sijacki, Lj. Simic

Belgrade Vinca
T. Agatonovic-Jovin, I. Bozovic-Jelisavcic, P. Cirkovic, J. Mamuzic

Slovak Republic
Bratislava
R. Astalos, L. Batkova, T. Blazek, P. Federic, I. Sykora, S. Tokár, T. Ženiš

Kosice
J. Antos, D. Bruncko, J. Ferencei, E. Kladiva, P. Strizenec

Slovenia
Ljubljana
V. Cindro, M. Deliyergiyev, A. Filipčič, A. Gorišek, B.P. Kerševan, G. Kramberger, I. Mandić, B. Maček, M. Mikuž, A. Tykhonov

South Africa
Cape Town
A. Hamilton

Johannesburg
M. Aurousseau, E. Castaneda-Miranda, S. Yacoob

Witwatersrand
G.D. Carrillo-Montoya, Y. Huang, K.J.C. Leney, B.R. Mellado Garcia, W.B. Quayle, X. Ruan, O.E. Vickey Boeriu, T. Vickey

Spain
Barcelona
J. Abdallah, M. Bosman, R. Caminal Armadans, M.P. Casado, M. Cavalli-Sforza, M.C. Conidi, A. Cortes-Gonzalez, X. Espinal Curull, P. Francavilla, V. Giangiobbe, G. Gonzalez Parra, S. Grinstein, A. Juste Rozas, I. Korolkov, E. Le Menedeu, M. Martinez, L.M. Mir, J. Montejo Berlingen, J. Nadal, A. Pacheco Pages, C. Padilla Aranda, X. Portell Bueso, I. Riu, V. Rossetti, F. Rubbo, A. Succurro, S. Tsiskaridze

Madrid UA
V. Arnal, F. Barreiro, J. Cantero, H. De la Torre, J. Del Peso, C. Glasman, J. Llorente Merino, J. Terron

Spain Granada
J.A. Aguilar-Saavedra

Valencia
S. Cabrera Urbán, V. Castillo Gimenez, M.J. Costa, F. Fassi, A. Ferrer, L. Fiorini, J. Fuster, C. García, J.E. García Navarro, S. González de la Hoz, Y. Hernández Jiménez, E. Higón-Rodriguez, A. Irles Quiles, M. Kaci, C. Lacasta, V.R. Lacuesta, L. March, S. Marti-Garcia, V.A. Mitsou, M. Miñano Moya, R. Moles-Valls, M. Moreno Llácer, E. Oliver Garcia, S. Pedraza Lopez, M.T. Pérez García-Estañ, E. Romero Adam, E. Ros, J. Salt, V. Sanchez Martinez, U. Soldevila, J. Sánchez, E. Torró Pastor, A. Valero, E. Valladolid Gallego, J.A. Valls Ferrer, M. Villaplana Perez, M. Vos

Sweden
Lund
S.S. Bocchetta, L. Bryngemark, A. Floderus, A.D. Hawkins, V. Hedberg, G. Jarlskog, E. Lytken, B. Meirose, J.U. Mjörnmark, O. Smirnova, O. Viazlo, M. Wielers, T.P.A. Åkesson

Stockholm
Y. Abulaiti, K. Bendtz, O. Bessidskaia, C. Bohm, C. Clement, K. Gellerstedt, S. Hellman, K.E. Johansson, K. Jon-And, H. Khandanyan, H. Kim, P. Klimek, J. Lundberg, O. Lundberg, D.A. Milstead, T. Moa, S. Molander, A. Papadelis, A. Petridis, P. Plucinski, S.B. Silverstein, J. Sjölin, S. Strandberg, M. Tylmad, B. Åsman

Stockholm KTH
J. Jovicevic, E.S. Kuwertz, B. Lund-Jensen, A.K. Morley, J. Strandberg

Uppsala
R. Brenner, C.P. Buszello, E. Coniavitis, T. Ekelof, M. Ellert, A. Ferrari, C. Isaksson, A. Madsen, D. Pelikan

Switzerland

Bern

M. Agustoni, L.S. Ancu, H.P. Beck, C. Borer, A. Cervelli, A. Ereditato, V. Gallo, S. Haug, T. Kruker, L.F. Marti, B. Schneider, F.G. Sciacca, M.S. Weber

CERN

M. Aleksa, C. Anastopoulos, N. Andari, G. Avolio, M.A. Baak, M. Backes, D. Banfi, M. Battistin, M. Bellomo, O. Beltramello, D. Berge, M. Bianco, J. Boyd, H. Burckhart, S. Campana, M.D.M. Capeans Garrido, T. Carli, A. Catinaccio, J.R. Catmore, A. Cattai, C.A. Chavez Barajas, J.T. Childers, D. Chromek-Burckhart, A. Dell'Acqua, A. Di Girolamo, B. Di Girolamo, F. Dittus, D. Dobos, J. Dopke, A. Dudarev, M. Dührssen, N. Ellis, M. Elsing, G. Facini, P. Farthouat, P. Fassnacht, S. Franchino, D. Francis, D. Froidevaux, V. Garonne, F. Gianotti, D. Gillberg, J. Godlewski, L. Goossens, B. Gorini, H.M. Gray, M. Hauschild, R.J. Hawkings, M. Heller, C. Helsens, A.M. Henriques Correia, L. Hervas, A. Hoecker, Z. Hubacek, M. Huhtinen, M.R. Jaekel, H. Jansen, P. Jenni, R.M. Jungst, M. Kaneda, T. Klioutchnikova, K. Lantzsch, M. Lassnig, G. Lehmann Miotto, B. Lenzi, D. Macina, S. Malyukov, L. Mapelli, B. Martin, A. Messina, J. Meyer, S. Michal, A. Molfetas, G. Mornacchi, A.M. Nairz, Y. Nakahama, G. Negri, M. Nessi, M. Nordberg, C.C. Ohm, S. Palestini, T. Pauly, H. Pernegger, B.A. Petersen, K. Peters, K. Pommès, A. Poppleton, G. Poulard, S. Prasad, M. Raymond, C. Rembser, L. Rodrigues, S. Roe, D. Salek, A. Salzburger, D.O. Savu, T. Scanlon, S. Schlenker, K. Schmieden, C. Serfon, A. Sfyrla, C.A. Solans, G. Spigo, G.A. Stewart, F.A. Teischinger, H. Ten Kate, L. Tremblet, A. Tricoli, C. Tsarouchas, G. Unal, W. Vandelli, D. van der Ster, N. van Eldik, R. Vigne, R. Voss, R. Vuillermet, P.S. Wells, T. Wengler, S. Wenig, P. Werner, H.G. Wilkens, F. Winklmeier, J. Wotschack, L. Zwalinski

Geneva

G. Alexandre, G. Barone, P.J. Bell, W.H. Bell, E. Benhar Noccioli, J. Bilbao De Mendizabal, F. Bucci, R. Camacho Toro, A. Clark, C. Doglioni, D. Ferrere, S. Gadomski, S. Gonzalez-Sevilla, M.P. Goulette, J.L. Gramling, F. Guescini, G. Iacobucci, A. Katre, A. La Rosa, B. Martin dit Latour, P. Mermod, C. Mora Herrera, D. Muenstermann, S. Nektarijevic, M. Nessi, K. Nikolics, A. Picazio, M. Pohl, G. Pásztor, K. Rosbach, S. Vallecorsa, X. Wu

Taiwan

Taipei AS

S. Hou, D.O. Jamin, C.A. Lee, S.C. Lee, B. Li, S.C. Lin, B. Liu, D. Liu, R. Mazini, D.A. Soh, P.K. Teng, J. Wang, S.M. Wang, Z. Weng, L. Zhang

Turkey

Ankara

O. Cakir, A.K. Ciftci, R. Ciftci, H. Duran Yildiz, S. Kuday

Bogazici Istanbul

M. Arik, S. Istin, V.E. Ozcan

Dogus

S.A. Cetin

Gazi

M. Yilmaz

Gaziantep

A. Beddall, A.J. Beddall, A. Bingul

TOBB
S. Sultansoy

Turkey Atomic EA

United Kingdom
Birmingham
B.M.M. Allbrooke, L. Aperio Bella, H.S. Bansil, J. Bracinik, D.G. Charlton, A.S. Chisholm, A.C. Daniells, C.M. Hawkes, S.J. Head, S.J. Hillier, T. Mclaughlan, R.D. Mudd, J.A. Murillo Quijada, P.R. Newman, K. Nikolopoulos, J.D. Palmer, M. Slater, J.P. Thomas, P.D. Thompson, P.M. Watkins, A.T. Watson, M.F. Watson, J.A. Wilson

Cambridge
S. Ask, N. Barlow, J.R. Batley, F.M. Brochu, W. Buttinger, J.R. Carter, J.D. Chapman, S.T. French, J.A. Frost, T.P.S. Gillam, J.C. Hill, S. Kaneti, T.J. Khoo, C.G. Lester, V. Moeller, T. Mueller, M.A. Parker, D. Robinson, T. Sandoval, M. Thomson, C.P. Ward, S. Williams

Edinburgh
W. Bhimji, T.M. Bristow, A.G. Buckley, P.J. Clark, C. Debenedetti, N.C. Edwards, F.M. Garay Walls, R.D. Harrington, A. Korn, V.J. Martin, B.J. O'Brien, S.A. Olivares Pino, M. Proissl, A. Schaelicke, K.E. Selbach, B.H. Smart, A. Washbrook, B.M. Wynne

Glasgow
S.E. Allwood-Spiers, R.L. Bates, D. Britton, P. Bussey, C.M. Buttar, A. Buzatu, C. Collins-Tooth, S. D'Auria, T. Doherty, A.T. Doyle, S. Ferrag, J. Ferrando, D.E. Ferreira de Lima, A. Gemmell, U. Gul, N.G. Gutierrez Ortiz, D. Kar, A. Moraes, V. O'Shea, C. Oropeza Barrera, D. Quilty, T. Ravenscroft, A. Robson, R.D. St. Denis, G. Steele, A.S. Thompson, K. Wraight, M. Wright

Lancaster
L.J. Allison, A.E. Barton, G. Borissov, E.V. Bouhova-Thacker, A. Chilingarov, W.J. Dearnaley, H. Fox, K. Grimm, R.C.W. Henderson, G. Hughes, R.W.L. Jones, V. Kartvelishvili, R.E. Long, P.A. Love, H.J. Maddocks, M. Smizanska, J. Walder

Liverpool
P.P. Allport, A.C. Bundock, S. Burdin, M. D'Onofrio, P. Dervan, C.B. Gwilliam, H.S. Hayward, J.N. Jackson, M. Jackson, T.J. Jones, B.T. King, M. Klein, U. Klein, J. Kretzschmar, P. Laycock, A. Lehan, S. Mahmoud, S.J. Maxfield, A. Mehta, S. Migas, J. Price, Y.J. Schnellbach, G. Sellers, J.H. Vossebeld, P. Waller, B. Wrona

London QMUL
M. Bona, L. Cerrito, K. Ellis, G. Fletcher, J.R. Goddard, R. Hickling, M.P.J. Landon, S.L. Lloyd, J.D. Morris, E. Piccaro, E. Rizvi, G. Salamanna, G. Snidero, M. Teixeira Dias Castanheira

London RHBNC
M.A. Alam, T. Berry, V. Boisvert, T. Brooks, R. Cantrill, N.J. Cooper-Smith, G. Cowan, L. Duguid, C.A. Edwards, S. George, S.M. Gibson, R. Gonçalo, J.G. Panduro Vazquez, Fr. Pastore, M. Rose, F. Spanò, P. Teixeira-Dias

London UC
S. Baker, P. Bernat, S.P. Bieniek, J.M. Butterworth, M. Campanelli, D. Casadei, R.T. Chislett, I.A. Christidi, B.D. Cooper, A.R. Davison, E. Dobson, C. Gutschow, G.G. Hesketh, E. Jansen, N. Konstantinidis, L. Lambourne, M. Nash, E. Nurse, M.I. Ochoa, A.D. Pilkington, R. Prabhu, P. Sherwood, B. Simmons, C. Taylor, D.R. Wardrope, B.M. Waugh, P.A. Wijeratne

Manchester
J. Almond, M. Borri, G. Brown, V. Chavda, B.E. Cox, C. Da Via, A. Forti, J. Howarth, K.D. Joshi, J.A. Klinger, F.K. Loebinger, J. Masik, T.J. Neep, A. Oh, M. Owen, J.R. Pater, J.E.M. Robinson, L. Tomlinson, S. Watts, S. Webb, M.J. Woudstra, T.R. Wyatt, U.K. Yang

Oxford
R. Apolle, A.J. Barr, C.R. Boddy, J. Buchanan, R.M. Buckingham, A.M. Cooper-Sarkar, A. Dafinca, E. Davies, E.J. Gallas, S. Gupta, C. Gwenlan, D. Hall, C.P. Hays, J. Henderson, J. Howard, T.B. Huffman, C. Issever, R.S.B. King, L.A. Kogan, A. Larner, A. Lewis, Z. Liang, S.S.A. Livermore, C. Mattravers, R.B. Nickerson, K. Pachal, A. Pinder, A. Robichaud-Veronneau, N.C. Ryder, C. Sawyer, D. Short, J.C-L. Tseng, T. Vickey, G.H.A. Viehhauser, A.R. Weidberg, C.J.S. Young, J. Zhong

RAL
T. Adye, R. Apolle, J.T. Baines, B.M. Barnett, S. Burke, E. Davies, A. Dewhurst, D. Emeliyanov, B.J. Gallop, C.N.P. Gee, S.J. Haywood, J. Kirk, C. Mattravers, S.J. McMahon, R.P. Middleton, W.J. Murray, M. Nash, P.W. Phillips, D.P.C. Sankey, W.G. Scott, F.J. Wickens, M. Wielers

Sheffield
D. Costanzo, T. Cuhadar Donszelmann, I. Dawson, G.T. Fletcher, M.C. Hodgkinson, P. Hodgson, P. Johansson, E.V. Korolkova, B. Lopez Paredes, J.A. Mcfayden, P.S. Miyagawa, S. Owen, E. Paganis, K. Suruliz, D.R. Tovey, A. Tua

Sussex
V. Bartsch, A. De Santo, Z.J. Grout, S. Martin-Haugh, C.J. Potter, A. Rose, F. Salvatore, I. Santoyo Castillo, M.R. Sutton

Warwick
S.M. Farrington, P.F. Harrison, M. Janus, C. Jeske, G. Jones, T.A. Martin, E. Pianori

United States of America
Albany
W. Edson, J. Ernst, S. Guindon, V. Jain

Argonne
L. Asquith, B. Auerbach, R.E. Blair, S. Chekanov, E.J. Feng, A.T. Goshaw, T. LeCompte, J. Love, D. Malon, D.H. Nguyen, L. Nodulman, A. Paramonov, L.E. Price, J. Proudfoot, R.W. Stanek, P. van Gemmeren, A. Vaniachine, R. Yoshida, J. Zhang

Arizona
E. Cheu, K.A. Johns, V. Kaushik, C.L. Lampen, W. Lampl, R. Leone, P. Loch, F. O'grady, J.P. Rutherfoord, F. Rühr, M.A. Shupe, E.W. Varnes, J. Veatch

Arlington UT
A. Brandt, D. Côté, S. Darmora, K. De, A. Farbin, J. Griffiths, H.K. Hadavand, L. Heelan, C.M. Hernandez, M. Maeno, P. Nilsson, N. Ozturk, R. Pravahan, E. Sarkisyan-Grinbaum, M. Sosebee, A.R. Stradling, G. Usai, A. Vartapetian, A. White, J. Yu

Berkeley LBNL
A.M. Bach, R.M. Barnett, J. Beringer, J. Biesiada, G. Brandt, P. Calafiura, L.M. Caminada, A. Cerri, F. Cerutti, A. Ciocio, R.N. Clarke, M. Cooke, K. Copic, S. Dube, K. Einsweiler, M. Garcia-Sciveres, M. Gilchriese, C. Haber, M. Hance, B. Heinemann, I. Hinchliffe, M. Hurwitz, W. Lavrijsen, C. Leggett, P. Loscutoff, Z. Marshall, A. Ovcharova, S. Pagan Griso,

K. Potamianos, A. Pranko, D.R. Quarrie, M. Shapiro, L.A. Skinnari, A. Sood, M.J. Tibbetts, V. Tsulaia, D. Varouchas, J. Virzi, D.R. Yu

Boston
S.P. Ahlen, C. Bernard, K.M. Black, J.M. Butler, L. Dell'Asta, L. Helary, M. Kruskal, J.T. Shank, Z. Yan, S. Youssef

Brandeis
S. Aefsky, C. Amelung, M. Ben Moshe, J.R. Bensinger, L. Bianchini, C. Blocker, L. Coffey, R.K. Daya-Ishmukhametova, A. Dushkin, E.A. Fitzgerald, S. Gozpinar, K. Hashemi, D. Pomeroy, G. Sciolla, S. Zambito

Brookhaven BNL
D.L. Adams, K. Assamagan, M. Begel, H. Chen, V. Chernyatin, R. Debbe, M. Ernst, T. Gadfort, H.A. Gordon, X. Hu, A. Klimentov, A. Kravchenko, F. Lanni, D. Lynn, T. Maeno, H. Ma, J. Metcalfe, P. Nevski, H. Okawa, D. Oliveira Damazio, F. Paige, S. Panitkin, M.-A. Pleier, V. Polychronakos, S. Protopopescu, M. Purohit, S. Rajagopalan, G. Redlinger, J. Schovancova, S. Snyder, P. Steinberg, H. Takai, M.C. Tamsett, N. Triplett, A. Undrus, T. Wenaus, S. Ye, A. Zaytsev

Chicago
J. Alison, K.J. Anderson, A. Boveia, F. Canelli, Y. Cheng, G. Choudalakis, M. Fiascaris, R.W. Gardner, I. Jen-La Plante, A. Kapliy, H.L. Li, S. Meehan, C. Melachrinos, F.S. Merritt, C. Meyer, D.W. Miller, Y. Okumura, P.U.E. Onyisi, M.J. Oreglia, B. Penning, J.E. Pilcher, M.J. Shochet, L. Tompkins, J.M. Tuggle, I. Vukotic, J.S. Webster

Columbia
A. Altheimer, T. Andeen, A. Angerami, T. Bain, G. Brooijmans, Y. Chen, B. Cole, J. Guo, D. Hu, E.W. Hughes, N. Nikiforou, J.A. Parsons, A. Penson, D.V. Perepelitsa, M.I. Scherzer, M. Spousta, E.N. Thompson, F. Tian, P.M. Tuts, D. Urbaniec, E. Williams, E. Wulf, L. Zhou

Dallas SMU
T. Cao, K. Dindar Yagci, A. Firan, J. Hoffman, S. Kama, R. Kehoe, A.S. Randle-Conde, R.R. Rios, S.J. Sekula, R. Stroynowski, H. Wang, J. Ye

Dallas UT
M. Ahsan, J.M. Izen, X. Lou, H. Namasivayam, K. Reeves, W.C. Wong

Duke
A.T.H. Arce, D.P. Benjamin, A. Bocci, B. Cerio, K.D. Finelli, E. Kajomovitz, A. Kotwal, M.K. Kruse, S. Li, M. Liu, S.H. Oh, C.S. Pollard, C. Wang

Hampton
V.I. Vassilakopoulos

Harvard
J. Barreiro Guimarães da Costa, A. Belloni, B. Butler, P. Catastini, G. Conti, M. Franklin, J. Huth, L. Jeanty, D. Lopez Mateos, K.M. Mercurio, C. Mills, M. Morii, H.P. Skottowe, W.R. Spearman, A.L. Yen, G. Zevi della Porta

Indiana
S. Brunet, H. Evans, P. Gagnon, F. Luehring, H. Ogren, J. Penwell, J. Poveda, D. Price, D. Whittington, D. Zieminska

Iowa
D. Cinca, R.P. Gandrajula, G. Halladjian, U. Mallik, R. Mandrysch, N. Morange, Y. Pylypchenko, R. Zaidan

Iowa State
C. Chen, J. Cochran, F. De Lorenzi, F. Dudziak, N. Krumnack, S. Prell, A. Ruiz-Martinez, S. Shrestha, K. Yamamoto

Louisiana Tech
C. Bernius, R. Dhullipudi, Z.D. Greenwood, L. Sawyer, A. Sircar, R. Subramaniam, M.C. Tamsett

MIT
F.E. Taylor

Massachusetts
B. Brau, G. Colon, C. Dallapiccola, A. Meade, E.J.W. Moyse, P. Pais, E. Pueschel, T. Varol, D. Ventura, S. Willocq

Michigan
A.J. Armbruster, M.A. Chelstowska, T. Dai, E.B. Diehl, J. Dubbert, H. Feng, C. Ferretti, S. Goldfarb, D. Harper, D. Levin, L. Liu, X. Li, S.P. Mc Kee, H.A. Neal, N. Panikashvili, J. Qian, D. Scheirich, J. Searcy, R.P. Thun, S. Walch, A. Wilson, G. Wooden, Y. Wu, L. Xu, D. Zhang, B. Zhou, J. Zhu

Michigan SU
B. Alvarez Gonzalez, G. Arabidze, R. Brock, S. Caughron, P. Ge, R. Hauser, D. Hayden, J. Huston, J. Koll, J.T. Linnemann, B. Martin, B.G. Pope, R. Schwienhorst, H.J. Stelzer, D. Ta, K. Tollefson, P. True, H. Zhang

NYU New York
B. Budick, K. Cranmer, A. Haas, L. Hooft van Huysduynen, B. Kaplan, K. Karthik, R. Konoplich, A. Krasznahorkay, S. Kreiss, G.H. Lewis, A.I. Mincer, P. Nemethy, R.M. Neves, K. Prokofiev

New Mexico
I. Gorelov, M.R. Hoeferkamp, S.C. Seidel, K. Toms, R. Wang

Northern Illinois
R. Calkins, D. Chakraborty, S. Cole, J.G. Rocha de Lima, C. Suhr, A. Yurkewicz, V. Zutshi

Ohio SU
M.J. Fisher, K.K. Gan, R. Ishmukhametov, H. Kagan, R.D. Kass, H. Merritt, J. Moss, A. Nagarkar, D.T. Pignotti, Y. Yang

Oklahoma
B. Abbott, P. Gutierrez, D.K. Jana, A. Marzin, R. Meera-Lebbai, S. Norberg, M. Saleem, H. Severini, P. Skubic, J. Snow, M. Strauss

Oklahoma SU
B. Abi, A. Khanov, F. Rizatdinova, D. Sidorov, J. Yu

Oregon
J.E. Brau, E. Brost, S. Majewski, C.T. Potter, E. Ptacek, P. Radloff, A. Reinsch, M. Shamim, N.B. Sinev, D.M. Strom, E. Torrence

Pennsylvania
K. Brendlinger, J. Degenhardt, S. Fratina, S. Heim, E. Hines, T.M. Hong, B. Jackson, J. Kroll, J. Kunkle, C.M. Lester, E. Lipeles, D. Olivito, R. Ospanov, R. Reece, J. Saxon, D. Schaefer, J. Stahlman, E. Thomson, A.N. Tuna, H.H. Williams

Pittsburgh
R.M. Bianchi, J. Boudreau, C. Escobar, T. Kittelmann, J. Mueller, D. Prieur, K. Sapp, V. Savinov, R. Yoosoofmiya

SLAC
I. Aracena, J. Backus Mayes, T. Barklow, R. Bartoldus, H.S. Bawa, J.E. Black, J.G. Cogan, T. Eifert, B.G. Fulsom, Y.S. Gao, N. Garelli, P. Grenier, P. Hansson, M. Kagan, M. Kocian, T. Koi, A.J. Lowe, C. Malone, R. Mount, T.K. Nelson, G. Piacquadio, A. Salnikov, A. Schwartzman, D. Silverstein, E. Strauss, D. Su, M. Swiatlowski, M. Wittgen, C. Young

Santa Cruz UC
D.S. Damiani, A.A. Grillo, A.M. Litke, W.S. Lockman, P.M. Manning, J. Mitrevski, J. Nielsen, H.F-W. Sadrozinski, B.A. Schumm, A. Seiden

Seattle Washington
M. Beckingham, D. Blackburn, A. Coccaro, A.G. Goussiou, O.M. Harris, S.-C. Hsu, J.S. Keller, H.J. Lubatti, M. Marx, N. Rompotis, R. Rosten, J. Rothberg, M. Verducci, G. Watts

Stony Brook
A. Ahmad, S. Arfaoui, K. Chen, B. DeWilde, R. Engelmann, J.J. Goodson, V. Grassi, J.A. Gray, J. Hobbs, J. Jia, H. Li, B.E. Lindquist, P. Mastrandrea, R.L. McCarthy, S. Mohapatra, D. Puldon, M. Rijssenbeek, R.D. Schamberger, J. Stupak, D. Tsybychev

Tufts
P.H. Beauchemin, S. Hamilton, E. Meoni, A. Napier, K. Sliwa, J. Wetter

UC Irvine
S. Farrell, D. Gerbaudo, A.J. Lankford, L. Magnoni, A.S. Mete, A. Nelson, K. Rao, M. Relich, D.A. Scannicchio, M. Schernau, A. Taffard, B. Toggerson, G. Unel, M. Werth, D. Whiteson, N. Zhou

UI Urbana
M. Atkinson, A. Basye, N. Benekos, V. Cavaliere, P. Chang, J. Coggeshall, D. Errede, S. Errede, K. Lie, T.M. Liss, A. McCarn, T.C. Moore, M.S. Neubauer, I. Vichou

Wisconsin
Sw. Banerjee, X. Chen, L.R. Flores Castillo, O. Gutzwiller, A.S. Hard, H. Ji, X. Ju, L. Kashif, A. Kruse, Y. Ming, Y.B. Pan, M.I. Pedraza Morales, H. Wang, W. Wiedenmann, S.L. Wu, H. Yang, G. Zobernig

Yale
J. Adelman, O.K. Baker, S. Bedikian, C. Cuenca Almenar, J. Cummings, Z. Czyczula, S. Demers, J. Erdmann, F. Garberson, T. Golling, D. Guest, A. Henrichs, T. Lagouri, L. Lee, A.G. Leister, A. Loginov, P. Tipton, R. Wall, B. Walsh, X. Wang

Acknowlegments

We wish to offer a special acknowledgement for their important contribution to all the technical staff from all the institutes involved in the project. In particular we would like to thank: D. Attié, M. Ben Moshe, J. Bendotti, A. D'Andagora, P. Daniel-Thomas, H. Danielsson, G. De Geronimo, R. De Oliveira, J. Fried, W. Gamache, A. Giganon, S. Herlant, A. Hoffmann, B. Iankovski, P. Lenoir, N. Lupu, S. Martoiu, H. Muller, N. Nambiar, J. Narevicius, F. Perez Gomez, D. Pierrepont, O. Pizzirusso, A. Roich, A. Teixeira, A. Vdovin, and E. Vernon.

We offer our sincere appreciation for their careful review and constructive suggestions to the teams of reviewers from i) the MUON collaboration: F. Ceradini, G. Herten and F. Taylor, and ii) the ATLAS collaboration: A. Cattai, T. Doyle, K. Moenig, T. Pauly, S. Rajogopalan and C. Rembser.

We acknowledge the support of all the NSW and MUON Institutes and funding agencies.

We are greatly indebted to all CERN departments and to the LHC project for their immense efforts not only in building the LHC, but also for their direct contributions to the construction and installation of the ATLAS detector and its infrastructure. We acknowledge equally warmly all our technical colleagues in the collaborating institutions without whom the ATLAS detector could not have been built. Furthermore we are grateful to all the funding agencies which supported generously the construction and the commissioning of the ATLAS detector and also provided the computing infrastructure. The ATLAS detector design and construction has taken about fifteen years, and our thoughts are with all our colleagues who sadly could not see its final realization.

Bibliography

[1] Rossi, L. and Brüning, O., *High Luminosity Large Hadron Collider A description for the European Strategy Preparatory Group*, Tech. Rep. CERN-ATS-2012-236, CERN, Geneva, Aug, 2012.

[2] ATLAS Collaboration, *The ATLAS Experiment at the CERN Large Hadron Collider*, JINST **3** (2008) S08003.

[3] ATLAS Collaboration, *Letter of Intent for the Phase-I Upgrade of the ATLAS Experiment*, CERN-LHCC-2011-012. LHCC-I-020, Geneva, Nov, 2011.

[4] ATLAS Collaboration, *Letter of Intent for the Phase-II Upgrade of the ATLAS Experiment*, CERN-LHCC-2012-022. LHCC-I-023, Geneva, Dec, 2012. Draft version for comments.

[5] ATLAS Collaboration, *Physics at a High-Luminosity LHC with ATLAS (Update)*, ATL-PHYS-PUB-2012-004, CERN, Geneva, Oct, 2012.

[6] *ATLAS Muon Spectrometer: Technical Design Report*. Technical Design Report ATLAS. CERN, Geneva, 1997. CERN/LHCC/97-22.

[7] ATLAS Collaboration, *Measurements of the properties of the Higgs-like boson in the $WW^{(*)} \to \ell\nu\ell\nu$ decay channel with the ATLAS detector using 25 fb^{-1} of proton-proton collision data*, Tech. Rep. ATLAS-CONF-2013-030, Mar, 2013.

[8] P. Sala and A. Vannini, *The FLUGG Project*,. `http://www.fluka.org/content/tools/flugg/`.

[9] G. Aielli, G. Conti, M. Franklin, M. Ishino, L. Jeanty, K. Mercurio, M. Schernau, T. Koi, and C. Young, *Comparisons of Cavern Background Simulation and Data in the ATLAS Muon Spectrometer for Proton-Proton Collisions at $\sqrt{s} = 7$ TeV*, ATL-COM-MUON-2011-037, CERN, Geneva, Oct, 2011.

[10] H. Kroha, B. Bittner, J. Dubbert, O. Kortner, A. Manfredini, S. Ott, R. Richter, P. Schwegler, D. Zanzi, O. Biebel, A. Engl, R. Hertenberger, and A. Zibell, *Construction and Test of a Full Prototype Drift-Tube Chamber for the Upgrade of the ATLAS Muon Spectrometer at High LHC Luminosities*, Nucl.Instrum.Meth. (2012).

[11] M. Deile, H. Dietl, J. Dubbert, S. Horvat, O. Kortner, A. Manz, s. Mohrdieck, F. Rauscher, R. Richter, and A. Staude, *Performance of the ATLAS precision muon chambers under LHC operating conditions*, Nucl.Instrum.Meth. **A518** (2004) 65–68.

[12] S. Horvat, D. Kharchenko, O. Kortner, S. Kotov, H. Kroha, A. Manz, S. Mohrdieck-Mock, K. Nikolaev, R. Richter, W. Stiller, C. Valderanis, J. Dubbert, F. Rauscher, and A. Staude, *Operation of the ATLAS muon drift-tube chambers at high background rates and in magnetic fields*, IEEE Trans.Nucl.Sci. **53** (2006) 562–566.

[13] ATLAS Collaboration, A. Haas, *Simulation of physics in the presence of pile-up at the ATLAS experiment*, ATL-SOFT-SLIDE-2012-188. http://cds.cern.ch/record/1446628/files/ATL-SOFT-SLIDE-2012-188.pdf.

[14] *ATLAS Technical Coordination: Technical Design Report.* Technical Design Report ATLAS. CERN, Geneva, 1999. CERN/LHCC/90-01.

[15] V. Smakhtin, G. Mikenberg, A. Klier, Y. Rozen, E. Duchovni, E. Kajamovitz, and A. Hershenhorn, *Thin Gap Chamber upgrade for SLHC: Position resolution in a test beam*, Nucl.Instrum.Meth. **A598** (2009) 196–200.

[16] R. Veenhof, *Garfield - simulation of gaseous detectors*,. http://garfield.web.cern.ch/garfield/.

[17] S. Biagi, *A multi term Boltzmann analysis of drift velocity, diffusion, gain and magnetic field effects in argon methane water vapor mixtures*, Nucl.Instrum.Meth. **A283** (1989) 716–722.

[18] D. Lazic, N. Lupu, A. Mincer, Y. Rozen, S. Tarem, A. Breskin, R. Chechik, D. Lellouch, G. Malamud, G. Mikenberg, K. Nagai, A. Pansky, and M. Shoa, *Drift velocity in n-pentane mixtures and its influence on timing properties of thin gap chambers*, Nucl.Instrum.Meth. **A410** (1998) 159–165.

[19] N. Amram, G. Bella, Y. Benhammou, a. Diaz, E. Duchovni, E. Etzion, A. Hershenhorn, a. Klier, N. Lupu, G. Mikenberg, D. Milstein, y. Munwes, O. Sasaki, M. Shoa, V. Smakhtin, and U. Volkmann, *Position resolution and efficiency measurements with large scale Thin Gap Chambers for the super LHC*, Nucl.Instrum.Meth. **A628** (2011) 177–181, arXiv:1006.0135 [physics.ins-det].

[20] Y. Benhammou, B. Bittner, J. Dubbert, E. Duchovni, E. Etzion, A. Klier, H. Kroha, N. Lupu, G. Mikenberg, D. Milstein, Y. Munwes, O. Sasaki, P. Schwegler, M. Shoa, and V. Smakhtin, *Test of spatial resolution and trigger efficiency of a combined Thin Gap and Fast Drift Tube Chambers for high-luminosity LHC upgrades*, IEEE Nucl.Sci.Symp.Conf.Rec. **2011** (2011) 1761–1766.

[21] Y. Giomataris, P. Rebourgeard, J. Robert, and G. Charpak, *MICROMEGAS: A High granularity position sensitive gaseous detector for high particle flux environments*, Nucl.Instrum.Meth. **A376** (1996) 29–35.

[22] C. Bernet, P. Abbon, J. Ball, Y. Bedfer, E. Delagnes, A. Giganon, F. Kunne, J. Le Goff, A. Magnon, C. Marchand, D. Neyret, S. Panebianco, H. Pereira, S. Platchkov, S. Procureur, P. Rebourgeard, G. Tarte, and D. Thers, *The 40-cm x 40-cm gaseous microstrip detector Micromegas for the high-luminosity COMPASS experiment at CERN*, Nucl.Instrum.Meth. **A536** (2005) 61–69.

[23] B. Peyaud, *KABES: A novel beam spectrometer for NA48*, Nucl.Instrum.Meth. **A535** (2004) 247–252.

[24] S. Anvar, P. Baron, M. Boyer, J. Beucher, D. Calvet, et al., *Large bulk Micromegas detectors for TPC applications*, Nucl.Instrum.Meth. **A602** (2009) 415–420.

[25] P. Colas, *First test results from a Micromegas large TPC prototype*, Nucl.Instrum.Meth. **A623** (2010) 100–101.

[26] H. Raether Z. Phys.**112** 464.

[27] V. Peskov, M. Cortesi, R. Chechik, and A. Breskin, *Further evaluation of a THGEM UV-photon detector for RICH - comparison with MWPC*, JINST **5** (2010) P11004, arXiv:1008.0151 [physics.ins-det].

[28] P. Beynel, P. Maier, and H. Schonbacher, *Compilation of radiation damage test data, vol. 3. material used around hight-energy accelerators*, CERN-82-10, CERN-YELLOW-82-10, 1982.

[29] ANSYS team. http://www.ansys.com.

[30] S. Biagi, *Magboltz - transport of electrons in gas mixtures*,. http://consult.cern.ch/writeup/magboltz/.

[31] T. Alexopoulos, A. Altintas, M. Alviggi, M. Arik, S. Cetin, et al., *Development of large size Micromegas detector for the upgrade of the ATLAS muon system*, Nucl.Instrum.Meth. **A617** (2010) 161–165.

[32] A. Bay, J. Perroud, F. Ronga, J. Derré, I. Giomataris, A. Delbart, and Y. Papadopoulos, *Study of sparking in Micromegas chambers*, Nucl.Instrum.Meth. **A488** (2002) 162.

[33] D. Thers, P. Abbon, J. Ball, Y. Bedfer, C. Bernet, et al., *Micromegas as a large microstrip detector for the COMPASS experiment*, Nucl.Instrum.Meth. **A469** (2001) 133–146.

[34] J. Galan, D. Attié, E. Ferrer-Ribas, A. Giganon, I. Giomataris, S. Herlant, F. Jeanneau, A. Peyaud, P. Schune, T. Alexopoulos, M. Byszewski, G. Iakovidis, P. Iengo, K. Ntekas, S. Leontsinis, R. de Oliveira, Y. Tsipolitis, and J. Wotschack, *An aging study of resistive micromegas for the HL-LHC environment*, JINST **8** (2013) P04028, arXiv:1301.7648 [physics.ins-det].

[35] J. Galan, D. Attié, J. Derré, E. Ferrer Ribas, A. Giganon, I. Giomataris, F. Jeanneau, J. Manjarres, R. de Oliveira, P. Schune, M. Titov, and J. Wotschack, *Aging studies of Micromegas prototypes for the HL-LHC*, JINST **7** (2012) C01041, arXiv:1111.5998 [physics.ins-det].

[36] F. Jeanneau, T. Alexopoulos, D. Attié, M. Boyer, J. Derré, G. Fanourakis, E. Ferrer-Ribas, J. Galan, E. Gazis, T. Geralis, A. Giganon, I. Giomataris, S. Herlant, J. Manjarres, E. Ntomari, P. Schune, M. Titov, and G. Tsipolitis, *Performances and ageing study of resistive-anodes Micromegas detectors for HL-LHC environment*, IEEE Trans.Nucl.Sci. **59** (2012) 1711–1716, arXiv:1201.1843 [physics.ins-det].

[37] T. Alexopoulos, J. Burnens, R. de Oliveira, G. Glonti, O. Pizzirusso, P. V., G. Sekhniaidze, G. Tsipolitis, and J. Wotschack, *A spark-resistant bulk-micromegas chamber for high-rate applications*, Nucl.Instrum.Meth. **A640** (2011) 110–118.

[38] C. Alba-Simionesco et al., *The Laboratoire Léon Brillouin and the Orphée Reactor: The French National Neutron Facility*, Neutron news **22, 4** (2011) 10–13.

[39] R. Chipaux and O. Toson, *Resistance Of Lead Tungstate And Cerium Fluoride To Low Rate Gamma Irradiation Or Fast Neutrons Exposure*, CMS Technical Note CMS TN, (1995) 95–126.

[40] S. Baranov et al., *Estimation of Radiation Background, Impact on Detectors, Activation and Shielding Optimization in ATLAS*, ATL-GEN-2005-001 (2005).

[41] S. Tanaka, H. Ohshita, K. Ishii, H. Iwasaki, Y. Arataki, T. Bando, Y. Homma, M. Ishino, T. Kondo, T. Kobayashi, H. Kurashige, G. Mikenberg, Y. Miyazaki, Y. Nakagawa, H. Nanjo, M. Ikeno, M. Nozaki, A. Ochi, O. Sasaki, M. Shoa, T. Sugimoto, H. Takeda, T. Takeshita, and C. Yokoyama, *Techniques developed for the ATLAS thin gap chambers mass production in Japan*, IEEE Trans.Nucl.Sci. **51** (2004) 934–938.

[42] E. Etzion, Y. Benhammou, J. Ginzburg, M. Ishino, L. Levinson, G. Mikenberg, N. Panikashvili, D. Primor, and V. Smakhtin, *The Certification of ATLAS thin gap chambers produced in Israel and China*, `arXiv:physics/0411136 [physics]`.

[43] A. Aloisio, M. Alviggi, M. Biglietti, V. Canale, M. Caprio, G. Carlino, F. Conventi, and R. de Asmundis, *The trigger chambers of the ATLAS muon spectrometer: Production and tests*, Nucl.Instrum.Meth. **A535** (2004) 265–271.

[44] M. Beretta, G. Bobbink, P. Branchini, C. Kourkoumelis, J. Dubbert, E. N. Gazis, R. Hertenberger, P. Hurst, A. Kojine, A. Lanza, A. Marin, P. Mockett, C. Petridou, E. G. Tskhadadze, P. Valente, J. Wotschack, Y. Xie, and Z. Zhao, *MDT Commissioning Procedures Guidelines for Certifying RFI Chambers*, CERN-ATL-MUON-2004-022, CERN-ATL-COM-MUON-2004-018, CERN, Geneva, 2004.

[45] E. Etzion, Y. Benhammou, J. Ginzburg, M. Ishino, L. Levinson, G. Mikenberg, N. Panikashvili, D. Primor, V. P. Smakhtin, and S. Tarem, *The Certification of ATLAS Thin Gap Chambers Produced in Israel and China 019*, physics/0411136. ATL-COM-MUON-2004-019. TAUP-2787, CERN, Geneva, Oct, 2004.

[46] S. Aefsky, C. Amelung, J. Bensinger, C. Blocker, A. Dushkin, M. Gardner, K. Hashemi, E. Henry, B. Kaplan, P. Keselman, M. Ketchum, U. Landgraf, A. Ostapchuk, J. Rothberg, A. Schricker, N. Skvorodnev, and H. Wellenstein, *The optical alignment system of the ATLAS muon spectrometer end-caps*, JINST **3** (2008) P11005.

[47] P. J.-F. Petit, *PPSPS for the installation of the two JD/SW in the cavern UX15.* CERN, January, 2008. `https://edms.cern.ch/document/889803/1`. ATL-JD-IP-0002, EDMS 889803 v.1.

[48] A. Fallou, *JD/SW Lifting from UX15 up to SX1 Buffer Zone (RBZ).* CERN, March, 2013. `https://edms.cern.ch/document/1273366/1`. ATL-HT-OP-0020, EDMS 1273366 v.1.

[49] A. Fallou, *PPSPS - JD/SW lifting up to SX1 Buffer Zone.* CERN, February, 2013. `https://edms.cern.ch/document/1270427/1.1`. ATC-TY-EY-0401, EDMS 1270427 v.1.1.

[50] D. Forkel-Wirth, *Zonage radiologique au CERN.* CERN, December, 2006. `https://edms.cern.ch/document/810149/1`. EDMS 810149 v.1.

[51] V. Hedberg, *Opening of the Small Wheel on the JD tube.* CERN, October, 2007. `https://edms.cern.ch/document/874816/1`. ATL-JD-AP-0003, EDMS 874816 v.1.

[52] M. Raymond, *Procedure for JD rotation in SX1.* CERN, January, 2008. `https://edms.cern.ch/document/889266/1`. ATL-JD-IP-0002, EDMS 889266 v.1.

[53] G. De Geronimo, *VMM1—An ASIC for Micropattern Detectors*, IEEE Trans.Nucl.Sci. **99** (2013) 1–8.

[54] G. De Geronimo et al., *VMM1 Data-sheet*,. https://atlas-proj-tgc.web.cern.ch/atlas-proj-tgc/doc/NSWTDR/VMM1_datasheet_v3a.pdf.

[55] N. Lupu and A. Vdovin, *sTGC experience with the VMM1 Front-end ASIC*,. https://atlas-proj-tgc.web.cern.ch/atlas-proj-tgc/doc/NSWTDR/sTGC_experience_with_VMM1.pdf.

[56] P. Moreira, S. Baron, S. Bonacini, O. Cobanoglu, F. Faccio, S. Feger, R. Francisco, P. Gui, J. Li, A. Marchioro, C. Paillard, D. Porret, and K. Wyllie, *The GBT-SerDes ASIC prototype*, Journal of Instrumentation **5** no. 11, (2010) C11022. http://stacks.iop.org/1748-0221/5/i=11/a=C11022.

[57] A. Gabrielli, F. Loddo, A. Ranieri, and G. De Robertis, *Design and submission of rad-tolerant circuits for future front-end electronics at S-LHC*, Nucl.Instrum.Meth. **A612** (2010) 455–459.

[58] F. Vasey, *The Versatile Link Project Overview*,. https://atlas-proj-tgc.web.cern.ch/atlas-proj-tgc/doc/NSWTDR/VersatileLinkOverview_Vasey.pdf.

[59] P. Phillips, *ATLAS strip tracker stavelets*, JINST **7** (2012) C02028.

[60] L. Feld, W. Karpinski, K. Klein, J. Merz, J. Sammet, et al., *A DC-DC converter based powering scheme for the upgrade of the CMS pixel detector*, JINST **6** (2011) C11031.

[61] S. Dhawan, O. Baker, H. Chen, R. Khanna, J. Kierstead, et al., *Commercial buck converters and custom coil development for the ATLAS inner detector upgrade*, IEEE Trans.Nucl.Sci. **57** (2010) 456–462.

[62] ATLAS Collaboration, *The ATLAS Experiment at the CERN Large Hadron Collider*, JINST **3** (2008) S08003.

[63] L. Levinson, N. Neufeld, and J. Vermuelen, *Integrating the GBT into standard networks*,. https://atlas-proj-tgc.web.cern.ch/atlas-proj-tgc/doc/NSWTDR/IntegratingGBTs.pdf.

[64] R. Bartoldus et al., *ATCA Developments and Experience at SLAC*,. https://atlas-proj-tgc.web.cern.ch/atlas-proj-tgc/doc/NSWTDR/Bartoldus-ATCA.pdf.

[65] M. Huffer et al., *RCE Status Update*,. https://atlas-proj-tgc.web.cern.ch/atlas-proj-tgc/doc/NSWTDR/RCEStatusUpdate.pdf.

[66] S. Gameiro et al., *The ROD crate DAQ software framework of the ATLAS data acquisition system*, IEEE Trans.Nucl.Sci. **53** (2006) 907–911.

[67] A. Barriuso et al., *The detector control system of the ATLAS experiment*, JINST **3** (2008) P05006.

[68] *Simatic WinCC Open Architecture*,. http://www.automation.siemens.com/mcms/human-machine-interface/en/visualization-software/simatic-wincc-open-architecture/pages/default.aspx.

[69] *OPC Unified Architecture,*. http://www.opcfoundation.org.

[70] CAEN S.p.A., Via della Vetraia, 11, 55049 Viareggio, Province of Lucca, Italy, *Technical Information Manual, MOD. EASY3000/4000*, revision 15 ed., March, 2012. http://www.caen.it/servlet/checkCaenManualFile?Id=8294.

[71] CAEN S.p.A., Via della Vetraia, 11, 55049 Viareggio, Province of Lucca, Italy, *Technical Information Manual, MOD. A3484/A3485*, revision 2 ed., January, 2008. http://www.caen.it/servlet/checkCaenManualFile?Id=5316.

[72] CAEN S.p.A., Via della Vetraia, 11, 55049 Viareggio, Province of Lucca, Italy, *Technical Information Manual, MOD. A3535*, revision 7 ed., May, 2012. http://www.caen.it/servlet/checkCaenManualFile?Id=8386.

[73] ATLAS Muon Collaboration Collaboration, A. Polini, *Design and performance of the detector control system of the ATLAS resistive-plate-chamber muon spectrometer*, Nucl.Instrum.Meth. **A661** (2012) S15–S18.

[74] SC-GS, *The use of plastic and other non-metallic materials at CERN with respect to fire safety and radiation resistance*. CERN, November, 2005. https://edms.cern.ch/document/335806/1.02. EDMS 335806 v.102.

[75] M. Raymond, *Procèdure d'ouverture «standard»de l'expèrience*. CERN, October, 2008. https://edms.cern.ch/document/971453/1. ATL-HT-OP-0011, EDMS 971453 v.1.

[76] M. Raymond, *Overview of Atlas Standard Opening sequence*. CERN, January, 2009. https://edms.cern.ch/document/983012/1. ATL-HT-OP-0014, EDMS 983012 v.1.

[77] M. Nessi and M. Raymond, *Xmas 2011 opening schedule of operations*. CERN, August, 2011. https://edms.cern.ch/document/1159233/1. ATC-P-SC-0002, EDMS 1159233 v.1.